NLO QCD Corrections to the Polarized Photo- and Hadroproduction of Heavy Quarks

Dissertation
zur Erlangung des Grades eines
Doktors der Naturwissenschaften
der Abteilung Physik
der Universität Dortmund

vorgelegt von

Ingo Bojak

April 2000

Für meine Eltern und meinen Bruder

From the side, a whole range; from the end, a single peak;
far, near, high, low, no two parts alike.
Why can't I tell the true shape of Lu-shan?
Because I myself am in the mountain.

Su Tung-p'o, 1084 A.D.,
transl. B. Watson

Contents

List of Figures

List of Tables

Chapter 1

Introduction

A fundamental property of nucleons (protons or neutrons) is that they carry spin $\frac{1}{2}$ and obey the appropriate Fermi-Dirac statistics, i.e., they are spin-$\frac{1}{2}$ fermions. As is indicated by their name, nucleons are the building blocks of atomic nuclei, and their spin plays a crucial role in determining the properties of these nuclei. For example, we can compare ^{3}H made up of one proton and two neutrons with ^{3}He made up of two protons and one neutron. In the dominant state of zero orbital angular momentum (S-wave) of the nucleons, the Pauli exclusion principle requires the two neutrons and the two protons, respectively, to be anti-aligned in spin. Thus we can expect that the nuclear spin effects mirror those of the unpaired nucleon. This can be seen in spin dependent quantities, like the magnetic moments: $\mu_{^3\mathrm{H}} = 2.9790 \simeq 2.7928 = \mu_p$ and $\mu_{^3\mathrm{He}} = -2.1276 \simeq -1.9130 = \mu_n$ [1, 2]. An even closer agreement is obtained when we compare

$$\frac{1}{2}\left(\mu_{^3\mathrm{H}} + \mu_{^3\mathrm{He}}\right) = 0.4257 \simeq 0.4399 = \frac{1}{2}\left(\mu_p + \mu_n\right) \ , \tag{1.1}$$

since then the difference in the interactions of protons and neutrons averages out. The remaining deviation can be attributed to higher orbital angular momentum states. Though spin certainly is an important property of the nucleon, as our little example has shown, the explanation of its origin is still fraught with uncertainties.

Since the advent of the QCD improved parton model, we know that the nucleon is not an elementary particle itself, but rather a bound state of more elementary particles (quarks, antiquarks and gluons) possessing rich internal structure. Hence high energy studies of the nucleon spin have always been challenging experimentally and theoretically. Determining the polarized gluon density $\Delta g(x, \mu_f^2)$ is currently a hot topic in this field. In order to better understand how the gluon polarization became a major issue, we will briefly sketch the historical development, starting with quark models which do not contain gluons at all. Several reviews of spin physics have been written, which offer a very complete account of the past and present status, see for example [3, 4]. In these references one can find the details we are omitting here. Take a simple valence quark model in which the entire nucleon spin is generated by two u_v-quarks plus one d_v-quark for the proton and by two d_v-quarks plus one u_v-quark for the neutron. We assume that there is no orbital angular momentum of the quarks and that the sea quarks carry no net spin. Since the quarks are spin-$\frac{1}{2}$ particles, the Pauli exclusion principle would require again that the spins of the two quarks with same flavor have to be anti-aligned, so that the nucleon spin would mirror the spin of the unpaired quark, in complete analogy to the ^{3}H and ^{3}He case. However, this simple picture cannot be true: the Ω^- baryon has spin $\frac{3}{2}$ and consists of three strange quarks in an S-wave. Thus it has three spin aligned quarks of the same flavor in spite of the Pauli exclusion principle! The solution is of course the new quantum number "color" of $SU(3)_{\text{color}}$. If the three s-quarks of the Ω^- all carry *different* color, then they can occupy the same spin state. But the direct relation of the nucleon spin to the spin of the unpaired quark is now lost, since there is no reason why color should not play a similar rôle in this case as well.

So let us just generally assume that color guarantees the absence of completely identical fermions in the wave function. Then we have to consider contributions of *both* valence quark flavors to the nucleon spin. The total polarization of quarks with flavor q will be denoted by Δq and similarly for the antiquarks. The total valence quark polarizations are then given by $\Delta u_v = \Delta u - \Delta\bar{u}$ and $\Delta d_v = \Delta d - \Delta\bar{d}$. Hence we expect[1]

$$\frac{1}{2}\Big|_{\text{proton}} \stackrel{!}{=} \frac{1}{2}\sum_q(\Delta q + \Delta\bar{q}) \equiv \frac{1}{2}\Delta\Sigma \tag{1.2}$$

$$\stackrel{!}{=} \frac{1}{2}(\Delta u_v + \Delta d_v)\ . \tag{1.3}$$

In (1.2) we have assumed that the quarks carry the spin and in (1.3) that the sea quarks have no net polarization. The same relation holds also for the neutron, but we have to exchange u- and d-quarks due to isospin symmetry. So we can write for the magnetic moments

$$\mu_p = \mu_u\Delta u_v + \mu_d\Delta d_v\ , \qquad \mu_n = \mu_d\Delta u_v + \mu_u\Delta d_v\ , \tag{1.4}$$

where we always use the polarizations for a *proton*. In a $SU(6)$ model compatible[2] with (1.3), which is constructed from $SU(3)_{\text{flavor}}\otimes SU(2)_{\text{spin}}$, we find for the $SU(6)$-symmetric wave function $\Delta u_v = \frac{4}{3}$ and $\Delta d_v = -\frac{1}{3}$, see for example [5]. Using the simple assumption $\mu_u = -2\mu_d$, because of the difference in charge $e_u = -2e_d$, one finally predicts with (1.4)

$$\frac{\mu_n}{\mu_p} = -\frac{2}{3} \stackrel{\text{exp.}}{\simeq} -0.685\ , \tag{1.5}$$

in fairly good agreement with experiment.

But this naïve model soon runs into difficulties when being compared to other experimental results. For example it predicts for the β-decay constants $F = \frac{2}{3}$ and $D = 1$, in

[1]The model is flawed, since it makes no distinction between constituent and current quarks.
[2]One obtains $\Delta\bar{u} = \Delta\bar{d} = \Delta s = \Delta\bar{s} = 0$ for $SU(6)$ symmetry.

conflict with the experimental[3] measurements [1, 6]

$$\begin{aligned} &\text{neutron } \beta-\text{decay:} \quad F+D = 1.2670 \pm 0.0035 \,, \\ &\text{hyperon } \beta-\text{decay:} \quad 3F-D = 0.579 \pm 0.025 \,. \end{aligned} \tag{1.6}$$

One can try to fix the problem by rewriting (1.2) as

$$\frac{1}{2}\Big|_{\text{proton}} = \frac{1}{2}\Delta\Sigma + L_z^q \,, \tag{1.7}$$

where we now introduce the orbital angular momentum of the quarks L_z^q as a relativistic effect [7, 8]. For vanishing strange sea polarization $\Delta s = \Delta\bar{s} = 0$, we have $\Delta\Sigma = 3F - D$ and hence we can accommodate the experimental result by assigning $L_z^q = 0.2105$, which indicates a sizeable contribution of quark orbital angular momentum to the proton spin!

In order to understand the impact of the next experimental result, we need to take strange quarks into account explicitly

$$\begin{aligned} F + D &\overset{SU(2)}{\underset{\text{isospin}}{=}} A_3 = \Delta u + \Delta\bar{u} - \Delta d - \Delta\bar{d} \,, \\ 3F - D &\overset{SU(3)}{\underset{\text{flavor}}{=}} A_8 = \Delta u + \Delta\bar{u} + \Delta d + \Delta\bar{d} - 2(\Delta s + \Delta\bar{s}) \,, \\ A_0 &= \Delta\Sigma \equiv \sum_q (\Delta q + \Delta\bar{q}) = A_8 + 3(\Delta s + \Delta\bar{s}) \,. \end{aligned} \tag{1.8}$$

The first moment of the structure function g_1 measured in lepton-nucleon scattering, for details see for example [4], can be written in this form

$$\Gamma_1^{p,n} = \frac{1}{2}\left(\pm\frac{1}{6}A_3 + \frac{1}{18}A_8 + \frac{2}{9}A_0\right) = \left\{\begin{matrix} 0.186 \pm 0.004 \\ -0.025 \pm 0.004 \end{matrix}\right\} + \frac{1}{3}(\Delta s + \Delta\bar{s}) \,, \tag{1.9}$$

by simply inserting the values of (1.6). In the QCD improved parton model discussed below, (1.8) and (1.9) remain valid in LO for the first moments of the parton densities. We can now derive the (Gourdin-)Ellis-Jaffe sum rule [9] $\Gamma_{1,\text{EJ}}^p \simeq 0.186$ by *assuming* $\Delta s = \Delta\bar{s} = 0$ in (1.9). However, in the Bjørken sum rule [10] for the difference $\Gamma_1^p - \Gamma_1^n = \frac{1}{6}(F + D) \simeq 0.2112$, the dependence on the strange quarks and on A_8 cancels, so that this result relies *only* on isospin symmetry. The combined experimental result of the EMC and SLAC collaborations[4], see [11] and references therein, disagrees with the Ellis-Jaffe prediction

$$\Gamma_1^p = 0.126 \pm 0.018 \quad \curvearrowright \quad \Delta s + \Delta\bar{s} \simeq -0.18 \quad \curvearrowright \quad \Delta\Sigma = 0.04 \,. \tag{1.10}$$

[3] The hyperon β-decay fit of [6] was performed using $F + D \overset{!}{=} 1.257$ and fitting F/D. With the new experimental value $F + D = 1.2670$ and their old value $3F - D = 0.579$, we obtain $F/D = 0.573$ instead of their old fitted $F/D = 0.575 \pm 0.016$. Thus a re-fit is not needed for our purposes here.

[4] We ignore the $\langle Q^2\rangle = 10.7$ GeV^2 (EMC), 4 GeV^2 (SLAC) dependence for the moment and add statistical and systematic errors in quadrature.

So experiment suggests that a large negative strange sea polarization drives the contribution of the quarks to the proton spin to basically zero: $\Delta\Sigma \simeq 0$! Later experiments agree within errors with this result, see for example [4].

This counter-intuitive result triggered the famous "spin crisis", though it should have been more appropriately named "spin surprise" and "intuition crisis", because there is a priori nothing wrong with the solution we have obtained in (1.10). But we certainly have come a long way from the naïve assumption $\Delta\Sigma = 1$ we started with in (1.2). By inspecting the equations (1.8) and (1.9), we find that one still can achieve a $\Delta s = \Delta\bar{s} = 0$ solution, *if* the $SU(3)_{\text{flavor}}$ symmetry assumption $A_8 = 3F - D$ is discarded. But we must leave the quark model level of studies anyway, since we note that the Bjørken sum rule also seems to be in trouble. The SLAC E143 experiment [12] finds $\Gamma_1^p - \Gamma_1^n = 0.163 \pm 0.017$ at $Q^2 = 3$ GeV^2, to be compared with the value $\Gamma_1^p - \Gamma_1^n \simeq 0.2112$ obtained above. However, the CERN SMC measurement at $Q^2 = 10$ GeV^2 [13] gives $\Gamma_1^p - \Gamma_1^n = 0.195 \pm 0.029$ and thus agrees much better with our quark model prediction. Since the Bjørken sum rule is based only on isospin invariance, it is not as easily cast aside as the Ellis-Jaffe sum rule. A better agreement with growing Q^2 immediately suggests that *perturbative QCD* corrections may help. Indeed one finds that the perturbative QCD corrections up to $\mathcal{O}(\alpha_s^3)$ [14] are all *negative*

$$\Gamma_1^p - \Gamma_1^n = \frac{1}{6}(F+D)\left[1 - \frac{\alpha_s(Q^2)}{\pi} - 3.5833\left(\frac{\alpha_s(Q^2)}{\pi}\right)^2 - 20.2153\left(\frac{\alpha_s(Q^2)}{\pi}\right)^3\right] , \tag{1.11}$$

and reasonable agreement with the experiments can be achieved when a running coupling $\alpha_s(Q^2)$ is used, see [4] and references therein. But it should be clear that perturbative QCD corrections come with a price, namely scale dependence of the partons and the introduction of gluons. Also the situation with respect to the Ellis-Jaffe sum rule does *not* significantly change due to the introduction of QCD corrections, see our discussion of a QCD fit below.

In conclusion, we see that additional experimental results forced us to adopt more sophisticated theoretical approaches, until we finally made use of perturbative QCD corrections to the Bjørken sum rule. So we should now consider the complete QCD improved parton model for consistency, which in hindsight would have been a good starting point anyway. For the spin of the proton one must then write instead of (1.7)

$$\frac{1}{2}|_{\text{proton}} \stackrel{!}{=} \frac{1}{2}\Delta\Sigma_{n=1}(\mu_f^2) + \Delta g_{n=1}(\mu_f^2) + L_z^q(\mu_f^2) + L_z^g(\mu_f^2) , \tag{1.12}$$

$$\Delta\Sigma(x,\mu_f^2) \equiv \sum_q [\Delta q(x,\mu_f^2) + \Delta\bar{q}(x,\mu_f^2)] , \tag{1.13}$$

$$a_n \equiv \int_0^1 dx\; x^{n-1} a(x) , \tag{1.14}$$

which introduces polarized parton densities, $\Delta q(x,\mu_f^2)$, $\Delta\bar{q}(x,\mu_f^2)$ and $\Delta g(x,\mu_f^2)$, depending on Bjørken x and the factorization scale μ_f^2. Their definition will be examined more

μ_f^2 [GeV^2]	$\Delta\Sigma_{n=1}$	$2\Delta s_{n=1}$	$\Delta g_{n=1}$	L_z
0.34	0.183	-0.132	0.507	-0.099
1	0.173	-0.136	0.961	-0.548
4	0.168	-0.136	1.443	-1.027
10	0.166	-0.138	1.737	-1.320

Table 1.1: First moments of GRSV standard densities taken from Tab. 1 in [15]. For these densities $\Delta s_{n=1} + \Delta \bar{s}_{n=1} = 2\Delta s_{n=1}$. The total partonic angular momentum $L_z \equiv L_z^g + L_z^q$ is calculated using (1.12).

closely in the next chapter. The first moment, $n = 1$ in (1.14), of these densities has the interpretation we have been using in our quark models, i.e., corresponds to the total polarization carried by the partons of this type. Note that the first moment of the polarized gluon density $\Delta g(x, \mu_f^2)$ was introduced explicitly in the spin sum rule, as was a possible angular momentum contribution of the gluons L_z^g. Extracting the values to be inserted in (1.12) from experiment is a challenging task. Currently no direct experimental information on the total partonic angular momentum $L_z \equiv L_z^g + L_z^q$ is available, it can only be derived indirectly from the fitted values for $\Delta\Sigma_{n=1}$ and $\Delta g_{n=1}$ via (1.12).

For illustration we show in Tab. 1.1 for a particular next-to-leading order (NLO) $\overline{\text{MS}}$ set of parton distributions, the GRSV standard[5] densities [15], the scale dependence of the first moments of the parton distributions and of the inferred parton angular momentum. The polarization of the strange sea $\Delta s_{n=1} + \Delta \bar{s}_{n=1}$, which here is equal to $2\Delta s_{n=1}$, is shown separately. Since this particular fit assumes $SU(3)_{\text{flavor}}$ symmetry, as expected a large negative strange sea polarization is needed to keep $\Delta\Sigma_{n=1}$ fairly small. We see that the quark sector has only a weak scale dependence. In contrast, the gluon polarization evolves rapidly and in response the angular momentum changes quickly as well. We would like to point out a particularly satisfying feature of this fit: at the low starting scale 0.34 GeV^2 one finds almost zero angular momentum. This suggests an intuitive picture, in which the gluon polarization and partonic angular momentum are built up at the same time by increasing gluon radiation for rising μ_f^2. Note however that the results are scheme dependent, i.e., are only directly valid for NLO $\overline{\text{MS}}$.

The good news is that the QCD improved parton model describes the data well, see for example [15]. The bad news are hidden in the uncertainties of the fit. Though the quark sector is fairly well determined, the gluon density can be varied freely without influencing the quality of the fit significantly. We will not try to describe the plethora of NLO QCD fits that have been published recently. There are several fits which are a bit more up-to-

[5]This fit uses the old value $F + D = 1.2573$. The authors also present a “valence” fit which does not assume $SU(3)_{\text{flavor}}$ symmetry and starts with zero strange sea polarization, see [15] for details.

date concerning the used data than the densities we will employ, see for example [16] for two recent ones. From a practical point of view, we note that only the older fits [15, 17, 18] used by us provide (x, μ_f^2)-grids of their *evolved* parton distributions. The interpolation routine that constructs the parton distributions at arbitrary (x, μ_f^2)-points from the grids is very fast. The newer fits by other groups just state the x-shape of the parton densities at a starting scale μ_{f0}^2, i.e., one has to evolve them to other μ_f^2 values. Since the Monte Carlo integrations for the hadronic cross sections require million-fold access to the parton distributions at varying x and μ_f^2, employing parton evolution every time would be far too time-consuming. Furthermore, the crucial problem of the basically undetermined gluon density is not resolved in the newer fits and so the uncertainties would remain basically unchanged if we used the newer densities.

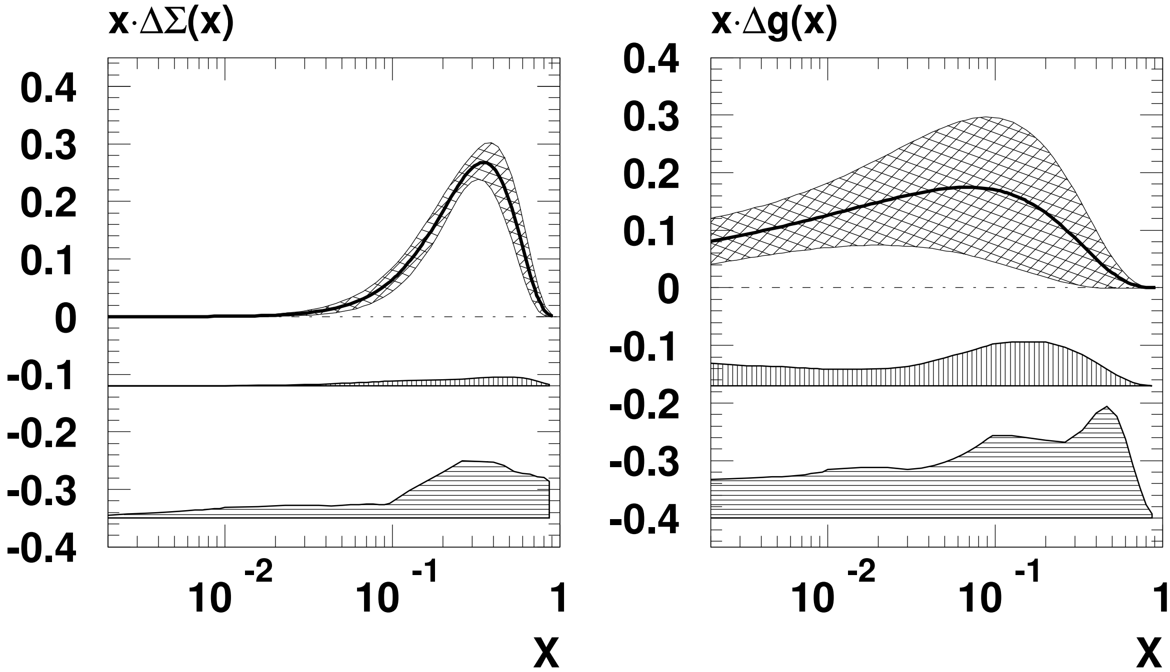

Figure 1.1: $\Delta\Sigma$ and Δg uncertainties as obtained in the SMC fit [19]. Shown are the best fits (solid line) and the statistical (crossed hatch band), experimental systematic (vertically hatched), and theoretical (horizontally hatched) uncertainties as a function of x at the evolution starting scale $\mu_{f0}^2 = 1\mathrm{GeV}^2$. Note that the densities are obtained in the AB scheme [20], but $\Delta g(x, \mu_f^2)$ remains unchanged by a scheme transformation to $\overline{\mathrm{MS}}$. The figure shown here is part of Fig. 5 in [19].

The extensive experimental and theoretical error analysis of the SMC fit [19] of polarized parton densities allows a particularly good estimate of these uncertainties. Part of the results are shown in Fig. 1.1, which has been extracted from their paper. Note that the densities shown there are in the AB scheme [20], not in $\overline{\mathrm{MS}}$. But the situation is basically the same for $\overline{\mathrm{MS}}$ and actually a scheme transformation from AB to $\overline{\mathrm{MS}}$ will leave the gluon untouched[6]. We see that the polarized quark singlet distribution $\Delta\Sigma$ is already constrained appreciably by the data. However, the gluon distribution is only very badly constrained, in particular if we take the systematic and theoretical uncertainties into account. We can compare this to the unpolarized gluon density in the left part of Fig. 1.2. This figure has been extracted from [21] and shows a not yet published fit to F_2 scaling violations of the H1 Collaboration, for details see [21]. Note that the uncertainties shown are probably an *over*estimate, since only a subset of the available unpolarized data has been used. Even taking into account that the uncertainties would be somewhat larger if the unpolarized gluon density was shown at the same low scale used in Fig. 1.1, in particular at small x, we can clearly see the big lead in precision of the unpolarized fit.

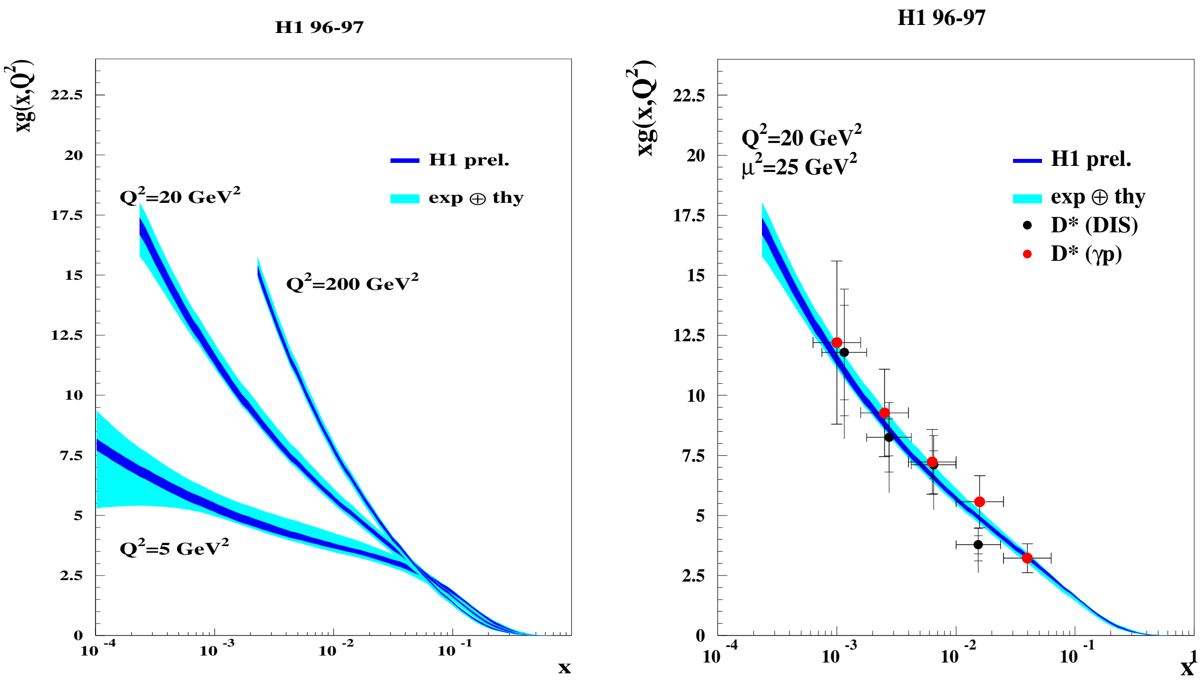

Figure 1.2: Uncertainty of the unpolarized gluon density $g(x, \mu_f^2 = Q^2)$ from the H1 fit to scaling violations [21] (left) and comparison of this fit to the gluon unfolded from charm structure function DIS and photoproduction data for D^* [22] (right). The inner dark band of the gluon density shows experimental, the outer light band theoretical uncertainties. The figure shown here is Fig. 14 of [21].

The quality of the determination of $g(x, \mu_f^2)$ from measurements of the structure function F_2 in deep inelastic scattering (DIS) may be surprising, since it is hampered by the absence of direct couplings of the gluons to the electroweak probes (γ^*, Z, $W^\pm$). However, Fig. 1.2 demonstrates, that the increasingly precise F_2 data from HERA still serve

[6]However, their *separately* fitted $\overline{\text{MS}}$ gluon density does *not* exactly match their AB gluon density transformed to $\overline{\text{MS}}$. No picture of the $\overline{\text{MS}}$ uncertainties is presented in [19].

to constrain the small-x behavior of $g(x,\mu^2)$ *indirectly* in the region $10^{-4} \lesssim x \lesssim 10^{-2}$ with satisfying accuracy from the observed scaling violations $\partial F_2(x,\mu_f^2)/\partial\mu_f^2$. To determine $g(x,\mu_f^2)$ over the entire x region, i.e., also at larger values of x, studies of exclusive reactions like direct photon or di-jet production, where the gluon already enters in leading order (LO), are often used in global fits. Such measurements are often experimentally much more involved and less precise than inclusive DIS. Nevertheless, our knowledge of the unpolarized gluon density has greatly improved in the past few years, except in the region $x \gtrsim 0.1$, where the situation is still far from being satisfactory. Here the relative uncertainty in $g(x,\mu_f^2)$ grows to about 100% [23, 24], which is not easily seen in Fig. 1.2, due to the small size of the gluon density.

The long list of spin-dependent DIS experiments [25] and the recently completed NLO framework for the evolution of the polarized parton densities [26, 27] may lead to the expectation that the polarized gluon distribution $\Delta g(x,\mu^2)$ should be known with almost similar accuracy as $g(x,\mu^2)$ by now. This is not the case, as we see clearly comparing Fig. 1.1 and Fig. 1.2. Consequently $\Delta g_{n=1}(\mu^2)$ can be estimated at best with an error of 100% for the time being. There are three main reasons why at present it is difficult to pin down $\Delta g(x,\mu_f^2)$:

- The measurements of the nucleon spin structure function g_1, the polarized observable analogous to the unpolarized structure function F_1, are still in a "pre-HERA" phase. The lever arm in $\mu_f^2 = Q^2$ of the fixed target experiments [25] is by far not sufficient to constrain $\Delta g(x,\mu_f^2)$ from scaling violations $\partial g_1(x,\mu_f^2)/\partial\mu_f^2$.

- As already mentioned, the unpolarized gluon density is also constrained by several exclusive reactions, but corresponding measurements in the polarized case are still missing.

- There is no energy-momentum sum rule for spin-dependent parton densities! In the unpolarized case this constraint on the *second* moments $\Sigma_{n=2}(\mu_f^2) + g_{n=2}(\mu_f^2) \stackrel{!}{=} 1$ is very important for the determination of the gluon density, since it relates the gluon densities to the directly probed, and hence more precisely known, quark densities. In addition, the spin-dependent parton densities are not required to be positive definite.

We cannot hope to use (1.12) similarly to the energy-momentum sum rule in the unpolarized case, until independent experimental information on the parton angular momentum is available. The small-x region of g_1 could be explored at HERA, *if* the option to longitudinally polarize also the proton beam [28] will be realized in the future. However, first measurements of Δg in exclusive reactions[7] will be provided by the COMPASS fixed target experiment at CERN [31] and the BNL RHIC polarized *pp*-collider [32], which both soon will start taking data. Thus corresponding theoretical calculations are urgently needed.

[7]The HERMES experiment has published such a measurement already [29]. But there are strong doubts concerning the applicability of perturbative QCD in this case [30].

We will now briefly describe the reactions investigated in our work, which are relevant for these experiments. For the determination of the gluon distribution, heavy quark ($Q = c, b$) photoproduction

$$\vec{\gamma}\vec{g} \to Q\overline{Q} \tag{1.15}$$

is an obvious choice (an arrow denotes a longitudinally polarized particle from now on). The reconstruction of an open heavy quark state is experimentally feasible, and in LO only the photon-gluon fusion (PGF) process contributes[8], as will be shown in the next chapter. This leads to the hope that an unambiguous determination of Δg can be performed. Thus polarized open charm photoproduction will be used by the upcoming COMPASS experiment [31] to measure Δg. In the publications [34, 35], we have provided the first NLO QCD predictions for this process. The partonic results and phenomenological predictions of [34] and the presentation of the calculational methods and the stability investigations of [35] already provide the information needed for the experiments in a compact form. In this thesis we will provide much more technical detail and also extend all the phenomenological investigations. We hope that the methods collected here will provide a convenient reference for future NLO calculations. Also the problems related to choosing inconsistent schemes in [34, 35] for the phenomenological predictions have been corrected here[9] according to [37]. Note that the right part of Fig. 1.2 suggests that photoproduction of charm is indeed a good process for determining the gluon distribution (here the unpolarized one). The agreement of the gluon density unfolded from the photoproduction measurement with the one obtained from the scaling violations is, within errors, perfect!

Similarly, gluon-gluon fusion producing heavy (anti)quarks

$$\vec{g}\vec{g} \to Q\overline{Q} \tag{1.16}$$

is a promising candidate for extracting the gluon density in $\vec{p}\vec{p}$-collisions. Of course here we also have the competing process of quark-antiquark annihilation $\vec{q}\vec{\bar{q}} \to Q\bar{Q}$ already at LO, which plays a rôle at high p_T. But the gluon induced reaction will dominate at small to medium p_T, except if Δg is very small, and the high statistics and smaller x that can be reached due to the higher center of mass energy of a $\vec{p}\vec{p}$-collider make this reaction a promising candidate for the extraction of Δg. A progress report on the corresponding NLO calculation has been given in [38] and we extend our discussion of it considerably here. Note that all theoretical studies of the polarized reactions (1.15) and (1.16) have been performed in LO only so far [39, 40, 41, 33, 31]. However, LO estimates usually suffer from a strong dependence on the a priori unknown factorization and renormalization scales. Also there are new NLO subprocesses induced by a light quark replacing a gluon

[8] The on-shell photons in (1.15) cannot only interact directly, but also via their partonic structure. However, LO estimates of this unknown "resolved" contribution are small for COMPASS energies [33].

[9] The partonic cross sections of [34, 35] were not calculated in the $\overline{\text{MS}}$ scheme, as it was wrongly assumed there, but rather in the $\overline{\text{MS}}_p$ scheme, see for example [36], and then convoluted with $\overline{\text{MS}}$ parton densities. The numerical consequences of this inconsistency are small. The partonic results shown and used here are in the $\overline{\text{MS}}$ scheme.

in the initial state. Here the question arises if there are kinematical regions in which this new subprocess can yield significant contributions and thus complicate a precise determination of Δg. NLO corrections are often more important for *polarized* differential cross sections, since they can oscillate. Small changes to the position of a zero crossing may then have large effects. Finally, the NLO corrections have been shown to be sizable near threshold and for high energies in the unpolarized case [42, 43, 44, 45, 46]. Clearly, a NLO calculation also for the spin-dependent case is warranted in order to provide a meaningful interpretation of the forthcoming experimental results.

In the next chapter we will introduce the notation and some basic methods used in our calculation of polarized processes. We will also derive the LO cross sections and the $2 \to 2$ phase space in $n = 4+\varepsilon$ dimensions, which is needed for treating the spurious singularities in the NLO corrections by dimensional regularization. In Chap. 3 the methods used for the calculation of virtual loops are explained. Formulae for the integration of basic scalar loop integrals are provided and for demonstration we show the calculation of a box graph step by step. Next we explain how tensor loop integrals can be reduced to a small set of these basic scalar loop integrals by using the Passarino-Veltman decomposition technique [47]. The ultraviolet divergencies that occur in these loop integrals are cured by renormalization, so this is the topic of Chap. 4. We show how to derive renormalization counterterms from the QCD Lagrangian, calculate them explicitly, and finally discuss their application. In doing so we explain our scheme choice, a somewhat modified $\overline{\mathrm{MS}}$ scheme, and briefly touch the subject of the running strong coupling α_s.

The following chapter is concerned with the methods used for calculating the other type of NLO corrections, the real $2 \to 3$ contributions. We show how collinear and soft singularities arise in these contributions. Partial fractioning of angular phase space integrations is a major technical issue here, which we consider in detail. Finally we calculate the minimal number of basic angular integrals needed and introduce the method of phase space slicing to analytically cancel the infrared virtual against the soft real singularities. The only divergencies left after the cancellation are collinear ones and in Chap. 6 their removal by mass factorization is discussed. To this end we analyze the process $\vec{\gamma}\vec{q} \to Q\overline{Q}q$, in which the only occurring singularities are collinear. It is shown how one can absorb these divergencies in a re-definition of the parton densities and the subtraction terms for all relevant subprocesses are derived. The "evolution" of parton densities also emerges naturally from our discussion. In Chap. 7 we present our partonic results for photoproduction and hadroproduction in full detail. Formulae for the soft real, for the pole part of the hard real, and for the virtual plus soft contributions are provided. So-called "scaling functions" related to the total partonic cross section are used to present the results graphically[10]. All the NLO results for photoproduction are presented. The same is true for hadroproduction, except for the virtual gluon contribution, which is almost finished and will be presented in a later publication. For the missing piece all necessary ingredients have been obtained already by the methods described in this thesis,

[10]Due to the scheme problems of [34, 35], which are discussed in [37], these curves show the correct $\overline{\mathrm{MS}}_m$ scheme results for the first time.

i.e., the matrix elements and tensor loop integrals have been calculated. Obtaining the final result is just a matter of putting all the parts together, but this is in practice a very time consuming job.

Thus in Chap. 8 we can present phenomenological studies only for NLO photoproduction. The dependence on the factorization and renormalization scales and on the heavy quark mass is investigated and the improved stability of the NLO calculation against variations of these scales becomes obvious. Next the possibility to *enhance* measured asymmetries by applying p_T-cuts is demonstrated, and this is used to provide improved predictions for the charm asymmetry at COMPASS [31] and for the bottom asymmetry at a possible future polarized HERA [28]. y- and x_F-differential distributions are also shown. Finally we briefly discuss indications from unpolarized experiments, that the heavy quark sector is not as well understood theoretically as we would like it to be for an extraction of Δg using heavy quark processes. However, we conclude that if the experiments can determine the polarized and unpolarized cross sections separately, instead of only their ratio (the spin asymmetry), then it should be possible to keep the uncertainties under control. We finish the main part with a short summary in Chap. 9. The first appendix collects the remaining results for the virtual loops. Several important technical issues are discussed in App. B: series expansion of hypergeometric functions, (di)logarithmic branch cuts, $SU(N)$ color-factors, and two Slavnov-Taylor identities. The last appendix contains the lengthy virtual plus soft formulae.

Chapter 2

Preliminaries

2.1 Techniques for Polarized Calculations

As has been explained in the introduction, our main goal is the determination of the polarized gluon density Δg. To elucidate the definition of this object, let us examine the general expression for the polarized differential cross section of a process with a longitudinally polarized (point-like) photon and a longitudinally polarized nucleon in the initial state:

$$d\Delta\sigma_{\gamma N} \equiv \frac{1}{4}\left[d\sigma_{\gamma N}^{++} + d\sigma_{\gamma N}^{--} - d\sigma_{\gamma N}^{+-} - d\sigma_{\gamma N}^{-+}\right] \ . \tag{2.1}$$

Here a "+" or "-" as first index means that the spin of the photon is aligned or anti-aligned to its momentum (the photon has positive or negative helicity), respectively. Similarly the second index denotes the helicity of the nucleon. Note that the factor 1/4 is a convention. If we had added all the cross sections in (2.1) indiscriminately, instead of subtracting those with mixed helicities, we would have obtained the unpolarized cross section $d\sigma_{\gamma N}$. The factor 1/4 is required in the *unpolarized* case for the *averaging* over the helicities of the initial states. Experimentalists prefer measuring asymmetries defined by counting rates N^{ij} as follows

$$\begin{aligned} A &\equiv \frac{N^{++} + N^{--} - N^{+-} - N^{-+}}{N^{++} + N^{--} + N^{+-} + N^{-+}} \leq 1 \\ &\stackrel{!}{=} \frac{d\Delta\sigma_{\gamma N}}{d\sigma_{\gamma N}} \ , \end{aligned} \tag{2.2}$$

where we assume a common luminosity $N^{ij} = \mathcal{L} d\sigma^{ij}$. In the ratio some experimental uncertainties are expected to cancel, in particular it is not necessary to know the absolute normalization. However, for example acceptance corrections do usually not cancel and are often quite important. If we now wish to match the experimental definition with the simple theoretical form displayed in the second line of (2.2), we obviously have to introduce the factor 1/4 in the polarized cross section as well.

Each of the $d\sigma^{ij}$ can be written in the following factorized form in QCD

$$d\sigma^{ij}_{\gamma N} = \sum_{f=g,q,\overline{q}} \int_0^1 dx \ \left[d\hat{\sigma}^{i+}_{\gamma f}(xK) f^j_+(x) + d\hat{\sigma}^{i-}_{\gamma f}(xK) f^j_-(x)\right] \widehat{=} \, d\hat{\sigma}^{i+}_{\gamma f} \circ f^j_+ + d\hat{\sigma}^{i-}_{\gamma f} \circ f^j_- \ , \tag{2.3}$$

with $i, j = +, -$ and the functional dependence on other quantities than x (in particular on the factorization scale μ_f) is not shown for brevity. $d\hat{\sigma}$ is the *partonic* cross section calculable in perturbative QCD. It depends on x through $k = xK$, where k is the momentum of the parton and K is the momentum of the nucleon. Its second polarization index now corresponds to the parton f involved. The upper polarization index of the parton f corresponds to the nucleon and the lower one to the parton itself, e.g., q^+_- would be the density of quarks with negative helicity in a nucleon with positive helicity. So we get

$$\begin{aligned}
d\Delta\sigma_{\gamma N} &\widehat{=} \frac{1}{4}\big[d\hat{\sigma}^{++}_{\gamma f} \circ f^+_+ + d\hat{\sigma}^{+-}_{\gamma f} \circ f^+_- + d\hat{\sigma}^{-+}_{\gamma f} \circ f^-_+ + d\hat{\sigma}^{--}_{\gamma f} \circ f^-_- \\
&\qquad - d\hat{\sigma}^{++}_{\gamma f} \circ f^-_+ - d\hat{\sigma}^{+-}_{\gamma f} \circ f^-_- - d\hat{\sigma}^{-+}_{\gamma f} \circ f^+_+ - d\hat{\sigma}^{--}_{\gamma f} \circ f^+_-\big] \\
&\stackrel{\mathbb{P}}{=} d\Delta\hat{\sigma}_{\gamma f} \circ \Delta f \ , && (2.4) \\
\Delta f &\equiv f^+_+ - f^+_- \equiv f_+ - f_- \ , && (2.5) \\
d\Delta\hat{\sigma}_{\gamma f} &\equiv \frac{1}{2}\left[d\hat{\sigma}^{++}_{\gamma f} - d\hat{\sigma}^{+-}_{\gamma f}\right] \ . && (2.6)
\end{aligned}$$

The important result used here is that parity $\mathbb{P}$ conservation of QCD guarantees for the partons and cross sections that

$$\begin{aligned}
f^+_+ = f^-_- &\equiv f_+ \qquad \text{and} \qquad f^+_- = f^-_+ \equiv f_- \ , \\
d\hat{\sigma}^{--}_{\gamma f} &= d\hat{\sigma}^{++}_{\gamma f} \qquad \text{and} \qquad d\hat{\sigma}^{-+}_{\gamma f} = d\hat{\sigma}^{+-}_{\gamma f} \ .
\end{aligned} \tag{2.7}$$

Of course these simplifications would not occur when treating parity breaking processes for example of the electroweak sector. Note that due to parity we can introduce a single polarization index for the partons f in (2.5) and (2.7), where now "+" or "-" mean the spin of the parton is aligned or anti-aligned with the *spin of the nucleon*, respectively.

We could of course repeat the same derivation for the unpolarized case by replacing all minus signs by plus signs. Furthermore it is obvious that the same conventions can be applied to the matrix elements, since the phase-space integration leading to the partonic cross sections can be factored out. Thus to collect our definitions that will be employed at the parton level, we have for a parton f with $f = g, q, \overline{q}$

$$\text{unpolarized:} \quad f(x, \mu_f^2) = f_+(x, \mu_f^2) + f_-(x, \mu_f^2) \ , \tag{2.8}$$

$$\text{polarized:} \quad \Delta f(x, \mu_f^2) = f_+(x, \mu_f^2) - f_-(x, \mu_f^2) \ . \tag{2.9}$$

where f_+ and f_- are the densities with the parton spin aligned and anti-aligned to the spin of the nucleon, respectively. And for the matrix elements we get from (2.6)

$$\text{unpolarized:} \quad \overline{|M|}^2 = \frac{1}{2}\left[|M|^2(++) + |M|^2(+-)\right] \ , \tag{2.10}$$

$$\text{polarized:} \quad \Delta |M|^2 = \frac{1}{2}\left[|M|^2(++) - |M|^2(+-)\right] \;, \tag{2.11}$$

where the polarization indices here denote the helicities of the incoming particles. The corresponding partonic differential cross sections $d\hat{\sigma}$ and $d\Delta\hat{\sigma}$ are obtained by phase-space integration over $\overline{|M|}^2$ and $\Delta |M|^2$, respectively. There is one more somewhat sophisticated complication. As we have noted above, the unpolarized cross section is averaged over the helicities, i.e., for both the incoming photon and nucleon we have divided by a factor 2 for both possible helicities. But we will regularize the spurious singularities occurring in the higher order corrections by calculating in $n = 4 + \varepsilon$ dimensions and only take the limit $\varepsilon \to 0$ when all singularities have canceled. A *massless* boson in n dimensions has $n - 2 = 2(1 + \varepsilon/2)$, and not 2, spin degrees of freedom[1]. So we should divide by $n - 2$ and not by 2 when calculating in $n = 4 + \varepsilon$ dimensions. We treat this issue by defining

$$E_\varepsilon \equiv \begin{cases} 1/(1+\frac{\varepsilon}{2}) & \text{unpolarized} \\ 1 & \text{polarized} \end{cases} \;, \tag{2.12}$$

and adding the rule that the matrix elements have to be multiplied by a factor E_ε for each incoming boson. Note that $E_\varepsilon = 1$ for the polarized case, since the factor 1/4 occurring in (2.1) just conveniently keeps experimental and theoretical definitions on par in the "real world" of four dimensions.

As is obvious from (2.10) and (2.11), it would be of great practical advantage if one could obtain matrix elements for specified helicities. By calculating $|M|^2(++)$ and $|M|^2(+-)$ separately, we would gain both the polarized and unpolarized matrix elements *simultaneously*. Since the unpolarized processes under consideration in this work have already been calculated, we could then use the re-calculation of the unpolarized results as a check of our new polarized results! The needed helicity projection operators are well known, see e.g. [48], so for the incoming (anti)quarks with momentum p, mass m and definite helicity $h = +1, -1$ we use

$$\begin{aligned} u(p,h)\bar{u}(p,h) &= \frac{1}{2}(\not{p} + m)(1 - h\gamma_5) \;, \\ v(p,h)\bar{v}(p,h) &= \frac{1}{2}(\not{p} - m)(1 + h\gamma_5) \;. \end{aligned} \tag{2.13}$$

Note that we recover the usual unpolarized completeness relations when summing over h. For outgoing (anti)quarks, where we have to sum over the unspecified helicities, we use the usual $\sum_h u\bar{u} = \not{p} + m$ and $\sum_h v\bar{v} = \not{p} - m$.

For a (real) incoming photon or gluon with momentum k and definite helicity λ, we have

$$\epsilon_\mu(k,\lambda)\,\epsilon^*_\nu(k,\lambda) = \frac{1}{2}\left[-g_{\mu\nu} + \frac{k_\mu\eta_\nu + k_\nu\eta_\mu}{k\cdot\eta} + i\lambda\epsilon_{\mu\nu\rho\sigma}\frac{k^\rho\eta^\sigma}{k\cdot\eta}\right] \;, \tag{2.14}$$

[1] A polarization *vector* has n components and satisfies two conditions: Lorentz $k \cdot \epsilon = 0$ and gauge freedom $\epsilon_\mu \to \epsilon'_\mu = \epsilon_\mu + a k_\mu$.

where η is an arbitrary light-like ($\eta^2 = 0$) four-vector with $k \cdot \eta \neq 0$. Upon summing over the helicities λ we obtain the well-known physical polarization tensor $P_{\mu\nu}$. Thus when we sum over the unspecified helicities of outgoing photons or gluons, we employ $\sum_\lambda \epsilon_\mu \epsilon^*_\nu = P_{\mu\nu} = -g_{\mu\nu} + \frac{k_\mu \eta_\nu + k_\nu \eta_\mu}{k \cdot \eta}$ as the ϵ-tensor term drops out. However, (2.14) introduces a lot of terms depending on the arbitrary vector η into the calculation. It is of course a nice internal check of the calculation to see this dependence cancel out in the end, but since the intermediate terms are very lengthy, we have chosen to minimize the number of occurring terms.

$$P_{\mu\nu} \mapsto \circ \quad = \quad -g_{\mu\nu} \mapsto \bullet \quad + \quad \frac{\eta_\mu k_\nu}{\eta \cdot k} \quad + \quad \frac{k_\mu \eta_\nu}{\eta \cdot k}$$

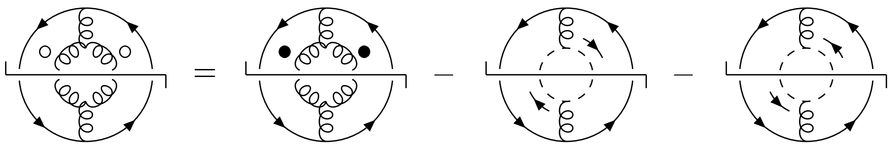

Figure 2.1: Graphical "rule" illustrating the replacement of the physical polarization sum $P_{\mu\nu}$ ($\circ$) by $-g_{\mu\nu}$ ($\bullet$) and appropriate ghost contributions (dashed lines). The minus signs in the lower half of the figure are due to the cut ghost loop.

We will simply ignore the $(k^\mu \eta^\nu + k^\nu \eta^\mu)/(k \cdot \eta)$ term, which will of course introduce unphysical polarizations. But they only contribute in graphs containing a triple-gluon vertex with two external gluons and we can eliminate these contributions by subtracting similar diagrams with two external ghosts, see Fig. 2.1 for illustration. Of course there is a trade-off: we got rid of all the "unpolarized" η-terms, but we need to calculate more diagrams. However, the number of triple-gluon graphs with two external gluons is small (one in the case of photoproduction), the ghost diagrams are easy to calculate and the cancellation of all the η-terms is implicit in the procedure. The graphical derivation shown in Fig. 2.1 is explained in more detail in [49, 50, 51]. Basically it exploits a Slavnov-Taylor identity derived in [52, 53], see also Sec. B.4. A further reduction of terms is achieved by setting the remaining η in the ϵ-tensor part of the polarization vector of an incoming particle to the momentum of the other incoming particle. Since we calculate with incoming *partons*, which are assumed to be on-shell and massless, the parton momenta k_1 and k_2 are light-like $k_1^2 = k_2^2 = 0$ and the scalar product $k_1 \cdot k_2 = s/2 \neq 0$, with s being the non-zero center-of-mass energy squared. So the momenta can be used as choices for η. Since then all scalar products in matrix elements are written in terms of the process momenta only, cancellations occur in each of the matrix elements instead of just in the sum. So effectively we will use for a (real) incoming photon or gluon with momentum k_1 and definite helicity λ_1

$$\epsilon_\mu(k_1, \lambda_1)\, \epsilon^*_\nu(k_1, \lambda_1) = \frac{1}{2} \left[-g_{\mu\nu} + i \lambda_1 \epsilon_{\mu\nu\rho\sigma} \frac{k_1^\rho k_2^\sigma}{k_1 \cdot k_2} \right] , \tag{2.15}$$

where the other incoming particle has momentum k_2. For the outgoing photons or gluons we just use the metric $\sum_\lambda \epsilon_\mu \epsilon_\nu^* = -g_{\mu\nu}$.

Note that parity conservation implies that the terms with and without dependence on the helicity do not mix. That is for helicities λ_1 and λ_2: $|M|^2(\lambda_1,\lambda_2) = A + \lambda_1 B + \lambda_2 C + \lambda_1\lambda_2 D$, with $|M|^2(++) = |M|^2(--)$ and $|M|^2(+-) = |M|^2(-+)$ implies $B = C = 0$. Thus (2.10) and (2.11) directly yield

$$|M|^2(\lambda_1,\lambda_2) = \overline{|M|}^2 + \lambda_1\lambda_2\Delta\,|M|^2 \ . \tag{2.16}$$

So if we do not specify the two helicities of the incoming particles, be it boson or fermion, we can directly read off the polarized matrix element as the coefficient of the product of the helicities and the unpolarized matrix element as the rest. In practice we have used this to obtain both matrix elements directly.

Only one problem remains: The quantities $\epsilon_{\mu\nu\rho\sigma}$ and γ_5 introduced by (2.15) and (2.13), respectively, are of purely four-dimensional nature and there exists no straightforward continuation to $n \neq 4$ dimensions. We treat them by applying the HVBM prescription [54], which provides an internally consistent extension of $\epsilon_{\mu\nu\rho\sigma}$ and γ_5 to arbitrary dimensions. In this scheme the ϵ-tensor continues to be a genuinely four-dimensional object and γ_5 is defined as in four dimensions, implying $\{\gamma^\mu, \gamma_5\} = 0$ for $\mu = 0,\ 1,\ 2,\ 3$, but $[\gamma^\mu, \gamma_5] = 0$ otherwise. This effectively splits the n-dimensional space into two subspaces, each one equipped with its own metric: one containing the four space-time dimensions and one containing the remaining $n-4$ dimensions, denoted "hat-space" henceforth. In the matrix elements we then encounter not only conventional n-dimensional scalar products of two momenta, like $k \cdot p = g_{\mu\nu} k^\mu p^\nu$, which can be expressed in terms of the usual Mandelstam variables, but also similar scalar products in hat-space $\widehat{k\cdot p} = \hat{g}_{\mu\nu}\hat{k}^\mu \hat{p}^\nu$.

It would seem that this complicates the polarized calculation considerably, as we have additional hat space terms which require separate treatment in the phase-space integration. However, we are going to calculate one-particle-inclusive (1PI) cross sections. That is, we *observe* one of the outgoing particles, a heavy (anti)quark, while integrating over the rest of the outgoing particles. Any external observed momentum is inherently four-dimensional and thus has no hat space components. We of course also observe the incoming particles, so three momenta are directly set four-dimensional. Furthermore energy-momentum conservation implies that the sum of the other momenta is also four-dimensional. Incoming partons will carry a fraction of the momentum of their parents, thus the same applies for the partonic sub-processes. So in 1PI $2 \to 2$ processes *all* momenta will be four-dimensional! Thus no hat contributions exist there. On the other hand in 1PI $2 \to 3$ processes, where we cannot eliminate all hat components, we can obviously chose to work in the center-of-mass system of the two momenta that can have non-zero hat components. Then their hat components are opposite and equal $\hat{p} = -\hat{k}$, and only one scalar hat product $\hat{k}^2$ occurs in the matrix elements and has to be taken care of in the phase-space integration. For this reason we just forget about hat space completely in this and the next chapter, which only treat $2 \to 2$ processes. In Chap. 5 we will introduce the Gottfried-Jackson frame [55, 56], which introduces center-of-mass hat components, to treat the $2 \to 3$ processes. There it is also shown, that almost all hat contributions are of $\mathcal{O}(\varepsilon)$ and hence drop out when the limit $\varepsilon \to 0$ is taken in the end. A final complication of the HVBM scheme [54] is the violation of the helicity conservation at the qqg-vertex, see [27] for a thorough discussion. However, this problem is easily treated by a finite scheme transformation during mass factorization, as is accordingly discussed in Chap. 6.

2.2 Born Cross Sections in $n = 4 + \varepsilon$ Dimensions

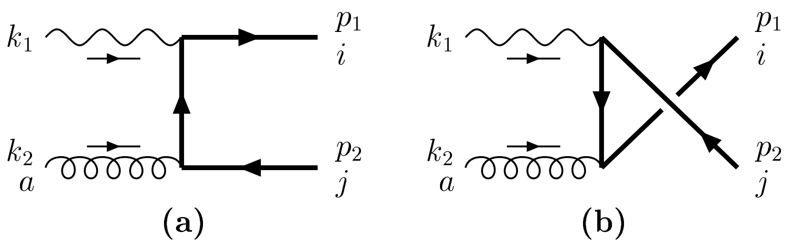

Figure 2.2: Feynman diagrams for the LO photon-gluon fusion process $\gamma g \to Q\overline{Q}$.

In this section we will re-calculate the well-known LO results for the unpolarized and polarized photo- and hadroproduction of heavy flavors. In our NLO calculations we will later encounter $1/\varepsilon^2$ and $1/\varepsilon$ poles, see Chap. 3 and Chap. 5, which will always multiply the corresponding Born results in some form. Naturally then the calculation of all finite parts, also in the removal of the infinities by renormalization (Chap. 4) and mass factorization (Chap. 6), requires the extension of the LO calculations up to $\mathcal{O}(\varepsilon^2)$ in $n = 4 + \varepsilon$ dimensions. In the following we derive the $2 \to 2$ phase-space integration and the squared matrix elements in n dimensions, in order to obtain the n-dimensional Born cross section. Of course we can also take the $n \to 4$ limit of the results to extract the LO predictions themselves.

We start by calculating LO photoproduction, which just has the photon-gluon-fusion (PGF) diagrams depicted in Fig. 2.2. We use the following external momentum and color assignment (color is discussed in App. B.3)

$$\vec{\gamma}(k_1) + \vec{g}^{\,a}(k_2) \to Q_i(p_1) + \overline{Q}_j(p_2) \ , \tag{2.17}$$

and the corresponding Mandelstam variables are given by

$$\begin{aligned} s &\equiv (k_1 + k_2)^2 = 2k_1 \cdot k_2 \ , \\ t_1 &\equiv t - m^2 = (k_2 - p_2)^2 - m^2 = -2k_2 \cdot p_2 \ , \\ u_1 &\equiv u - m^2 = (k_1 - p_2)^2 - m^2 = -2k_1 \cdot p_2 \ , \end{aligned} \tag{2.18}$$

$$k_1 + k_2 = p_1 + p_2 \qquad \curvearrowright \qquad s + t_1 + u_1 = 0 \ . \tag{2.19}$$

All the external lines are on-shell: $k_1^2 = k_2^2 = 0$ (real photon) and $p_1^2 = p_2^2 = m^2$, with m denoting the heavy quark mass. All trace calculations in $n = 4 + \varepsilon$ dimensions are performed using the `Mathematica` [57] package `Tracer` [58].

In order to present the unpolarized and polarized results simultaneously in the most compact form, we will use henceforth $|\tilde{M}|^2$ to denote *both* the unpolarized $\overline{|M|}^2$ and polarized $\Delta |M|^2$ *color-averaged* squared matrix elements calculated according to (2.10) and (2.11), respectively. Similarly, in (2.20) below, $\tilde{B}_{\text{QED}}$ denotes either the unpolarized B_{QED} or the polarized ΔB_{QED} and we will use this kind of tilde notation for all occurring unpolarized and polarized pairs. The LO result for PGF can then be expressed as

$$|\tilde{M}|^2_{\text{LO}\gamma g} = E_\varepsilon^2\, g^2 e^2 e_Q^2 \tilde{B}_{\text{QED}} \,, \tag{2.20}$$

$$\begin{aligned} \Delta B_{\text{QED}} &= \left(\frac{t_1}{u_1} + \frac{u_1}{t_1}\right)\left(\frac{2m^2 s}{t_1 u_1} - 1\right) \,, \\ B_{\text{QED}} &= \frac{t_1}{u_1} + \frac{u_1}{t_1} + \frac{4m^2 s}{t_1 u_1}\left(1 - \frac{m^2 s}{t_1 u_1}\right) + \varepsilon\left(\frac{s^2}{t_1 u_1} - 1\right) + \varepsilon^2 \frac{s^2}{4 t_1 u_1} \,, \end{aligned} \tag{2.21}$$

where g and e are the strong and electromagnetic coupling constants, respectively, and e_Q is the electromagnetic charge of the heavy quark in units of e, e.g., $e_Q = e_c = 2/3$ for charm quarks. Notice that the polarized ΔB_{QED} retains its four-dimensional form and receives no $\mathcal{O}(\varepsilon)$ contributions, in contrast to the unpolarized B_{QED}. Furthermore the color-averaged color-factor[2] for the squared matrix elements simply gives $\operatorname{Tr}\langle T^a T^a\rangle / (N_C^2 - 1) = 1/2$, with the number of colors $N_C = 3$, so compared to the $\delta_{ii} = N_C$ of the $\gamma\gamma \to Q\overline{Q}$ process we find a characteristic factor $1/(2N_C)$. The name $\tilde{B}_{\text{QED}}$ is hence motivated by the fact that we find the same function even in the pure QED process. We will see that it still appears when the remaining photon is also replaced by a gluon.

To obtain the n-dimensional cross section, we also need to perform the $2 \to 2$ phase-space integration in n dimensions. Choosing the center-of-mass system (CMS) with $k_1 = \sqrt{s/4}(1, 0, 0, 1, \hat{0})$ and $p_2 = (E_2, 0, |\vec{p}_2|\sin\xi, |\vec{p}_2|\cos\xi, \hat{0})$, with all hat components zero as discussed in the previous section, we find

$$\begin{aligned} \text{dPS}_2 &= \int \frac{d^n p_1}{(2\pi)^{n-1}} \frac{d^n p_2}{(2\pi)^{n-1}} \delta(p_1^2 - m^2)\Theta(E_1)\delta(p_2^2 - m^2)\Theta(E_2)(2\pi)^n \delta^{(n)}(k_1 + k_2 - p_1 - p_2) \\ &= \frac{1}{(2\pi)^{n-2}} \delta(s + t_1 + u_1) \int d^n p_2 \delta(p_2^2 - m^2)\Theta(E_2) \\ &= \frac{\pi^{\frac{n}{2}-1}}{(2\pi)^{n-2}} \frac{\delta(s + t_1 + u_1)}{\Gamma(\frac{n}{2} - 1)} \int dE_2 (E_2^2 - m^2)^{\frac{n-3}{2}} \Theta(E_2) \int_0^\pi d\xi \sin^{n-3}\xi \,. \end{aligned} \tag{2.22}$$

By transforming to invariant variables $(E_2, \xi) \to (t_1, u_1)$, we immediately get the standard $2 \to 2$ phase-space in $n = 4 + \varepsilon$ dimensions

$$\text{dPS}_2 = \frac{2\pi}{s} \delta(s + t_1 + u_1) \left[(4\pi)^{2+\frac{\varepsilon}{2}} \Gamma(1 + \frac{\varepsilon}{2})\right]^{-1} \left(\frac{t_1 u_1 - m^2 s}{s}\right)^{\frac{\varepsilon}{2}} dt_1 du_1 \,. \tag{2.23}$$

[2]See App. B.3 for details on the calculation of $SU(n)$ color-factors. In (2.20) the color-factor 1/2 is already included, i.e., the colorless matrix elements give $2E_\varepsilon^2\, g^2 e^2 e_Q^2 \tilde{B}_{\text{QED}}$.

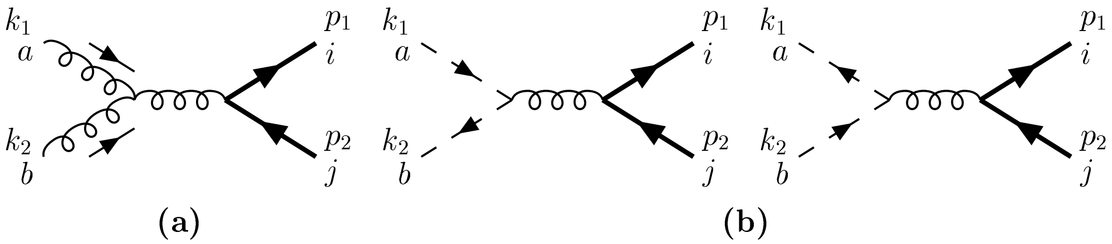

Figure 2.3: Feynman diagrams for (a) the LO triple-gluon vertex contribution and (b) the corresponding ghost graphs according to Fig. 2.1 for the gluon-gluon fusion process $gg \to Q\overline{Q}$.

Now one can write the n-dimensional $2 \to 2$ cross section as

$$\frac{d^2\tilde{\sigma}_{2\to 2}}{dt_1 du_1} = F_\varepsilon \delta(s + t_1 + u_1)|\tilde{M}|^2 , \tag{2.24}$$

$$F_\varepsilon \equiv \frac{\pi}{s^2}\left[(4\pi)^{2+\frac{\varepsilon}{2}}\Gamma(1+\frac{\varepsilon}{2})\right]^{-1}\left(\frac{t_1 u_1 - m^2 s}{\mu^2 s}\right)^{\frac{\varepsilon}{2}} , \tag{2.25}$$

where F_ε collects all phase-space factors given in (2.23), the flux factor $1/2s$, and the mass parameter μ is introduced to keep the gauge couplings g and e dimensionless in n dimensions. $\tilde{\sigma}$ denotes the unpolarized and polarized cross section σ and $\Delta\sigma$, respectively. $d\tilde{\sigma}_{g\gamma}^{(0)}$ can now be obtained from (2.24) by inserting the squared matrix elements of (2.20). If one is only interested in the Born result itself, one can of course perform the $\varepsilon \to 0$ limit in (2.20) and simply use $F_{\varepsilon=0} = 1/(16\pi s^2)$. Our four-dimensional LO photoproduction results for $\sigma_{g\gamma}^{(0)}$ and $\Delta\sigma_{g\gamma}^{(0)}$ agree with those in [59, 46] and those derivable from [41, 60], respectively.

Next we will calculate the gluon-gluon cross section for LO hadroproduction. We replace in Fig. 2.2 the photon by a gluon and use the external momentum and color assignment

$$\vec{g}^{\,a}(k_1) + \vec{g}^{\,b}(k_2) \to Q_i(p_1) + \overline{Q}_j(p_2) . \tag{2.26}$$

Of course we now have to add the triple-gluon contribution of Fig. 2.3, which has the same external momenta and color and an internal gluon with the color index c. To obtain incoming physical gluons, we subtract the incoming ghost contributions, shown in Fig. 2.3 (b), according to Fig. 2.1. Concerning the color-factors we now get two distinct contributions. After replacing the photon by a gluon in Fig. 2.2, the squared matrix element of graph (a) with (a) and (b) with (b) both have a (color-averaged) color-factor $X = \mathrm{Tr}\left\langle T^a T^b T^b T^a\right\rangle/(N_C^2-1)^2 = 2C_F/[4(N_C^2-1)] = 1/(4N_C)$, with $C_F = (N_C^2-1)/(2N_C)$. However, the interference of these two graphs gives similarly $\mathrm{Tr}\left\langle T^a T^b T^a T^b\right\rangle/(N_C^2-1)^2 = X - Y$, with $Y = C_A/[4(N_C^2-1)]$ and $C_A = N_C$. The same color-factor Y multiplied with a (complex) number also appears *on its own* for the square of, and interference with, the triple-gluon vertex diagram of Fig. 2.3 (and of course also for the ghost contributions), e.g., for the interference of Fig. 2.2 (a), $\gamma \to g$, with Fig. 2.3 (a) we obtain $\mathrm{Tr}\left\langle T^a T^b T^c \right\rangle f^{abc}/(N_C^2-1)^2 = iY$. We see that for the color-factor X we add the same "colorless" squared matrix elements with the same weight as in the photoproduction case, whereas for the color-factor Y we collect the new non-abelian matrix elements and an abelian interference contribution. The result

$$|\tilde{M}|^2_{\mathrm{LO}gg} = E_\varepsilon^2\, g^4 \frac{1}{2(N_C^2-1)} \left[2C_F - C_A \frac{2t_1u_1}{s^2}\right] \tilde{B}_{\mathrm{QED}} \;, \tag{2.27}$$

to be used with (2.21) and (2.24), then displays in the color-factor X part the photoproduction result of (2.20) with strong couplings only and with the characteristic factor $1/(2N_C)$ for changing a photon to a gluon. On the other hand, the color-factor Y part has different dynamics, as is evident by the additional factor $2t_1u_1/s^2$. This pattern of recovering "abelian" parts as coefficients for certain color-factors will repeat itself throughout the calculations. Our result (2.27) can be compared to [41, 44], see also [61, 49] for earlier work on the unpolarized hadroproduction of heavy quarks in LO.

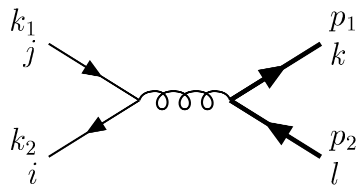

Figure 2.4: The LO quark-antiquark annihilation process $q\overline{q} \to Q\overline{Q}$.

Finally, we will calculate the LO quark-antiquark annihilation process depicted in Fig. 2.4. The external momentum and color assignment is

$$\vec{q}_j(k_1) + \vec{\overline{q}}_i(k_2) \to Q_k(p_1) + \overline{Q}_l(p_2) \;. \tag{2.28}$$

Here the color-factor is simply $\mathrm{Tr}\left\langle T^a T^b \right\rangle \mathrm{Tr}\left\langle T^a T^b \right\rangle / N_C^2 = C_F/(2N_C)$, where a and b are the color indices of the internal gluon in amplitude and complex conjugate amplitude, respectively. Then we get

$$|\tilde{M}|^2_{\mathrm{LO}q\overline{q}} = \frac{C_F}{N_C} g^4 \tilde{A}_{\mathrm{QED}} \;, \tag{2.29}$$

$$\begin{aligned} \Delta A_{\mathrm{QED}} &= -\frac{t_1^2+u_1^2}{s^2} - \frac{2m^2}{s} + \frac{\varepsilon}{2} \;, \\ A_{\mathrm{QED}} &= \frac{t_1^2+u_1^2}{s^2} + \frac{2m^2}{s} + \frac{\varepsilon}{2} \;. \end{aligned} \tag{2.30}$$

There is no $\mathcal{O}(\varepsilon^2)$ contribution. If we had calculated the same process with an internal photon, we would have obtained the same result except for the changed color-factor

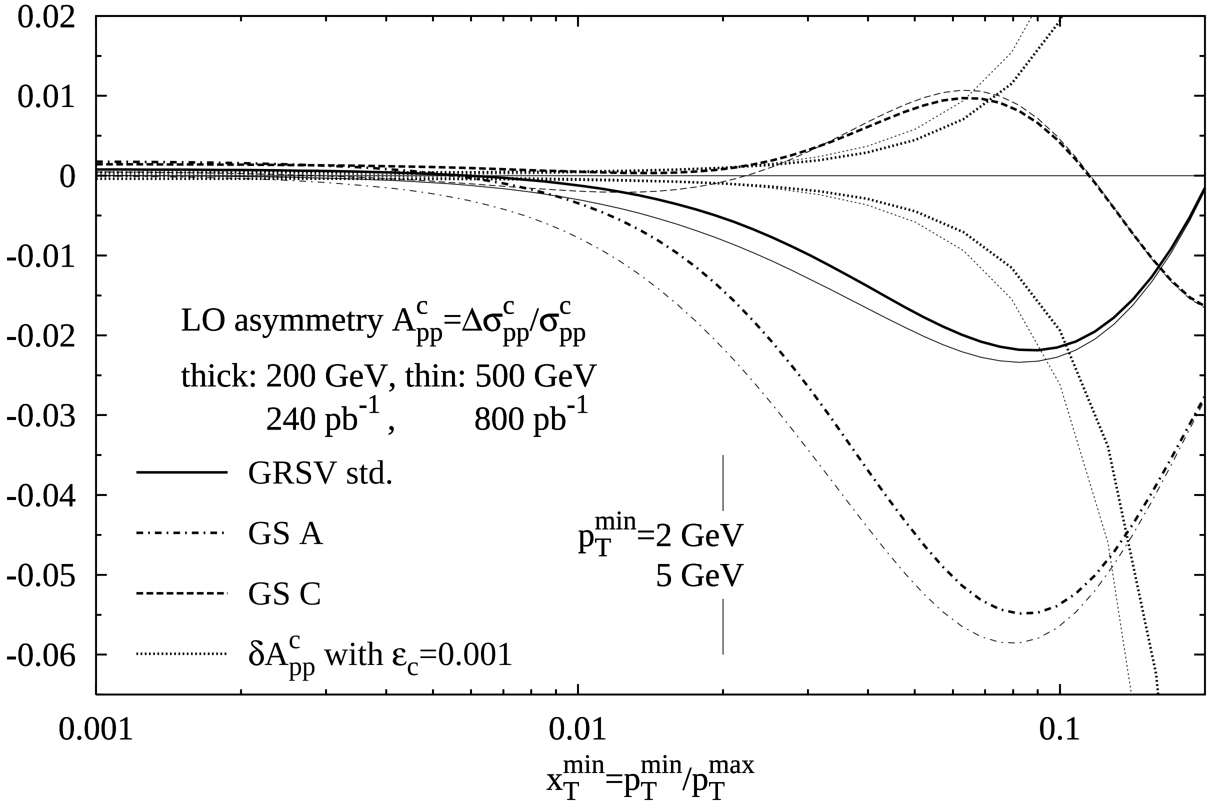

Figure 2.5: Total LO charm spin asymmetry at RHIC [32] for $\sqrt{S} = 200,\ 500$ GeV (thick, thin lines) for different polarized parton sets [15, 18] and the unpolarized GRV'94 densities [62], plotted as function of $x_T^{\rm min}$. This means varying the p_T-cut $p_T \geq p_T^{\rm min}$, where $x_T^{\rm min} = p_T^{\rm min}/p_T^{\rm max}$. For illustration the two $p_T^{\rm min}$ values corresponding to $x_T^{\rm min} = 0.02$ and $\sqrt{S} = 200$ and 500 GeV, respectively, are inserted. An estimate of $\pm\delta A^c_{pp}$ according to (2.31) is also shown.

$\delta_{ii}\delta_{kk}/N_C^2 = 1$ and the electromagnetic instead of the strong coupling, hence the name $\tilde{A}_{\rm QED}$. The unpolarized n-dimensional result agrees with the one in [46].

Note that helicity conservation at a (massless) quark-*anti*quark vertex requires that $|M|^2(++) = 0$. Thus according to (2.10) and (2.11) we must have $\Delta|M|^2 = -\overline{|M|}^2$. But we find from (2.30) that $\Delta|M|^2 + \overline{|M|}^2 \sim \varepsilon \neq 0$! This is due to the commuting γ_5 in the ε-dimensional hat-space of the HVBM scheme [54]. However, this violation of helicity conservation only becomes relevant when $\tilde{A}_{\rm QED}$ appears in front of NLO poles $1/\varepsilon$. For the pure LO process the limit $\varepsilon \to 0$ can be taken and helicity conservation is restored. In NLO, we have to subtract $\Delta A_{\rm QED}$ of (2.30) in the mass factorization procedure of Chap. 6, if the NLO subprocesses are calculated in the HVBM scheme as well, as they are here. This corresponds to a finite scheme transformation and will help restoring helicity conservation. Only similar helicity violations due to ΔP_{qq} remain to be removed then, see Chap. 6 for details. It is for this reason that we quote the "unphysical" HVBM result for the $\mathcal{O}(\varepsilon)$ of $\Delta A_{\rm QED}$, instead of using $\Delta A_{\rm QED} = -A_{\rm QED}$. This completes our derivation of the LO matrix elements and cross sections for photoproduction and hadroproduction. The corresponding QED process with two gammas in the initial state can also be derived from the results shown here.

In the next chapters we will show how NLO corrections to these processes can be obtained. The theoretical motivation for doing so already has been given in the introduction. So we will here simply include a plot, Fig. 2.5, showing a LO prediction for the total charm hadroproduction asymmetry $A^c_{pp} = \Delta\sigma^c_{pp}/\sigma^c_{pp}$ at RHIC [32] for two different center-of-mass energies ($\sqrt{S} = 200$ GeV with $\mathcal{L} = 240$ pb^{-1} as thick and $\sqrt{S} = 500$ GeV with $\mathcal{L} = 800$ pb^{-1} as thin lines). A cut on minimal transverse momentum $p_T^{\rm min}$ has been introduced, so the dependence on $x_T = p_T^{\rm min}/p_T^{\rm max}$, with the maximal kinematically allowed transverse momentum $p_T^{\rm max} = \sqrt{S/4 - m_c^2}$ is shown. For details on deriving hadronic cross sections see Chap. 8. A rough statistical error estimate using the formula

$$\delta A^c_{pp} \simeq \frac{1}{P_p^2}\frac{1}{\sqrt{\varepsilon_c \mathcal{L} \sigma^c_{pp}}} \tag{2.31}$$

with a detection efficiency of $\varepsilon_c = 0.001$ is also displayed. The distance between the lines for $\pm\delta A^c_{pp}$ is a crude estimate of the expected statistical error bars. By inspecting this plot, it is obvious that in LO this process, which will be measured soon at an experimental facility, allows a very good separation of different Δg on the market [15, 18]. Hence the calculation of NLO corrections is needed also from a phenomenological point of view. Similar conclusions concerning (LO) photoproduction have already been drawn earlier, see for example [63].

Chapter 3

Virtual Contributions

3.1 Dimensional Regularization

Virtual contributions are characterized by the additional *internal* exchange of particles, so in NLO there is the same number of incoming and outgoing particles as in the Born diagrams. For the reactions considered here the virtual parts are $2 \to 2$ processes with the same simple kinematics (2.18) and phase-space (2.23) as the tree level diagrams. Since an internal line has to couple at its two endpoints, each of them yielding an additional factor g, only one additional internal line is allowed in NLO QCD, where we compute corrections of the order $\alpha_s \sim g^2$. Thus only three different topologies can arise as part of the amplitude, which are shown in Fig. 3.1.

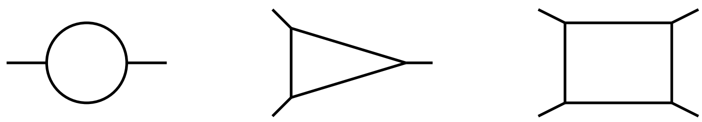

(a) (b) (c)

Figure 3.1: The topologies that can occur in the NLO virtual contributions: (a) self-energy, (b) vertex correction, and (c) box diagram. Note that the straight lines here can symbolize photons, gluons, ghosts, or quarks, as is appropriate.

The first type of diagram, Fig. 3.1 (a), is called self-energy, because the "same" particle appears at both (truncated) legs. It will also be denoted as bubble graph because of its shape and as 2-point function (2PF) graph, because it has two vertices. The second topology, Fig. 3.1 (b), is called vertex correction, because it results from an interaction between the legs of a vertex. It will also be named triangle or 3-point function (3PF) graph. Finally, Fig. 3.1 (c), is identified by its shape as box diagram or 4-point function (4PF) graph. Since the virtual diagrams contain the same number of external (observed) particles as the Born diagrams, the new matrix elements have to be added *coherently*. But since a single virtual amplitude already supplies the additional α_s of NLO, one only has to consider the interference of the virtual with the tree level amplitudes when squaring the matrix elements. The products of the virtual diagrams with themselves can be discarded as being beyond NLO. Thus virtual contributions in general have simpler kinematics, phase-space and combinatorics than the real contributions, which will be considered in Chap. 5. However, in practice the virtual contributions can become quite numerous and are at least as difficult to compute as the real ones, because the additional particle exchange itself complicates the calculation considerably. In the following we will show step by step how to deal with the problems one encounters.

Since this additional particle is virtual and since energy-momentum conservation does not provide any constraint on it, its four-momentum can take on any value whatsoever and one has to integrate over all the possibilities. To illustrate the ensuing difficulties, we will consider a simplified integral first [64]. A massless virtual particle with four-momentum q will introduce a q^2 in the denominator, so let us consider the integral

$$\int \frac{d^4q}{(-q^2)^\omega} \qquad \text{with} \qquad \omega = 1, 2, \dots \tag{3.1}$$

By inspecting the dimensions, we see that the integral is infrared (IR) divergent for $4 \leq 2\omega$ and ultraviolet (UV) divergent for $4 \geq 2\omega$. Thus it is divergent for *all* ω. We regularize the integral by shifting the dimension of q to $n = 4+\varepsilon$. Obviously then $\varepsilon_{\mathrm{IR}} > 2(\omega-2)$ and $\varepsilon_{\mathrm{UV}} < 2(\omega-2)$ to obtain finite results. By performing a Wick rotation to the Euclidean momentum $Q^2 = q_0^2+q_1^2+q_2^2+q_3^2$, integrating out the angles in a polar coordinate system[1] and splitting the integral we obtain

$$\begin{aligned} -i\frac{\Gamma(n/2)}{\pi^{n/2}} \int \frac{d^nq}{(-q^2)^\omega} &= \int_0^{\Lambda^2} dQ^2 (Q^2)^{n/2-\omega-1} + \int_{\Lambda^2}^{\infty} dQ^2 (Q^2)^{n/2-\omega-1} \\ &= \frac{2\Lambda^{\varepsilon_{\mathrm{IR}}-2(\omega-2)}}{\varepsilon_{\mathrm{IR}}-2(\omega-2)} - \frac{2\Lambda^{\varepsilon_{\mathrm{UV}}-2(\omega-2)}}{\varepsilon_{\mathrm{UV}}-2(\omega-2)} \,. \end{aligned} \tag{3.2}$$

For $\omega = 2$ one explicitly sees both the UV and IR pole. For other ω values we find as expected, that the first (IR regulated) term diverges in the UV limit $\Lambda \to \infty$ and the second (UV regulated) term diverges in the IR limit $\Lambda \to 0$.

Now we can on one hand chose to treat the UV and IR singularities separately, see for example [65]. Typically one would then first calculate the UV divergencies with $\varepsilon_{\mathrm{UV}}$ while keeping the external legs off-shell. The latter provides the cutoff for the IR singularities which we introduced by hand in (3.2). Then one would remove the UV poles by renormalization, continue analytically $\varepsilon_{\mathrm{UV}} \to \varepsilon_{\mathrm{IR}}$ and put the external legs back on shell, exposing the IR poles which are later canceled against real contributions. This method has the advantage of clearly exhibiting the source of the poles, but leads to a rather tedious procedure. We can on the other hand decide to do without this distinction and immediately use analytical continuation to unify $\varepsilon_{\mathrm{UV}} = \varepsilon_{\mathrm{IR}} = \varepsilon$ with $\varepsilon > 0$. Then

[1] For more details on the used calculation techniques see App. A.1.

(3.2) appears in the simplest possible form

$$\int \frac{d^n q}{(-q^2)^\omega} = 0 \; , \tag{3.3}$$

and one can take here the $n \to 4$ limit immediately, since the integral now vanishes and thus no dependence on ε remains on the r.h.s. Note that our choice of setting $\varepsilon_{\rm UV} = \varepsilon_{\rm IR}$ is well motivated by the fact, that in (3.2) the l.h.s. of the equation does not depend on a mass scale, whereas the r.h.s has two parts which do. Hence we should chose the continuation procedure in such a way, that the dependence on Λ cancels. All this does not mean that the divergencies have somehow magically disappeared in four dimensions. Rather we have made a special choice of evaluating the per se undetermined integral (3.1). This *only* makes sense if the end result of the complete calculation is finite and thus independent of the treatment of spurious divergencies in the intermediate steps, as it has to be for a physical process. We have chosen to use the unified ε approach throughout the calculations for simplicity.

3.2 Basic Scalar n-Point Functions

After having chosen our general method for dealing with the virtual corrections in the last section, we can now proceed to deal with the loop integrals that will actually appear in the calculation. The QCD propagators that can appear in the loops of Fig. 3.1 are shown in Fig. 3.2.

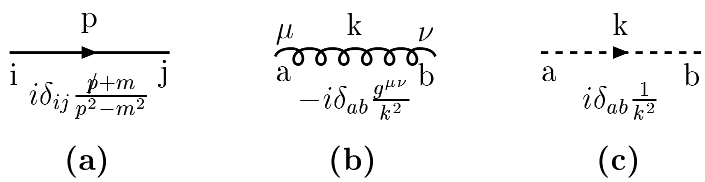

Figure 3.2: Feynman Rules for the QCD propagators of (a) quark, (b) gluon and (c) ghost in the Feynman gauge. The $i\epsilon$ shift in the denominators is omitted for brevity.

Obviously in the denominator of the loop integrals, terms of the general form $L_i \equiv l_i^2 - m_i^2 + i\epsilon$ will be appearing, where l_i is the four-momentum of the i-th propagating particle, m_i is its mass and the $i\epsilon$-prescription is used to ensure causality[2]. With respect to the loops in Fig. 3.1 one arbitrary propagator can be set to carry the loop momentum q only: $l_1 = q$. Counting all external particles as *incoming*, at the next vertex the incoming four-momentum q_1 will be added into the loop and the next propagator has $l_2 = q + q_1$

[2]This causal ϵ has nothing to do with the ε of dimensional regularization.

and so forth. Thus we can define the following basic scalar integrals:

$$
\begin{aligned}
&\text{1PF:} && A_0(m_1) \equiv \mu^{-\varepsilon} \int \frac{d^n q}{(2\pi)^n} \frac{1}{L_1} \, , \\
&\text{2PF:} && B_0(q_1, m_1, m_2) \equiv \mu^{-\varepsilon} \int \frac{d^n q}{(2\pi)^n} \frac{1}{L_1 L_2} \, , \\
&\text{3PF:} && C_0(q_1, q_2, m_1, m_2, m_3) \equiv \mu^{-\varepsilon} \int \frac{d^n q}{(2\pi)^n} \frac{1}{L_1 L_2 L_3} \, , \\
&\text{4PF:} && D_0(q_1, q_2, q_3, m_1, m_2, m_3, m_4) \equiv \mu^{-\varepsilon} \int \frac{d^n q}{(2\pi)^n} \frac{1}{L_1 L_2 L_3 L_4} \, .
\end{aligned}
\tag{3.4}
$$

We have added a 1-point function (1PF) A_0 for completeness. Furthermore the $\mu^{-\varepsilon}$ with an arbitrary mass scale μ in front guarantees for $n = 4 + \varepsilon$ that the integral has an integer mass dimension[3], i.e., $[\mu^{-\varepsilon}][d^n q] = \text{mass}^{4-n}\text{mass}^n = \text{mass}^4$. Note that the virtual processes considered here are $2 \to 2$, i.e., there are only four external momenta. Thus the 4PF diagrams must couple directly to those external momenta at NLO. We have defined the q_i to be incoming, so the momenta of the outgoing particles will enter with a negative sign. Thus energy-momentum conservation implies that $l_4 = q + q_1 + q_2 + q_3 = q - q_4$ here.

In App. A.1 it is shown that the integrals (3.4) can be brought into the general form

$$
A_0|_{j=1}, B_0|_{j=2}, C_0|_{j=3}, D_0|_{j=4} = iC_\varepsilon \, P_\varepsilon(j) \, (m^2)^{2-j} \mathcal{J}_j \, K^{2-j+\frac{\varepsilon}{2}} \, , \tag{3.5}
$$

with j being the number of propagators, e.g., $j = 3$ for the 3PF C_0. In our processes the masses m_i in (3.4) are either zero (for light quarks, gluons or ghosts) or equal to the heavy quark mass m, so this single mass scale has been factored out. We have introduced

$$
\begin{aligned}
C_\varepsilon &\equiv \frac{1}{16\pi^2} e^{\frac{\varepsilon}{2}(\gamma_E - \ln 4\pi)} \left(\frac{m^2}{\mu^2} \right)^{\frac{\varepsilon}{2}} \, , \qquad S_l(n) \equiv \sum_{k=1}^{n} \frac{1}{k^l} \, , \\
P_\varepsilon(j) &\equiv (-1)^j \frac{1 - \frac{\varepsilon}{2} S_1(j-1) + \frac{\varepsilon^2}{8} \left[\zeta(2) + S_1^2(j-1) - S_2(j-1) \right] + \mathcal{O}(\varepsilon^3)}{(j - 2 - \frac{\varepsilon}{2})(j - 1 - \frac{\varepsilon}{2})} \, ,
\end{aligned}
\tag{3.6}
$$

and furthermore used Riemann $\zeta(2) = \pi^2/6$, Euler $\gamma_E = 0.5772\ldots$ and $S_l(0) = 0$. $\mathcal{J}_j$ is a suitable Feynman parameter integration which is used to bring the denominator into the form $(q^2 - K)^j$, e.g.,

$$
\mathcal{J}_1 = 1 \, , \; \mathcal{J}_2 = \int_0^1 dx \, , \; \mathcal{J}_3 = 2 \int_0^1 dx \; dy \; x \, , \; \mathcal{J}_4 = 6 \int_0^1 dx \; dy \; dz \; x^2 y \, . \tag{3.7}
$$

For $j = 1, 2$ the power of K is $2 - j + \frac{\varepsilon}{2} > 0$, so the integration is finite and P_ε is only needed to $\mathcal{O}(1)$. For $j > 2$ the power of K becomes negative and thus the integration can

[3]This scale can also be viewed as keeping the regularized coupling dimensionless, see Chap. 4.

yield poles in ε. Examining Tab. 3.1, which collects the parametrization formulae, we see that poles can appear when there are terms of the type $x^{-1+\varepsilon/2}$ or $(1-x)^{-1+\varepsilon/2}$. This can happen for none, one or two parameters, so that we get finite, $1/\varepsilon$ or $1/\varepsilon^2$ contributions, respectively. Note that the integration over z is always finite for the 4PF: if K has a zero in z, it will be of the form $z^{-2+\varepsilon/2}$ or $(1-z)^{-2+\varepsilon/2}$ which can be integrated without leading to a pole. Thus even for the box integrals we get at most $1/\varepsilon^2$, which is of course expected, since the real contributions canceling the poles can not provide higher powers of $1/\varepsilon$ in NLO: simultaneous collinear and infrared limits in the emission of *one* gluon yields only $1/\varepsilon^2$.

Note also that the causal ϵ−prescription is important for determining the correct analytical continuation of the (di-)logarithms appearing in the calculation. Fortunately here we can drop all imaginary parts of the $\mathcal{J}_j$ integrals, which simplifies the continuation procedure. The reason is that they will be included in the virtual corrections, for which only the interference term with the Born amplitudes contributes at NLO, see the discussion in Sec. 3.1. That interference term can be written as $2\mathrm{Re}\,[M_{\text{virt.}}M^*_{\text{Born}}]$, so the imaginary parts of the virtual matrix element do not contribute, since the Born matrix element is real. For virtual NLO graphs one always has five extra i from the Feynman rules as compared to the tree graphs. This together with the multiplication of $i\ldots$ in (3.5) gives a *real* prefactor multiplying the $\mathcal{J}_j$ Feynman parameter integrations. So we will need only the *real* parts of the Feynman parameter integrals, like for (3.11) and (3.14) below, which leads to a purely *imaginary* integral (3.15) below by multiplication with i and then to a *real* contribution with the five i's coming from the Feynman rules. For a discussion of some possible simplifications under these circumstances see App. B.2. Basically we can drop the causal ϵ by treating logarithms with arguments on the branch cut appropriately, if we are only interested in the real parts.

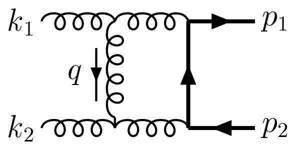

Figure 3.3: The hadroproduction box graph leading to the basic scalar integral (3.15).

The needed set of basic scalar integrals has been collected in [44] and will be recalculated in App. A.2. Here we will show how to perform the integration of the box integral $D_0(-k_1, p_1, p_2, 0, 0, m, 0)$ in some detail, to demonstrate the practical difficulties. It arises in the hadroproduction graph displayed in Fig. 3.3. By inserting the momenta in the expression of Tab. 3.1, we can write $K = ac\tilde{t} - bd\tilde{s} + c^2$ with $\tilde{t} \equiv -t_1/m^2$ and $\tilde{s} \equiv s/m^2$, where we have used the fact that $a + b + c + d = 1$. Next we pick the parameters so that K is linear in z, in order to facilitate the first integration. The choice $\{a, b, c, d\} = \{xy(1-z), xyz, x(1-y), 1-x\}$ satisfies this and upon integrating $K^{-2+\varepsilon/2}$ over z and multiplying with x^2y – see (3.7), the factor 6 cancels against the 1/6 of $P_\varepsilon(4)$

j	$P_\varepsilon(j)$	$m^2(K+i\epsilon)$	$\{a,b,c,\ldots\}$
1	$-\frac{2}{\varepsilon}+1+\mathcal{O}(\varepsilon)$	am_1^2	$\{1\}$
2	$-\frac{2}{\varepsilon}+\mathcal{O}(\varepsilon)$	$-abq_1^2+am_1^2+bm_2^2$	$\{x,1-x\}$
3	$-\frac{1}{2}\left(1+\frac{\varepsilon^2}{8}\zeta(2)\right)$ $+\mathcal{O}(\varepsilon^3)$	$-abq_1^2-ac\,(q_1+q_2)^2-bcq_2^2$ $+am_1^2+bm_2^2+cm_3^2$	$\{xy,x(1-y),$ $1-x\}$
4	$\frac{1}{6}\left(1-\frac{\varepsilon}{2}+\frac{\varepsilon^2}{8}\zeta(2)\right)$ $+\mathcal{O}(\varepsilon^3)$	$-abq_1^2-ac\,(q_1+q_2)^2-ad\,(q_1+q_2+q_3)^2$ $-bcq_2^2-bd(q_2+q_3)^2-cdq_3^2$ $+am_1^2+bm_2^2+cm_3^2+dm_4^2$	$\{xyz,xy(1-z),$ $x(1-y),1-x\}$

Table 3.1: The factor P_ε and the Feynman parametrized kernels of the basic j-point functions (3.4) used with (3.5) and (3.7). P_ε is given up to the relevant order in ε. Note that $a+b+c+\ldots=1$ and that the assignment of the shown sets can be in any order, i.e., there are $j!$ possibilities.

– we get the sum of two parts $I_{xy}+II_{xy}$:

$$\underbrace{\frac{2x^{-1+\varepsilon}(1-y)^{-1+\frac{\varepsilon}{2}}(1+(\tilde{t}-1)y)^{-1+\frac{\varepsilon}{2}}}{(-2+\varepsilon)(\tilde{s}(1-x)+\tilde{t}x(1-y))}}_{I_{xy}}\underbrace{-\frac{2x^{\frac{\varepsilon}{2}}\left\{-\tilde{s}y+x\left[(1-y)^2+\tilde{s}y\right]\right\}^{-1+\frac{\varepsilon}{2}}}{(-2+\varepsilon)(\tilde{s}(1-x)+\tilde{t}x(1-y))}}_{II_{xy}}\,. \tag{3.8}$$

Beginning with part I_{xy}, we can perform the x-Integration, which leads to the hypergeometric function ${}_2\mathrm{F}_1(1,\varepsilon,1+\varepsilon,[\tilde{s}-\tilde{t}(1-y)]/\tilde{s})$, of which we take the series expansion, see (B.5) in App. B.1, to get:

$$I_y=\frac{2(1-y)^{-1+\frac{\varepsilon}{2}}(1+(\tilde{t}-1)y)^{-1+\frac{\varepsilon}{2}}\left[1-\varepsilon\ln\left(\frac{\tilde{t}}{\tilde{s}}(1-y)\right)-\varepsilon^2\,\mathrm{Li}_2\left(\frac{\tilde{s}-\tilde{t}(1-y)}{\tilde{s}}\right)\right]}{(-2+\varepsilon)\varepsilon\tilde{s}}\,, \tag{3.9}$$

with the dilogarithmic function $\mathrm{Li}_2(z)$. The remaining y integration diverges for $y\to1$ and is too complicated to be tackled directly. We define a counterterm which corresponds to the $y\to1$ limit:

$$I_y^c\equiv\frac{2(1-y)^{-1+\frac{\varepsilon}{2}}\tilde{t}^{-1+\frac{\varepsilon}{2}}\left[1-\varepsilon\ln\left(\frac{\tilde{t}}{\tilde{s}}(1-y)\right)-\varepsilon^2\frac{\pi^2}{6}\right]}{(-2+\varepsilon)\varepsilon\tilde{s}}\,. \tag{3.10}$$

So $I_y-I_y^c$ is *finite* with respect to the y integration, which means that we can expand it in ε to $\mathcal{O}(1)$ before integrating! The resulting integral can be done. Furthermore I_y^c is simple enough to be integrated, keeping the ε dependence, and expanding in ε only *after* the integration. It is important that (3.10) mirrors the complete $y \to 1$ structure, e.g., the ε^2 part cannot be dropped since it will contribute at $\mathcal{O}(1)$, but will not occur in the integration of the $\mathcal{O}(1)$ expansion of $I_y - I_y^c$. The sum of both gives the result:

$$I = -\frac{1}{\tilde{s}\tilde{t}}\left[\frac{6}{\varepsilon^2} + \frac{3 + 2\ln\tilde{s} + 2\ln\tilde{t}}{\varepsilon} + \frac{3}{2} - \frac{\pi^2}{3} + \ln\tilde{t}\left(1 - \ln\tilde{t}\right) + \ln\tilde{s}\left(1 + 2\ln\tilde{t}\right)\right] . \quad (3.11)$$

Turning to II_{xy}, we note that the integral only diverges when $x \to 1$. But $x^{\varepsilon/2} = 1 + \frac{\varepsilon}{2}\ln x + \frac{\varepsilon^2}{8}\ln^2 x + \ldots$, i.e., that term gives contributions other than unity only when multiplied by a pole in ε. However, since the poles occur only for $x = 1$ where $\ln(x = 1) = 0$, we can simply set $x^{\varepsilon/2} \to 1$ prior to integration. Then we can perform the x integration. The resulting hypergeometric functions are best transformed linearly, see for example [66], in order to exhibit the y-structure clearly. One gets:

$$\begin{aligned} II_y = &-\frac{4i\pi\tilde{s}^{-1+\frac{\varepsilon}{2}}\left(\tilde{s} - \tilde{t}(1-y)\right)^{-\frac{\varepsilon}{2}}(1-y)^{-1+\frac{\varepsilon}{2}}\left(1 + (\tilde{t}-1)y\right)^{-1+\frac{\varepsilon}{2}}}{-2+\varepsilon} \\ &- \frac{4(1-y)^{-1+\varepsilon}\,{}_2\mathrm{F}_1\left(1, \frac{\varepsilon}{2}, 1+\frac{\varepsilon}{2}, \frac{\left(\tilde{s}-\tilde{t}(1-y)\right)(1-y)}{\tilde{s}\left(1+(\tilde{t}-1)y\right)}\right)}{(-2+\varepsilon)\varepsilon\tilde{s}\left(1+(\tilde{t}-1)y\right)} + 4(1-y)^{-1+\frac{\varepsilon}{2}}(-1)^{\frac{\varepsilon}{2}}\tilde{s}^{-1+\frac{\varepsilon}{2}}y^{\frac{\varepsilon}{2}} \\ &\cdot \frac{\left((1-y)^2 + \tilde{s}y\right)^{-\frac{\varepsilon}{2}}\left(1+(\tilde{t}-1)y\right)^{-1+\frac{\varepsilon}{2}}\,{}_2\mathrm{F}_1\left(\frac{\varepsilon}{2}, \frac{\varepsilon}{2}, 1+\frac{\varepsilon}{2}, \frac{\left(\tilde{s}-\tilde{t}(1-y)\right)y}{(1-y)^2+\tilde{s}y}\right)}{(-2+\varepsilon)\varepsilon} . \end{aligned} \quad (3.12)$$

The series expansion of the new hypergeometric function can also be found in App. B.1. Again we find a divergence in y and define an appropriate counterterm for the $y \to 1$ limit:

$$II_y^c \equiv \frac{-24(1-y)^{-1+\varepsilon} + (1-y)^{-1+\frac{\varepsilon}{2}}\left[-24i\varepsilon\pi + (-1)^{\frac{\varepsilon}{2}}\left(24 + \varepsilon^2\pi^2\right)\right]\tilde{t}^{\frac{\varepsilon}{2}}}{6(-2+\varepsilon)\varepsilon\tilde{s}\tilde{t}} . \quad (3.13)$$

Proceeding like for I_y, we can complete the integration

$$II = -\frac{1}{\tilde{s}\tilde{t}}\left[\frac{2}{\varepsilon^2} + \frac{1 + 2\ln\tilde{t}}{\varepsilon} + \frac{1 - \pi^2 + 2(1 + \ln\tilde{t})\ln\tilde{t}}{2}\right] . \quad (3.14)$$

We have dropped any imaginary parts that occur in our final integrated results as mentioned above. Summing $I + II$ and multiplying by $iC_\varepsilon \frac{1}{m^4}\left(1 - \frac{\varepsilon}{2} + \frac{\varepsilon^2}{8}\zeta(2)\right)$, we then get the final answer

$$D_0(-k_1, p_1, p_2, 0, 0, m, 0) = \frac{iC_\varepsilon}{st_1}\left[\frac{8}{\varepsilon^2} + \frac{2}{\varepsilon}\left(2\ln\tilde{t} + \ln\tilde{s}\right) + 2\ln\tilde{s}\ln\tilde{t} - 4\zeta(2)\right] , \quad (3.15)$$

in accordance with Eqn. (A4) of [44].

3.3 Passarino-Veltman Decomposition

The fermion propagators of the virtual contributions Fig. 3.1 have the form $i\delta_{ij}(\not{p}+m)/(p^2-m^2)$ and thus they introduce the loop momentum also in the *numerator*. We can generalize the basic definitions of (3.4) to take the more complicated numerator into account, e.g.,

$$D_{\{0,\mu,\mu\nu,\mu\nu\rho\}}(q_1,q_2,q_3,m_1,m_2,m_3,m_4) \equiv \mu^{-\varepsilon}\int \frac{d^nq}{(2\pi)^n}\frac{\{1,q_\mu,q_\mu q_\nu,q_\mu q_\nu q_\rho\}}{L_1L_2L_3L_4}\ . \tag{3.16}$$

It is generally more difficult to calculate this type of *tensor* integral than the scalar integrals we have encountered up to this point. Note that for the processes we will be calculating tensors integrals of rank three or less have to be considered. A box diagram with four fermion propagators is of course possible, but it would require two outgoing photons or gluons, respectively, whereas we need here two outgoing heavy quarks. For this reason we do not have to examine integrals of the type $D_{\mu\nu\rho\sigma}$.

We know that the Lorentz covariant structure of the tensor loop integrals can only depend on the momenta of the attached legs and on the metric $g_{\mu\nu}$. This immediately suggests decomposing the integrals accordingly, a technique called Passarino-Veltman decomposition [47], which is also conveniently summarized in Ref. [67]. One can easily write down the possible Lorentz covariant combinations:

$$\begin{aligned}
B^\mu &= q_1^\mu B_1\ ,\\
B^{\mu\nu} &= q_1^\mu q_1^\nu B_{21} + g^{\mu\nu}B_{22}\ ,\\[1em]
C^\mu &= q_1^\mu C_{11} + q_2^\mu C_{12}\ ,\\
C^{\mu\nu} &= q_1^\mu q_1^\nu C_{21} + q_2^\mu q_2^\nu C_{22} + \{q_1q_2\}^{\mu\nu}C_{23} + g^{\mu\nu}C_{24}\ ,\\
C^{\mu\nu\rho} &= q_1^\mu q_1^\nu q_1^\rho C_{31} + q_2^\mu q_2^\nu q_2^\rho C_{32} + \{q_1q_1q_2\}^{\mu\nu\rho}C_{33} + \{q_1q_2q_2\}^{\mu\nu\rho}C_{34}\\
&\quad + \{q_1g\}^{\mu\nu\rho}C_{35} + \{q_2g\}^{\mu\nu\rho}C_{36}\ ,\\[1em]
D^\mu &= q_1^\mu D_{11} + q_2^\mu D_{12} + q_3^\mu D_{13}\ ,\\
D^{\mu\nu} &= q_1^\mu q_1^\nu D_{21} + q_2^\mu q_2^\nu D_{22} + q_3^\mu q_3^\nu D_{23} + \{q_1q_2\}^{\mu\nu}D_{24} + \{q_1q_3\}^{\mu\nu}D_{25}\\
&\quad + \{q_2q_3\}^{\mu\nu}D_{26} + g^{\mu\nu}D_{27}\ ,\\
D^{\mu\nu\rho} &= q_1^\mu q_1^\nu q_1^\rho D_{31} + q_2^\mu q_2^\nu q_2^\rho D_{32} + q_3^\mu q_3^\nu q_3^\rho D_{33} + \{q_1q_1q_2\}^{\mu\nu\rho}D_{34} + \{q_1q_1q_3\}^{\mu\nu\rho}D_{35}\\
&\quad + \{q_1q_2q_2\}^{\mu\nu\rho}D_{36} + \{q_1q_3q_3\}^{\mu\nu\rho}D_{37} + \{q_2q_2q_3\}^{\mu\nu\rho}D_{38} + \{q_2q_3q_3\}^{\mu\nu\rho}D_{39}\\
&\quad + \{q_1q_2q_3\}^{\mu\nu\rho}D_{310} + \{q_1g\}^{\mu\nu\rho}D_{311} + \{q_2g\}^{\mu\nu\rho}D_{312} + \{q_3g\}^{\mu\nu\rho}D_{313}\ .
\end{aligned} \tag{3.17}$$

The scalar coefficient integrals on the r.h.s. can depend on all the possible scalar invariants of the leg momenta and on the masses m_i. The arguments of the tensor and scalar integrals have been omitted for brevity. The brackets $\{\dots\}^{\mu\nu\cdots}$ are a shorthand denoting the sum of all possible *different* Lorentz index permutations, for example $\{q_1q_1q_2\}^{\mu\nu\rho} = q_1^\mu q_1^\nu q_2^\rho +$

$q_1^\nu q_1^\rho q_2^\mu + q_1^\rho q_1^\mu q_2^\nu$ and $\{q_1 g\}^{\mu\nu\rho} = q_1^\mu g^{\nu\rho} + q_1^\nu g^{\rho\mu} + q_1^\rho g^{\mu\nu}$. All Lorentz index permutations must have the same scalar integral as coefficient, since the tensor integrals like (3.16) stay invariant under these permutations. This property will later be shown to result in stringent consistency checks on the decomposition, since the same coefficient will be obtained no matter how the projection is ordered.

The decomposition, a 13×13 matrix problem in case of $D^{\mu\nu\rho}$, looks forbidding, but it is possible to reduce it to at most a 3×3 matrix problem by taking into account the fact that leg momenta are added one by one into the loop. As already mentioned above, in the propagators $L_i \equiv l_i^2 - m_i^2 + i\epsilon$ the momentum l_i has then the simple progression $l_1 = q,\ l_2 = q + q_1,\ l_3 = q + q_1 + q_2$ and $l_4 = q + q_1 + q_2 + q_3$. Thus we can rewrite the scalar product of the leg momenta and the loop momentum in the following way

$$\begin{aligned}
q_1 \cdot q &= (L_2 - L_1 + f_1)/2 \qquad \text{with} \qquad f_1 \equiv m_2^2 - m_1^2 - q_1^2 \ , \\
q_2 \cdot q &= (L_3 - L_2 + f_2)/2 \qquad \text{with} \qquad f_2 \equiv m_3^2 - m_2^2 - (q_1 + q_2)^2 + q_1^2 \ , \\
q_3 \cdot q &= (L_4 - L_3 + f_3)/2 \qquad \text{with} \qquad f_3 \equiv m_4^2 - m_3^2 - (q_1 + q_2 + q_3)^2 + (q_1 + q_2)^2 \ .
\end{aligned} \tag{3.18}$$

Since the L_i terms introduced by rewriting the scalar product will cancel against the propagators in the denominator and since the f_i do not contain the loop momentum, we can effectively remove q from the numerator this way! The price to be paid is the introduction of new scalar integrals of the form occurring for loops with one propagator less. To make this clear, consider as an example

$$\begin{aligned}
q_2^\mu D_\mu &= \mu^{-\varepsilon} \int \frac{d^n q}{(2\pi)^n} \frac{q_2 \cdot q}{L_1 L_2 L_3 L_4} = \int \frac{(L_3 - L_2 + f_2)/2}{L_1 L_2 L_3 L_4} \\
&= \frac{1}{2} \Bigg[\underbrace{\int \frac{1}{L_1 L_2 L_4}}_{C_0(1,2,4)} - \underbrace{\int \frac{1}{L_1 L_3 L_4}}_{C_0(1,3,4)} + f_2 D_0 \Bigg]
\end{aligned} \tag{3.19}$$

where the integration sign is a shorthand for $\mu^{-\varepsilon} \int d^n q/(2\pi)^n$ here and below.

Apart from the expected scalar integral D_0 corresponding to the tensor integral D_μ, one has two new scalar integrals $C_0(1,2,4)$ and $C_0(1,3,4)$ having three propagator terms in the denominator, which however differ from those of the generic $C_0 = C_0(1,2,3)$ introduced directly by the vertex corrections. But now all we have to do is to project onto these scalar products of loop and leg momenta, which at worst for the boxes is a 3×3 matrix problem, and calculate the (new) scalar integrals. To this end one defines a projective momentum

$$P_l^\mu q_{i\mu} = \delta_{il} \ , \tag{3.20}$$

where the indices $i, l = 1, 2, \ldots, d$ run over the number of independent leg momenta d, that is the number of propagators in the loop minus one. For self-energies B we have only one independent leg momentum and thus

$$P_1^\mu = X_B^{-1} q_1^\mu \quad \text{with} \quad X_B = q_1^2 \ . \tag{3.21}$$

For vertex corrections C there are two independent leg momenta and so

$$\begin{pmatrix} P_1^\mu \\ P_2^\mu \end{pmatrix} = X_C^{-1} \begin{pmatrix} q_1^\mu \\ q_2^\mu \end{pmatrix} \quad \text{with} \quad X_C = \begin{pmatrix} q_1^2 & q_1 \cdot q_2 \\ q_1 \cdot q_2 & q_2^2 \end{pmatrix} . \tag{3.22}$$

Finally for box integrals there are three

$$\begin{pmatrix} P_1^\mu \\ P_2^\mu \\ P_3^\mu \end{pmatrix} = X_D^{-1} \begin{pmatrix} q_1^\mu \\ q_2^\mu \\ q_3^\mu \end{pmatrix} \quad \text{with} \quad X_D = \begin{pmatrix} q_1^2 & q_1 \cdot q_2 & q_1 \cdot q_3 \\ q_1 \cdot q_2 & q_2^2 & q_2 \cdot q_3 \\ q_1 \cdot q_3 & q_2 \cdot q_3 & q_3^2 \end{pmatrix} . \tag{3.23}$$

Only when the inverse of the matrices X exists can this simplification be used.

Using these definitions we can already treat all the vector integrals occurring in the nPF graphs. As an example $C^\mu = q_1^\mu C_{11} + q_2^\mu C_{12}$ will be worked out explicitly here:

$$\begin{pmatrix} C_{11} \\ C_{12} \end{pmatrix} = \begin{pmatrix} P_1^\mu \\ P_2^\mu \end{pmatrix} C_\mu = X_C^{-1} \begin{pmatrix} q_1^\mu C_\mu \\ q_2^\mu C_\mu \end{pmatrix} \equiv X_C^{-1} \begin{pmatrix} R_1 \\ R_2 \end{pmatrix} , \tag{3.24}$$

with

$$R_1 = \frac{1}{2}\left[B_0(1,3) - B_0(2,3) + f_1 C_0\right] , \quad R_2 = \frac{1}{2}\left[B_0(1,2) - B_0(1,3) + f_2 C_0\right] , \tag{3.25}$$

and the inverse of X_C is easily calculated to be

$$X_C^{-1} = \frac{1}{q_1^2 q_2^2 - (q_1 \cdot q_2)^2} \begin{pmatrix} q_2^2 & -q_1 \cdot q_2 \\ -q_1 \cdot q_2 & q_1^2 \end{pmatrix} . \tag{3.26}$$

Note that for the calculation of $B_0(2,3)$, we can shift the integration $q + q_1 \to q$

$$B_0(2,3) = \int \frac{1}{\left[(q+q_1)^2 - m_2^2\right]\left[(q+q_1+q_2)^2 - m_3^2\right]} = \int \frac{1}{(q^2 - m_2^2)\left[(q+q_2)^2 - m_3^2\right]} , \tag{3.27}$$

bringing it into the standard form for B_0. Similarly one proceeds for $C_0(2,3,4)$.

Next we need to construct a projective tensor which singles out the metric $g^{\mu\nu}$, using the projective momentum P_l^μ,

$$P^{\mu\nu} \equiv \frac{1}{n-d}\left[g^{\mu\nu} - \sum_{l=1}^{d} P_l^\mu q_l^\nu\right] , \tag{3.28}$$

where d again is the number of independent leg momenta and $n = 4 + \varepsilon$ is the spacetime dimension. This leads to the desired properties

$$P^{\mu\nu} q_{i\mu} = P^{\mu\nu} q_{i\nu} = 0 \ , \qquad P^{\mu\nu} g_{\mu\nu} = 1 \ . \tag{3.29}$$

As an example, the 3PF coefficient of the metric is obtained using this projective tensor:

$$\begin{aligned}
C_{24} = P^{\mu\nu} C_{\mu\nu} &= \frac{1}{n-2} \left[g^{\mu\nu} - P_1^\mu q_1^\nu - P_2^\mu q_2^\nu \right] \int \frac{q_\mu q_\nu}{L_1 L_2 L_3} \\
&= \frac{1}{n-2} \left[\int \frac{1}{L_2 L_3} + m_1^2 \int \frac{1}{L_1 L_2 L_3} - R_3 - R_6 \right] \\
&= \frac{1}{n-2} \left[m_1^2 C_0 - \frac{1}{2} \left(f_1 C_{11} + f_2 C_{12} - B_0(2,3) \right) \right] \ ,
\end{aligned} \tag{3.30}$$

$$\begin{aligned}
R_3 &\equiv \frac{1}{2} P_1^\mu \int \left[\frac{q_\mu}{L_1 L_3} - \frac{q_\mu}{L_2 L_3} + f_1 \frac{q_\mu}{L_1 L_2 L_3} \right] \\
&= \frac{1}{2} P_1^\mu \left\{ B_\mu(1,3) - \left[B_\mu(2,3) - q_{1\mu} B_0(2,3) \right] + f_1 C_\mu \right\} \\
&= \frac{1}{2} \left[B_1(1,3) + B_0(2,3) + f_1 C_{11} \right] \ ,
\end{aligned} \tag{3.31}$$

$$R_6 \equiv \frac{1}{2} P_2^\mu \int \left[\frac{q_\mu}{L_1 L_2} - \frac{q_\mu}{L_1 L_3} + f_2 \frac{q_\mu}{L_1 L_2 L_3} \right] = \frac{1}{2} \left[-B_1(1,3) + f_2 C_{12} \right] \ . \tag{3.32}$$

In the first step $q^2 = L_1 + m_1^2$ and (3.18) were used. Note the shift $q \to q + q_1$ in the second integration in the first step of calculating R_3, so that $B_\mu(2,3) = q_{2\mu} B_1(2,3)$, which gives no contribution when contracted with P_1^μ. It is of great advantage that this type of projection properties can be used on the tensors with reduced rank[4] in the intermediate steps.

Turning to the $C_{\mu\nu}$ coefficients depending on the leg momenta, we can use the projective momentum twice

$$\begin{aligned}
\begin{pmatrix} C_{21} \\ C_{23} \end{pmatrix} &= P_1^\mu \begin{pmatrix} P_1^\nu \\ P_2^\nu \end{pmatrix} \tilde{C}_{\mu\nu} = X_C^{-1} \begin{pmatrix} R_3 - C_{24} \\ R_4 \end{pmatrix} \ , \\
\begin{pmatrix} C_{23} \\ C_{22} \end{pmatrix} &= P_2^\mu \begin{pmatrix} P_1^\nu \\ P_2^\nu \end{pmatrix} \tilde{C}_{\mu\nu} = X_C^{-1} \begin{pmatrix} R_5 \\ R_6 - C_{24} \end{pmatrix} \ ,
\end{aligned} \tag{3.33}$$

$$\begin{aligned}
R_4 &\equiv P_1^\mu q_2^\nu C_{\mu\nu} = \frac{1}{2} \left[B_1(1,2) - B_1(1,3) + f_2 C_{11} \right] \ , \\
R_5 &\equiv P_2^\mu q_1^\nu C_{\mu\nu} = \frac{1}{2} \left[B_1(1,3) - B_1(2,3) + f_1 C_{12} \right] \ ,
\end{aligned} \tag{3.34}$$

[4]For $P^{\mu\nu} B_{\mu\nu}$ one needs $P_1^\mu \int q_\mu / L_1 = 0$, easily proven in the rest frame of q_1, because then $q_1 \cdot q = q_1^0 q_0$ yields an integral odd in the energy component q_0.

where $\tilde{C}_{\mu\nu} \equiv C_{\mu\nu} - g_{\mu\nu}C_{24}$ has the metric contribution subtracted. Since there are two ways of projecting out C_{23}, depending on whether P_1 or P_2 is used first, this coefficient is obtained twice. This kind of redundancy occurs for all possible permutations of the projection order and allows one to perform internal consistency checks for all the multiply obtained coefficients!

For $C_{\mu\nu\rho}$, we already know how to project out the terms with the metric, e.g.,

$$\begin{pmatrix} C_{35} \\ C_{36} \end{pmatrix} = P^{\mu\nu} \begin{pmatrix} P_1^\rho \\ P_2^\rho \end{pmatrix} C_{\mu\nu\rho} = X_C^{-1} \begin{pmatrix} R_{10} \\ R_{11} \end{pmatrix} , \tag{3.35}$$

$$\begin{aligned} R_{10} &\equiv P^{\mu\nu} q_1^\rho C_{\mu\nu\rho} = \frac{1}{2}\left[B_{22}(1,3) - B_{22}(2,3) + f_1 C_{24}\right] , \\ R_{11} &\equiv P^{\mu\nu} q_2^\rho C_{\mu\nu\rho} = \frac{1}{2}\left[B_{22}(1,2) - B_{22}(1,3) + f_2 C_{24}\right] . \end{aligned} \tag{3.36}$$

It is convenient to construct a complementary tensor to $P^{\mu\nu}$, which projects onto specific combinations of *two* leg momenta:

$$P_{kl}^{\mu\nu} \equiv P_k^\mu P_l^\nu - (P_k \cdot P_l) P^{\mu\nu} , \tag{3.37}$$

with the properties

$$P_{kl}^{\mu\nu} q_{i\mu} q_{j\nu} = \delta_{ik}\delta_{jl} , \qquad P_{kl}^{\mu\nu} g_{\mu\nu} = 0 . \tag{3.38}$$

Then we can for example write

$$\begin{pmatrix} C_{31} \\ C_{33} \end{pmatrix} = P_{11}^{\mu\nu} \begin{pmatrix} P_1^\rho \\ P_2^\rho \end{pmatrix} \tilde{C}_{\mu\nu\rho} = X_C^{-1} \begin{pmatrix} R_{12} - 2C_{35} \\ R_{13} \end{pmatrix} , \tag{3.39}$$

$$\begin{aligned} R_{12} &\equiv P_{11}^{\mu\nu} q_1^\rho C_{\mu\nu\rho} = \frac{1}{2}\left[B_{21}(1,3) - B_0(2,3) + f_1 C_{21}\right] , \\ R_{13} &\equiv P_{11}^{\mu\nu} q_2^\rho C_{\mu\nu\rho} = \frac{1}{2}\left[B_{21}(1,2) - B_{21}(1,3) + f_2 C_{21}\right] , \end{aligned} \tag{3.40}$$

where $\tilde{C}_{\mu\nu\rho} \equiv C_{\mu\nu\rho} - \{q_1 g\}_{\mu\nu\rho} C_{35}$ has the metric part contributing here subtracted.

This completes the necessary collection of projection operators. We have already performed part of the necessary decompositions for the vertex corrections in the examples given above, and the self-energy and box integrations can be treated likewise. A collection of further results can be found in App. A.3. Though this procedure is straightforward, its actual implementation requires a computer algebra system like `Mathematica` [57]. The general decomposition for *arbitrary* momenta and masses of the 4PF alone results in `Mathematica` output of more than three MByte length before simplification. Managing this lengthy result was facilitated by defining a space in the possible basic functions B_0, C_0 and D_0, so that the coefficient relations become vector equations in that space. Simplifying the formulae for specific momenta and inserting the basic functions will usually reduce the length of the 4PF formulae by two orders of magnitude.

3.4 Some Final Remarks

Upon calculating the actual virtual processes using the formalism of Sec. 3.3 and App. A.3, one will need numerous scalar integrals which do not seem to be included in the basic set of App. A.2. But those integrals can always be brought into a form where they are either seen to be directly equal to one of the basic integrals or derivable by simple manipulations. There are several "physical" ways to arrive at such transformations. Many of them can be obtained by simple crossing. For example the integral $B_0(p_1 - k_2, 0, m)$ obviously is obtained from the known integral $B_0(p_1 - k_1, 0, m)$ by crossing $k_1 \leftrightarrow k_2$. To this end we can simply replace $t, t_1 \to u, u_1$ in the known result (A.20). Also one often obtains integrals which just correspond to assigning the loop momentum in a different way, see Fig. 3.4 for the simple case of 2PFs. Similarly we can derive for 3PFs that $C_0(p_1, p_2, m_1, m_2, m_3) = C_0(-p_1, -p_2, m_1, m_2, m_3) = C_0(p_1 + p_2, -p_2, m_1, m_3, m_2) = C_0(-p_1, p_1 + p_2, m_2, m_1, m_3) = C_0(p_2, p_1, m_3, m_2, m_1)$ by reassigning the loop momentum and of course we can also treat the 4PF D_0's this way.

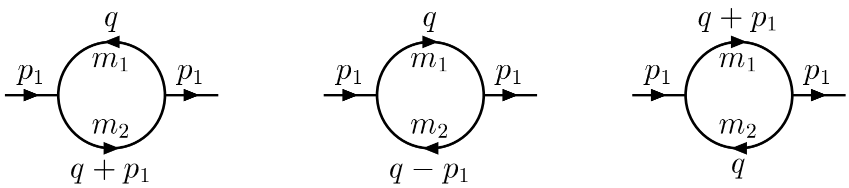

Figure 3.4: By assigning the loop momentum differently in one graph, it is shown that $B_0(p_1, m_1, m_2) = B_0(-p_1, m_1, m_2) = B_0(p_1, m_2, m_1)$.

One can also simply shift the loop momentum, which does not change the value of the integral. For example setting $q \to q + p_2$ in $C_0(p_1, -k_1 - k_2, 0, m, m)$ yields the integral $C_0(p_2, p_1, m, 0, m)$, proving their equality. But in practice it is much simpler to just insert the momenta in the kernels K of Tab. 3.1 and compare to those of the standard set. For instance in the example above, $C_0(p_1, -k_1 - k_2, 0, m, m)$ gives $K = -bc\frac{s}{m^2} + (1-a)^2$. But we know that the basic integral $C_0(p_2, p_1, m, 0, m)$, see (A.24), leads to $K = -ac\frac{s}{m^2} + (1-b)^2$, so since the assignment of the parameters a, b, c is arbitrary, both integrals are equal. Also equalities due to the reassignment of the loop momentum are immediately obvious. Taking the case covered in Fig. 3.4, one always obtains $K = -ab + am_1^2 + bm_2^2$, switching $a \leftrightarrow b$ if needed. Furthermore changes of the kinematic variables due to crossing are trivial, e.g., $B_0(p_1 - k_2, 0, m)$ leads to $K = -ab\frac{u}{m^2} + b$ and $B_0(p_1 - k_1, 0, m)$ gives $K = -ab\frac{t}{m^2} + b$. Also equalities like $C_0(p_1 - k_1, -k_2, 0, m, m) = C_0(p_1, -k_1, 0, m, m)$, which need some work to be proven otherwise, are obtained by just writing down the kernels. With this method it is an easy exercise to obtain the needed relations between integrals, about 40 were needed in our calculation.

A special simplification can be used when working on the QED-like box integrals. Since we calculate $2 \to 2$ processes, there are only three independent momenta, the fourth can be calculated using energy-momentum conservation $-q_4 = q_1 + q_2 + q_3$, counting all momenta as incoming. Taking a look at the propagators in D_0 in (3.4), we can write

$$\left.\begin{array}{c} q^2-m_1^2+i\epsilon \\ (q+q_1)^2-m_2^2+i\epsilon \\ (q+q_1+q_2)^2-m_3^2+i\epsilon \\ (q+q_1+q_2+q_3)^2-m_4^2+i\epsilon \end{array}\right\} \Rightarrow \left\{\begin{array}{c} q^2-m_1^2+i\epsilon \\ (q-q_4-q_3-q_2)^2-m_2^2+i\epsilon \\ (q-q_4-q_3)^2-m_3^2+i\epsilon \\ (q-q_4)^2-m_4^2+i\epsilon \end{array}\right. . \tag{3.41}$$

Simply by replacing $q \to -q$ in the integration[5] we then obtain the relation

$$D_0(q_1,q_2,q_3,m_1,m_2,m_3,m_4) = D_0(q_4,q_3,q_2,m_1,m_4,m_3,m_2) \stackrel{\text{abbr.}}{\longrightarrow} D_0 = \overline{D}_0 . \tag{3.42}$$

We can also show this by inserting the momenta into the kernel K given in Tab. 3.1. $\overline{D}_0$ leads to the same kernel as D_0 upon switching the assignment $b \leftrightarrow d$. In the tensor integrals the $q \to -q$ shift adds a minus for every loop momentum, so using the same abbreviation as in (3.42), we can write

$$D^\mu = -\overline{D}^\mu , \qquad D^{\mu\nu} = \overline{D}^{\mu\nu} , \qquad D^{\mu\nu\rho} = -\overline{D}^{\mu\nu\rho} . \tag{3.43}$$

Now we can insert this in the tensor decomposition (3.17), for example

$$\begin{aligned} D^\mu &= q_1^\mu D_{11} + q_2^\mu D_{12} + q_3^\mu D_{13} \\ &= -\overline{D}^\mu = -\left(q_4^\mu \overline{D}_{11} + q_3^\mu \overline{D}_{12} + q_2^\mu \overline{D}_{13}\right) \\ &= q_1^\mu \overline{D}_{11} + q_2^\mu(\overline{D}_{11} - \overline{D}_{13}) + q_3^\mu(\overline{D}_{11} - \overline{D}_{12}) \\ \Rightarrow \quad D_{11} = \overline{D}_{11} , \qquad & D_{12} = \overline{D}_{11} - \overline{D}_{13} , \qquad D_{13} = \overline{D}_{11} - \overline{D}_{12} . \end{aligned} \tag{3.44}$$

Similar relations can be derived for the other tensor coefficients.

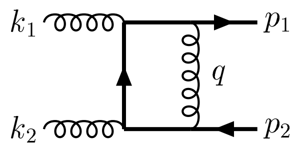

Figure 3.5: For this QED-like box graph a simplified tensor decomposition (3.47) is possible.

By itself this is not very helpful, except as a further method for checking the decomposition. But in the QED-like box Fig. 3.5, we get for $D \to D(p_1,-k_1,-k_2,0,m,m,m)$ and $\overline{D} \to D(p_2,-k_2,-k_1,0,m,m,m)$ *exactly* the same projection coefficients. This can be easily checked by noting that the matrix X_D of the projective momenta in (3.23) and

[5] For every of the n components the minus in the measure is compensated by the minus in the integration limits, effectively only the kernel changes.

the f_i collected in (3.18) are the same in both cases. The new scalar integrals obtained by the projection will also be the same, since the second and fourth propagator, L_2 and L_4, which are interchanged in $D \leftrightarrow \overline{D}$, have on one hand the same mass and on the other hand the same square of the sum of external q_i. As an explicit example compare $C_0(1,3,4)$ with $\overline{C}_0(1,3,4)$. Both have the same masses m_i and inserting $q_1 = p_1 - k_1,\ q_2 = -k_2$ and $q_1 = p_2 - k_2,\ q_2 = -k_1$, respectively, in the K found in Tab. 3.1 will yield the same kernel. A different way of coming to this conclusion is noting that (A.3) introduces Feynman parameters to a numerator with loop four momenta $q^\mu q^\nu \dots$, so that for the *tensor* integrals the assignment of $a,\ b,\ c,\ d$ changes the result obtained for the projection coefficients. But in the QED-like integral here the switch $b \leftrightarrow d$ mentioned below (3.42) is not necessary: the propagators already lead to the same K, because of the similarity between L_2 and L_4. So the projection coefficients will be equal. At any rate, we can set $D_{ij} = \overline{D}_{ij}$ here! Then of course the relations like in (3.44) can be used to eliminate dependent scalar coefficients. One finds eight relations:

$$\begin{gathered}
D_{11} = D_{12} + D_{13}\ , \qquad D_{24} = (D_{21} + D_{22} - D_{23})/2\ , \\
D_{25} = (D_{21} - D_{22} + D_{23})/2\ , \qquad D_{31} = -2D_{32} - 2D_{33} + 3D_{36} + 3D_{37}\ , \\
D_{34} = -D_{32} - D_{33} + 2D_{36} + D_{37}\ , \qquad D_{35} = -D_{32} - D_{33} + D_{36} + 2D_{37}\ , \\
D_{310} = (-D_{32} - D_{33} + D_{36} + D_{37} + D_{38} + D_{39})/2\ , \qquad D_{311} = D_{312} + D_{313}\ .
\end{gathered} \tag{3.45}$$

We can now write the Lorentz structure of $D(p_1, -k_1, -k_2, 0, m, m, m)$ in a neat way, using the following further redefinitions:

$$\begin{gathered}
\tilde{D}_{21} = -\frac{1}{2}(D_{21} - D_{22} - D_{23})\ , \quad \tilde{D}_{36} = \frac{1}{2}(D_{32} - D_{36})\ , \\
\tilde{D}_{37} = \frac{1}{2}(D_{33} - D_{37})\ , \quad \tilde{D}_{38} = \frac{1}{2}D_{38}\ , \quad \tilde{D}_{39} = \frac{1}{2}D_{39}
\end{gathered} \tag{3.46}$$

The final simplified result is then

$$\begin{aligned}
D^\mu &= t^\mu D_{12} + u^\mu D_{13}\ , \\
D^{\mu\nu} &= \{p_1 p_2\}^{\mu\nu} \tilde{D}_{21} + t^\mu t^\nu D_{22} + u^\mu u^\nu D_{23} + \{k_1 k_2\}^{\mu\nu} D_{26} + g^{\mu\nu} D_{27}\ , \\
D^{\mu\nu\rho} &= t^\mu t^\nu t^\rho D_{32} + u^\mu u^\nu u^\rho D_{33} + \{t p_1 p_2\}^{\mu\nu\rho} \tilde{D}_{36} + \{u p_1 p_2\}^{\mu\nu\rho} \tilde{D}_{37} \\
&\quad + \{t k_1 k_2\}^{\mu\nu\rho} \tilde{D}_{38} + \{u k_1 k_2\}^{\mu\nu\rho} \tilde{D}_{39} + \{tg\}^{\mu\nu\rho} D_{312} + \{ug\}^{\mu\nu\rho} D_{313}\ ,
\end{aligned} \tag{3.47}$$

where we have used the abbreviations $t^\mu = (p_1 - k_1)^\mu$ and $u^\mu = (p_1 - k_2)^\mu$. This compares favorably with (3.17). The other occurring boxes cannot be simplified like that, since the $b \leftrightarrow d$ interchange has to be performed. There we can only check relations like $D_{12} - \overline{D}_{12} = D_{13} - \overline{D}_{13}$, which always have to be fulfilled.

Finally, as has been mentioned already when introducing the projective momenta in (3.21) to (3.23), the Passarino-Veltman decomposition breaks down when the inverse of the matrix X does not exist. In our calculations this occurs only in simple bubble diagrams of the type depicted in Fig. 3.6, inserted in the incoming *on-shell* gluons. They

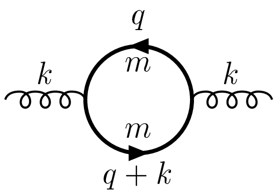

Figure 3.6: This bubble graph with $k^2 = 0$ and $m \neq 0$ cannot be decomposed with the Passarino-Veltman technique.

lead to integrals $B(k, m, m)$ with $k^2 = 0$ but $m \neq 0$. But here $X_B = k^2$, so obviously it cannot be inverted. The integral occurring in this situation is

$$\begin{aligned} I &= \mu^{-\varepsilon} \int \frac{d^n q}{(2\pi)^n} \frac{\mathrm{Tr}\,\langle \gamma^\mu (\not{q} + m) \gamma^\nu (\not{q} + \not{k} + m) \rangle}{(q^2 - m^2)[(q+k)^2 - m^2]} \\ &= 4\mu^{-\varepsilon} \int_0^1 dx \int \frac{d^n q}{(2\pi)^n} \frac{2q^\mu q^\nu + (k^\mu q^\nu + q^\mu k^\nu) + (m^2 - k \cdot q - q^2) g^{\mu\nu}}{[q^2 + 2xk \cdot q - m^2 + k^2 x]^2} \\ &= -8(k^\mu k^\nu - g^{\mu\nu} k^2) \mu^{-\varepsilon} \int_0^1 dx\, x(1-x) I_0 \ , \end{aligned} \tag{3.48}$$

where we have used Equations (A.18)-(A.20) of [68], see also Appendix C of [69]. The basic integral I_0 is given to $\mathcal{O}(1)$ by

$$I_0 = -\frac{i}{16\pi^2} \left[\frac{2}{\varepsilon} + \gamma_E - \ln(4\pi) + \ln(k^2 x(1-x) - m^2) \right] \ , \tag{3.49}$$

with the Euler γ_E. If $m = 0 = k^2$, then $I_0 = 0$ and thus $I = 0$. Otherwise we get

$$\begin{aligned} I = \frac{i}{2\pi^2} (k^\mu k^\nu - g^{\mu\nu} k^2) \mu^{-\varepsilon} \Bigg\{ & \frac{1}{6} \left[\frac{2}{\varepsilon} + \gamma_E - \ln(4\pi) \right] \\ & + \int_0^1 dx\, x(1-x) \ln(k^2 x(1-x) - m^2) \Bigg\} \ . \end{aligned} \tag{3.50}$$

This formula is valid in general, it is for example easy to obtain Equation (III.29) of [69] for $k^2, m \neq 0$ from it. But here we are interested in the case of $k^2 = 0$ with $m \neq 0$, and then using C_ε defined in (3.6) to $\mathcal{O}(\varepsilon)$, we can write the integral to $\mathcal{O}(1)$ as

$$I = iC_\varepsilon (k^\mu k^\nu - k^2 g^{\mu\nu}) \frac{8}{3\varepsilon} \ , \tag{3.51}$$

where we have kept k^2 in the Lorentz structure, since there will be a $1/k^2$ dependence due to a gluon propagator when attaching Fig. 3.6 to the rest of the Feynman diagram. The limit $k^2 \to 0$ is possible in the Lorentz structure only after contracting the Lorentz indices in the matrix element.

Chapter 4

Renormalization

4.1 The QCD Lagrangian and its Renormalization

The last chapter has shown that we encounter singularities when we calculate higher order corrections using the Feynman rules derived from the bare QCD Lagrangian. The infrared singularities cancel in the sum with the real contributions which will be introduced in the next chapter. This is guaranteed by the Bloch-Nordsieck and Kinoshita-Lee-Nauenberg theorems [70], respectively. The real contributions also have a new type of singularities called collinear or mass singularities, which will be dealt with by the mass factorization procedure of Chap. 6. Basically this amounts to a redefinition of the parton densities of the hadrons (and photons). This leaves us with the ultraviolet divergencies. We will see in this chapter how a redefinition of the fields and parameters of the bare Lagrangian can be used to eliminate the UV singularities. We note that details about our particular scheme for the renormalization of QCD, which uses the $\overline{\mathrm{MS}}$ scheme for light quarks and an on-shell scheme with explicit decoupling for the heavy quarks, cannot easily be found in the literature. In the corresponding unpolarized calculations, which also use this scheme, an effective procedure using only mass and strong coupling renormalization is used, see for example Eqns. (2.9)-(2.11) in [46]. However, no derivations of the formulae are given, so we will supply them here. Furthermore, the only calculation of the needed renormalization constants Z_i known to us is [71], which however does not provide much technical detail on their derivation. Actually this reference was pointed out to us only after we had already (re-)calculated the Z_i. Since the available information on this scheme seems to be scarce, we will provide sufficient detail of our independent calculation.

Let us start by writing down the bare QCD Lagrangian[1]. It can be split into parts

$$\mathscr{L} = \mathscr{L}_G + \mathscr{L}_{GF} + \mathscr{L}_{FP} + \mathscr{L}_F = \mathscr{L}_0 + \mathscr{L}_I \ , \tag{4.1}$$

where the parts are

gauge: $$\mathscr{L}_G = -\frac{1}{4} F^a_{\mu\nu} F^{a\mu\nu} \quad \text{with} \quad F^a_{\mu\nu} = \partial_\mu A^a_\nu - \partial_\nu A^a_\mu + g f^{abc} A^b_\mu A^c_\nu \ , \tag{4.2}$$

[1] The following derivation of the counterterm Feynman rules is standard and follows closely [64].

$$\text{gauge fixing:} \quad \mathscr{L}_{GF} = -\frac{1}{2\alpha}\left(\partial^\mu A_\mu^a\right)^2 \quad \text{with} \quad \alpha = 1 \quad \text{in Feynman gauge}\,, \tag{4.3}$$

$$\text{Faddeev-Popov:} \quad \mathscr{L}_{FP} = \left(\partial^\mu \xi^{a*}\right) D_\mu^{ab} \xi^b \quad \text{with} \quad D_\mu^{ab} = \delta^{ab}\partial_\mu - g f^{abc} A_\mu^c\,, \tag{4.4}$$

$$\text{fermion:} \quad \mathscr{L}_F = \overline{\Psi}_i \left(i \not{D}_{ij} - m\delta_{ij}\right)\Psi_j \quad \text{with} \quad D_{ij}^\mu = \delta_{ij}\partial^\mu - i g T_{ij}^a A^{a\mu}\,, \tag{4.5}$$

where T^a and f^{abc} are the generators and structure constants of $SU(3)_{\text{color}}$, respectively, and the "gluon" color indices can take the values $a, b, c, \ldots = 1, \ldots, 8$ and the "quark" ones can have $i, j, \ldots = 1, 2, 3$. See App. B.3 for more details about the $SU(N)$ groups. Also the ξ^a and ξ^{a*} ghost fields should be viewed as independent, i.e., one could write $\xi^a = (\xi_1^a + i\xi_2^a)/\sqrt{2}$ with two independent real ghost fields ξ_1^a and ξ_2^a. Furthermore we have only written the fermion field for one quark flavor in (4.5) for simplicity. Splitting into a free part $\mathscr{L}_0$ and an interaction part $\mathscr{L}_I$ then gives

$$\begin{aligned}
\mathscr{L}_0 &= -\frac{1}{4}\left(\partial_\mu A_\nu^a - \partial_\nu A_\mu^a\right)\left(\partial^\mu A^{a\nu} - \partial^\nu A^{a\mu}\right) - \frac{1}{2\alpha}\left(\partial^\mu A_\mu^a\right)^2 + \left(\partial^\mu \xi^{a*}\right)\left(\partial_\mu \xi^a\right) \\
&\quad + \overline{\Psi}_i (i\not{\partial} - m)\Psi_i\,, \qquad (4.6) \\
\mathscr{L}_I &= -\frac{g}{2} f^{abc}\left(\partial_\mu A_\nu^a - \partial_\nu A_\mu^a\right) A^{b\mu} A^{c\nu} - \frac{g^2}{4} f^{abe} f^{cde} A_\mu^a A_\nu^b A^{c\mu} A^{d\nu} - g f^{abc}\left(\partial^\mu \xi^{a*}\right)\xi^b A_\mu^c \\
&\quad + g\overline{\Psi}_i T_{ij}^a \gamma^\mu \Psi_j A_\mu^a\,. \qquad (4.7)
\end{aligned}$$

Now the bare Lagrangian (4.1) will be renormalized by introducing renormalization constants Z_i

$$\text{fields} \quad A_\mu^a = \sqrt{Z_3} A_{r\mu}^a\,, \qquad \xi^{a(*)} = \sqrt{Z_{3h}}\xi_r^{a(*)}\,, \qquad \Psi = \sqrt{Z_2}\Psi_r\,, \tag{4.8}$$

$$\text{parameters} \quad g = Z_g g_r\,, \qquad \alpha = Z_3 \alpha_r\,, \qquad m = Z_m m_r\,. \tag{4.9}$$

Note that the gauge fixing parameter α is renormalized with the same constant as the gluon field. The reason can be seen by examining the Lorentz structure of the gluon propagator $g^{\mu\nu} - (1-\alpha)k^\mu k^\nu/k^2$. A Slavnov-Taylor identity $ik^\mu k^\nu \tilde{D}_{\mu\nu}^{ab}(k)/\alpha = \delta^{ab}$ for the full gluon propagator $\tilde{D}_{\mu\nu}^{ab}$ can be derived, see [52, 53, 72] and App. B.4. It implies for the gluon self-energy $\Pi_{\mu\nu}^{ab}(k)$ that $k^\mu k^\nu \Pi_{\mu\nu}^{ab}(k) = 0$, since $\tilde{D}_{\mu\nu}^{ab} = D_{0\mu\nu}^{ab} + D_{0\mu\rho}^{ac}\Pi^{cd\rho\sigma}D_{0\sigma\nu}^{db} + \ldots$ with the free gluon propagator $D_{0\mu\nu}^{ab} = -i\delta_{ab}[g_{\mu\nu} - (1-\alpha)k_\mu k_\nu/k^2]/k^2$. Thus $\Pi_{\mu\nu}^{ab}(k) = \delta^{ab}(k_\mu k_\nu - k^2 g_{\mu\nu})\Pi(k^2)$ and we see that only the *transversal* part of the gluon propagator will receive higher order corrections. Then only *one* multiplicative renormalization constant Z_3 is enough for the full gluon propagator, and from the Lorentz structure of the propagator one gets $\alpha \stackrel{!}{=} Z_3\alpha_r$.

Now we can insert (4.8) and (4.9) into (4.1) and obtain a renormalized Lagrangian

$$\mathscr{L}_r = \mathscr{L}_{r0} + \mathscr{L}_{rI} + \mathscr{L}_C\,. \tag{4.10}$$

The first two terms are simply obtained from the free (4.6) and interaction (4.7) parts of the bare Lagrangian by adding a subscript "r" to every field and parameter, i.e., writing down the bare Lagrangian structure with renormalized quantities. Obviously then $\mathscr{L}_C$ collects the Z_i terms and we find

$$\begin{aligned}\mathscr{L}_C = \frac{1}{2}(Z_3-1)\delta^{ab}A^a_{r\mu}\left(g^{\mu\nu}\Box - \partial^\mu\partial^\nu\right)A^b_{r\nu} - (Z_{3h}-1)\delta^{ab}\xi^{a*}_r\Box\xi^b_r \\ + (Z_2-1)\delta_{ij}\overline{\Psi}_{ri}(i\partial\!\!\!/)\Psi_{rj} + (Z_2Z_m-1)\delta_{ij}\overline{\Psi}_{ri}(-m_r)\Psi_{rj} \\ - (Z_1-1)\frac{g_r}{2}f^{abc}\left(\partial_\mu A^a_{r\nu} - \partial_\nu A^a_{r\mu}\right)A^{b\mu}_r A^{c\nu}_r - (Z_4-1)\frac{g_r^2}{4}f^{abe}f^{cde}A^a_{r\mu}A^b_{r\nu}A^{c\mu}_r A^{d\nu}_r \\ - (Z_{1h}-1)g_r f^{abc}\left(\partial^\mu\xi^{a*}_r\right)\xi^b_r A^c_{r\mu} + (Z_{1f}-1)g_r\overline{\Psi}_{ri}T^a_{ij}\gamma^\mu\Psi_{rj}A^a_{r\mu}\,,\end{aligned} \tag{4.11}$$

with

$$Z_1 \equiv Z_g Z_3^{\frac{3}{2}}\,, \quad Z_{1h} \equiv Z_g Z_{3h}\sqrt{Z_3}\,, \quad Z_{1f} \equiv Z_g Z_2\sqrt{Z_3}\,, \quad Z_4 \equiv Z_g^2 Z_3^2\,, \tag{4.12}$$

and the first two terms of (4.11) are rewritten using the fact that a total divergence does not change the equations of motion.

For practical calculation one should now derive the Feynman rules from the Lagrangian. This derivation is lengthy but straightforward and can be found for example in [64], it will not be demonstrated here. But it is important to note the following point: $\mathscr{L}_{r0}$ and $\mathscr{L}_{rI}$ are identical to $\mathscr{L}_0$ and $\mathscr{L}_I$, respectively, in structure. The only difference is that every quantity has been replaced by the corresponding renormalized quantity. So we can simply use the bare QCD Feynman rules for them and set the coupling $g \to g_r$ and the mass $m \to m_r$ to the renormalized values! The new part of the renormalized Lagrangian $\mathscr{L}_C$ of course leads to additional Feynman rules. Note that we have written them in the form of new "interaction vertices", which is possible since $\mathscr{L}_C$ is suppressed by powers of g^2. We will return to this point at the end of the next section. The last four terms of $\mathscr{L}_C$ are identical in structure to the terms in $\mathscr{L}_I$, so we can simply multiply the corresponding bare QCD vertex rules with the appropriate $(Z_i - 1)$ term. The first three terms are written in a form that allows us to (heuristically) read off the corresponding "vertex" rules by assuming the terms act on the $e^{-ik\cdot x}$ or $e^{-ip\cdot x}$ of a four-dimensional Fourier-transformation to momentum space, dropping the fields[2] and multiplying by a factor i. The set of new vertex rules we have found in this way are commonly called *counterterms* and we collect them in Tab. 4.1. Note that we have included a photon-quark counterterm, which is obtained in a completely similar manner as the gluon-quark counterterm from the QED Lagrangian[3]. To avoid confusion with the QCD Z_{1f}, we have used the Ward identity $Z_{1f}^{\mathrm{QED}} = Z_2$ [73] for writing down the rule.

It is far from trivial to prove that the renormalizations introduced in (4.8) and (4.9) are sufficient in all orders to remove the UV singularities. For a thorough discussion one should turn to the appropriate literature, for example to [74]. On the other hand for a one-loop calculation such as ours this is easy to see. Basically for every type of diverging

[2] The two gluon fields contribute a factor 2 for exchanging identical bosons.
[3] But only QCD corrections are considered.

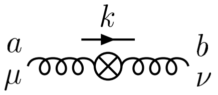	$i(Z_3-1)\delta^{ab}(k^\mu k^\nu - k^2 g^{\mu\nu})$	
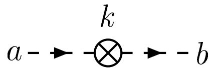	$i(Z_{3h}-1)\delta^{ab}k^2$	
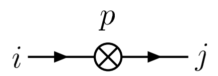	$i\delta_{ij}[(Z_2-1)\not{p} - (Z_2 Z_m - 1)m_r]$	
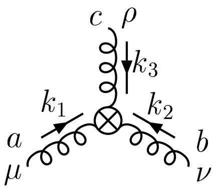	$-(Z_1-1)g_r f^{abc}[g^{\mu\nu}(k_1-k_2)^\rho + g^{\nu\rho}(k_2-k_3)^\mu + g^{\rho\mu}(k_3-k_1)^\nu]$	
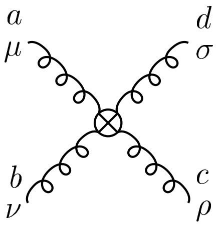	$-i(Z_4-1)g_r^2[f^{abe}f^{cde}(g^{\mu\rho}g^{\nu\sigma} - g^{\mu\sigma}g^{\nu\rho}) + f^{ace}f^{bde}(g^{\mu\nu}g^{\rho\sigma} - g^{\mu\sigma}g^{\nu\rho}) + f^{ade}f^{cbe}(g^{\mu\rho}g^{\nu\sigma} - g^{\mu\nu}g^{\rho\sigma})]$	
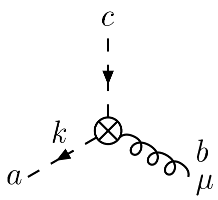	$\longleftarrow\!\!\!\prec$ $(Z_{1h}-1)g_r f^{abc}k^\mu$ $\succ\!\!\!\longrightarrow$	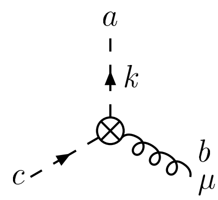
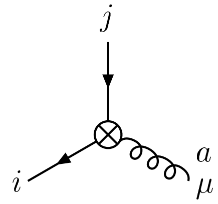	$\longleftarrow\!\!\!\prec$ $-i(Z_{1f}-1)g_r T^a_{ij}\gamma^\mu$ $i(Z_2-1)e_q e\delta_{ij}\gamma^\mu$ $\succ\!\!\!\longrightarrow$	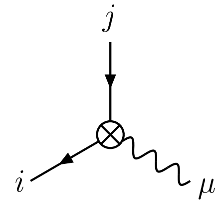

Table 4.1: The Feynman rules for the renormalization counterterms derived from $\mathscr{L}_C$ in (4.11). For convenience both directions of the ghost-gluon counterterm are shown. Also the photon-quark counterterm obtained similarly from the QED Lagrangian is included, where e_q is the fractional quark charge and we do not consider QED corrections: $\alpha = e^2/(4\pi) \simeq 1/137$.

loop we will also have one particular counterterm contribution, so that we can adjust the Z_i to cancel the singularities. This will become clear in the next section, where the Z_i will be worked out. One important point remains: We see from (4.12) that

$$Z_g \sqrt{Z_3} = \frac{Z_1}{Z_3} = \frac{Z_{1h}}{Z_{3h}} = \frac{Z_{1f}}{Z_2} = \frac{Z_4}{Z_1} \,. \tag{4.13}$$

This is the Slavnov-Taylor identity [52, 53, 72] for the renormalization constants. It appears to result trivially from our renormalization procedure, but this is only the case because we have *assumed* the universality of the renormalized coupling g_r and hence that there is only one Z_g: $g = Z_g g_r$. In principle we could determine each of the Z_i in Tab. 4.1 separately by calculating the corresponding loop diagram(s) and canceling their divergencies. Then we could chose to regularize and subtract in such a way that (4.13) is violated. As one may intuitively guess from the involvement of the gauge coupling, this would amount to breaking the local gauge symmetry[4] of the renormalized Lagrangian. A detailed discussion of these points is beyond the scope of this work and can be found for example in [74].

Important for our practical calculation is that we should chose a regularization procedure and a renormalization scheme which respects (4.13) and thus local gauge symmetry. Our choice of using dimensional regularization and the (modified) $\overline{\text{MS}}$ renormalization scheme fulfills this condition. By comparing Tab. 4.1 with (4.13), we realize that then we only need to calculate the 2PF Z_i and *one* 3PF Z_j of our choice. Each 3PF Z_j is related to a corresponding 2PF Z_i in exactly the same way as the gluon 4PF Z_4 is to the gluon 3PF Z_1. In the following section the renormalization constants Z_{3h}, Z_{1h}, Z_3, Z_2, and Z_m will be calculated at one-loop. The remaining Z_1, Z_4 and Z_{1f} are then obtained by using (4.13). In this way local gauge symmetry allows us to obtain results that would require quite complicated calculations for free!

4.2 Renormalization Constants and Scheme Choice

Our scheme choice will be the following [43, 42, 46]: we wish to have n_{lf} *light* flavors active in the running of α_s and in the parton evolution in addition to one produced heavy flavor, i.e., the total number of flavors is $n_f = n_{lf} + 1$. To this end we renormalize the light flavors using the standard $\overline{\text{MS}}$ prescription. The heavy (anti)quark is however renormalized on-shell and furthermore we remove the heavy quark loop contribution to the gluon self-energy, see the calculation of Z_3 below, which explicitly decouples the heavy (anti)quark at low energies. This modified $\overline{\text{MS}}$ fixed flavor scheme, which singles out the heavy (anti)quark according to its pole mass scale m, will be called $\overline{\text{MS}}_m$ henceforth. We will use the Feynman gauge[5] and $n = 4 + \varepsilon$ in all our calculations. This is a variant of

[4] More precisely, due to the terms $\mathscr{L}_{GF}$ and $\mathscr{L}_{FP}$, the Lagrangian is Becchi-Rouet-Stora (BRS) symmetric [75], see also App. B.4. So it is BRS symmetry that would be violated.

[5] This implies that the *renormalized* gauge parameter $\alpha_r = 1$.

the Collins, Wilczek and Zee scheme [76, 71], whose factorization properties have been worked out explicitly in [77].

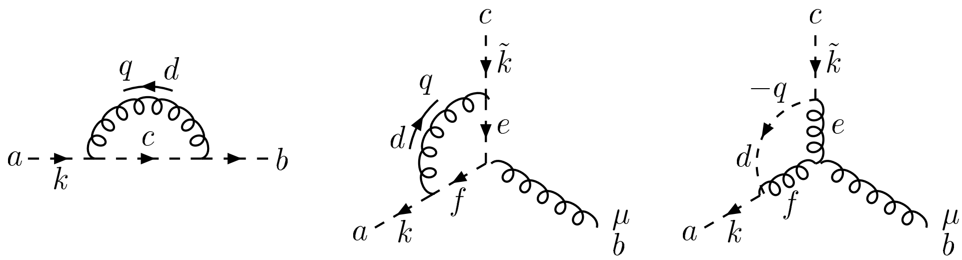

(a) (b)

Figure 4.1: The loop contributions needed for the calculation of (a) Z_{3h} (ghost self-energy) and (b) Z_{1h} (ghost vertex).

It is convenient to fix the gauge sector first. The ghost graphs are particularly simple and so we begin by calculating Z_{3h} and Z_{1h}, which are needed to cancel the divergent expressions of the loop graphs displayed in Fig. 4.1. The ghost self-energy loop has a color factor $f^{acd}f^{cbd} = -C_A\delta^{ab}$ and the ghost vertex loop contributions both have a color factor $f^{adf}f^{feb}f^{edc} = \frac{C_A}{2}f^{abc}$. Thus as expected the color structure corresponds to a color-factor times δ^{ab} and f^{abc}, respectively. We start by writing down the self-energy, equating[6] $-i\tilde{\Pi}$ to the (truncated) loop diagram:

$$\begin{aligned}\tilde{\Pi}(k^2) &= -iC_A\delta^{ab}g_r^2\mu^{-\varepsilon}\int\frac{d^nq}{(2\pi)^n}\frac{k^2+k\cdot q}{q^2(k+q)^2}\\ &= C_A\delta^{ab}g_r^2k^2\left(-\frac{2}{\varepsilon}\right)\frac{\Gamma\left(1-\frac{\varepsilon}{2}\right)}{(16\pi^2)^{1+\frac{\varepsilon}{4}}}\left(-\frac{k^2}{\mu^2}\right)^{\frac{\varepsilon}{2}}\int_0^1 dx\,x^{\frac{\varepsilon}{2}}(1-x)^{1+\frac{\varepsilon}{2}}\\ &= -C_A\delta^{ab}\frac{g_r^2}{32\pi^2}k^2\left[\frac{2}{\hat{\varepsilon}}-2+\ln\left(-\frac{k^2}{\mu^2}\right)\right]\ .\end{aligned}\tag{4.14}$$

Here and in the following we have made frequent use of standard Feynman integral relations for "simple" cases. One can find them for example in Appendix A of [68] and Appendix C of [69]. We have defined the typical pole related terms

$$\frac{2}{\hat{\varepsilon}} = \frac{2}{\varepsilon} + \gamma_E - \ln(4\pi) \qquad \text{and} \qquad \frac{2}{\hat{\varepsilon}_m} = \frac{2}{\hat{\varepsilon}} - \ln\frac{\mu^2}{m_r^2}\ ,\tag{4.15}$$

where $\frac{2}{\hat{\varepsilon}_m}$ will occur later on. It is just this $\frac{2}{\hat{\varepsilon}}$ combination of pole and finite terms which is subtracted in $\overline{\text{MS}}$. The counterterm comes with a factor i, see Tab. 4.1, and so we set

$$Z_{3h} - 1 = -C_A\frac{g_r^2}{32\pi^2}\frac{2}{\hat{\varepsilon}}\ .\tag{4.16}$$

[6]The convention of having a factor $-i$ comes from considering this correction as a term in a geometric sum, see the discussion at (4.52) below.

Next we add both ghost vertex contributions

$$\tilde{\Gamma}^\mu(k) = i\frac{C_A}{2} f^{abc} g_r^3 \mu^{-\varepsilon} \int \frac{d^n q}{(2\pi)^n} \frac{(b)-(c)}{q^2(\tilde{k}+q)^2(k+q)^2}$$

$$\text{with} \quad \begin{aligned} (b) &= \left[k\cdot(\tilde{k}+q)(k+q)^\mu\right] \\ (c) &= \left[q^\mu(k^2-2k\cdot\tilde{k}+k\cdot q)+k^\mu(-q^2-k\cdot q+\tilde{k}\cdot q)+\tilde{k}^\mu k\cdot q\right] \end{aligned}$$

$$\overset{\tilde{k}^\mu=0}{\curvearrowright} i\frac{C_A}{2} f^{abc} g_r^3 \mu^{-\varepsilon} \int \frac{d^n q}{(2\pi)^n} \frac{[k\cdot q(k+q)^\mu]-[(q^\mu k - k^\mu q)\cdot(k+q)]}{q^4(k+q)^2}$$

$$= C_A f^{abc} g_r^3 k^\mu \left(-\frac{2}{\varepsilon}\right) \frac{\Gamma\left(1-\frac{\varepsilon}{2}\right)}{(16\pi^2)^{1+\frac{\varepsilon}{4}}} \left(-\frac{k^2}{\mu^2}\right)^{\frac{\varepsilon}{2}} \int_0^1 dx\, x^{1+\frac{\varepsilon}{2}}(1-x)^{\frac{\varepsilon}{2}}$$

$$= -C_A g_r f^{abc} k^\mu \frac{g_r^2}{32\pi^2}\left[\frac{2}{\hat{\varepsilon}} - 2 + \ln\left(-\frac{k^2}{\mu^2}\right)\right] , \tag{4.17}$$

where we have used the non-trivial fact that $\tilde{k}^\mu$ can be set zero without influencing the singularity structure [69], to shorten our presentation. We can immediately read off the $\overline{\text{MS}}$ renormalization constant

$$Z_{1h} - 1 = C_A \frac{g_r^2}{32\pi^2}\frac{2}{\hat{\varepsilon}} . \tag{4.18}$$

Thus we can determine to $\mathcal{O}(g_r^2)$

$$Z_g\sqrt{Z_3} = \frac{Z_{1h}}{Z_{3h}} = 1 + C_A \frac{g_r^2}{16\pi^2}\frac{2}{\hat{\varepsilon}} , \tag{4.19}$$

which confirms the naïve expectation that pure gauge loops get a "non-abelian" C_A contribution only.

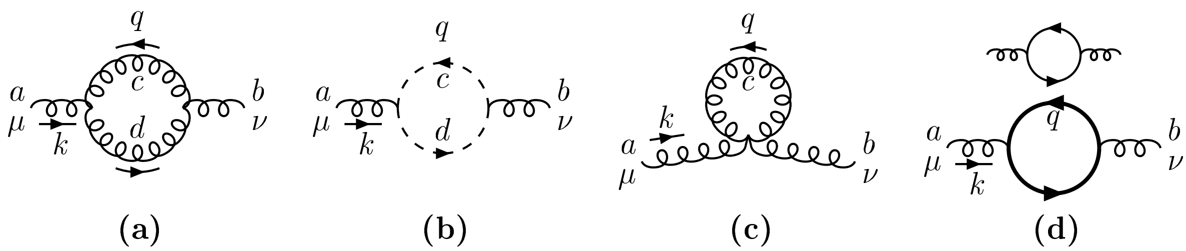

Figure 4.2: The loop contributions needed for the calculation of Z_3: (a)+(b) gauge loops, (c) vanishing gluon tadpole, and (d) massless and massive quark loop.

The obvious next step is to calculate Z_3. The needed loop diagrams are shown in Fig. 4.2 and we equate $-i\Pi^{\mu\nu}$ to them. It is not difficult to calculate these contributions directly, however for brevity we here use the fact, mentioned already in the last section, that we know their Lorentz structure due to the Slavnov Taylor identity (B.31):

$$\Pi^{ab}_{\mu\nu}(k) = \delta^{ab}\left(k_\mu k_\nu - k^2 g_{\mu\nu}\right)\Pi(k^2) \quad \curvearrowright \quad \delta^{ab}\Pi(k^2) = -\frac{1}{(3+\varepsilon)k^2} g^{\mu\nu}\Pi^{ab}_{\mu\nu} . \tag{4.20}$$

Thus we will only calculate the $\Pi(k^2)$. Next we see immediately that the tadpole contribution Fig. 4.2 (c) vanishes, since it leads to an integral of the type (3.3). We must treat the gluon and ghost loops together, since only their sum will conform to (4.20). Their color factor is of course the same as for the ghost self-energy. Note that we have to multiply the loops with two identical particles by 1/2! and -1 due to the boson and fermion statistics, respectively. After the Lorentz contraction and dropping terms of the type (3.3), we obtain the simple integral

$$\begin{aligned}\Pi(k^2) &\overset{(a)+(b)}{=} iC_A \frac{g_r^2\mu^{-\varepsilon}}{(3+\varepsilon)k^2}\int \frac{d^nq}{(2\pi)^n}\frac{(8+3\varepsilon)k\cdot q - k^2}{q^2(q+k)^2} \\ &= C_A\frac{g_r^2}{3+\varepsilon}\left(-\frac{2}{\varepsilon}\right)\frac{\Gamma\left(1-\frac{\varepsilon}{2}\right)}{(16\pi^2)^{1+\frac{\varepsilon}{4}}}\left(-\frac{k^2}{\mu^2}\right)^{\frac{\varepsilon}{2}}\int_0^1 dx\,[(8+3\varepsilon)x+1]x^{\frac{\varepsilon}{2}}(1-x)^{\frac{\varepsilon}{2}} \\ &= -C_A\frac{g_r^2}{16\pi^2}\frac{5}{3}\left[\frac{2}{\hat{\varepsilon}}+\ln\left(-\frac{k^2}{\mu^2}\right)-\frac{31}{15}\right]\ . \end{aligned} \tag{4.21}$$

The quark loop contribution Fig. 4.2 (d) has to be calculated both for massive and massless quarks. For one quark flavor we have

$$\begin{aligned}\Pi(k^2) &\overset{(d)}{=} iC_A\frac{g_r^2\mu^{-\varepsilon}}{2(3+\varepsilon)k^2}\int\frac{d^nq}{(2\pi)^n}\frac{\mathrm{Tr}\,\langle\gamma^\mu(\not{q}+m_r)\gamma_\mu(\not{q}+\not{k}+m_r)\rangle}{(q^2-m_r^2)[(q+k)^2-m_r^2]} \\ &= \frac{g_r^2}{4\pi^2}\mu^{-\varepsilon}\left\{\frac{1}{6}\frac{2}{\hat{\varepsilon}}+\int_0^1 dx\,x(1-x)\ln\left[-k^2x(1-x)+m_r^2\right]\right\} \\ &= \frac{g_r^2}{4\pi^2}\frac{1}{6}\begin{cases}\frac{2}{\hat{\varepsilon}}+\ln\left(-\frac{k^2}{\mu^2}\right)-\frac{5}{3} & \text{for}\quad m_r=0 \\ \frac{2}{\hat{\varepsilon}_m}-\frac{5}{3}-\frac{4m_r^2}{k^2}-\left(1+2\frac{m_r^2}{k^2}\right)b_k\ln(-\varkappa_k) & \text{for}\quad m_r\neq 0\end{cases}\ , \end{aligned} \tag{4.22}$$

with $b_k=\sqrt{1-4m_r^2/k^2}$ and $\varkappa_k=(1-b_k)/(1+b_k)$. Here we see the basic problem of a pure $\overline{\text{MS}}$ treatment when quark masses come into play. The gauge (4.21) and massless quark parts have a $\ln(-k^2/\mu^2)$ term, whereas the heavy quark part has a $\ln(\mu^2/m_r^2)$ term from the $\frac{2}{\hat{\varepsilon}_m}$. But for low energies $k^2 \ll m_r^2$, this means that no matter what the arbitrary mass scale μ is, we will keep at least one large logarithm after subtracting only the poles. So here we deviate from the pure $\overline{\text{MS}}$ treatment and do not ignore the (finite) logarithm depending on the heavy quark mass.

Then the total sum of (4.21), of n_{lf} light flavors, and of one heavy flavor is

$$\begin{aligned}\Pi(k^2) &= \frac{g_r^2}{16\pi^2}\left[-\frac{5}{3}C_A\frac{2}{\hat{\varepsilon}}+n_{lf}\frac{2}{3}\frac{2}{\hat{\varepsilon}}+\frac{2}{3}\frac{2}{\hat{\varepsilon}_m}+\dots\right] \\ &= \frac{g_r^2}{16\pi^2}\left[(2C_A-\beta_0)\frac{2}{\hat{\varepsilon}}+\frac{2}{3}\frac{2}{\hat{\varepsilon}_m}+\dots\right] \\ &= \frac{g_r^2}{16\pi^2}\left[(2C_A-\beta_0^f)\frac{2}{\hat{\varepsilon}}-\frac{2}{3}\ln\left(\frac{\mu^2}{m_r^2}\right)+\dots\right]\ , \end{aligned} \tag{4.23}$$

with $\beta_0 = (11C_A - 2n_{lf})/3$ and $\beta_0^f = (11C_A - 2n_f)/3$ and the dots stand for the remaining finite terms. It becomes obvious from the last line in (4.23) that our choice

$$Z_3 - 1 = \frac{g_r^2}{16\pi^2}\left[(2C_A - \beta_0)\frac{2}{\hat{\varepsilon}} + \frac{2}{3}\frac{2}{\hat{\varepsilon}_m}\right] = \frac{g_r^2}{16\pi^2}\left[(2C_A - \beta_0^f)\frac{2}{\hat{\varepsilon}} - \frac{2}{3}\ln\left(\frac{\mu^2}{m_r^2}\right)\right] \tag{4.24}$$

does not only subtract the usual $\overline{\mathrm{MS}}$ term $(2C_A - \beta_0^f)\frac{2}{\hat{\varepsilon}}$, but in addition the $\ln(\mu^2/m_r^2)$ term. Note that if we had calculated (4.22) with $m_r^2 = k^2 = 0$, it would have given zero[7]. But with $k^2 = 0$ and $m_r^2 \neq 0$ the integral gives $-\frac{g_r^2}{4\pi^2}\frac{1}{6}\frac{2}{\hat{\varepsilon}_m}$. This term is exactly eliminated by our subtraction, whereas the normal $\overline{\mathrm{MS}}$ prescription would leave the $\ln(\mu^2/m_r^2)$ term. Thus we see that in the limit of small energies $k^\mu \to 0$ flowing into the heavy quark loop (and actually for all light-like momenta, as encountered in external partonic legs), the heavy quarks explicitly decouple with the prescription used here.

From (4.24) and (4.19) we directly obtain

$$Z_g - 1 = \frac{g_r^2}{32\pi^2}\left[\beta_0\frac{2}{\hat{\varepsilon}} - \frac{2}{3}\frac{2}{\hat{\varepsilon}_m}\right] . \tag{4.25}$$

At this point a short digression concerning the renormalization group equation (RGE) is helpful, in order to derive the effect of our choice on the running coupling. First note that the action $\int d^n x \mathscr{L}$ should be dimensionless, which means that the dimension of the Lagrangian density $[\mathscr{L}] = \mathrm{mass}^n$. By inspecting (4.1), we can directly determine the dimensions of the parameters and fields. In particular we find $[g] = \mathrm{mass}^{(4-n)/2}$ and similarly from (4.10) $[g_r] = \mathrm{mass}^{(4-n)/2}$. So let us define a mass scale for the bare and renormalized coupling

$$g \equiv \tilde{g}(\mu_b)\mu_b^{-\frac{\varepsilon}{2}} \quad \text{and} \quad g_r \equiv \tilde{g}_r(\mu)\mu^{-\frac{\varepsilon}{2}} . \tag{4.26}$$

Here $\tilde{g}$ and $\tilde{g}_r$ are *dimensionless* quantities. Also g and g_r do *not* depend on the scales μ_b and μ. However, if we take a look at our treatment of the loop integrals until now, e.g., the self-energy (4.22), we see that we have treated g_r as being dimensionless and introduced an arbitrary mass scale μ to keep the correct dimensionality of the occurring integrals. It is obvious from (4.26) that we should have more precisely written

$$g_r \to \tilde{g}_r(\mu) \quad \curvearrowright \quad Z_g(g_r, \mu) \to Z_g[\tilde{g}_r(\mu), \mu] , \tag{4.27}$$

in the results obtained so far. Note that $\tilde{g}_r$ depends explicitly on the scale μ. Performing the replacements in $g = Z_g g_r$ and inserting (4.26) gives

$$\tilde{g}_r(\mu) = \left(\frac{\mu_b}{\mu}\right)^{-\frac{\varepsilon}{2}} \frac{\tilde{g}(\mu_b)}{Z_g(\tilde{g}_r, \mu)} . \tag{4.28}$$

[7]The expansion to the logarithmic integral is not valid then, the integral is of the same type as (3.3).

By simple differentiation we obtain

$$\begin{aligned}
\beta \equiv \mu \frac{d\tilde{g}_r(\mu)}{d\mu} &= \left(\frac{\varepsilon}{2} - \frac{\mu}{Z_g} \frac{dZ_g(\tilde{g}_r, \mu)}{d\mu} \right) \tilde{g}_r(\mu) \\
&= \frac{\left(\frac{\varepsilon}{2} - \frac{\mu}{Z_g} \frac{\partial Z_g(\tilde{g}_r,\mu)}{\partial \mu} - \frac{\mu}{Z_g} \frac{dm_r}{d\mu} \frac{\partial Z_g(\tilde{g}_r,\mu)}{\partial m_r} \right) \tilde{g}_r(\mu)}{1 + \frac{\tilde{g}_r(\mu)}{Z_g(\tilde{g}_r,\mu)} \frac{\partial Z_g(\tilde{g}_r,\mu)}{\partial \tilde{g}_r}} \\
&= -\beta_0 \frac{\tilde{g}_r^3(\mu)}{16\pi^2} + \mathcal{O}(\tilde{g}_r^5, \varepsilon) \; . \qquad (4.29)
\end{aligned}$$

In the last step we have used the fact that the $dm_r/d\mu$ term only contributes at $\mathcal{O}(g^5)$. Note that this result means that in the running coupling only the n_{lf} light flavors contribute due to our choices for Z_g! The contribution of the heavy quark flavor cancels due to the subtraction of the massive loop logarithm, i.e., because of the explicit decoupling of the heavy quark at small energies. Without this subtraction, we would have found β_0^f with $n_f = n_{lf} + 1$ flavors instead.

With $\alpha_s = \tilde{g}_r^2/(4\pi)$ we can immediately obtain from (4.29) the RGE of the *running* coupling constant at LO

$$\frac{d\alpha_s(\mu^2)}{d\ln(\mu^2)} = -\frac{\beta_0}{4\pi} \alpha_s^2(\mu^2) + \mathcal{O}(\alpha_s^3) \qquad (4.30)$$

The solution is easily obtained as

$$\alpha_s(\mu_r^2) = \frac{\alpha_s(\mu_0^2)}{1 + \alpha_s(\mu_0^2) \frac{\beta_0}{4\pi} \ln \frac{\mu_r^2}{\mu_0^2}} = \frac{4\pi}{\beta_0 \ln \frac{\mu_r^2}{\Lambda_{\mathrm{LO}}^2}} \; , \qquad (4.31)$$

$$\Lambda_{\mathrm{LO}}^2 \equiv \mu_0^2 \exp \left[-\frac{4\pi}{\beta_0 \alpha_s(\mu_0^2)} \right] \; . \qquad (4.32)$$

In (4.31) we have integrated from a scale at which we renormalize the coupling, μ_0^2, to a large scale, μ_r^2, at which we chose to evaluate α_s, i.e., we use $\alpha_s(\mu^2 = \mu_r^2)$ in our final results. We see here the property of *asymptotic freedom*, i.e., for $\mu_r^2 \to \infty$ (and fixed small μ_0^2) the coupling constant $\alpha_s \to 0$, which of course is the reason why the expansion in α_s we have been using is justified for a large scale μ_r^2! Due to $\mu = \mu_r$, we find in our cross sections logarithms $\ln(\mu_r/m)$ depending on a typical scale m of the process. To prevent these terms from becoming large, we must set μ_r approximately equal to this typical scale. So we need a *large* scale m, provided in our cases by the heavy quark mass. In (4.32) we have introduced the *QCD scale parameter* in LO Λ_{LO}, which brings our result for the running coupling in a convenient form. It is, apart from the quark masses, the only free parameter of QCD and has to be determined by experiment. Note that we require α_s to be continuous when changing the number of (light) flavors, which is still possible at NLO. We will follow the usual prescription of doing so at the quark mass scales. This means Λ_{LO}^2 has to be adjusted at these thresholds accordingly and we will have to quote the number of (light) flavors when stating the value used for it. We see that the dimensionless coupling constant at the renormalization point $\alpha_s(\mu_0^2)$ and the renormalization point scale μ_0 itself are hidden in (4.31) by the introduction of the mass scale Λ^2_{LO} in (4.32). This is an example of "dimensional transmutation" [78]. Thus only μ_r will appear in our results and so it, and not μ_0, is usually called the *renormalization scale*. As a final point we note that taking two loop corrections into account, we would find for (4.29) and (4.30)

$$\beta \equiv \mu \frac{d\tilde{g}_r(\mu)}{d\mu} = -\beta_0 \frac{\tilde{g}_r^3(\mu)}{16\pi^2} - \beta_1 \frac{\tilde{g}_r^5(\mu)}{(16\pi^2)^2} + \mathcal{O}(\tilde{g}_r^7, \varepsilon)\ . \tag{4.33}$$

$$\frac{d\alpha_s(\mu^2)}{d\ln(\mu^2)} = -\frac{\beta_0}{4\pi}\alpha_s^2(\mu^2) - \frac{\beta_1}{(4\pi)^2}\alpha_s^3(\mu^2) + \mathcal{O}(\alpha_s^4) \tag{4.34}$$

Where we have the new coefficient[8] $\beta_1 = 102 - \frac{38}{3}n_{lf}$ [79]. Thus the two-loop correction to the running coupling is of relative order $\tilde{g}^2 \sim \alpha_s$. If we now use the running coupling in the LO part of our calculation, this two-loop correction to the coupling leads to a contribution of the same order as the NLO part! Thus it should be used when we calculate in NLO. In practice we will follow the usual prescription of using (4.31) when calculating in LO, and the solution of (4.33) when calculating in NLO[9]. To obtain a solution of (4.34), we must integrate

$$\ln\frac{\mu_r^2}{\mu_0^2} \overset{2\ \mathrm{loop}}{=} \int_{\alpha_s(\mu_0^2)}^{\alpha_s(\mu_r^2)} \frac{d\alpha_s}{-\frac{\beta_0}{4\pi}\alpha_s^2 - \frac{\beta_1}{(4\pi)^2}\alpha_s^3} \tag{4.35}$$

and obtain after again absorbing $\alpha_s(\mu_0^2)$ for convenience

$$L \equiv \ln\frac{\mu_r^2}{\Lambda^2_{\mathrm{NLO}}} = \frac{4\pi}{\beta_0\alpha_s(\mu_r^2)} - \frac{\beta_1 \ln[\frac{4\pi}{\beta_0\alpha_s(\mu_r^2)} + \frac{\beta_1}{\beta_0^2}]}{\beta_0^2}\ , \tag{4.36}$$

$$\Lambda^2_{\mathrm{NLO}} \equiv \mu_0^2 \exp\left[-\frac{4\pi}{\beta_0\alpha_s(\mu_0^2)}\right]\left(\frac{4\pi}{\beta_0\alpha_s(\mu_0^2)} + \frac{\beta_1}{\beta_0^2}\right)^{\frac{\beta_1}{\beta_0^2}}\ . \tag{4.37}$$

We can now solve (4.36) numerically, given a value for Λ_{NLO}, for $\alpha_s(\mu_r^2)$ at any μ_r^2. Alternatively an approximate solution of (4.36) can be obtained by iteration and expansion in $1/L$. The first iteration at $\mathcal{O}(1/L^2)$ then yields

$$\alpha_s(\mu_r^2) = \frac{4\pi}{\beta_0 \ln\frac{\mu_r^2}{\Lambda^2_{\mathrm{NLO}}}}\left[1 - \frac{\beta_1}{\beta_0^2}\frac{\ln\left(\ln\frac{\mu_r^2}{\Lambda^2_{\mathrm{NLO}}}\right)}{\ln\frac{\mu_r^2}{\Lambda^2_{\mathrm{NLO}}}}\right]\ , \tag{4.38}$$

[8]Subtracting the heavy quark loop contributions at $k^2 = 0$ in $\overline{\mathrm{MS}}_m$ naturally leads to the well-known $\overline{\mathrm{MS}}$ results, but with $n_f \to n_{lf} = n_f - 1$.

[9]The error of using the two loop correction to α_s with the NLO part is next-to-NLO (NNLO).

and this formula will be used in our calculations for the NLO running coupling, since a typical scale μ_r in our processes is of the order of the heavy quark mass and then the deviation between a numerical solution of (4.36) and (4.38) is below 1% even for the charm mass with $n_{lf} = 3$. In the remainder of the chapter we will again use our old notation with g_r instead of $\tilde{g}_r(\mu)$ for brevity, but the identification (4.27) and the scale of evaluation $\mu = \mu_r$ are implied.

Back to the calculation of the renormalization constants: Z_3 together with (4.13) also allows us to easily derive

$$Z_1 - 1 = -\frac{g_r^2}{16\pi^2}\frac{2}{3}\left[C_A\frac{2}{\hat{\varepsilon}} - \left(n_{lf}\frac{2}{\hat{\varepsilon}} + \frac{2}{\hat{\varepsilon}_m}\right)\right]\,, \tag{4.39}$$

$$Z_4 - 1 = \frac{g_r^2}{16\pi^2}\frac{1}{3}\left[C_A\frac{2}{\hat{\varepsilon}} + 2\left(n_{lf}\frac{2}{\hat{\varepsilon}} + \frac{2}{\hat{\varepsilon}_m}\right)\right]\,, \tag{4.40}$$

which completes the gauge sector counterterms. The only missing piece is the quark sector and it is sufficient to calculate the quark self-energy displayed in Fig. 4.3 to determine it. Before we start, let us motivate our scheme choices. For the light quarks we will use the usual $\overline{\text{MS}}$ scheme throughout. But the heavy quark will be treated differently. We use the *on-shell* prescription to fix the renormalized mass at the pole mass. The pole mass is the only mass parameter of perturbative QCD which is independent of the renormalization scale, renormalization scheme, and gauge parameter and is IR insensitive [80], thus it is certainly a "good" mass scale to use. Furthermore, we note that the Slavnov-Taylor identity we need for being allowed to eliminate the unphysical gluon polarizations with external ghosts[10], is only valid if additional external lines are *on-shell*! Since the renormalization procedure keeps massless particles massless, gluons and light quarks are on-shell anyway. But we need to renormalize the heavy quark mass on-shell as well, if we wish to use the "ghost trick" in our calculations.

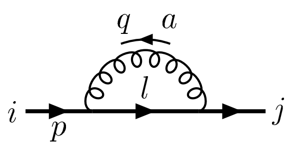

Figure 4.3: The quark self-energy loop contribution needed for the calculation of Z_m and Z_2.

The general expression for the quark self-energy can be read off the loop diagram Fig. 4.3. We set $-i\Sigma$ equal to the (truncated) loop and obtain

$$\Sigma(\not{p}, m_r) = -i\delta_{ij}C_F g_r^2\mu^{-\varepsilon}\int\frac{d^nq}{(2\pi)^n}\frac{1}{q^2}\gamma^\mu\frac{1}{\not{p}+\not{q}-m_r}\gamma_\mu$$

[10]External ghosts appear in our unpolarized calculation since we use the metric instead of the physical polarization tensor, see (2.15).

$$
\begin{aligned}
&= -i\delta_{ij} C_F g_r^2 \mu^{-\varepsilon} \int_0^1 dx \int \frac{d^n q}{(2\pi)^n} \frac{(2-n)(1-x)\not{p} + n m_r}{\left[q^2 - (x m_r^2 - x(1-x)p^2)\right]^2} \\
&= \delta_{ij} C_F g_r^2 \mu^{-\varepsilon} \frac{\Gamma\left(1-\frac{\varepsilon}{2}\right)}{(16\pi^2)^{1+\frac{\varepsilon}{4}}} \left(-\frac{2}{\varepsilon}\right) \mathscr{I}
\end{aligned}
\tag{4.41}
$$

We have already performed the sum over loop colors: $T^a_{jl} T^a_{li} = C_F \delta_{ij}$. Note that the divergence already is manifest, thus the integral $\mathscr{I}$ must be finite and can be expanded in ε, due to the pole $1/\varepsilon$ in (4.41), we must calculate it to $\mathcal{O}(\varepsilon)$:

$$
\begin{aligned}
\mathscr{I} &= \int_0^1 dx[-(2+\varepsilon)(1-x)\not{p} + m_r(4+\varepsilon)][x m_r^2 - x(1-x)p^2]^{\frac{\varepsilon}{2}} \\
&= m_r \left\{ 3 + \frac{\varepsilon}{2}\left[-5 + \frac{m_r^2}{p^2} - \frac{m_r^2}{p^2}\left(\frac{m_r^2}{p^2} - 4\right)\ln m_r^2 + \left(3 - \frac{4m_r^2}{p^2} + \frac{m_r^4}{p^4}\right)\ln(m_r^2 - p^2)\right]\right\} \\
&\quad + (\not{p} - m_r)\left\{ -1 + \frac{\varepsilon}{2}\left[1 + \frac{m_r^2}{p^2} - \frac{m_r^4}{p^4}\ln m_r^2 + \left(\frac{m_r^4}{p^4} - 1\right)\ln(m_r^2 - p^2)\right]\right\} + \mathcal{O}(\varepsilon^2) \, .
\end{aligned}
\tag{4.42}
$$

Inserting this back into (4.41) and expanding in ε, we get the final result

$$
\Sigma(\not{p}, m_r) = \delta_{ij}\left[A m_r + B(\not{p} - m_r)\right] \, , \tag{4.43}
$$

$$
\begin{aligned}
A &= -C_F \frac{g_r^2}{16\pi^2}\left[3\left(\frac{2}{\hat{\varepsilon}} - \ln\frac{\mu^2}{m_r^2}\right) - 5 + \frac{m_r^2}{p^2} + \left(3 - \frac{4m_r^2}{p^2} + \frac{m_r^4}{p^4}\right)\ln\frac{m_r^2 - p^2}{m_r^2}\right] \, , \\
B &= -C_F \frac{g_r^2}{16\pi^2}\left[-\left(\frac{2}{\hat{\varepsilon}} - \ln\frac{\mu^2}{m_r^2}\right) + 1 + \frac{m_r^2}{p^2} + \left(\frac{m_r^4}{p^4} - 1\right)\ln\frac{m_r^2 - p^2}{m_r^2}\right] \, .
\end{aligned}
$$

We see from Tab. 4.1 that the counterterm contribution, obtained similarly to (4.41) by equating $-i\Sigma_C$ to the counterterm insertion, is

$$
\Sigma_C = -\delta_{ij}[(Z_2 - 1)\not{p} - (Z_2 Z_m - 1)m_r] \overset{\mathcal{O}(\alpha_s)}{\simeq} \delta_{ij}\left[(Z_m - 1)m_r - (Z_2 - 1)(\not{p} - m_r)\right] \, , \tag{4.44}
$$

where we have used the general structure $Z_i = 1 + \alpha_s z_i + \mathcal{O}(\alpha_s^2)$ of the renormalization constants to separate the contributions. Thus the sum of (4.43) and (4.44) is

$$
\Sigma + \Sigma_C = \delta_{ij}\left\{[A + (Z_m - 1)]m_r + [B - (Z_2 - 1)](\not{p} - m_r)\right\} \, , \tag{4.45}
$$

and has to be (UV) finite.

The $\overline{\text{MS}}$ prescription used for $m_r = 0$ requires the subtraction of only the $2/\hat{\varepsilon}$ pole, see (4.15). So from (4.45) we directly see

$$
m_r = 0: \qquad Z_m - 1 = \frac{g_r^2}{16\pi^2} C_F \frac{6}{\hat{\varepsilon}} \qquad \text{and} \qquad Z_2 - 1 = \frac{g_r^2}{16\pi^2} C_F \frac{2}{\hat{\varepsilon}} \, . \tag{4.46}
$$

In practical calculations we do not need Z_m for the *massless* quarks, since then the Z_m counterterm part vanishes, see (4.44). For the heavy quarks we will renormalize the mass on-shell as discussed above. This means the inverse propagator (the proper two-point function), which is given by $\Gamma^{(2)}(\not{p}, m_r) = -i[\not{p} - m_r - (\Sigma + \Sigma_C)]$, is supposed to become zero at $\not{p} = m_r$, so the condition we use is

$$m_r \neq 0 : \qquad (\Sigma + \Sigma_C)|_{\not{p}=m_r} \stackrel{!}{=} 0 \quad \Rightarrow \quad Z_m - 1 = -A|_{\not{p}=m_r} \,. \tag{4.47}$$

We now have to chose a way to also determine Z_2. Since we are going to determine Z_{1f} from (4.13), any choice will respect the Slavnov-Taylor identities *by construction*. We chose here the simplest possible extension[11] of the $\overline{\mathrm{MS}}$ choice, which subtracts the mass logarithm $\ln(\mu_r^2/m^2)$ as well

$$m_r \neq 0 : \qquad Z_m - 1 = C_F \frac{g_r^2}{16\pi^2}\left(\frac{6}{\hat{\varepsilon}_m} - 4\right) \qquad \text{and} \qquad Z_2 - 1 = C_F \frac{g_r^2}{16\pi^2}\frac{2}{\hat{\varepsilon}_m} \,. \tag{4.48}$$

Now we can immediately derive the last missing renormalization constant, the quark-gluon vertex correction, from (4.13) to be

$$Z_{1f} = Z_2 + C_A \frac{g_r^2}{16\pi^2}\frac{2}{\hat{\varepsilon}} \,, \tag{4.49}$$

where for massless quarks at the vertex one inserts Z_2 from (4.46) and for massive ones from (4.48).

After completing the derivation of the renormalization constants, we should come back to their application. First let us reconsider why we were allowed to write down "interaction vertices" even for those three first terms of $\mathscr{L}_C$ (4.11) which should have by analogy yielded propagator rules. To this end consider the simpler example of the well-known Klein-Gordon Lagrangian for a free massive field

$$\mathscr{L} = \frac{1}{2}(\partial_\mu \phi)(\partial^\mu \phi) - \frac{1}{2}m^2\phi^2 \tag{4.50}$$

and interpret it as the Lagrangian of a massless field with an *interaction* given by the second term. Then we have the Feynman rules

 $= \dfrac{i}{p^2}\,,$ 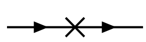 $= -im^2\,,$ (4.51)

and the massive propagator appears as an infinite sum of interactions

$$\begin{aligned} &= \frac{i}{p^2} + \frac{i}{p^2}(-im^2)\frac{i}{p^2} + \frac{i}{p^2}(-im^2)\frac{i}{p^2}(-im^2)\frac{i}{p^2} + \ldots \\ &= \frac{i}{p^2 - m^2} \,. \end{aligned} \tag{4.52}$$

[11] With this choice the derivative of the inverse propagator $\partial\Gamma^{(2)}(\not{p}, m_r)/\partial\not{p}$ remains finite for $\not{p} \to 0$, compare also [76, 71].

Similarly, in our case we could have derived "counter-propagator" rules, and they would have corresponded to an infinite sum of counter-interactions. However, each of the counter-interactions is suppressed by α_s. Hence for our *one loop* calculation it is sufficient to stop the series after only the *first* two-point interaction counterterm, all other terms would be of higher order. For this reason we have interpreted the first three rules in Tab. 4.1 as "vertices". Note that the first interaction of a counterterm will always contribute negatively, since it is defined $\sim i$ instead of the $-im^2$ above. For example take the ghost counterterm put on a propagator line. Then instead of just one propagator, we have the propagator, then the counterterm and then again the same propagator:

$$\left[i\delta^{ac}\frac{1}{k^2}\right] i(Z_{3h}-1)\delta^{cd}k^2 \left[i\delta^{db}\frac{1}{k^2}\right] = -(Z_{3h}-1)\left[i\delta^{ab}\frac{1}{k^2}\right] , \tag{4.53}$$

compared to the one propagator $i\delta^{ab}/k^2$ we had before, just a factor $-(Z_{3h}-1)$ appears. It is also clear, that counterterm contributions only come from inserting elements from Tab. 4.1 into graphs of at least one order in α_s below the highest order being calculated, since the elements are of order α_s themselves. This means for our NLO calculation, that we will just insert them in the LO graphs. Let us assume that mass renormalization with Z_m has already been performed on-shell, as discussed above, then (4.44) will give similarly a factor $-(Z_2-1)$ when inserted at a quark propagator. For the gluon two point counterterm inserted at a gluon propagator, we get a factor $-(Z_3-1)$ for the same reason[12]. On the other hand the lower four counterterms in Tab. 4.1 have exactly the same structure as the bare Feynman rules. So for example replacing the quark-gluon vertex by the quark-gluon three-point counterterm will just yield a factor $(Z_{1f}-1)$ and so on.

Thus we conclude, that upon inserting the renormalization counterterms in the LO graphs, we will simply get the LO amplitudes times a sum of appropriate factors $-(Z_i-1)$ for each propagator and appropriate factors Z_j-1 for each vertex. What about external lines? We can insert two-point counterterms there as well, getting contributions with a factor $-(Z_i-1)$. But we must remember that according to (4.8), for example an outgoing electron will now appear in the amplitudes as $u=\sqrt{Z_2}u_r$. Since we have always the same external legs in coherently added amplitudes, we can factor out these terms, and use only the *renormalized* fields, like u_r, in the amplitudes. However, since $Z_i = 1+\alpha_s z_i$, the factor obtained from k external (anti)quarks, l external gluons and m external ghosts (keeping our "external ghost trick" in mind), will give

$$\begin{aligned} Z_2^{\frac{k}{2}} Z_3^{\frac{l}{2}} Z_{3h}^{\frac{m}{2}} &= 1+\alpha_s\left(\frac{k}{2}z_2+\frac{l}{2}z_3+\frac{m}{2}z_{3h}\right)+\mathcal{O}(\alpha_s^2) \\ &= 1+\frac{k}{2}(Z_2-1)+\frac{l}{2}(Z_3-1)+\frac{m}{2}(Z_{3h}-1)+\mathcal{O}(\alpha_s^2) . \end{aligned} \tag{4.54}$$

[12] The gauge term $\sim k^\mu k^\nu$ does not contribute in the gauge invariant final result. There will be a finite correction $\sim k^2$ to the gluon propagator, for the photon called Uehling term, important for the Lamb shift. However, in $\overline{\text{MS}}$ we do not subtract finite terms, except for the artifacts of regularization.

This factor multiplied with the NLO and counterterm amplitudes gives no new contributions at NLO, as it is $1 + \mathcal{O}(\alpha_s)$. But multiplied with the LO amplitudes we get the $\mathcal{O}(\alpha_s)$ part of (4.54) as new contribution. The end result of all this is, that for each external line we get into the sum a factor $-(Z_i - 1)$ from the two-point counterterm and a factor $(Z_i - 1)/2$ from the redefinition of the fields, which gives a total of $-(Z_i - 1)/2$. This is exactly 1/2 of what we got for inserting counterterms at a propagator! But then a propagator has two ends, so if we associate 1/2 of the counterterm contribution with each end, we have the following simple effective rule: for each LO vertex, we take the factor $Z_j - 1$ of the corresponding counterterm vertex and add factors $-(Z_i - 1)/2$ of the corresponding counterterm two-point interactions for each of the (three or four) attached legs. Then we sum the results for all LO vertices and get a factor, which times the sum of the LO amplitudes is equal to the total sum of counterterm amplitudes, including the effect of external field renormalization. Perhaps it is easier to describe this in a pictorial fashion, as in Fig. 4.4 for a quark-gluon vertex. Note that previous removal of the mass divergencies with the Z_m counterterms is always implied.

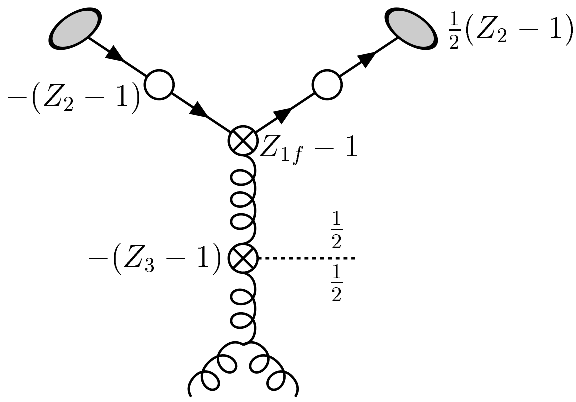

Figure 4.4: Effective counterterm contributions to be summed for the renormalization of the quark-gluon vertex. An example configuration is shown, where both quark lines are external and the gluon internal. The (crossed) circles indicate the contributions from Tab. 4.1, and the empty circle means mass renormalization with Z_m has been done previously. The gray ovals indicate the wave functions and the dotted line splits the internal contribution.

We can go even one step further, by now simply calculating what contribution we get at each vertex[13]:

$$\text{quark-gluon:} \qquad 2\left(-\frac{Z_2 - 1}{2}\right) - \frac{Z_3 - 1}{2} + Z_{1f} - 1 = Z_g - 1\ ,$$

$$\text{quark-photon:} \qquad 2\left(-\frac{Z_2 - 1}{2}\right) + Z_2 - 1 = 0\ ,$$

[13]Remember that we do not consider QED corrections, hence the quark-photon QED vertex is not being renormalized.

$$\begin{aligned}
&\text{ghost-gluon:} && 2\left(-\frac{Z_{3h}-1}{2}\right)-\frac{Z_3-1}{2}+Z_{1h}-1=Z_g-1 \\
&\text{3-gluon:} && 3\left(-\frac{Z_3-1}{2}\right)+Z_1-1=Z_g-1\ , \\
&\text{4-gluon:} && 4\left(-\frac{Z_3-1}{2}\right)+Z_4-1=2(Z_g-1)\ .
\end{aligned} \tag{4.55}$$

But actually this means, that we can get the sum of the LO amplitudes and the counterterm amplitudes, by just setting $g \to Z_g g_r$ in the sum of bare LO amplitudes! To $\mathcal{O}(\alpha_s)$ we have $g_r^k \to [1+(Z_g-1)]^k g_r^k = [1+k(Z_g-1)+\mathcal{O}(\alpha_s^2)]g_r^k$, so we get the LO part from the one and for every vertex a factor $Z_g - 1$. As is appropriate, a 4-gluon vertex with g^2, counts as $2(Z_g-1)$. A quark-photon vertex, which has no power of g, does not add a factor. Finally, since the contribution to the cross section of the counterterms comes from the interference of the LO amplitudes with counterterm amplitudes, we derive the following effective formula for renormalizing the NLO cross section:

$$d\tilde{\sigma}_r^{(1)} = d\tilde{\sigma}^{(1)} + 2k(Z_g-1)d\tilde{\sigma}^{(0)}\ , \tag{4.56}$$

where k is the power of the strong coupling constant in the LO cross section $d\tilde{\sigma}^{(0)} \sim \alpha_s^k \sim g_r^{2k}$, and mass renormalization has to be performed first.

Basically we have proven painstakingly this way, that we only need to renormalize the coupling and the masses of the cross section. Then (4.56) just follows from the fact, that a change in the coupling $g \to Z_g g_r$ has to be compensated at the order we are considering, since the cross section is a renormalization group invariant. So for the cross sections all our detailed scheme choices are superfluous, except for the Z_m in (4.46) and (4.48), the Z_g in (4.25) and the statement that we respect the Slavnov-Taylor identities (4.13) with our scheme. But of course knowing all the renormalization constants allows checks on the amplitude level, so we can test whether the singularities coming from a particular loop are cured by the appropriate counterterm. In addition, the explicit derivation of Z_g and Z_m showed in detail the physical content of our choices. Nevertheless, (4.56) is a convenient master formula for renormalization, in particular if we want to change to a different scheme. Finally, it should be mentioned that we have not derived a RGE for the mass as we did for the coupling (4.30). The simple reason is, that of course the heavy quark mass does not run, as we have renormalized it *on-shell*. It is easy to check this by explicit calculation. On the other hand, the light quark masses do "run" in principle, but as they start with zero mass at μ_0, they stay at zero mass. So effectively, all the masses have constant values independent of the renormalization scale.

Chapter 5

Real Contributions

5.1 $2 \to 3$ Phase-Space and Singularities

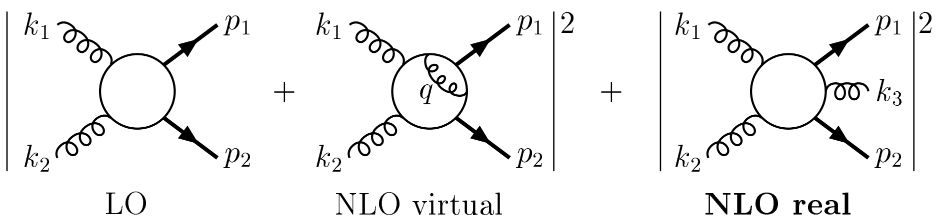

Figure 5.1: The structure of LO and NLO contributions and the way in which the amplitudes are added is shown symbolically. Incoming particles could also be photons or light (anti)quarks and in the real case the outgoing gluon could instead be a light (anti)quark.

The processes under consideration here are one-particle-inclusive, which means that only one outgoing particle, an open heavy (anti)quark state, is observed. Thus we lose all information about the other particles involved in the hard subprocess, except for what we can conclude from the conservation laws. In particular we do not know the number of other particles involved and the four momentum of each. Since we are only considering NLO here, i.e., only one additional power of α_s, it is obvious that compared to the tree graphs we can at most produce *one* additional particle. Thus at NLO we need to consider $2 \to 3$ graphs, which mutually interfere, but of course will be added *incoherently* to the $2 \to 2$ LO and NLO virtual contributions of Chap. 2 and Chap. 3, respectively. See Fig. 5.1 for a graphical representation of the structure of the contributions including the general naming scheme for the momenta. The $2 \to 3$ "real contributions", so-called because they involve the production of a (quasi-)real particle, have to be integrated over the appropriate $2 \to 3$ phase-space. In particular the unknown four momentum of the additional particle has to be integrated out. It is in this integration that singularities will arise when the additional particle sets the denominator of an internal propagator to zero.

In order to see this more clearly, let us calculate two simple *sub*-diagrams occurring in the calculation, displayed in Fig. 5.2.

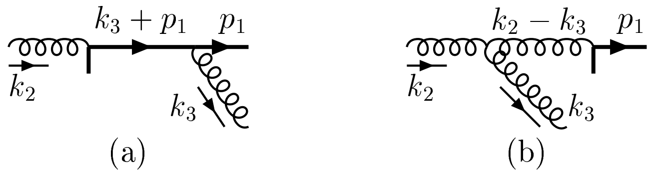

Figure 5.2: Two examples of $1 \to 2$ sub-diagrams occurring in the real NLO graphs. The full $2 \to 3$ process is decomposed in a $2 \to 2$ process followed by a $1 \to 2$ decay, examples of the latter are shown here.

We will formally treat the $2 \to 3$ process as a $2 \to 2$ process, with one of the three outgoing particles and a pseudo-particle as products, followed by a $1 \to 2$ decay of the pseudo-particle to the other two outgoing particles. We only observe one outgoing particle and we will stay in the c.m.s. of those two outgoing particles which are not observed, i.e., whose momenta have to be integrated over[1]. We chose the two outgoing particles of Fig. 5.2 with the momenta k_3 and p_1 as unobserved decay products of the pseudo-particle. Thus the $1 \to 2$ decay proceeds in the "laboratory" frame, the c.m.s. of the unobserved decay products, and we keep the momentum of the pseudo-particle p unspecified for now. It will be integrated out later. To simplify the phase-space integration further, we can chose to align the z-axis with one of the other three momenta k_1, k_2 and p_2, which will result in three distinct parametrizations. Here we will align the z-axis with the incoming momentum of the sub-diagram examples in Fig. 5.2, k_2, a choice called "set one" below. The parametrization used for the n-dimensional vectors occurring in Fig. 5.2 is then

$$\begin{aligned} p_1 &= (E_1, p_1^x, -\omega_3 \sin\theta_1 \cos\theta_2, -\omega_3 \cos\theta_1, \hat{p}_1)\ , \\ k_3 &= (\omega_3, -p_1^x, \omega_3 \sin\theta_1 \cos\theta_2, \omega_3 \cos\theta_1, -\hat{p}_1)\ , \\ k_2 &= \left(\omega_2, 0, 0, \omega_2, \hat{0}\right)\ . \end{aligned} \tag{5.1}$$

Here the "hat" momenta symbolize the $n-4$ additional components introduced in dimensional regularization. So we get for the $1 \to 2$ decays of Fig. 5.2 with pseudo-particle momentum $p \equiv k_3 + p_1 = (p, 0, 0, 0, \hat{0})$

$$\begin{aligned} 1 \to 2 &= \int d^n k_3\ d^n p_1\ \delta(k_3^2)\Theta(\omega_3)\delta(p_1^2 - m^2)\Theta(E_1)\delta^{(n)}(p - k_3 - p_1) \\ &= \int d^n p_1\ \delta(p^2 - 2pE_1 + m^2)\Theta(p - E_1)\delta(p_1^2 - m^2)\Theta(E_1) \\ &= \frac{\pi^{\frac{n-4}{2}}}{\Gamma\left(\frac{n-4}{2}\right)} \frac{\omega_3^2}{2p} \iint\limits_0^{\pi} d\theta_1\ d\theta_2\ \sin^2\theta_1 \sin\theta_2 \int\limits_0^{\hat{p}_{1\max}^2} d\hat{p}_1^2\ \frac{\left(\hat{p}_1^2\right)^{\frac{n-6}{2}}}{\sqrt{\frac{(p^2-m^2)^2}{4p^2} \sin^2\theta_1 \sin^2\theta_2 - \hat{p}_1^2}} \end{aligned}$$

[1] In the following the Gottfried-Jackson frame [55] is introduced. Similar phase-space calculations appear in [56, 44], but the hat momenta are *only* treated here. Our notation follows Appendix B of [44].

$$= \frac{\pi^{\frac{n-4}{2}}}{4} \frac{\Gamma\left(\frac{n}{2}-1\right)}{\Gamma(n-3)} \frac{(p^2-m^2)^{n-3}}{(p^2)^{\frac{n}{2}-1}} \int d\Omega_{n-4}\, \mathcal{I} \,. \tag{5.2}$$

In the third step we have integrated over the x-components. This implies that the matrix elements to be integrated do not depend on these components. Thus we must later chose the momentum of the observed particle, p_2, to lie in the $y-z$ plane, which is always possible. Furthermore we have used

$$\begin{aligned} d^{n-4}\hat{p}_1 &= \frac{\pi^{\frac{n-4}{2}}}{\Gamma\left(\frac{n-4}{2}\right)} \left(\hat{p}_1^2\right)^{\frac{n-6}{2}} d\hat{p}_1^2 \,, \\ \hat{p}_{1\max}^2 &= \frac{(p^2-m^2)^2}{4p^2} \sin^2\theta_1 \sin^2\theta_2 \,, \end{aligned} \tag{5.3}$$

and defined

$$\int d\Omega_{n-4} \equiv \iint_0^\pi d\theta_1 d\theta_2 \sin^{n-3}\theta_1 \sin^{n-4}\theta_2 \,, \tag{5.4}$$

$$\mathcal{I} \equiv \frac{1}{B\left(\frac{1}{2},\frac{n-4}{2}\right)} \int_0^1 dx \frac{x^{\frac{n}{2}-3}}{\sqrt{1-x}} \,, \tag{5.5}$$

$$x \equiv \frac{\hat{p}_1^2}{\hat{p}_{1\max}^2} = \frac{4(s_4+m^2)\hat{p}_1^2}{s_4^2 \sin^2\theta_1 \sin^2\theta_2} \,, \tag{5.6}$$

where $s_4 \equiv (k_3+p_1)^2 - m^2 = p^2 - m^2$ and $B(v,w)$ is the Euler Beta function. Note that the integral-operator $\mathcal{I}$ is normalized in the sense that for those parts of the matrix element independent of hat momenta we have $\mathcal{I} \cdot 1 = 1$! We will postpone the discussion of the hat momenta and continue here by setting that integration to one, i.e., by not considering hat momenta.

Now $p^2 = 2\omega_3(E_1+\omega_3) + m^2 \geq m^2$, as is evident from $k_3^2 = 0$ and $p_1^2 = m^2$. So the variable s_4 introduced below (5.6) is positive $s_4 \geq 0$, and $s_4 \to 0$ when the additional massless particle emission becomes *infrared*, i.e., $\omega_3 \to 0$. In (5.2), we find a term $(p^2 - m^2)^{1+\varepsilon} = s_4^{1+\varepsilon}$ with $n = 4+\varepsilon$. On the other hand the gluon emission in Fig. 5.2 (a) leads to a massive fermion propagator with momentum $k_3 + p_1$, so upon integrating over the momentum of the pseudo-particle later in the $2 \to 3$ phase space, the square of that particular amplitude will led to terms of the following form

$$\int ds_4\, s_4^{1+\varepsilon} \left[\frac{1}{(k_3+p_1)^2 - m^2}\right]^2 = \int ds_4\, s_4^{-1+\varepsilon} \underset{\varepsilon\to 0}{\overset{\omega_3\to 0}{\longrightarrow}} \infty \,. \tag{5.7}$$

This means we have found an IR singularity! It is regularized by our shift to $4+\varepsilon$ dimensions. We can make this explicit by introducing a Δ-distribution[2] corresponding to

[2]If $v \equiv 1 + t_1/s$ and $w \equiv -u_1/s + t_1$ are introduced, then $s_4 \to 0$ poles show up for $w \to 1$, i.e., $1/s_4 \to 1/(1-w)$. The singular $w \to 1$ behavior can then be treated with the usual +-distribution $1/(1-w)_+$ [56].

cutting off the s_4-divergence:

$$\int_0^\Delta ds_4\, f(s_4)[g(s_4)]_\Delta \equiv \int_0^\Delta ds_4\, [f(s_4) - f(0)]\, g(s_4)\,, \tag{5.8}$$

where $g(s_4)$ is singular and $f(s_4)$ is finite for $s_4 \to 0$. Then we can write the following identity

$$s_4^{-1+\varepsilon} = \frac{\Delta^\varepsilon}{\varepsilon}\delta(s_4) + [s_4^{-1+\varepsilon}]_\Delta\,. \tag{5.9}$$

For this reason, those squared matrix elements that have a $1/s_4^2$ dependence will lead to infrared $1/\varepsilon$ poles. These poles will cancel the $1/\varepsilon$ IR poles of the virtual contributions in accordance with the Bloch-Nordsieck and Kinoshita-Lee-Nauenberg theorems [70].

In Fig. 5.2 (b) we encounter a propagator with the denominator $t' \equiv (k_2 - k_3)^2 = -2\omega_2\omega_3(1 - \cos\theta_1)$. We immediately see the potential for an infrared divergence when $\omega_3 \to 0$. But for the moment let us assume that the phase-space integration is infrared finite, i.e., we are looking at a term in the squared matrix element which does not introduce a second ω_3 in the denominator. What about the angular dependence? We see in (5.1) that for $\theta_1 \to 0$ the momenta k_2 and k_3 can become *collinear*, both pointing along the z-axis[3]. The propagator with t' will lead to following terms in the phase-space integration

$$\int d\Omega_{n-4}\,\frac{1}{t'^j} \sim \int d\Omega_{n-4}\frac{1}{(1-\cos\theta_1)^j} = \frac{2^{(2-j)}\pi}{n-4}\frac{\Gamma\left(\frac{n-2(1+j)}{2}\right)}{\Gamma\left(\frac{n-4}{2}\right)}\frac{\Gamma(n-3)}{\Gamma(n-(2+j))}\,. \tag{5.10}$$

Obviously, for $j = 1$ and $n = 4+\varepsilon$ one again gets a $1/\varepsilon$ pole, a collinear one. If we had given k_2 a mass, then the integral in (5.10) would become finite for $j = 1$. A singularity would occur in the limit of this mass going to zero. For this reason the collinear singularities are also often called mass singularities. They are absorbed by a redefinition of the parton densities in the so-called mass factorization procedure, as will be shown in Chap. 6. As a final point we note that it is of course possible that a second ω_3 is introduced into the denominator with $j = 1$, for example from the the interference of sub-diagrams (a) and (b) of Fig. 5.2. Then we will get an infrared and collinear pole at the same time, leading to $1/\varepsilon^2$ poles. These will also be canceled against virtual double poles according to the theorems [70] mentioned above.

Now we will calculate the full $2 \to 3$ phase-space. First to complete the kinematical parametrization, we will place p_2 in the $y-z$ plane, as discussed below (5.2), and k_1 then follows from momentum conservation $\vec{k}_1 + \vec{k}_2 = \vec{p}_1 + \vec{p}_2 + \vec{k}_3$

$$\begin{aligned} p_2 &= \left(E_2, 0, |\vec{p}_2|\sin\Psi, |\vec{p}_2|\cos\Psi, \hat{0}\right)\,, \\ k_1 &= \left(\omega_1, 0, |\vec{p}_2|\sin\Psi, |\vec{p}_2|\cos\Psi - \omega_2, \hat{0}\right)\,. \end{aligned} \tag{5.11}$$

[3] The x- and hat-space components are integrated over in the phase space, so they can become zero.

Remembering the definitions of the $2 \to 2$ variables (2.18), which with this choice do not contain the θ_1, θ_2 angles, and adding the c.m.s. momenta variable s_4, we have

$$\begin{aligned} s &\equiv (k_1+k_2)^2 = (\omega_1+\omega_2)^2 - |\vec{p}_2|^2 \ , \\ t_1 &\equiv (k_2-p_2)^2 - m^2 = 2\omega_2(|\vec{p}_2|\cos\Psi - E_2) \ , \\ u_1 &\equiv (k_1-p_2)^2 - m^2 = -\omega_2^2 - m^2 + (\omega_1 - E_2)^2 \ , \\ s_4 &\equiv (k_3+p_1)^2 - m^2 = 2\omega_3(E_1+\omega_3) = s + t_1 + u_1 \ . \end{aligned} \tag{5.12}$$

By using the non-trivial squared momenta[4] and energy-momentum conservation, we find

$$\begin{aligned} &k_1^2 \stackrel{!}{=} 0 = \omega_1^2 - (|\vec{p}_2|^2 - 2|\vec{p}_2|\omega_2\cos\Psi + \omega_2^2) \ , \qquad && p_1^2 \stackrel{!}{=} m^2 = E_1^2 - \omega_3^2 \ , \\ &p_2^2 \stackrel{!}{=} m^2 = E_2^2 - |\vec{p}_2|^2 \ , && \omega_1+\omega_2 \stackrel{!}{=} E_1 + E_2 + \omega_3 \ . \end{aligned} \tag{5.13}$$

Then we can solve towards three arbitrary independent variables, e.g.,

$$\begin{aligned} \omega_2 = \frac{s+t_1}{2\sqrt{s_4+m^2}} \ , \quad |\vec{p}_2| &= \frac{\sqrt{(t_1+u_1)^2 - 4m^2 s}}{2\sqrt{s_4+m^2}} \ , \\ \cos\Psi &= \frac{t_1 s_4 - s(u_1+2m^2)}{(s+t_1)\sqrt{(t_1+u_1)^2-4m^2 s}} \ . \end{aligned} \tag{5.14}$$

The remaining variables $\omega_1,\ \omega_3,\ E_1,\ E_2$ immediately follow from (5.13). So together with θ_1, θ_2 we find five independent variables, as it should be for three independent four-vectors with three mass and four energy-momentum constraints.

We can now write down the the $2 \to 3$ phase-space dPS_3

$$\begin{aligned} \int \mathrm{dPS}_3 =& \int \frac{d^n k_3}{(2\pi)^{n-1}} \frac{d^n p_1}{(2\pi)^{n-1}} \frac{d^n p_2}{(2\pi)^{n-1}} \delta(k_3^2)\Theta(\omega_3)\delta(p_1^2-m^2)\Theta(E_1)\delta(p_2^2-m^2)\Theta(E_2) \\ & \cdot (2\pi)^n \delta^{(n)}(k_1+k_2-k_3-p_1-p_2) \\ =& \frac{1}{(2\pi)^{2n-3}} \int d^n p \; d^n p_2 \; \delta(p_2^2-m^2)\Theta(E_2)\delta^{(n)}(k_1+k_2-p-p_2) \cdot (1 \to 2) \\ =& \frac{\pi^{\frac{n-4}{2}}}{4} \frac{\Gamma\left(\frac{n}{2}-1\right)}{\Gamma(n-3)} \frac{1}{(2\pi)^{2n-3}} \int d^n p_2 \; \delta(p_2^2-m^2)\Theta(E_2) \frac{s_4^{n-3}}{(s_4+m^2)^{\frac{n}{2}-1}} \int d\Omega_{n-4}\, \mathcal{I} \end{aligned} \tag{5.15}$$

where we have split the $2 \to 3$ process into a $2 \to 2$ process with a pseudo-particle of four-momentum p, which subsequently decays in a $1 \to 2$ process. That way we are able to use (5.2). After the integration over p in (5.15) any frame can be used for the remaining $2 \to 2$ integration with the pseudo-particle. The c.m.s. is advantageous and we chose

$$k_{1,2} = \frac{\sqrt{s}}{4}\left(1,0,0,\pm 1,\hat{0}\right) \ , \qquad p_2 = \left(E_2, 0, |\vec{p}_2|\sin\xi, |\vec{p}_2|\cos\xi, \hat{0}\right) \ . \tag{5.16}$$

[4]From $k_3^2 \stackrel{!}{=} 0$ we know that $(p_1^x)^2 + \hat{p}_1^2 = \omega_3^2 \sin^2\theta_1 \sin^2\theta_2$.

Then (5.15) becomes

$$\int \mathrm{dPS}_3 = \frac{2}{(4\pi)^n}\frac{1}{\Gamma(n-3)}\int dE_2(E_2^2-m^2)^{\frac{n-3}{2}}\Theta(E_2) \cdot \int_0^\pi \sin^{n-3}\xi \frac{s_4^{n-3}}{(s_4+m^2)^{\frac{n}{2}-1}}\int d\Omega_{n-4}\,\mathcal{I}\ . \quad (5.17)$$

Using $\sqrt{E_2-m^2}\sin\xi = \sqrt{t_1u_1-m^2s}/\sqrt{s}$ and $dE_2d\xi = dt_1du_1/(2\sqrt{s}\sqrt{t_1u_1-m^2s})$, we arrive at the final result

$$\mathrm{dPS}_3 = dt_1du_1\,\frac{1}{(4\pi)^n\Gamma(n-3)s}\left(\frac{t_1u_1-m^2s}{s}\right)^{\frac{n-4}{2}}\frac{s_4^{n-3}}{(s_4+m^2)^{\frac{n}{2}-1}}\int d\Omega_{n-4}\,\mathcal{I}\ . \quad (5.18)$$

For the double differential real cross section, the flux factor $1/(2s)$ is introduced. Also an auxiliary mass parameter $\mu^{(4-n)/2}$ for every power of the gauge coupling has to be multiplied, so that the gauge coupling stays dimensionless in n dimensions. The final result to be used for the NLO real $2\to3$ cross sections is then with $n=4+\varepsilon$:

$$\frac{d^2\tilde{\sigma}^{(1)}_{2\to3}}{dt_1du_1} = F_\varepsilon G_\varepsilon\int d\Omega_\varepsilon\,\mathcal{I}\,|\tilde{M}_R|^2\ , \quad (5.19)$$

$$G_\varepsilon \equiv \frac{\mu^{-\varepsilon}}{2\pi(4\pi)^{2+\frac{\varepsilon}{2}}}\frac{\Gamma\left(1+\frac{\varepsilon}{2}\right)}{\Gamma(1+\varepsilon)}\frac{s_4^{1+\varepsilon}}{(s_4+m^2)^{1+\frac{\varepsilon}{2}}}\ , \quad (5.20)$$

where F_ε is given in (2.25) and G_ε parametrizes the difference to the LO cross section, as compared to (2.24).

5.2 Partial Fractioning of Angular Integrals

Now we should complete the set of kinematical invariants occurring in the matrix elements by writing down those depending on the angles θ_1, θ_2. We define in addition to (5.12)

$$\begin{aligned} &s_3 = (k_3+p_2)^2-m^2\ , \quad s_5 = (p_1+p_2)^2 = -u_5\ , \quad t' = (k_2-k_3)^2\ , \\ &u' = (k_1-k_3)^2\ , \quad u_6 = (k_2-p_1)^2-m^2\ , \quad u_7 = (k_1-p_1)^2-m^2\ . \end{aligned} \quad (5.21)$$

Since they represent only the two angular degrees of freedom, we can find four independent relations between them, e.g.,

$$\begin{aligned} u' &= -s-u_1-u_7\ , \qquad & t' &= -s-t_1-u_6\ , \\ u_5 &= t_1+u_1+s_3\ , \qquad & s_3 &= s+u_6+u_7\ . \end{aligned} \quad (5.22)$$

Furthermore we see that, for example, u_7 would be identical to t_1 in $2\to2$ kinematics with $k_1+k_2=p_1+p_2$. Thus in the infrared limit, $\omega_3\to0$, or equivalently $s_4\to0$, we

	set	a or A	b or B	C	coll.
$\underline{s_3}$	I	r_6	r_3	r_5	
$\underline{s_3}$	II	$\uparrow$ with $t_1 \leftrightarrow u_1$ $\uparrow$			
$\underline{t'}$	I	r_1	$-r_1$		✓
$\underline{u'}$	II	$\uparrow$ with $t_1 \leftrightarrow u_1$ $\uparrow$			✓
$\underline{u'}$	I	$r_1(t_1 \leftrightarrow u_1)$	r_4	$-r_5$	✓
$\underline{t'}$	II	$\uparrow$ with $t_1 \leftrightarrow u_1$ $\uparrow$			✓
$\underline{u_5}$	I	r_7	r_3	r_5	
$\underline{u_5}$	II	$\uparrow$ with $t_1 \leftrightarrow u_1$ $\uparrow$			
$\underline{u_6}$	I	r_2	r_1		
$\underline{u_7}$	II	$\uparrow$ with $t_1 \leftrightarrow u_1$ $\uparrow$			
$\underline{u_7}$	I	$r_2(t_1 \leftrightarrow u_1)$	$-r_4$	r_5	
$\underline{u_6}$	II	$\uparrow$ with $t_1 \leftrightarrow u_1$ $\uparrow$			

Table 5.1: The θ_1, θ_2-coefficients according to (5.25) for the angular Mandelstam variables (5.21). For brevity, (5.23), (5.24) and (5.26) have been employed. Results for "set one" and "set two" with k_2 and k_1 aligned with the z-axis, respectively, are shown. It is indicated which variables can develop a collinear divergence, see Sec. 5.3. $\uparrow \ldots \uparrow$ symbols mean inserting the columns of the row above changed as indicated.

find $u_7 \to t_1$. On the other hand s_3 will simply vanish in that limit. For the invariants of (5.21) we can write

$$s_3 = s_4 \underline{s_3}\ , \quad t' = s_4 \underline{t'}\ , \quad u' = s_4 \underline{u'}\ , \tag{5.23}$$

$$u_5 = -s + s_4 \underline{u_5}\ , \quad u_6 = u_1 + s_4 \underline{u_6}\ , \quad u_7 = t_1 + s_4 \underline{u_7}\ , \tag{5.24}$$

where the underlined quantities are dimensionless and become finite functions of the $2 \to 2$ Mandelstam variables (5.12) and m^2 in the $s_4 \to 0$ limit.

The angular variables (5.21) all have one of the following two structures

$$[ab] \rightsquigarrow a + b\cos\theta_1 \quad \text{or} \quad [ABC] \rightsquigarrow A + B\cos\theta_1 + C\sin\theta_1\cos\theta_2\ , \tag{5.25}$$

and we will symbolize the angle independent variables of (5.12) as $[\cdot]$. Whether an angular variable is of $[ab]$ or $[ABC]$ type depends on the chosen parametrization. In our calculation we really only need the "set one" parametrization given above. A "set two" parametrization can be helpful at times, however. Compared to (5.1) and (5.11), we align k_1 with the z-axis and adjust k_2, so that all other momenta stay untouched. Then in (5.14) in the $\cos\Psi$ we get a $t_1 \leftrightarrow u_1$ crossing and no other changes. The third possibility of putting p_2 on the z-axis is not employed by us. In Tab. 5.1 we have collected the angular coefficients in terms of the $[\cdot]$ variables for both sets of parametrizations. We have used the following abbreviations

$$\begin{gathered} r_1 = -\frac{s+t_1}{2(s_4+m^2)}\ , \quad r_2 = -\frac{s_4+u_1+2m^2}{2(s_4+m^2)}\ , \quad r_3 = \frac{2m^2 s - s_4 t_1 + s u_1}{2(s+t_1)(s_4+m^2)}\ , \\ r_4 = -\frac{s(s_4+m^2)+m^2 s - t_1 u_1}{2(s+t_1)(s_4+m^2)}\ , \quad r_5 = -\frac{\sqrt{s(s_4+m^2)(t_1u_1-m^2 s)}}{(s+t_1)(s_4+m^2)}\ , \\ r_6 = -\frac{t_1+u_1+2m^2}{2(s_4+m^2)}\ , \quad r_7 = \frac{s+s_4}{2(s_4+m^2)}\ . \end{gathered} \tag{5.26}$$

The variables in Tab. 5.1 have been grouped so that one can easily see the effects of switching between the sets: on one hand there is $t_1 \leftrightarrow u_1$ crossing, on the other hand the pairs t', u' and u_6, u_7 exchange their rôle as $[ab]$ and $[ABC]$ variables.

Let us quickly return to the question of hat momenta. We noted already concerning (5.5) that $\mathcal{I}\cdot 1 = 1$. Squares of hat momenta occur always linearly in the squared matrix elements, so we need to look at

$$\begin{aligned} \mathcal{I}\cdot \hat{p}_1^2 &= \frac{s_4^2 \sin^2\theta_1 \sin^2\theta_2}{4(s_4+m^2)} \frac{1}{B\left(\frac{1}{2},\frac{n-4}{2}\right)} \int_0^1 dx \frac{x^{\frac{n}{2}-2}}{\sqrt{1-x}} \\ &= \frac{n-4}{n-3}\frac{s_4^2 \sin^2\theta_1 \sin^2\theta_2}{4(s_4+m^2)} = \varepsilon \frac{s_4^2 \sin^2\theta_1 \sin^2\theta_2}{4(s_4+m^2)} + \mathcal{O}(\varepsilon^2)\ . \end{aligned} \tag{5.27}$$

In the squared matrix elements at worst a $1/s_4^2$ can appear, since in the amplitudes emitting one real particle can result in only one infrared divergent propagator. From (5.27) and (5.19) we get for a $1/s_4^2$ hat term a factor of $s_4^{1+\varepsilon}/(s_4+m^2)^{2+\varepsilon/2}$, which is obviously infrared $s_4 \to 0$ safe. Thus we will not get infrared divergencies from the hat terms, no $1/\varepsilon^2$ poles are possible and the expansion to $\mathcal{O}(\varepsilon)$ in (5.27) is justified. Note that for $m \to 0$ we would get an infrared divergence, i.e., the mass acts as an infrared regulator here. Concerning collinear divergencies stemming from terms like (5.10), we note again that only one propagator can become collinearly divergent by the emission of one real particle in the amplitude, so that $j=1$ or $j=2$. The sines of (5.27) when inserted into (5.10), basically shift $n \to n+2$. Then for $j=1$ we will obtain no divergence. But $j=2$ in (5.10) gives $2\pi/(n-6)$ which yields a $1/\varepsilon$ pole for this shift. In this case the ε factor of (5.27) will be canceled and a finite contribution at $\mathcal{O}(1)$ exists. This means, that in our calculation the only hat terms we have to keep are those having a double collinear form, i.e., with $1/t'^2$ or $1/u'^2$, the others can be dropped.

As we have seen, the variables (5.21) have either the $[ab]$ or the $[ABC]$ form of (5.25). In the matrix elements, various complicated combinations of those variables can occur. It is impossible to directly perform the angular integrations over them, in particular not in n dimensions. But it turns out to be possible to reduce all of the integrals to the following standard form

$$I_\varepsilon^{(k,l)} = \int d\Omega_\varepsilon (a + b\cos\theta_1)^{-k} (A + B\cos\theta_1 + C\sin\theta_1\cos\theta_2)^{-l} \,, \tag{5.28}$$

i.e., an angular integration with (5.4) and an $[ab]$ variable to the power k and an $[ABC]$ variable to the power l in the denominator. We also set $n = 4+\varepsilon$ here and in the remainder of the chapter. How can one obtain such a form from expressions like $(t_1u')/(s_4t'u_7)$ occurring in the squared matrix elements? The trick is to use Mandelstam relations like (5.22) for partial fractioning. These expressions are of the type

$$e[ABC] = f[\cdot] + g[ab] + h[ABC] \,. \tag{5.29}$$

Since $[\cdot]$ variables can be factored out of the angular expressions, we only have to worry about terms with e, g, and h. Also expressions with only powers of e and g or g and h in the denominator already comply with the (5.28) form. So the only terms we have to look at are combinations of all three e, g, and h or of only e and h, i.e., those cases that have two $[ABC]$ variables.

Starting with the combinations of all three variables, we have

$$\begin{gathered}
\frac{1}{egh} = \frac{1}{f}\left(\frac{1}{gh} - \frac{1}{eg} - \frac{1}{eh}\right) , \qquad \frac{e}{gh} = \frac{1}{g} + \frac{1}{h} + \frac{f}{gh} , \qquad \frac{g}{eh} = \frac{1}{h} - \frac{1}{e} - \frac{f}{eh} , \\
\frac{h}{eg} = \frac{1}{g} - \frac{1}{e} - \frac{f}{eg} , \qquad \frac{eg}{h} = g + \frac{fg}{h} + \frac{g^2}{h} , \qquad \frac{gh}{e} = g - \frac{fg}{e} - \frac{g^2}{e} , \\
\frac{eh}{g} = h + \frac{fh}{g} + \frac{h^2}{g} , \qquad egh = fgh + g^2h + gh^2 \,.
\end{gathered} \tag{5.30}$$

In order to rewrite the combinations of two variables, we use the fact that $[\cdot]+[ab] \to [ab]$. So with

$$g_f[ab] \equiv f[\cdot] + g[ab] \quad \Rightarrow \quad e[ABC] = g_f[ab] + h[ABC] \,, \tag{5.31}$$

terms with only powers of e, g_f or g_f, h in the denominator also comply with the (5.28) form. Then

$$\frac{1}{eh} = \frac{1}{g_fh} - \frac{1}{g_fe} , \qquad \frac{e}{h} = 1 + \frac{g_f}{h} , \qquad \frac{h}{e} = 1 - \frac{g_f}{e} , \qquad eh = g_fh + h^2 \,. \tag{5.32}$$

Equations of the form $[ab], [ABC] = [\cdot] + [\cdot] + [ab], [ABC]$ can also be treated by (5.32). Powers of the variables can be treated by repeated application of these rules, for example

$$\frac{gh^2}{e^2} = \frac{gh}{e} - \frac{fgh}{e^2} - \frac{g^2h}{e^2} = g - \frac{2fg}{e} - \frac{2g^2}{e} + \frac{2fg^2}{e^2} + \frac{f^2g}{e^2} + \frac{g^3}{e^2} \,. \tag{5.33}$$

So we can find, e.g., the appropriate expressions for $u_6 u_7^2/s_3^2$, complying with (5.28), by setting $\{e,f,g,h\} \to \{s_3, s, u_6, u_7\}$ in (5.33). If we have for example $1/(s_3 u_7)$, then the first relation of (5.32) tells us that we need to introduce the auxiliary variable $u_{6s} = s + u_6$ to write the result in the desired form.

Our goal is to eliminate all occurrences of two $[ABC]$ variables. As we see from the example (5.33), repeated application of the appropriate rules (5.30) and (5.32) will achieve this aim. In order to automate this procedure in a `Mathematica` [57] program, one has to chose a complete set of relations like (5.22) in order to eliminate all such terms:

$$\begin{aligned} u' &= -s - u_1 - u_7 \,, \quad u_5 = u_1 - t' + u_7 \,, \quad s_3 = -t_1 - t' + u_7 \,, \\ u' &= -s_4 - t' - s_3 \,, \quad u_5 = t_1 + u_1 + s_3 \,, \\ u' &= -s - t' - u_5 \,, \qquad\qquad\qquad\qquad\quad t' = -s - t_1 - u_6 \,. \end{aligned} \tag{5.34}$$

Though using this completely computerized method of obtaining standard form integrals has the advantage of producing error free results quickly, it has the disadvantage of often yielding unnecessarily complicated expressions. For example

$$\frac{1}{(s_3 u')^2} \xrightarrow[\text{automatic}]{\text{set one}} \frac{2}{u_5 (t_1 + u_6)^3} + \frac{1}{u_5^2 (t_1 + u_6)^2} + \frac{1}{u'^2 (t_1 + u_6)^2} + \frac{2}{u' (t_1 + u_6)^3} \,, \tag{5.35}$$

whereas the original expression $1/(s_3 u')^2$ is already in the standard form (5.28) if we use "set two" instead. In general we have used the automatic partial fractioning using "set one" for the long expressions, where also often cancellations occur upon fractioning, and proceeded term by term using both sets for short expressions, like in the soft $s_4 \to 0$ limits.

5.3 Calculation of Basic Angular Integrals

After performing the extensive partial fractioning of the squared matrix elements described in the last section and collecting the terms, what remains to be done is the calculation of the integrals brought to the standard form (5.28):

$$I_\varepsilon^{(k,l)} = \iint_0^\pi d\theta_1 d\theta_2 \frac{\sin^{1+\varepsilon}\theta_1}{(a + b\cos\theta_1)^k} \frac{\sin^\varepsilon \theta_2}{(A + B\cos\theta_1 + C\sin\theta_1\cos\theta_2)^l} \,. \tag{5.36}$$

The first important point to notice is that there are four classes of integrals, depending on the collinear structure. The $[ab]$ and $[ABC]$ variable can both be either "collinear" or not, which yields four combinations. In the case of the $[ab]$ variable, collinearly divergent behavior is possible for $a^2 = b^2$, so that $(a + b\cos\theta_1) \to a(1 \pm \cos\theta_1)$. Then the zero occurs at the edge of the θ_1 integration region and is not integrable. For the $[ABC]$ variable the same comments apply for θ_2 when $A^2 = B^2 + C^2$. This is more difficult to see due to the more complicated structure including a θ_1 dependence. In principle integration over

θ_1 will give terms with a $A^2 - B^2 - C^2\cos^2\theta_2$ dependence, which explicitly shows the appropriate "collinear" behavior. But in practice it is more convenient to integrate out θ_2 first, which means that the divergence will be shifted to the θ_1 integration. Note that the $\mathcal{D}_\pm$-rotation introduced below demonstrates the similarity of the collinear behavior in θ_1 and θ_2. Perhaps simple integration examples show the possible collinear poles most clearly: setting $k = 2$, $l = 0$ and $\varepsilon = 0$ in (5.36), we get $2\pi/(a^2 - b^2)$, whereas $k = 0$, $l = 2$ and $\varepsilon = 0$ gives $2\pi/(A^2 - B^2 - C^2)$. It has already been pointed out in Tab. 5.1 that the only "collinear" variables in our calculation are t' and u'.

We shall use the following notation for angular integrals $I_\varepsilon^{(k,l)}$

$$\begin{aligned}
a^2 \neq b^2 \quad &\text{and} \quad A^2 \neq B^2 + C^2 \quad \Rightarrow \quad I_0^{(k,l)}\,,\\
a^2 = b^2 \quad &\text{and} \quad A^2 \neq B^2 + C^2 \quad \Rightarrow \quad I_a^{(k,l)}\,,\\
a^2 \neq b^2 \quad &\text{and} \quad A^2 = B^2 + C^2 \quad \Rightarrow \quad I_A^{(k,l)}\,,\\
a^2 = b^2 \quad &\text{and} \quad A^2 = B^2 + C^2 \quad \Rightarrow \quad I_{aA}^{(k,l)}\,.
\end{aligned} \tag{5.37}$$

I_0 integrals are finite and so for them we could set $\varepsilon = 0$. The others require regularization. Note for the I_{aA} integrals that when one angular integral is diverging the other is not, as is obvious from $A + B\cos\theta_1 + C\sin\theta_1\cos\theta_2 \to A \pm B \neq 0$ at $\theta_1 = 0,\ \pi$, see Tab. 5.1. This means concerning regularization that no double poles $1/\varepsilon \cdot 1/\varepsilon$ appear, when performing the angular integrations. Double poles only appear when there is in addition an infrared pole for $s_4 \to 0$. In principle, if one could calculate all integrals keeping the full ε dependence, i.e., calculate $I_\varepsilon^{(k,l)}$ without approximation, one could obtain all results by inserting the conditions (5.37) afterwards. In practice, most of the time it is necessary to split up the integrations according to (5.37) first, so that one calculate the integrals by exploiting the divergence structure.

We wish to calculate the minimal number of integrals necessary. As a first step we will show, that all I_A integrals can be transformed to I_a ones. With the unit vector

$$\vec{e}^{\,T} = (\sin\theta_1\cos\theta_2, \sin\theta_1\sin\theta_2, \cos\theta_1)\,, \qquad \vec{e}^{\,2} = 1\,, \tag{5.38}$$

where T signifies transposition, we can write the scalars

$$\begin{aligned}
A + B\cos\theta_1 + C\sin\theta_1\cos\theta_2 &= A + (C, 0, B)\cdot\vec{e}\,,\\
a + b\cos\theta_1 &= a + (0, 0, b)\cdot\vec{e}\,.
\end{aligned} \tag{5.39}$$

So the parameter vector of the $[ab]$ variable points along the z-axis. Now we use a rotation that puts the parameter vector of the $[ABC]$ variable on the z-axis [81]:

$$\mathcal{D}_\pm = \begin{pmatrix} \mp\frac{B}{\sqrt{B^2+C^2}} & 0 & \pm\frac{C}{\sqrt{B^2+C^2}} \\ 0 & 1 & 0 \\ \pm\frac{C}{\sqrt{B^2+C^2}} & 0 & \pm\frac{B}{\sqrt{B^2+C^2}} \end{pmatrix}, \qquad \mathcal{D}_\pm^{-1} = \mathcal{D}_\pm^T\,. \tag{5.40}$$

Obviously a rotation will simply transform a unit vector to a new one and we have

$$\vec{e}\,'^T \equiv (\mathcal{D}_\pm \cdot \vec{e})^T = (\sin\theta_1' \cos\theta_2', \sin\theta_1' \sin\theta_2', \cos\theta_1') \;, \qquad \vec{e}\,'^2 = 1 \;, \tag{5.41}$$

$$(C,0,B)\cdot\mathcal{D}_\pm^T = (0,0,\pm\sqrt{B^2+C^2}) \;, \qquad (0,0,b)\cdot\mathcal{D}_\pm^T = \frac{1}{\sqrt{B^2+C^2}}(\pm bC, 0, \pm bB) \;.$$

Now we can rewrite the scalars by inserting a one, which gives

$$\begin{aligned} (C,0,B)\cdot\vec{e} &= (C,0,B)\cdot\mathcal{D}_\pm^{-1}\cdot\mathcal{D}_\pm\cdot\vec{e} = (0,0,\pm\sqrt{B^2+C^2})\cdot\vec{e}\,' \;, \\ (0,0,b)\cdot\vec{e} &= (0,0,b)\cdot\mathcal{D}_\pm^{-1}\cdot\mathcal{D}_\pm\cdot\vec{e} = \frac{1}{\sqrt{B^2+C^2}}(\pm bC, 0, \pm bB)\cdot\vec{e}\,' \;. \end{aligned} \tag{5.42}$$

The integration ranges $0 \le \theta_1,\ \theta_2 \le \pi$ in (5.38) cover the complete half-space of positive y-components of $\vec{e}$. Since the rotation (5.40) leaves the y-components intact, this remains unchanged by the transformation, i.e., we must have $0 \le \theta_1',\ \theta_2' \le \pi$, so that the same is true for $\vec{e}\,'$. Then we can rewrite (5.36) as

$$\begin{aligned} I_\varepsilon^{(k,l)} &\xrightarrow{\mathcal{D}_\pm} I_\varepsilon^{(l,k)}\left[a \leftrightarrow A,\ b \to \pm\sqrt{B^2+C^2},\ B \to \pm\frac{bB}{\sqrt{B^2+C^2}},\ C \to \pm\frac{bC}{\sqrt{B^2+C^2}}\right] \\ &= \iint_0^\pi d\theta_1' d\theta_2' \frac{\sin^{1+\varepsilon}\theta_1'}{(A \pm \sqrt{B^2+C^2}\cos\theta_1')^l} \frac{\sin^\varepsilon\theta_2'}{(a \pm \frac{bB}{\sqrt{B^2+C^2}}\cos\theta_1' \pm \frac{bC}{\sqrt{B^2+C^2}}\sin\theta_1'\cos\theta_2')^k} \;. \end{aligned} \tag{5.43}$$

We see clearly, that an $I_A^{(k,l)}$ integral will directly transform to an $I_a^{(l,k)}$ integral, and vice versa. So in our collection of integral results no $I_A^{(k,l)}$ integrals will appear, since they can be directly obtained from the corresponding $I_a^{(l,k)}$ results, which are easier to calculate, using the substitutions displayed in (5.43). Note that there is an ambiguity inherent in our definitions of I_a, I_A and I_{aA} concerning the *sign* of the “collinear” solutions for the variables in (5.37). This ambiguity is of course present when (5.43) is used to relate I_A to I_a, since we must chose whether $\sqrt{B^2+C^2}$ is $+A$ or $-A$. Since in “set one” t' and in “set two” u' have $b = -a$, i.e., the collinear divergence appears for forward emission, we calculate our integrals for $b = -a$. In particular we will relate I_A to I_a in such a way, that a becomes $-b$ after transformation. If we are not deriving general formulae, but already inserting specific variables, we can still get relations from $\mathcal{D}_\pm$. From (5.26) we have $r_1 = -\sqrt{r_4^2 + r_5^2}$, and so Tab. 5.1 shows

$$\mathcal{D}_+ : \qquad I_\varepsilon^{(k,l)}(t',u') = I_\varepsilon^{(l,k)}(t',u')\big|_{t_1 \leftrightarrow u_1} \;, \tag{5.44}$$

$$\mathcal{D}_- : \qquad I_\varepsilon^{(k,l)}(u_6,u_7) = I_\varepsilon^{(l,k)}(u_6,u_7)\big|_{t_1 \leftrightarrow u_1} \;. \tag{5.45}$$

To further reduce the number of integrals that have to be calculated, we can use the technique of differentiating with respect to a parameter. The obvious targets are the parameters $a,\ A$, which do not multiply an angular dependence, and we find

$$
\begin{aligned}
I_\varepsilon^{(k,l)} &\stackrel{k\geq 1}{=} \frac{(-1)^{k-1}}{(k-1)!}\frac{\partial^{k-1}}{\partial a^{k-1}} I_\varepsilon^{(1,l)} \quad \text{with} \quad a^2 \neq b^2 \ , \\
&\stackrel{l\geq 1}{=} \frac{(-1)^{l-1}}{(l-1)!}\frac{\partial^{l-1}}{\partial A^{l-1}} I_\varepsilon^{(k,1)} \quad \text{with} \quad A^2 \neq B^2 + C^2 \ , \\
I_\varepsilon^{(k,l)} &\stackrel{m<k\leq 0}{=} \frac{(-k)!}{(-m)!}\frac{\partial^{k-m}}{\partial a^{k-m}} I_\varepsilon^{(m,l)} \text{with} \quad a^2 \neq b^2 \ , \\
&\stackrel{m<l\leq 0}{=} \frac{(-l)!}{(-m)!}\frac{\partial^{l-m}}{\partial A^{l-m}} I_\varepsilon^{(k.m)} \text{with} \quad A^2 \neq B^2 + C^2 \ .
\end{aligned}
\tag{5.46}
$$

Note that for the parameter differentiation to work properly, we need to assume that the parameters are independent. Hence the *collinear* cases are excluded.

At this point we can state which basic integrals we need to calculate in order to obtain *all* other required integrals with the methods explained above. Firstly, those integrals where $l = 0$ and $k \leq 0$ can be performed keeping the complete ε dependence, so that the I_0 and I_a (and I_A using $\mathcal{D}_\pm$) cases can be easily derived from I_ε by taking the $\varepsilon \to 0$ and $b^2 \to a^2$ limits. We need $k = -2, -1, 0$. For the non-divergent $I_0^{(k,l)}$, the (k, l) combinations $(-1, -1)$, $(1, -3)$ and $(1, 1)$ are needed. For the single collinear $I_a^{(k,l)}$, (and thus $I_A^{(k,l)}$), the combinations $(1, -2)$, $(1, 0)$, $(1, 1)$, $(2, -2)$, $(2, 0)$ and $(2, 1)$ are necessary. Finally for the double collinear $I_{aA}^{(k,l)}$ we only need $(1, 1)$. So by calculating only 13 integrals we can reproduce the 29 integrals of [44] which are needed for the processes[5]. Let us start with the $l = 0,\ k \leq 0$ cases. They are simple enough to be directly computed with the help of `Mathematica` [57] or integral tables like [82], yielding

$$
I_\varepsilon^{(0,0)} = 2\pi \frac{1}{1+\varepsilon} \ , \tag{5.47}
$$

$$
I_\varepsilon^{(-1,0)} = 2\pi \frac{a}{1+\varepsilon} \ , \tag{5.48}
$$

$$
I_\varepsilon^{(-2,0)} = \pi \left[\frac{2a^2+b^2}{1+\varepsilon} - \frac{b^2}{3+\varepsilon} \right] \ . \tag{5.49}
$$

Next concerning the non-divergent $I_0^{(k,l)}$, we find for those with negative l

$$
I_0^{(-1,-1)} = \pi \left[\frac{2aA+bB}{1+\varepsilon} - \frac{bB}{3+\varepsilon} \right] \ . \tag{5.50}
$$

$$
I_0^{(1,-3)} = \frac{\pi}{6b^4} \Big\{ 4bB(9A^2b^2 - 9aAbB + (3a^2+b^2)B^2) + 6b(3aAb - 3a^2B
$$

[5] In [44] there are two additional integrals, $I_{aA}^{(-1,1)}$ and $I_{aA}^{(-2,1)}$, not appearing in our decomposition procedure. They can be obtained directly using (5.61) below and App. B.1. Some integrals not found in [44], that do appear in our decomposition, follow from the 13 integrals listed here.

$$+ 2b^2B)C^2 + 3(Ab - aB)(2(Ab - aB)^2 - 3(a^2 - b^2)C^2) \ln \frac{a+b}{a-b}$$
$$+ \frac{\varepsilon}{12}\Big[4b(-4B(27A^2b^2 - 27aAbB + (9a^2 + 4b^2)B^2) + 3(-27aAb$$
$$+ 27a^2B - 16b^2B)C^2) + (Ab - aB)(9 \ln \frac{a+b}{a-b}(6(a^2 - b^2)C^2$$
$$+ (2(Ab - aB)^2 - 3(a^2 - b^2)C^2) \ln \frac{a+b}{a-b}) + 36(2(Ab - aB)^2$$
$$- 3(a^2 - b^2)C^2) \operatorname{Li}_2\left(-\frac{2b}{a-b}\right))\Big]\Big\} + \mathcal{O}(\varepsilon^2)\ . \tag{5.51}$$

To obtain these results we have done the θ_2 integration part by part as is demonstrated in (5.55) below. In the case of $I_0^{(1,-3)}$ the θ_1 integration gives hypergeometric functions that were expanded using (B.7) and (B.8) and linear transformations. The last finite integral is to $\mathcal{O}(1)$ given by

$$\begin{aligned} I_0^{(1,1)} &= \frac{\pi}{\sqrt{X}} \ln\left(\frac{aA - bB + \sqrt{X}}{aA - bB - \sqrt{X}}\right)\ , \\ X &= (aA - bB)^2 - (A^2 - B^2 - C^2)(a^2 - b^2)\ , \end{aligned} \tag{5.52}$$

which is obtained by straightforward integration with $\varepsilon = 0$.

In the single collinear case, we begin with those integrals having $l = 0$. It is easy to perform them directly, and we obtain

$$I_a^{(1,0)} = \frac{\pi}{a}\frac{2}{\varepsilon}\ , \tag{5.53}$$
$$I_a^{(2,0)} = -\frac{\pi}{a^2}\frac{2}{2-\varepsilon}\ . \tag{5.54}$$

We note the curious fact, that $I_a^{(2,0)}$ is *finite* for $\varepsilon \to 0$, whereas the integral *diverges* when we set $\varepsilon = 0$ before integrating. Actually we used this integral above as a simple divergent example! The situation is exactly like for (3.3). We can transform the integral using $t = (1 - \cos\theta_1)/2$ and then introduce a cutoff Λ with $0 < \Lambda < 1$. We find hypergeometric functions and the integration $[\Lambda, 1]$ has to be analytically continued from $\mathrm{Re}\ \varepsilon' > 2$ exactly in such a fashion, that its Λ-dependence cancels against that of the $[0, \Lambda]$ integration, which is unproblematic with $\mathrm{Re}\ \varepsilon > -2$. Using linear transformations of the hypergeometric functions, we find that this is the case for $\varepsilon' \to \varepsilon$. A finite rest remains which gives (5.54) after the θ_2-integration. Next we treat the I_a integrals with $l = -2$. Here we can expand the $[ABC]$ term and then the θ_2-integration of the parts is easy, resulting in

$$\int_0^\pi d\theta_2\ \sin^\varepsilon\theta_2 (A + B\cos\theta_1 + C\sin\theta_1\cos\theta_2)^2$$

$$= \frac{\sqrt{\pi}\Gamma\left(\frac{1+\varepsilon}{2}\right)}{\Gamma\left(1+\frac{\varepsilon}{2}\right)} \left[A^2 + B^2 + 2AB\cos\theta_1 + \left(\frac{C^2}{2+\varepsilon} - B^2\right)\sin^2\theta_1\right] . \quad (5.55)$$

The integration over θ_1 of the parts again delivers only gamma functions and so the full ε dependence can be obtained

$$I_a^{(1,-2)} = \frac{2\pi}{a}\left[\frac{(A+B)^2}{\varepsilon} - \frac{B^2+2AB-C^2}{1+\varepsilon} - \frac{C^2}{2+\varepsilon}\right] , \quad (5.56)$$

$$I_a^{(2,-2)} = \frac{2\pi}{a}\left[\frac{(A+B)^2}{-2+\varepsilon} + \frac{C^2-2B(A+B)}{\varepsilon} + \frac{B^2-C^2}{1+\varepsilon}\right] . \quad (5.57)$$

Next let us treat the two remaining cases which have an $[ABC]$ term in the denominator. For t' we have $a=-b$ and so the divergence appears with $1-\cos\theta_1$ in the denominator. We subtract the $\cos\theta_1 \to 1$ limit of $1/(A+B\cos\theta_1+C\sin\theta_1\cos\theta_2)$, multiplied by the rest of the kernel, as a counterterm. Then the remaining integral is finite, can be expanded in ε prior to integration and is thus easily performed. Adding the integrated counterterm, which is expanded in ε only after integration, yields the complete answer. The needed limits are

$$I_a^{(1,1)}: \ \frac{1}{A+B} , \qquad I_a^{(2,1)}: \ \frac{1}{A+B} + \frac{B(A+B)+C^2\cos^2\theta_2}{(A+B)^3}(1-\cos\theta_1) , \quad (5.58)$$

where a term $\sim \cos\theta_2$ has been dropped in the latter since it does not contribute. The results are

$$\begin{aligned} I_a^{(1,1)} = \frac{\pi}{a(A+B)}\Bigg\{ & \frac{2}{\varepsilon} + \ln\left[\frac{(A+B)^2}{A^2-B^2-C^2}\right] + \frac{\varepsilon}{2}\Bigg[\ln^2\left(\frac{A-\sqrt{B^2+C^2}}{A+B}\right) \\ & - \frac{1}{2}\ln^2\left(\frac{A+\sqrt{B^2+C^2}}{A-\sqrt{B^2+C^2}}\right) + 2\,\mathrm{Li}_2\left(-\frac{B+\sqrt{B^2+C^2}}{A-\sqrt{B^2+C^2}}\right) \\ & - 2\,\mathrm{Li}_2\left(\frac{B-\sqrt{B^2+C^2}}{A+B}\right)\Bigg]\Bigg\} + \mathcal{O}(\varepsilon^2) , \end{aligned} \quad (5.59)$$

$$\begin{aligned} I_a^{(2,1)} = \frac{\pi}{a^2(A+B)}\Bigg\{ & \frac{B^2+AB+C^2}{(A+B)^2}\left[\frac{2}{\varepsilon} + \ln\left[\frac{(A+B)^2}{A^2-B^2-C^2}\right]\right] \\ & - \frac{2C^2}{(A+B)^2} - 1\Bigg\} + \mathcal{O}(\varepsilon) . \end{aligned} \quad (5.60)$$

The double collinear case occurs in our calculation for t' and u'. t' has $a=-b$ and u' has $A=-\sqrt{B^2+C^2}$ with $0 \le -\frac{C}{A}$, $\frac{B}{A} \le 1$. Then by setting $\cos\kappa = -\frac{B}{A}$ in the results (A4) and (A11) of [83], we obtain

$$I_{aA}^{(k,l)} \underset{0\le\frac{B}{A}\le 1}{\overset{0\le-\frac{C}{A}\le 1}{=}} \frac{2\pi}{a^k A^l} 2^{-(k+l)} \frac{\Gamma(1+\varepsilon)}{\Gamma\left(1+\frac{\varepsilon}{2}\right)^2} B\left(1+\frac{\varepsilon}{2}-k, 1+\frac{\varepsilon}{2}-l\right) {}_2\mathrm{F}_1\left(k, l, 1+\frac{\varepsilon}{2}; \frac{A-B}{2A}\right) . \quad (5.61)$$

which, using a linear transformation of the third result in (B.6), immediately gives

$$I_{aA}^{(1,1)} = \frac{2\pi}{a(A+B)}\left[\frac{2}{\varepsilon} + \ln\left(\frac{A+B}{2A}\right) - \frac{\varepsilon}{2}\,\mathrm{Li}_2\left(-\frac{A-B}{A+B}\right)\right] + \mathcal{O}(\varepsilon^2)\ . \tag{5.62}$$

This finishes the derivation of basic angular integrals. We will give one quick example of how they are used in practice. In our decomposition procedure we may find a term $\sim u_6/u'$, with no other angular variables. In set one, u' is an $[ABC]$ variable and can diverge collinearly, whereas u_6 is an $[ab]$ variable and cannot diverge collinearly, compare Tab. 5.1. So we need the integral $I_A^{(-1,1)}$. We can relate this integral to $I_a^{(1,-1)}$ by $\mathcal{D}_\pm$. So first we use $I_a^{(1,-1)} = \frac{1}{2}\frac{\partial}{\partial A} I_a^{(1,-2)}$, compare (5.46) and (5.56), then apply $\mathcal{D}_+$ with $\sqrt{B^2+C^2} = -A$. We could of course also use $\mathcal{D}_-$ with $\sqrt{B^2+C^2} = A$ to derive the same general formula, but the former corresponds to $u' \to t'$ directly. We get

$$I_A^{(-1,1)} = \frac{\pi(aA-bB)}{A^2}\left[\frac{2}{\varepsilon} + \frac{2bB(1+\varepsilon)}{(aA-bB)}\right]\ . \tag{5.63}$$

Now we plug in the values from Tab. 5.1 and finally find

$$\begin{aligned} I_A^{(-1,1)}(u_6,u') = {} & \frac{2\pi(m^2+s_4)t_1u_1}{s_4(s_4-t_1)^2} \\ & \cdot \left\{\frac{2}{\varepsilon} + \frac{(1+\varepsilon)s_4[(2m^2+s_4)(s_4-t_1)-(2m^2+s_4+t_1)u_1]}{(m^2+s_4)t_1u_1}\right\}\ . \end{aligned} \tag{5.64}$$

Most of the integrals presented here were already derived in [44] and we agree on the common results. Note however that we have extended almost all integrals to $\mathcal{O}(\varepsilon)$. We need $\mathcal{O}(\varepsilon)$ when the integrals also have a soft divergence, i.e., when they are $\sim 1/s_4^2$, which will result in an extra $1/\varepsilon$, see next section. Of course those $\mathcal{O}(\varepsilon)$ parts needed in our processes were already presented in [44], but our extended results may become useful for other processes.

5.4 Phase-Space Slicing

Now that we have completed the necessary angular integrations and identified the collinear singularities, let us briefly return to the infrared singularities. Remember that (5.9) allows us to isolate the infrared singularities by introducing a cut Δ on an integration diverging for $s_4 \to 0$. Take the s_4-integration of a function $\mathcal{H}(s_4)$ with a soft pole $s_4^{-1+\varepsilon}\mathcal{S}(s_4)$ and a finite $\mathcal{F}(s_4)$ part, i.e., both $\mathcal{S}$ and $\mathcal{F}$ are well behaved for $s_4 \to 0$ when $\varepsilon = 0$ and $\mathcal{S}(0) \neq 0$. Then

$$\int_0^{s_4^{\max}} ds_4 \mathcal{H}(s_4) \equiv \int_0^{s_4^{\max}} ds_4 \left[s_4^{-1+\varepsilon}\mathcal{S}(s_4) + \mathcal{F}(s_4)\right]$$

$$
\begin{aligned}
&= \int_0^{\Delta} ds_4 \left[\frac{\Delta^\varepsilon}{\varepsilon}\delta(s_4)\mathcal{S}(s_4) + \{\mathcal{S}(s_4) - \mathcal{S}(0)\}s_4^{-1+\varepsilon} + \mathcal{F}(s_4)\right] + \int_{\Delta}^{s_4^{\max}} ds_4 \mathcal{H}(s_4) \\
&\simeq \int_0^{s_4^{\max}} ds_4 \left[\frac{\Delta^\varepsilon}{\varepsilon}\delta(s_4)\mathcal{S}(s_4) + \Theta(s_4 - \Delta)\mathcal{H}(s_4)\right] \qquad (5.65)
\end{aligned}
$$

In the last step we have assumed that Δ is chosen small enough to be negligible with respect to the $2 \to 2$ Mandelstam variables (5.12) and m^2. Then $\mathcal{S}(s_4) - \mathcal{S}(0) \simeq 0$ in the range $0 \le s_4 \le \Delta$ and the integral of $\mathcal{F}(s_4)$ from 0 to Δ gives approximately zero as well. In practice one has to chose Δ so small that the integral over s_4 does not change anymore, $\Delta = 10^{-5} \ldots 10^{-7} m^2$ guarantees that the approximation is valid for our cross sections.

As we can see the integral has been split into two parts. The part with the soft pole $\mathcal{S}(s_4)$ is now evaluated in $2 \to 2$ kinematics due to the $\delta(s_4)$. This means that it can be considerably simplified! How can we extract this part from the total result $\mathcal{H}(s_4)$? If we remember that the $s_4 \to 0$ dependence of G_ε in (5.20) is $s_4^{1+\varepsilon}$ and the only infrared poles come from $s_4^{-1+\varepsilon}$ terms as shown above, then obviously we have to isolate all the $\sim 1/s_4^2$ parts of the matrix elements. By rewriting the results with the underlined variables of (5.23), we make the hidden s_4-poles due to $s_3 = s_4\underline{s_3}$, $t' = s_4\underline{t'}$ and $u' = s_4\underline{u'}$ appear explicitly. Then we can directly collect all contributing terms and drop the rest. We can also use the $s_4 \to 0$ limit of (5.24) to simplify the algebraic structure further: $u_5 \to -s$, $u_6 \to u_1$ and $u_7 \to t_1$. Thus it is easy to extract and simplify the part $\delta(s_4)\mathcal{S}(s_4)$ in (5.65). It will be given in terms of the $2 \to 2$ Mandelstam variables s, t_1 and u_1 and the reduced $2 \to 3$ Mandelstam variables $\underline{s_3}$, $\underline{t'}$ and $\underline{u'}$.

Let us examine what we get including the G_ε factor. Say we have collected all pole terms in $s_4^{-2}\mathcal{S}(s_4)$, then

$$
\begin{aligned}
G_\varepsilon s_4^{-2}\mathcal{S}(s_4) &= \frac{\mu^{-\varepsilon}}{2\pi(4\pi)^{2+\frac{\varepsilon}{2}}} \frac{\Gamma\left(1+\frac{\varepsilon}{2}\right)}{\Gamma(1+\varepsilon)} \frac{s_4^{-1+\varepsilon}}{(s_4+m^2)^{1+\frac{\varepsilon}{2}}}\mathcal{S}(s_4) \\
&\to \frac{\mu^{-\varepsilon}}{2\pi(4\pi)^{2+\frac{\varepsilon}{2}}} \frac{\Gamma\left(1+\frac{\varepsilon}{2}\right)}{\Gamma(1+\varepsilon)} (m^2)^{-1-\frac{\varepsilon}{2}} \frac{\Delta^\varepsilon}{\varepsilon}\mathcal{S}(0) \\
&= C_\varepsilon \left(1 - \frac{3}{8}\zeta(2)\varepsilon^2\right) \left(\frac{\Delta}{m^2}\right)^{\varepsilon} \frac{1}{\varepsilon}\frac{\mathcal{S}(0)}{2\pi m^2} + \mathcal{O}(\varepsilon^3)\,. \qquad (5.66)
\end{aligned}
$$

Note that we can rewrite G_ε, which parametrizes the difference of the $2 \to 3$ and $2 \to 2$ phase-spaces, see (5.19), using the integration factor C_ε that occurs in all the *virtual* loop integrals, see (3.5) and (3.6). This is of course expected, since the soft limit has effectively $2 \to 2$ kinematics and its infrared poles cancel those of the virtual contributions. The $1/\varepsilon$ infrared pole is clearly exhibited in (5.66) and can in combination with a potential collinear pole in $\mathcal{S}(0)$ give rise to $1/\varepsilon^2$ poles.

It is easy to calculate $\mathcal{S}(0)$ algebraically and thus the cancellation of the infrared poles can be performed explicitly. The remaining “hard” real piece is infrared safe due to the Δ cutoff. This method which singles out the part of the phase-space which is infrared divergent is called "phase-space slicing" and has also been used in the unpolarized calculations, see e.g., [44]. In principle the splitting in a hard and soft part in (5.65) is already sufficient for a numerical evaluation after the poles have been canceled. However, note the term $\left(\frac{\Delta}{m^2}\right)^\varepsilon$ in (5.66). In combination with $1/\varepsilon$ or $1/\varepsilon^2$, logarithms of Δ/m^2 after expansion and cancellation of the poles will be left over[6]. Though these logarithms are finite they of course grow large for $\Delta \to 0$. In the integral (5.65) they cancel in the sum with the $\Theta(s_4 - \Delta)\mathcal{H}(s_4)$ part.

It is thus advisable to shift the logarithmic Δ terms to the, in this way redefined, hard part in order to achieve a numerically directly stable result independent of Δ. For any numerical calculation of physically relevant hadronic cross sections, it is also useful to directly add the complete soft plus virtual piece to the hard part. In both cases this can be achieved by rewriting the soft plus virtual piece, expanded in powers of $\ln^k \Delta/m^2$ ($k = 0, 1, 2$), as follows [45]

$$\delta(s_4) \sum_{k=0}^{2} \alpha_k \ln^k \frac{\Delta}{m^2} \to \Theta(s_4 - \Delta)\mathcal{A}_k \alpha_k \,|_{s_4=0} \tag{5.67}$$

with coefficients α_k which are finite for $s_4 = 0$. Proper care is taken in (5.67) concerning the different distributions $\delta(s_4)$ and $\Theta(s_4 - \Delta)$ multiplying the soft and hard parts, respectively, see (5.65). As indicated in (5.67), the α_k have to be always evaluated using the "elastic" $2 \to 2$ kinematics, i.e., $s_4 = 0$, even when added to the $2 \to 3$ hard cross section. The coefficients $\mathcal{A}_k$ are given by

$$\mathcal{A}_0 = \frac{1}{s_4^{\max} - \Delta}, \qquad \mathcal{A}_1 = \frac{\ln(s_4^{\max}/m^2)}{s_4^{\max} - \Delta} - \frac{1}{s_4}, \qquad \mathcal{A}_2 = \frac{\ln^2(s_4^{\max}/m^2)}{s_4^{\max} - \Delta} - \frac{2\ln(s_4/m^2)}{s_4} \tag{5.68}$$

as can be easily verified by integrating the r.h.s. of (5.67) with $\int_\Delta^{s_4^{\max}} ds_4$, which recovers the $\ln^k \Delta/m^2$ terms. As a final note we mention that G_ε of course has to be expanded only to $\mathcal{O}(\varepsilon)$ for the hard part, since at worst we still find collinear $1/\varepsilon$ poles there.

[6]Terms of the form $\log\left(\frac{\Delta}{m^2}\right)/\varepsilon$ are eliminated by mass factorization, see Chap. 6.

Chapter 6

Mass Factorization

Using the work of the last three chapters, we find that the infrared singularities cancel in the sum of virtual and real contributions, as guaranteed by the Bloch-Nordsieck and Kinoshita-Lee-Nauenberg theorems [70], respectively. This includes collinear (mass) singularities, if they are accompanied by an infrared singularity, i.e., $1/\varepsilon^2 = 1/\varepsilon|_{\rm IR} \cdot 1/\varepsilon|_{\rm M}$ terms. However, there still can be singularities $1/\varepsilon$ left over, which are purely collinear in nature. We wish to show now how these singularities can be "absorbed" in a redefinition of the parton densities, which are convoluted with the partonic cross sections to obtain the experimentally measurable hadronic cross sections. A complete proof of mass factorization is of course not the aim here. However, it is useful to see in detail how the method works for one particular subprocess, since one can then by analogy easily write down the formulae for all the other kinds of subprocesses occurring here. The proof that this procedure can indeed be generalized and that the redefinition of the parton densities is *universal*, i.e., the same in all QCD processes, can be found in the literature. An extension of the methods used here is for example employed in [84] for the general proof. Note that we will have to deal with *initial* collinear singularities only in our subprocesses.

It is fortunate that one of the $2 \to 3$ subprocesses of our calculation is ideal for the demonstration. In NLO photoproduction one encounters a new type of subprocess with a light (anti)quark in the initial state, for which we will use the external momentum and color assignment

$$\vec{\gamma}(k_1) + \vec{q}_j(k_2) \to Q_k(p_1) + \overline{Q}_l(p_2) + q_i(k_3) \; . \tag{6.1}$$

The squared matrix element calculated from the graphs shown in Fig. 6.1 can be decomposed according to whether the photon couples to the heavy quark with charge e_Q (in units of e) in the "Bethe-Heitler" graphs (a) and (b), or to the light quark with charge e_q, as for the "Compton" graphs (c) and (d):

$$|\tilde{M}_{\gamma q}|^2 = \widetilde{M_{\gamma q} M^*_{\gamma q}} = E_\varepsilon g^4 e^2 \frac{C_F}{2} \left[e_Q^2 \tilde{A}_1 + e_q^2 \tilde{A}_2 + e_q e_Q \tilde{A}_3 \right] \; , \tag{6.2}$$

where $\tilde{A}_3$ denotes the contribution of the interference of both types of subprocesses. Notice that since we now have only one boson in the initial state, the photon, only one factor

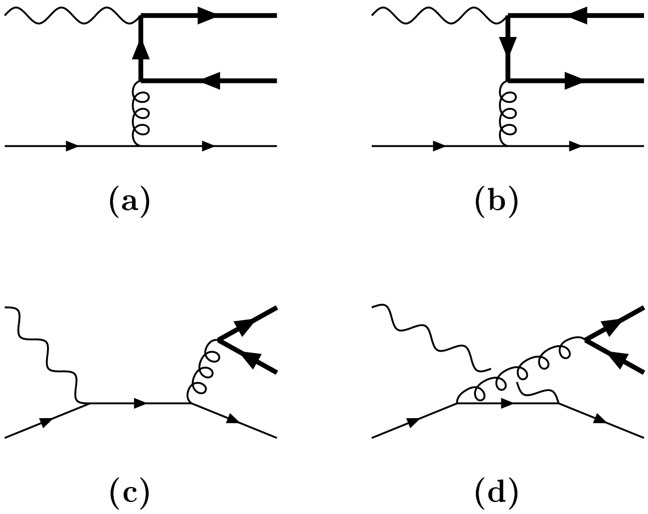

Figure 6.1: Feynman diagrams for the NLO light quark initiated subprocess $\gamma q \to Q\overline{Q}q$: "Bethe-Heitler" graphs (a) and (b), "Compton" graphs (c) and (d).

E_ε appears in (6.2), see the discussion of (2.12). Since this production mechanism occurs for the first time in NLO and there are no gluons in the final state, we do not encounter IR singularities in the calculation. All (single) poles can be *solely* attributed to collinear configurations, hence our choice of this subprocess to show the treatment of collinear singularities.

The $2 \to 3$ phase space integration including the partial fractioning proceeds just as was explained in Chap. 5, and so we can immediately quote the results here

$$
\begin{aligned}
\frac{d^2\tilde{\sigma}^{(1)}_{\gamma q, A_i}}{dt_1 du_1} &= \frac{C_F}{2} F_\varepsilon G_\varepsilon^H E_\varepsilon \alpha_s^2 \alpha e_i^2 \frac{2}{\varepsilon} \tilde{A}_i^{\text{pole}} + \mathcal{O}(1) \,, \\
\Delta A_1^{\text{pole}} &= -\frac{1}{u_1}(2-x_2)\left(\frac{x_2 t_1}{u_1} + \frac{u_1}{x_2 t_1}\right)\left[\frac{2m^2(x_2 s)}{(x_2 t_1) u_1} - 1\right] \,, \\
A_1^{\text{pole}} &= -\frac{1}{u_1}\frac{1+(1-x_2)^2}{x_2}\left\{\frac{x_2 t_1}{u_1} + \frac{u_1}{x_2 t_1} + \frac{4m^2(x_2 s)}{(x_2 t_1) u_1}\left[1 - \frac{m^2(x_2 s)}{(x_2 t_1) u_1}\right]\right\} \,, \\
\Delta A_2^{\text{pole}} &= -\frac{1}{t_1}(2x_1 - 1)\left[-\frac{t_1^2 + (x_1 u_1)^2}{(x_1 s)^2} - \frac{2m^2}{x_1 s}\right] \,, \\
A_2^{\text{pole}} &= -\frac{1}{t_1}\left[x_1^2 + (1-x_1)^2\right]\left[\frac{t_1^2 + (x_1 u_1)^2}{(x_1 s)^2} + \frac{2m^2}{x_1 s}\right] \,,
\end{aligned}
\tag{6.3}
$$

where only the (collinear) pole contributions are given and e_i^2 denotes e_Q^2, e_q^2, and $e_Q e_q$ for $i = 1$, 2, and 3, respectively. The interference contribution $\tilde{A}_3$ is not shown, because it is completely finite. $\tilde{A}_3$ together with the other finite parts is available upon request, the lengthy expressions will not be given here. Two new variables have been introduced:

$$x_1 \equiv -\frac{t_1}{s+u_1} \qquad \text{and} \qquad x_2 \equiv -\frac{u_1}{s+t_1} \,. \tag{6.4}$$

Note that we have not minimized the occurrence of these new variables in (6.3) to keep the combination of these variables with s, t_1, and u_1 in the results obvious. As no double poles can exist due to the absence of IR singularities, one needs G_ε in (5.19) only to $\mathcal{O}(\varepsilon)$ when writing down the partonic cross section (6.3):

$$G^H_\varepsilon \equiv \frac{2(4\pi)^4(s_4+m^2)}{s_4}G_\varepsilon = 16\pi\left[1+\frac{\varepsilon}{2}\left(\gamma_E - \ln(4\pi) + \ln\frac{s_4^2}{\mu^2(s_4+m^2)}\right)\right] + \mathcal{O}(\varepsilon^2) \,, \tag{6.5}$$

where we have also absorbed some additional factors into G^H_ε for convenience.

We see that $\tilde{A}_1^{\text{pole}}$ corresponds to the $\mathcal{O}(1)$ of $\tilde{B}_{\text{QED}}$ found in the LO photon-gluon subprocess (2.21), but with the replacement $(s,t_1,u_1) \to (x_2 s, x_2 t_1, u_1)$. Noting that

$$\delta[(x_2 s)+(x_2 t_1)+u_1] = \frac{1}{s+t_1}\delta\left(x_2+\frac{u_1}{s+t_1}\right) = -\frac{x_2}{u_1}\delta\left(x_2+\frac{u_1}{s+t_1}\right) \,, \tag{6.6}$$

we find that the δ-function of the $2 \to 2$ phase space (2.24) sets x_2 to just the right value (6.4) with the same replacement. Thus collecting all the factors, we find that we can write the $\tilde{A}_1^{\text{pole}}$-part of (6.3) in the following form

$$\frac{\alpha_s}{2\pi}\int_0^1 dx_2 \tilde{P}_{gq}(x_2)\left[\frac{2}{\varepsilon}+\tilde{E}_{gq}(\mu^2)\right] x_2 \left[\frac{d^2\tilde{\sigma}^{(0)}_{\gamma g}}{dt_1 du_1}\right]\begin{pmatrix} s \to x_2 s \\ t_1 \to x_2 t_1\end{pmatrix} . \tag{6.7}$$

Here $\tilde{E}_{gq}$ collects finite terms and depends not only on the usual kinematic variables, but also on the mass scale μ introduced to keep the coupling dimensionless. The functions $\tilde{P}_{gq}$ can be directly read off

$$P_{gq}(x) = P_{g\bar{q}}(x) = C_F\left[\frac{1+(1-x)^2}{x}\right] \,, \qquad \Delta P_{gq}(x) = \Delta P_{g\bar{q}}(x) = C_F(2-x) \,. \tag{6.8}$$

We find that this is exactly the LO (anti)quark to gluon splitting function of [85]!

This splitting function corresponds to the probability that a quark with momentum k sends out a *collinear* gluon with momentum xk and thus moves on with momentum $(1-x)k$. In our $\tilde{A}_1^{\text{pole}}$ case we then obviously must have the momentum of the exchanged gluon in Fig. 6.1 (a) and (b) set to $x_2 k_2$, i.e., the gluon is emitted collinearly to the light quark with a fraction x_2 of its momentum. This explains the appearance of the splitting function depending on x_2. The outgoing light quark has then the momentum $k_3 = (1-x_2)k_2$. The propagator of the gluon is found to be $\sim 1/t' = 1/(x_2 k_2)^2 =$ "$1/0$", which is readily identified as the source of the collinear poles, see (5.10). Finally, the exchanged gluon with momentum x_2k_2 couples to the heavy quark line. But then this upper part of the diagram is just like the Born amplitude for $\gamma g \to Q\overline{Q}$ with the replacement $k_2 \to x_2k_2$. So the appearance of the LO cross section with $(s, t_1, u_1) \to (x_2s, x_2t_1, u_1)$ is a natural consequence of the incoming light-like momentum x_2k_2, e.g., $t_1 = -2k_2{\cdot}p_2 \to -2x_2k_2{\cdot}p_2 = x_2t_1$, and x_2 is fixed by (6.6). Our results so far are depicted by Fig. 6.2 (a) and (b).

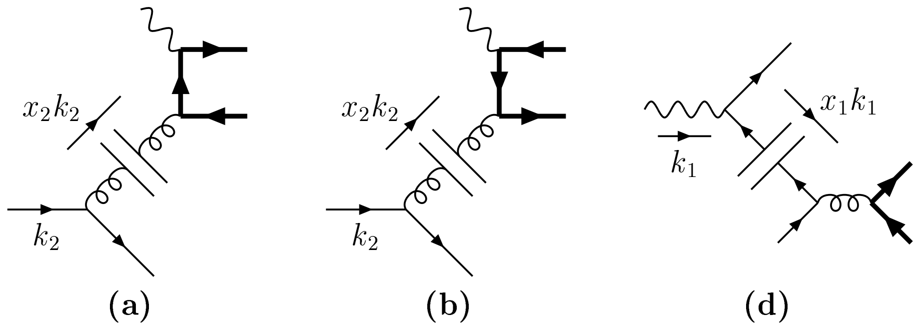

Figure 6.2: Factorized Feynman diagrams for obtaining the collinear contributions of Fig. 6.1. There is no factorized diagram corresponding to Fig. 6.1 (c).

Why did no similar collinear singularity occur for setting the heavy quark propagator on-shell in Fig. 6.1 (a) and (b)? The heavy quark propagator momentum in Fig. 6.1 (a) is $k_1 - p_1$. So let us assume for the three-momenta collinear emission $\vec{k}_1 - \vec{p}_1 \overset{!}{=} x\vec{k}_1$ with[1] $x \geq 0$. Then the denominator of the propagator becomes

$$u_7 = -2k_1 \cdot p_1 = -2\left[|\vec{k}_1|\sqrt{(1-x)^2\vec{k}_1^2 + m^2} - (1-x)\vec{k}_1^2\right] . \tag{6.9}$$

We see, that this can only become zero for $m = 0$ and $x \leq 1$! Then for $m = 0$ we recover four-momentum collinearity $k_1 - p_1 = xk_1$ with $0 \leq x \leq 1$. Note that there is no soft limit $k_1 \to 0$ possible here to set the propagator on-shell, since the center-of-mass energy $s = 2k_1 \cdot k_2 \geq 4m^2$. The next possibility, with a propagating gluon decaying to a heavy quark and antiquark pair, is realized in Fig. 6.1 (c) and (d) and can be treated similarly: The propagator momentum is $p_1 + p_2$, so we assume a collinear decay $\vec{p}_1 = x(\vec{p}_1 + \vec{p}_2)$ with[2] $x \geq 0$. So this time the denominator of the propagator is

$$s_5 = (p_1 + p_2)^2 = 2m^2 + 2\left[\sqrt{\vec{p}_1^{\,2} + m^2}\sqrt{\left(\frac{1-x}{x}\right)^2\vec{p}_1^{\,2} + m^2} - \frac{1-x}{x}\vec{p}_1^{\,2}\right] , \tag{6.10}$$

which again can only become zero for $m = 0$ and $x \leq 1$. We once more find for $m = 0$ the four-momentum collinearity $p_1 = x(p_1 + p_2)$ with $0 \leq x \leq 1$ and that no soft limit is

[1] $x \geq 0$ is necessary for energy conservation.

[2] The special case $x = 0$ leads to the same conclusions, we assume $x \neq 0$ in the following.

possible. The final possibility in QCD involving massive particles, emitting an external gluon from a heavy quark line $Q \to Qg$, will become relevant for $\gamma g \to Q\overline{Q}g$ and can be analyzed in exactly the same fashion as $g \to Q\overline{Q}$ with almost the same result. The only difference is that now for soft collinear emission ($k_3 = 0$), we *can* obtain an on-shell propagator in spite of the masses. However, these *soft* plus collinear singularities cancel against virtual contributions and thus do not have to be factorized. So we find that for non-zero mass propagators, we do not have any (surviving) collinear singularities. Hence we could have regularized the collinear singularities by giving the massless particles a small mass λ. Then the expressions would have diverged for $\lambda \to 0$. This explains the alternative name "mass singularities" and the label "mass (singularity) factorization".

Turning now to the "Compton" graphs of Fig. 6.1 (c) and (d), we see that (c) can not have a collinear part, since the light quark propagator is attached to two incoming particles. If it became on-shell, then indeed the center-of-mass energy would be zero, so this is kinematically forbidden. We do not have to worry about the gluon propagator either, since it is attached to heavy particles. On the other hand in Fig. 6.1 (d) the light quark propagator is attached only to one incoming particle, the photon, and thus we expect the collinear case depicted in Fig. 6.2 (d). So the antiquark propagator now has momentum $x_1 k_1$ and correspondingly we find for the outgoing light quark $k_3 = (1 - x_1)k_1$. The collinear propagator diverges $\sim 1/u' = (xk_1)^2 =$"1/0" and the attached LO subprocess is the quark-antiquark annihilation[3] (2.29) with the replacement $(s, t_1, u_1) \to (x_1 s, t_1, x_1 u_1)$ due to the incoming antiquark momentum $x_1 k_1$. So we expect for the A_2^{pole}-part

$$\frac{\alpha_s}{2\pi} \int_0^1 dx_1 \tilde{P}_{\bar{q}\gamma}(x_1) \left[\frac{2}{\varepsilon} + \tilde{E}_{\bar{q}\gamma}(\mu^2)\right] x_1 \left[\frac{d^2\tilde{\sigma}^{(0)}_{\bar{q}q}}{dt_1 du_1}\right] \begin{pmatrix} s \to x_1 s \\ u_1 \to x_1 u_1 \end{pmatrix} , \tag{6.11}$$

which is readily confirmed by comparing with (6.3). We can also read off the photon-(anti)quark splitting functions

$$P_{\bar{q}\gamma} = P_{q\gamma} = e_q^2 N_C \left[x^2 + (1-x)^2\right] , \qquad \Delta P_{\bar{q}\gamma} = \Delta P_{q\gamma} = e_q^2 N_C (2x - 1) , \tag{6.12}$$

and they indeed have exactly the form derivable from [85].

At this point we should try to give more physical meaning to our results. We have found that the singularities occur when the propagator of an internal (massless) particle goes on-shell. But the propagator basically corresponds to the *time* the virtual particle can propagate according to the uncertainty principle[4]! So as the propagator denominator goes to zero, the propagation time becomes *infinite*. In other words, the internal particle then becomes (quasi-)real and can be treated on the same footing as external particles. This can occur whenever an internal momentum happens to become parallel to the momentum of an

[3] The momenta are reassigned $\vec{\bar{q}}(k_1) + \vec{q}(k_2) \to Q(p_1) + \overline{Q}(p_2)$, which leaves (2.29) unchanged.

[4] This is most evident in non-relativistic perturbation theory, where the "propagator" is simply the inverse of the energy difference between the virtual and real state and $\Delta t \sim 1/\Delta E$. That the relativistic propagator is the corresponding generalization is easily shown, see for example [86].

external (massless) particle. But that this happens by chance for two unrelated (internal and external, respectively) particles, both obeying their local momentum constraints, is unlikely and hence suppressed by phase space. The only probable subprocesses leading to a contribution will be those, in which either an incoming particle decays collinearly to an internal particle or an internal particle decays collinearly into an external particle. We will only consider the first case in the following, because it is relevant for our calculation, but the second case can be analyzed analogously. Obviously this reaction happens in two steps with very different associated time scales. First one has the collinear decay into a quasi-real particle followed by a long ("infinite") propagation of the produced particle. Then on a very short time scale (large propagator virtuality) a hard scattering subprocess occurs. It is obvious that we can describe this by the probability of the external particle decaying into the (quasi-)real particle (the splitting function) times the cross-section of the hard scattering with the (quasi-)real particle (for NLO cross sections this will be a LO cross section, as one interaction is used up for the collinear splitting) times the regularized infinity of the on-shell propagator and then integrated over the possible collinear momenta. This is exactly the form of our results encountered in (6.7) and (6.11).

We can now draw some additional conclusions: Firstly, we immediately understand why the interference of Fig. 6.1 (a) and (b) with (c) and (d) gives $\tilde{A}_3^{\rm pole} = 0$. The LO amplitudes left over after separating off the long time scale subprocess (splitting and propagating) belong to different subprocesses and hence cannot interfere. Secondly, it is clear that we need to add Fig. 6.2 (a) and (b) amplitudes coherently to obtain $\tilde{A}_1^{\rm pole}$, since both short time scale LO amplitudes are needed, see Fig. 2.2. Thirdly, we can simply square Fig. 6.2 (d) on its own to obtain $\tilde{A}_2^{\rm pole}$, since Fig. 6.1 (c) cannot have the same long time scale subprocess and indeed one short time scale LO amplitude is enough, see Fig. 2.4. However, the last statement concerns contributions *within* a gauge invariant part, and is strictly only true when we use a *physical* gauge, for example an axial one[5]. When using our polarization sum (2.15), one obtains singularities from the interference of Fig. 6.1 (c) with (d). But the final (gauge invariant) result (6.11) has of course the structure we expect from the third argument. However, the first two conclusions are directly valid in any gauge, since they concern gauge invariant parts. The final step leading to the mass factorization procedure now becomes conceptionally simple: as the on-shell propagating internal particles are (quasi-)real, we should be able to pass them off as "partons". We can then try to absorb the singularities in a redefinition of the "bare" parton distributions used in calculating *hadronic* cross sections. Since these distributions parametrize our ignorance about processes at large time scales and distances anyway, we can safely declare these redefined densities as the "measurable" ones. Of course as mentioned above, we skip here the all important but difficult proof, that this redefinition is *universal*, e.g., the same in all (factorizable) QCD processes, see for example [84]. The final procedure is remarkably similar to the redefinition of the "bare" fields and couplings

[5]One then finds, that the divergence of the interference term between Fig. 6.1 (c) and (d) is $\sim \eta_\mu[(s_4 - u_1)k_3^\mu - s_4 k_1^\mu]/(\eta \cdot k_1)$, i.e., vanishes identically in the collinear limit $k_3 = (1 - x_1)k_1$. Of course in the end all terms proportional to η^μ, which fixes the gluon field A^μ via $\eta \cdot A = 0$, vanish.

in the renormalization procedure. But here we will be forced to leave the purely partonic level in order to obtain the final finite results. This reflects the fact that partons are not directly observable.

First let us define a *finite* reduced cross section $d\hat{\tilde{\sigma}}^{(1)}_{\gamma q}$ by

$$\frac{d^2\hat{\tilde{\sigma}}^{(1)}_{\gamma q}}{dt_1 du_1}(\mu_f^2) = \frac{d^2\tilde{\sigma}^{(1)}_{\gamma q}}{dt_1 du_1}(\mu^2) - \frac{d^2\tilde{\sigma}^{(1)}_{\mathrm{M}\gamma q}}{dt_1 du_1}(\mu_f^2, \mu^2) \,, \tag{6.13}$$

$$\begin{aligned}\frac{d^2\tilde{\sigma}^{(1)}_{\mathrm{M}\gamma q}}{dt_1 du_1}(\mu_f^2, \mu^2) = &\int_0^1 dx_1\; x_1 G_{\bar{q}\gamma}(x_1, \mu_f^2, \mu^2) \left[\frac{d^2\tilde{\sigma}^{(0)}_{\bar{q}q}}{dt_1 du_1}\right] \begin{pmatrix} s \to x_1 s \\ u_1 \to x_1 u_1\end{pmatrix} \\ &+ \int_0^1 dx_2\; x_2 G_{gq}(x_2, \mu_f^2, \mu^2) \left[\frac{d^2\tilde{\sigma}^{(0)}_{\gamma g}}{dt_1 du_1}\right] \begin{pmatrix} s \to x_2 s \\ t_1 \to x_2 t_1\end{pmatrix}\end{aligned} \tag{6.14}$$

$$G_{ij}(x_k, \mu_f^2, \mu^2) = \frac{\alpha_s(\mu^2)}{2\pi} \left[\tilde{P}_{ij}(x_k)\frac{2}{\varepsilon} + \tilde{F}_{ij}(x_k, \mu_f^2, \mu^2)\right] \,. \tag{6.15}$$

Comparing this to (6.7) and (6.11), we see that $d\hat{\tilde{\sigma}}^{(1)}_{\gamma q}$ becomes finite as long as the $\tilde{F}_{ij}$ are finite. What we use for the $\tilde{F}_{ij}$ is then another *choice of scheme*, which is in principle independent of our choice in the renormalization procedure. Also the *factorization scale* should in principle be independent of the regularization scale μ, which we had set equal to the renormalization scale μ_r. We see that due to the G^H_ε of (6.5) this scale is introduced in a logarithm proportional to the splitting function in the finite $\tilde{E}_{ij}(\mu^2)$ of (6.7) and (6.11). To eliminate this logarithmic dependence on the renormalization scale explicitly in the reduced cross section, we will subtract $\ln(\mu_f^2/\mu^2)$ proportional to the splitting function in the $\tilde{F}_{ij}$ of (6.15). Then the reduced cross section will only depend on the new factorization scale μ_f. Furthermore a glance at (6.5) suggests, that the pole again comes with the usual finite artifacts of dimensional regularization. So we will use the $\overline{\mathrm{MS}}$ prescription and additionally only eliminate these artifacts. The general $\overline{\mathrm{MS}}$ factorization choice then amounts to

$$\tilde{F}_{ij}(x, \mu_f^2, \mu^2) = \tilde{P}_{ij}(x) \left(\gamma_E - \ln(4\pi) + \ln\frac{\mu_f^2}{\mu^2}\right) \,, \tag{6.16}$$

and we will use it throughout our calculation. Finally there is a hidden choice of finite terms implied in (6.14). To what order in ε are we going to use the LO cross sections? Our choice is to use them to $\mathcal{O}(\varepsilon)$, not $\mathcal{O}(1)$, which leads to *finite* terms in conjuction with the $1/\varepsilon$ pole. This is consistent with the conventional definition of $\overline{\mathrm{MS}}$ factorization, which uses n-dimensional cross sections! If we considered our processes at next-to-NLO (NNLO) using $\overline{\mathrm{MS}}$ factorization, then $\mathcal{O}(\varepsilon^2)$ parts of the n-dimensional LO cross sections would have to be included, since they yield finite contributions with the double collinear emission $1/\varepsilon^2$ poles. In principle one could chose to never subtract this type of finite terms by adjusting the order in ε appropriately, but in our case the conventional $\overline{\mathrm{MS}}$ choice is *mandatory*! As has been mentioned in the discussion of (2.30), helicity conservation is broken by the commuting $[\gamma_5, \gamma_\mu] = 0$ of the HVBM scheme [54] in the non-physical $n-4=\varepsilon$ dimensions. The effect is thus naturally of $\mathcal{O}(\varepsilon)$ and can contribute only when the LO cross section is multiplied by a pole $1/\varepsilon$. But such finite terms will be generated from the collinear pole contributions in (6.11). In order to restore helicity conservation, we have to subtract them via (6.14) again, which is simply possible by inserting the LO cross sections to $\mathcal{O}(\varepsilon)$.

In order to finally factorize the singularities, we use the result, that to all orders in α_s and lowest order in α, we can write the collinear-singular partonic cross section as

$$d\tilde{\sigma}_{ij}(\mu^2, k_1, k_2) = \sum_{l,m} \int_0^1 dz_1 \int_0^1 dz_2 \; \Gamma_{li}(z_1, \mu_f^2, \mu^2)\Gamma_{mj}(z_2, \mu_f^2, \mu^2) d\hat{\tilde{\sigma}}_{lm}(\mu_f^2, z_1 k_1, z_2 k_2) \; , \tag{6.17}$$

with $i, j, l, m = g, q, \bar{q}, \gamma$ and to first order in α_s we have

$$\Gamma_{ij}(z, \mu_f^2, \mu^2) = \delta_{ij}\delta(1-z) + G_{ij}(z, \mu_f^2, \mu^2) \; . \tag{6.18}$$

In writing the dependence on the scales μ and μ_f in (6.17) and (6.18), we refer here only to the *additional* $\ln(\mu_f^2/\mu^2)$, see (6.16). We continue using $\alpha_s(\mu^2)$ and $F_\varepsilon(\mu^2)$, see (2.25), throughout, and this dependence on μ is always implied. It is a simple exercise to convince ourselves that (6.17) together with (6.18) reproduces exactly our result (6.14), when we drop all higher order terms and those suppressed by α/α_s. The only remaining structures are then $\Gamma_{\gamma\gamma}\Gamma_{qq} d\hat{\tilde{\sigma}}_{\gamma q}$, $\Gamma_{\bar{q}\gamma}\Gamma_{qq} d\hat{\tilde{\sigma}}_{\bar{q}q}$ and $\Gamma_{\gamma\gamma}\Gamma_{gq} d\hat{\tilde{\sigma}}_{\gamma g}$, and in $\mathcal{O}(\alpha_s)$ only the G_{ij} terms found in (6.14) appear. Note that the extra x_1 and x_2 cancel against $\frac{d}{d(x_1 u_1)} = \frac{1}{x_1}\frac{d}{du_1}$ and $\frac{d}{d(x_2 t_1)} = \frac{1}{x_2}\frac{d}{dt_1}$, respectively. The general factorization prediction for a hadronic cross section with two initial hadrons a and b can be written as

$$d\tilde{\sigma}^{ab}(K_1, K_2) = \sum_{i,j} \int_0^1 dy_1 \int_0^1 dy_2 \; \tilde{f}_i^a(y_1, \mu^2) \; \tilde{f}_j^b(y_2, \mu^2) \; d\tilde{\sigma}_{ij}(\mu^2, y_1 K_1, y_2 K_2) \; , \tag{6.19}$$

where $\tilde{f}_i^a(y, \mu^2)$ denotes the "bare" density of partons of type i in hadron a with longitudinal momentum fraction y. Their dependence on the regularization scale μ is dictated by the fact[6], that the all orders physical cross section $d\tilde{\sigma}^{ab}$ cannot depend on an arbitrary scale. K_1 and K_2 are the external hadronic momenta of the hadrons a and b, respectively. If we now define "dressed" parton densities

$$\begin{aligned} \tilde{f}_l^a(x_1, \mu_f^2) &= \sum_i \int_0^1 dy_1 \int_0^1 dz_1 \delta(x_1 - y_1 z_1) \tilde{f}_i^a(y_1, \mu^2) \Gamma_{li}(z_1, \mu_f^2, \mu^2) \; , \\ \tilde{f}_m^b(x_2, \mu_f^2) &= \sum_j \int_0^1 dy_2 \int_0^1 dz_2 \delta(x_2 - y_2 z_2) \tilde{f}_j^b(y_2, \mu^2) \Gamma_{mj}(z_2, \mu_f^2, \mu^2) \; , \end{aligned} \tag{6.20}$$

[6]The regularization dependence is often not shown and depends on the regularization method used.

we can rearrange the sums and integrations that occur after inserting (6.17) in (6.19) to an outer sum in l and m over the "dressed" parton densities, where outer integrations over x_1 and x_2 with the appropriate δ-functions have been added. So our final result has a form very similar to (6.19)

$$d\tilde{\sigma}^{ab}(K_1, K_2) = \sum_{l,m} \int_0^1 dx_1 \int_0^1 dx_2 \; \tilde{f}_l^a(x_1, \mu_f^2) \; \tilde{f}_m^b(x_2, \mu_f^2) \; d\hat{\tilde{\sigma}}_{lm}(\mu_f^2, x_1 K_1, x_2 K_2) \; , \quad (6.21)$$

where we now however have a sum over the *finite* reduced $d\hat{\tilde{\sigma}}_{lm}$! The singularities have disappeared in our definition of "dressed" partons (6.20). Since the physical cross section $d\tilde{\sigma}^{ab}$ and the reduced cross sections are finite, we now assume the dressed partons to be finite by construction. Thus (6.21) finally allows us to obtain physical predictions after we have computed the relevant (reduced) cross sections, like in (6.13). Note that in other subprocesses there are LO contributions, i.e., generally one has $d\hat{\tilde{\sigma}} = d\hat{\tilde{\sigma}}^{(0)} + d\hat{\tilde{\sigma}}^{(1)}$. We see from (6.17) and (6.18), that we can generally extract the needed reduced cross sections to $\mathcal{O}(\alpha_s)$ from

$$\begin{aligned} d\hat{\tilde{\sigma}}_{ij}^{(0)} &= d\tilde{\sigma}_{ij}^{(0)} \; , \\ d\hat{\tilde{\sigma}}_{ij}^{(1)}(\mu_f^2) &= d\tilde{\sigma}_{ij}^{(1)}(\mu^2) - d\tilde{\sigma}_{Mij}^{(1)}(\mu_f^2, \mu^2) \; , \\ d\tilde{\sigma}_{Mij}^{(1)} &= \sum_{l,m} \int_0^1 dz_1 \int_0^1 dz_2 \; G_{li}(z_1, \mu_f^2, \mu^2) G_{mj}(z_2, \mu_f^2, \mu^2) d\tilde{\sigma}_{lm}^{(0)}(z_1 k_1, z_2 k_2) \; . \end{aligned} \quad (6.22)$$

The dependence of the "dressed" partons (6.20) on only the factorization scale μ_f is again motivated by the fact, that the physical cross section in (6.21) is independent of the arbitrary scale μ_f. Technically, the "dressed" partons in (6.20) depend on the scale μ_f through the logarithm in the Γ_{ij} functions according to (6.18), (6.15) and (6.16). Thus we can by simple differentiation obtain the LO RGE of the form

$$\begin{aligned} \frac{df_i(x, \mu_f^2)}{d\ln(\mu_f^2)} &= \frac{\alpha_s(\mu^2)}{2\pi} \sum_j \int_x^1 \frac{dy}{y} f_j(y, \mu^2) P_{ij}\left(\frac{x}{y}\right) \\ &\underset{\text{all LL}}{\overset{\mathcal{O}(\alpha_s)}{=}} \frac{\alpha_s(\mu_f^2)}{2\pi} \sum_j \int_x^1 \frac{dy}{y} f_j(y, \mu_f^2) P_{ij}\left(\frac{x}{y}\right) \; . \end{aligned} \quad (6.23)$$

In the second line of (6.23), we have assumed that μ_f is of the order μ, which means that both $\alpha_s(\mu_f^2)$ and $\alpha_s(\mu^2)$ are sufficiently small to serve as expansion parameter. Also then the logarithm of the ratio of these two scales cannot become large and spoil the expansion. So we can employ $\alpha_s(\mu^2) \simeq \alpha_s(\mu_f^2) + \mathcal{O}[\alpha_s^2(\mu_f^2), \alpha_s^2(\mu_f^2)\ln(\mu^2/\mu_f^2)]$, compare (4.31), and $\tilde{f}_i(x, \mu_f^2) = \tilde{f}_i(x, \mu^2) + \mathcal{O}[\alpha_s(\mu^2), \alpha_s(\mu^2)\ln(\mu_f^2/\mu^2)]$, see (6.20) and (6.18). But we have also changed the nature of the differential equation by writing the second line! This is however justified upon closer physical examination: We can now construct parton distributions at a low scale μ_{f0}^2, where we first trust factorization to be valid. So this is our *initial* scale, setting a lower limit for "hard" scales whose occurrence allows to separate off a "hard" subprocess calculable with perturbative methods. Then we use (6.23) to "evolve" these partons to a higher scale[7] $\mu_f \simeq \mu \simeq m$ close to the typical hard scale m of the process, so that the reduced cross sections do not contain large logarithms of the type $\ln(\mu_f/m)$. We see that we are summing logarithms along the way from μ_{f0} to μ_f, when iteratively solving (6.23). Indeed it can be shown, that our mathematical sin of writing the second line in (6.23) corresponds to the physical good work of resumming the leading logarithmic (LL) corrections to all orders. These appear in axial gauges as strongly ordered ladder graphs $\mu_{f0}^2 \ll k_{1T}^2 \ll \ldots \ll k_{nT}^2 \ll \mu_f^2$, with the k_{iT} being the transverse momenta along the rungs of the ladders. Summation over all ladders will lead to (6.23). A detailed derivation can be found in [87], see also [88]. In the first line of (6.23), we have basically derived the result for only one rung. We can now use the LO RGE for determining the scale dependence of the parton distributions to LL accuracy. A corresponding NLO RGE, which additionally resums logarithms accompanied by an extra power of α_s, next-to-leading logarithms (NLL), can be obtained similarly.

Since however the partons in (6.21) are convoluted with both the LO and NLO (reduced) cross sections, one should use the $\mathcal{O}(\alpha_s^2)$ NLO RGE [26, 27, 89] and thus the summation of NLL. To see this, we will write down the solution of (6.23) for LO and NLO in the hypothetical case[8] when there is only one parton f and one $f \to f$ splitting function P. The LO and NLO cases correspond to inserting $P = P^{(0)} + \mathcal{O}(\alpha_s)$ and $P = P^{(0)} + \frac{\alpha_s}{2\pi} P^{(1)} + \mathcal{O}(\alpha_s^2)$ in (6.23), respectively. The appropriate LO and NLO "running" of α_s also has to be used, see (4.30) and (4.34), respectively. We exploit the fact that for Mellin moments $a_n \equiv \int_0^1 dx x^{n-1} a(x)$ the convolution becomes a simple product $\left[\int_0^1 \frac{dy}{y} a(y) b\left(\frac{x}{y}\right)\right]_n = a_n b_n$. Then we get from (6.23) the simple NLO differential equation and its solution in Mellin moment space

$$\frac{df_n(\mu_f^2)}{d\alpha_s(\mu_f^2)} = -\frac{2}{\beta_0 \alpha_s(\mu_f^2)} f_n(\mu_f^2) \left\{ P_n^{(0)} + \frac{\alpha_s(\mu_f^2)}{2\pi} \left(P_n^{(1)} - \frac{\beta_1}{2\beta_0} P_n^{(0)} \right) + \mathcal{O}[\alpha_s^2(\mu_f^2)] \right\} , \quad (6.24)$$

$$\begin{aligned} f_n(\mu_f^2) &= f_n(\mu_{f0}^2) \left[\frac{\alpha_s(\mu_f^2)}{\alpha_s(\mu_{f0}^2)} \right]^{-\frac{2}{\beta_0} P_n^{(0)}} \\ &\quad \cdot \left\{ 1 - \frac{\alpha_s(\mu_f^2) - \alpha_s(\mu_{f0}^2)}{\pi \beta_0} \left(P_n^{(1)} - \frac{\beta_1}{2\beta_0} P_n^{(0)} \right) + \mathcal{O}[\alpha_s^2(\mu_f^2, \mu_{f0}^2)] \right\} , \end{aligned} \quad (6.25)$$

and the LO differential equation and solution correspond to taking $\mathcal{O}(1)$ in the curled brackets. We see that $f_n^{\rm NLO} - f_n^{\rm LO} \sim \alpha_s$. The inversion of the Mellin transformation[9] $a(x) = \frac{1}{2\pi i} \int_{\mathcal{C}} dn x^{-n} a_n$ applied to $f_n(\mu_f^2)$, keeps this α_s-structure intact. Thus a LO cross

[7] To not confuse names, one can think of (6.23) written with μ' instead of μ_f as "evolution" variable. We then "evolve" from μ_{f0} to μ_f.

[8] This is in practice realized for the evolution of flavor non-singlet *combinations* of quark distributions.

[9] The simplest integration contour $\mathcal{C}$ runs from $c - i\infty$ to $c + i\infty$ with real c, which lies to one side of *all* singularities of a_n in the complex n-plane, see for example [90].

sections times the α_s part of the NLO partons has the same order as a NLO reduced cross section times the $\mathcal{O}(1)$ LO partons, and the error of multiplying a NLO reduced cross sections with the α_s part of the NLO partons is NNLO. So we have to use the NLO RGE evolved partons in our NLO calculations (and the LO ones for LO calculations) to achieve consistent orders of α_s. A final point is that collinear singularities occur only for massless particles, so we should stay consistent with our renormalization choice and always evolve only the n_{lf} light flavors as partons and not the heavy one.

It is important to realize that (6.20) mixes different contributions. In particular in our example we have to introduce the bare parton distribution $f_{\bar{q}}^{\gamma}(y_1, \mu^2)$, and thus of course also its "dressed" counterpart, to absorb $\Gamma_{\bar{q}\gamma}(z_1, \mu_f^2, \mu^2)$. So for a factorization scheme independent result we need to consider "resolved" photons with their own parton content. The photon *can* act like a hadron, by fluctuating into a virtual state with the appropriate quantum numbers, and thus it should not surprise us to see that this possibility has to be included. Obviously we will then also get resolved contributions to the cross section, in which the *physical* photon interacts via its partonic content. In the hadronic cross section (6.21), setting $a = \gamma$ denotes a physical photon and $l = \gamma$ an elementary photon. So for the "direct" part of (6.21), we use the (zeroth order in α) probability distribution for finding an elementary photon in the physical photon $f_{\gamma}^{\gamma}(x_1, \mu_f^2) = \delta(1 - x_1)$ with the reduced partonic cross sections for photoproduction. On the other hand for the resolved part of (6.21), we use the probability distributions for finding a parton $l = g, q, \bar{q}$ in the physical photon $f_l^{\gamma}(x_1, \mu_f^2)$ with the reduced partonic cross sections for *hadroproduction*. Note that since photonic densities are of $\mathcal{O}(\alpha/\alpha_s)$, LO resolved contributions effectively have the same order in the coupling constants as LO direct contributions. Similarly, NLO direct and NLO resolved contributions belong together. So we use for photoproduction at $\mathcal{O}(\alpha)$

$$\begin{aligned} d\tilde{\sigma}^{\gamma b}(K_1, K_2) = & \sum_m \int_0^1 dx_2\; \tilde{f}_m^b(x_2, \mu_f^2)\; d\hat{\tilde{\sigma}}_{\gamma m}(\mu_f^2, K_1, x_2 K_2)\ , \\ & + \sum_{l,m} \int_0^1 dx_1 \int_0^1 dx_2\; \tilde{f}_l^{\gamma}(x_1, \mu_f^2)\; \tilde{f}_m^b(x_2, \mu_f^2)\; d\hat{\tilde{\sigma}}_{lm}(\mu_f^2, x_1 K_1, x_2 K_2)\ , \end{aligned} \tag{6.26}$$

with l now restricted to $g, q, \bar{q}$. A further complication arises here, because the parton content of longitudinally, i.e., circularly, polarized photons is experimentally completely unknown for the time being, and one has to rely on realistic models [91] when estimating the size of the resolved contribution. However, it has been demonstrated in [33] that even for large spin-dependent photonic densities, the "background" from resolved photon reactions should be very small for all experimentally relevant total or differential cross sections in the $\overline{\text{MS}}$ scheme. In particular this is the case at *fixed target* energies, as for COMPASS with $\sqrt{S_{\gamma p}} \simeq 10$ GeV.

For the polarized total charm production cross section at *collider* energies, the resolved contribution can become as large as about 1/3 of the direct contribution but with opposite sign [33]. When everything is taken into account, the total charm production spin asymmetry appears to be too small to be measurable [33] at the polarized HERA option [28]. However, it is expected that for bottom production the resolved part is less important: Though the change in the heavy quark charge $e_b^2/e_c^2 = \left(-\frac{1}{3}\right)^2 / \left(\frac{2}{3}\right)^2 = 1/4$ suppresses the direct part, the minimal x at which the photonic densities in the resolved part are evaluated becomes $m_b^2/m_c^2 \simeq 9$ times larger. For example at $\sqrt{S_{\gamma p}} = 200$ GeV with $m_b = 4.5$ GeV and $m_c = 1.5$ GeV, we find $x_{\min} = 2.025 \cdot 10^{-3}$ and $x_{\min} = 2.25 \cdot 10^{-4}$, respectively, see (8.10) in Chap. 8. This strongly suppresses the resolved part. So for polarized photoproduction in the $\overline{\mathrm{MS}}$ scheme, the resolved part can be neglected in experimentally relevant circumstances (fixed target energies or bottom at collider energies) as a first approximation. It should also be remarked that for NLO photonic parton densities, unpolarized [92] as well as polarized [93] ones, often the so-called DIS$_\gamma$ factorization scheme [94] rather than the $\overline{\mathrm{MS}}$ prescription is used, since it provides a better perturbative stability between LO and NLO quark densities. In this case one either has to transform the densities back to the $\overline{\mathrm{MS}}$ scheme [92, 93], before using them in the calculation of the NLO resolved contribution or one has to use the appropriate DIS$_\gamma$ expression for $\tilde{F}_{\bar{q}\gamma}$ in (6.14), see the Appendix of [94].

We will finish this chapter by quickly deriving the other needed mass factorization subtractions leading to the reduced cross sections. From diagram Fig. 6.3 (a) we see that for the photoproduction real emission we have to subtract

$$\frac{d^2\tilde{\sigma}^{(1)}_{\mathrm{M}\gamma g}}{dt_1 du_1}(\mu_f^2, \mu^2) = \int_0^1 dx_2\, x_2 G_{gg}(x_2, \mu_f^2, \mu^2) \left[\frac{d^2\tilde{\sigma}^{(0)}_{\gamma g}}{dt_1 du_1}\right] \begin{pmatrix} s \to x_2 s \\ t_1 \to x_2 t_1 \end{pmatrix}, \tag{6.27}$$

with G_{gg} defined according to (6.15) and the LO gluon splitting functions are[10]

$$\begin{aligned} P_{gg}(x) &= \Theta(1-x-\delta) 2C_A \left(\frac{1}{1-x} + \frac{1}{x} - 2 + x(1-x)\right) + P_{gg}^\delta(x)\,, \\ \Delta P_{gg}(x) &= \Theta(1-x-\delta) 2C_A \left(\frac{1}{1-x} - 2x + 1\right) + P_{gg}^\delta(x)\,, \\ P_{gg}^\delta(x) &= \delta(1-x)\left(\frac{\beta_0}{2} + 2C_A \ln\delta\right)\,. \end{aligned} \tag{6.28}$$

Since we have regularized all soft singularities in our calculation by a small parameter Δ as outlined in Sec. 5.4, we have to stick to the same framework here to deal with the soft $x \to 1$ divergence of $\tilde{P}_{gg}$ and cannot simply use the usual "plus-prescription" $1/(1-x)_+$ of [85]. In (6.28) we have thus introduced another small auxiliary quantity δ [46, 95]. Of course, Δ introduced above and δ are not independent. Inserting (6.28) in (6.27) one gets schematically

$$\int_0^1 dx_2[\delta(1-x_2)A + \Theta(1-x_2-\delta_2)B(x_2)] x_2 \delta(x_2(s+t_1)+u_1) C(x_2 s, x_2 t_1, u_1)$$

[10] This form is easy to derive from the conventional one with a +-distribution, by insuring that $\int_0^1 dx \tilde{P}_{gg}(x)$ gives the same total splitting probability upon taking the $\delta \to 0$ limit.

$$= \delta(s_4) AC(s,t_1,u_1) + \Theta(s_4-\delta_2)\left[-\frac{1}{u_1}B\left(\frac{-u_1}{s+t_1}\right)C\left(\frac{-u_1 s}{s+t_1},\frac{-u_1 t_1}{s+t_1},u_1\right)\right] , \quad (6.29)$$

where we define the small parameter $\delta_2 \equiv \Delta/(s+t_1)$ to obtain the appropriate cut-off $\Theta(s_4-\Delta)$ from $\Theta(\frac{s_4}{s+t_1}-\delta)$. A subtraction with respect to the other incoming leg would yield a similar expression with x_1, δ_1 and $t_1 \leftrightarrow u_1$. Thus the contribution from mass factorization naturally splits into a soft ($x_i > 1-\delta_i$) and a hard ($x_i < 1-\delta_i$) part, which can be added to the corresponding cross sections. β_0 in (6.28) again includes only the n_{lf} light flavors, since we let only these flavors run.

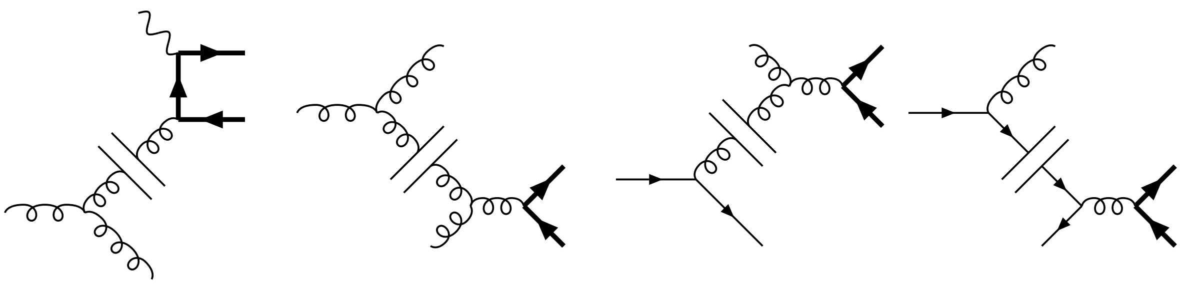

Figure 6.3: Factorized Feynman diagrams for obtaining the collinear contributions for the remaining photo- and hadroproduction subprocesses.

The gluon-gluon cross section of hadroproduction obviously has graphs like Fig. 6.3 (a) with the photon replaced by a gluon, but also those with "non-abelian" LO parts, see Fig. 6.3 (b). Thus we simply get here gluon-gluon fusion (GGF) instead of photon-gluon fusion (PGF) as the LO subprocess, see Fig. 2.2 and Fig. 2.3, and of course this time the graphs are symmetric concerning the incoming particles, so we have to subtract

$$\begin{aligned}\frac{d^2\tilde{\sigma}^{(1)}_{\mathrm{M}gg}}{dt_1du_1}(\mu_f^2,\mu^2) &= \int_0^1 dx_1\; x_1 G_{gg}(x_1,\mu_f^2,\mu^2)\left[\frac{d^2\tilde{\sigma}^{(0)}_{gg}}{dt_1du_1}\right]\begin{pmatrix} s\to x_1 s\\ u_1\to x_1 u_1\end{pmatrix}\\ &+\int_0^1 dx_2\; x_2 G_{gg}(x_2,\mu_f^2,\mu^2)\left[\frac{d^2\tilde{\sigma}^{(0)}_{gg}}{dt_1du_1}\right]\begin{pmatrix} s\to x_2 s\\ t_1\to x_2 t_1\end{pmatrix} .\end{aligned} \quad (6.30)$$

Similarly the addition of diagram Fig. 6.3 (c) will simply replace LO PGF (2.20) by LO GGF (2.27) for the NLO gluon-quark part of hadroproduction, and thus we need to subtract

$$\begin{aligned}\frac{d^2\tilde{\sigma}^{(1)}_{\mathrm{M}gq}}{dt_1du_1}(\mu_f^2,\mu^2) &= \int_0^1 dx_1\; x_1 G_{\bar{q}g}(x_1,\mu_f^2,\mu^2)\left[\frac{d^2\tilde{\sigma}^{(0)}_{\bar{q}q}}{dt_1du_1}\right]\begin{pmatrix} s\to x_1 s\\ u_1\to x_1 u_1\end{pmatrix}\\ &+\int_0^1 dx_2\; x_2 G_{gq}(x_2,\mu_f^2,\mu^2)\left[\frac{d^2\tilde{\sigma}^{(0)}_{gg}}{dt_1du_1}\right]\begin{pmatrix} s\to x_2 s\\ t_1\to x_2 t_1\end{pmatrix} ,\end{aligned} \quad (6.31)$$

and we need the additional LO splitting functions

$$P_{\bar{q}g} = P_{qg} = T_f \left[x^2 + (1-x)^2\right] , \qquad \Delta P_{\bar{q}g} = \Delta P_{qg} = T_f(2x-1) , \tag{6.32}$$

where $T_f = 1/2$ and we see compared to (6.12) the usual factor $1/(2N_C)$. Finally for NLO quark-antiquark annihilation in hadroproduction we have Fig. 6.3 (d) and similarly for the other incoming leg, so that we have to subtract

$$\begin{aligned}\frac{d^2\tilde{\sigma}^{(1)}_{\mathrm{M}q\bar{q}}}{dt_1du_1}(\mu_f^2,\mu^2) &= \int_0^1 dx_1\, x_1 G_{qq}(x_1,\mu_f^2,\mu^2)\left[\frac{d^2\tilde{\sigma}^{(0)}_{q\bar{q}}}{dt_1du_1}\right]\begin{pmatrix} s\to x_1 s\\ u_1\to x_1u_1\end{pmatrix}\\ &+\int_0^1 dx_2\, x_2 G_{\bar{q}\bar{q}}(x_2,\mu_f^2,\mu^2)\left[\frac{d^2\tilde{\sigma}^{(0)}_{q\bar{q}}}{dt_1du_1}\right]\begin{pmatrix} s\to x_2 s\\ t_1\to x_2t_1\end{pmatrix} .\end{aligned} \tag{6.33}$$

with the appropriately regulated LO splitting function

$$\begin{aligned}P_{qq} = P_{\bar{q}\bar{q}} &= C_F\left[\theta(1-x-\delta)\frac{1+x^2}{1-x} + \delta(1-x)\left(2\ln\delta+\frac{3}{2}\right)\right] ,\\ \Delta P_{qq} = \Delta P_{\bar{q}\bar{q}} &= P_{qq} + P_{qq}^{\mathrm{HVBM}} .\end{aligned} \tag{6.34}$$

Here we encounter the problem of the HVBM scheme [54], that helicity conservation at the qqg-vertex is violated due to the commuting γ_5 in the extra ε-dimensions, as was already mentioned in Chap. 2 and also discussed below (6.16). Thus actually the collinear singularities in the polarized quark-antiquark annihilation do not appear in conjunction with $\Delta P_{qq} = P_{qq}$, as they should. If helicity were conserved, then splitting that mixes helicities would be forbidden and hence the piece with mixed helicities, which is added in the unpolarized and subtracted in the polarized case, would be zero, leading to identical splitting functions. The HVBM violating effect is naturally of $\mathcal{O}(\varepsilon)$, but together with the collinear pole this will give rise to finite contributions. However, since we are eliminating the collinear contributions anyway by a redefinition of the parton densities, we can remove this unphysical property of the HVBM scheme by simply subtracting this finite contribution together with the poles. So we simply chose for P_{qq}^{HVBM} not the physical value zero, but rather the value it has in the HVBM scheme, see [27]:

$$P_{qq}^{\mathrm{HVBM}} = -\theta(1-x-\delta)2C_F(n-4)(1-x) = -\theta(1-x-\delta)2C_F\varepsilon(1-x) , \tag{6.35}$$

and thereby restore helicity conservation.

To finish this section, we note that after mass factorization all reduced cross sections will be finite. Thus for factors depending on ε one can then safely perform the $\varepsilon\to 0$ limit. Examining the factor (6.5) and our choice for the $\overline{\mathrm{MS}}$ factorization scheme in (6.16), it is easy to see that the former pure pole parts are converted to finite parts in the reduced cross sections by

$$F_\varepsilon \tilde{G}^H_\varepsilon \to \frac{1}{s^2} , \qquad E_\varepsilon \to 1 , \qquad \text{and} \qquad \frac{2}{\varepsilon} \to \ln\frac{s_4^2}{m^2(s_4+m^2)} - \ln\frac{\mu_f^2}{m^2} , \tag{6.36}$$

so one can easily obtain these contributions from the pole parts we will quote.

Chapter 7

Parton Level Results

7.1 Photon-(Anti)Quark Scaling Functions

We will now present our results for the different subprocesses on a parton level, i.e., we will present the appropriate reduced partonic cross sections. As has been explained in the last chapter, these will have to be convoluted with the dressed parton distribution to obtain hadronic cross sections and thus physical predictions. Interesting phenomenological applications will be examined in the next chapter. However, the convolution with the parton distribution functions makes it difficult to distinguish characteristic features of the reduced partonic cross sections themselves, so it is worthwhile to consider them on their own. In particular we will consider the *total* reduced partonic cross sections. That means, we have to integrate our double differential results, see (2.24) and (5.19), over the possible range of the partonic variables t_1 and u_1 to obtain "total" results. The reason is the following: we expect the cross section to depend logarithmically on the renormalization and factorization scale, due to (4.56) and (6.15). Furthermore the running α_s also depends logarithmically on μ_r, see (4.38). Let us concentrate on the factors multiplying these logarithms and α_s. When we integrate out t_1 and u_1, to obtain the total cross section, the only scales left will be the partonic center-of-mass energy s and the heavy quark mass m. We find that the total cross section is $\sim 1/m^2$, i.e., we see the expected divergence of the total cross section for $m \to 0$. If we take this factor out as well, then what is left must be dimensionless and hence can be rewritten in some scaling variable depending only on s/m^2. We will call these remaining expressions scaling functions and the form we give for the total cross section (7.2) below makes this scaling explicit. The usefulness of the scaling functions is simply that we can use them to display our results without specifying s and m.

In order to obtain the total partonic cross section, we must first consider the kinematic boundaries of the t_1, u_1-integrations. From the positivity of the energy of the third particle $\omega_3 \geq 0$, we get $s_4 = s + t_1 + u_1 \geq 0$. In the true $2 \to 2$ cross sections (2.22), s_4 is equal to zero due to energy-momentum conservation. It is sufficient to consider only the $2 \to 2$ phase space, in the case of $2 \to 3$ this corresponds to the effective $2 \to 2$ of (5.16), to find the limits of the t_1 and u_1 integrations. We have

$$t_1 = -\sqrt{s}(E_2 + |\vec{p}_2|\cos\xi) \ , \qquad u_1 = -\sqrt{s}(E_2 - |\vec{p}_2|\cos\xi) \ , \tag{7.1}$$

so we know that t_1 and u_1 are negative. Thus $s > s_4$ and from $\vec{p}_2^{\,2} \geq 0$ we find the threshold condition $s \geq 4m^2$. Obviously extreme values of t_1 and u_1 are obtained for $\cos\xi = \pm 1$. Using (7.1), we find $u_1 - t_1 = \cos\xi\sqrt{(t_1+u_1)^2 - 4m^2 s}$, so by squaring we directly get $t_1 u_1 \geq m^2 s$. Now we have two constraints, which we can solve for $-u_1$ to get $-m^2 s/t_1 \leq -u_1 \leq s + t_1$. This can serve as an inner integration range of u_1 depending on t_1. For the true $2 \to 2$ processes $-u_1$ is exactly at the upper limit. We next get the range of the outer integration over t_1 directly from the intersection of the u_1 limits: $-m^2 s/t_1 \stackrel{!}{=} s + t_1$. This yields $s(1-\beta)/2 \leq -t_1 \leq s(1+\beta)/2$, with $\beta \equiv \sqrt{1 - 4m^2/s}$. The (reduced) total partonic cross sections can then be expressed in terms of scaling functions in both the unpolarized and polarized case ($l, m = g,\, q,\, \bar{q}, \gamma$) [43, 46, 34]:

$$\begin{aligned}\hat{\tilde{\sigma}}_{lm}(s, m^2, \mu_f^2, \mu_r^2) &= \int_{\frac{s}{2}(1-\beta)}^{\frac{s}{2}(1+\beta)} d(-t_1) \int_{-\frac{m^2 s}{t_1}}^{s+t_1} d(-u_1) \frac{d^2\hat{\tilde{\sigma}}_{lm}(s,t_1,u_1)}{dt_1 du_1} \\ &= \frac{\alpha^{2-k}\alpha_s^k(\mu_r^2)}{m^2}\left\{ \tilde{f}_{lm}^{(0)}(\eta) + 4\pi\alpha_s(\mu_r^2)\left[\tilde{f}_{lm}^{(1)}(\eta) + \tilde{\bar{f}}_{lm}^{(1)}(\eta)\ln\frac{\mu_f^2}{m^2}\right]\right\} \ ,\end{aligned} \tag{7.2}$$

$$\beta = \sqrt{1 - \frac{4m^2}{s}} = \sqrt{\frac{\eta}{1+\eta}} \ , \qquad \eta = \frac{s}{4m^2} - 1 = \frac{\beta^2}{1-\beta^2} \ , \tag{7.3}$$

where $k = 1$ for photo- and $k = 2$ for hadroproduction. We have introduced the variable η in (7.3), since it will be particularly convenient for showing both the approach to threshold $\eta \to 0$ and high energy $\eta \to \infty$ in logarithmic plots of the scaling functions. The scaling functions $\tilde{f}_{lm}^{(0)}$ and $\tilde{f}_{lm}^{(1)}$, $\tilde{\bar{f}}_{lm}^{(1)}$ stand for the LO and NLO corrections, respectively[1].

We have not written a $\ln(\mu_r^2/m^2)$ piece in (7.2), though it of course exists. But we can extract the renormalization logarithms from (4.56):

$$d\tilde{\sigma}_r^{(1)} = d\tilde{\sigma}^{(1)} + k\frac{\alpha_s}{4\pi}\left[\beta_0\frac{2}{\hat{\varepsilon}} - \frac{2}{3}\frac{2}{\hat{\varepsilon}_m}\right] d\tilde{\sigma}^{(0)} \ , \tag{7.4}$$

with $d\tilde{\sigma}^{(0)} \sim \alpha_s^k$ and $\beta_0 = (11C_A - 2n_{lf})/3$. The general form of the UV singularities of the virtual contributions is $\sim C_\varepsilon \frac{2}{\varepsilon}$, i.e., in (3.5) the integral will give a pole $\sim 2/\varepsilon$ and there is an overall factor C_ε in front. For the UV renormalization we do not have to worry about double poles $\sim 1/\varepsilon^2$ that can occur in our loop integrals, since they only come from the infrared plus collinear limit. Note that $C_\varepsilon \frac{2}{\varepsilon} \sim \frac{2}{\hat{\varepsilon}_m} + \mathcal{O}(\varepsilon)$, with

$$\frac{2}{\hat{\varepsilon}_m} = \frac{2}{\hat{\varepsilon}} - \ln\frac{\mu_r^2}{m^2} = \frac{2}{\varepsilon} + \gamma_E - \ln(4\pi) - \ln\frac{\mu_r^2}{m^2} \ . \tag{7.5}$$

[1]Note that we still use the "tilde notation" as a shorthand to denote both the longitudinally polarized and unpolarized cross sections simultaneously.

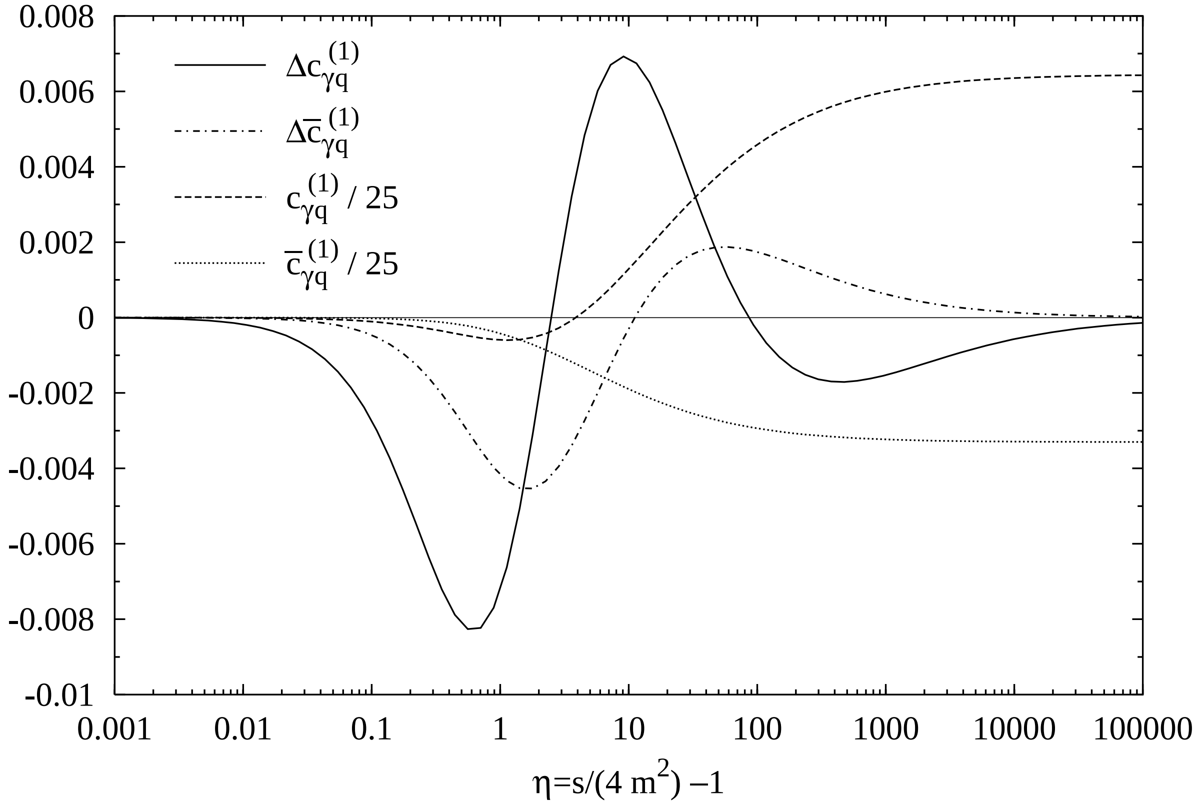

Figure 7.1: The NLO polarized and unpolarized "Bethe-Heitler" scaling functions $\tilde{c}^{(1)}_{\gamma q}$ and $\tilde{\bar{c}}^{(1)}_{\gamma q}$ in the $\overline{\mathrm{MS}}$ scheme as function of η as defined in (7.12). The unpolarized scaling functions have been divided by 25.

The counterterm of (7.4) will cancel the $2/\varepsilon$ poles, so they must come in the form

$$-k\frac{\alpha_s}{4\pi}\left[\beta_0\frac{2}{\hat{\varepsilon}_m}-\frac{2}{3}\frac{2}{\hat{\varepsilon}_m}\right]d\tilde{\sigma}^{(0)} \,, \tag{7.6}$$

where we however always have $\frac{2}{\hat{\varepsilon}_m}$ due to C_ε. We can ignore all *common* factors, even when they depend on ε like F_ε, since after the *cancellation* of these singularities only soft and collinear ones remain, which will not yield renormalization logarithms. Summing both contributions, we get

$$k\frac{\alpha_s}{4\pi}\beta_0\left(\frac{2}{\hat{\varepsilon}}-\frac{2}{\hat{\varepsilon}_m}\right)d\tilde{\sigma}^{(0)}=k\frac{\alpha_s}{4\pi}\beta_0\ln\frac{\mu_r^2}{m^2}d\tilde{\sigma}^{(0)} \,, \tag{7.7}$$

We chose to rewrite the renormalization logarithm as $\ln(\mu_r^2/m^2)\to\ln(\mu_r^2/\mu_f^2)+\ln(\mu_f^2/m^2)$ and absorb the $\ln(\mu_f^2/m^2)$ contribution in $\tilde{\bar{f}}^{(1)}_{lm}$ of (7.2). This is convenient in particular for the cases where the splitting function $\tilde{P}_{gg}$ appears in the factorization, since the β_0

term in the soft $\delta(1-x)$ part, see (6.28), exactly cancels this contribution. At any rate, keeping in mind that the k in (7.7) comes from the power of α_s in the Born cross section, we can get the renormalization log contribution missing in (7.2) by setting

$$\alpha_s(\mu_r^2) \to \alpha_s(\mu_r^2)\left(1 + \alpha_s(\mu_r^2)\frac{\beta_0}{4\pi}\ln\frac{\mu_r^2}{\mu_f^2}\right) , \tag{7.8}$$

and keeping only NLO terms. So in our case we have

$$\tilde{f}_{lm}^{(1)}(\eta) \to \tilde{f}_{lm}^{(1)}(\eta) + \frac{k\beta_0}{16\pi^2}\tilde{f}_{lm}^{(0)}(\eta)\ln\frac{\mu_r^2}{\mu_f^2} , \tag{7.9}$$

where again $k = 1$ for photo- and $k = 2$ for hadroproduction. So we see that the contribution depending on the ratio of the factorization and renormalization scale does not require a new scaling function and is furthermore easily derivable. Thus we will not worry about it any further in this chapter[2].

We have already performed the calculation of the photon-light quark contribution, including its factorization, in the last chapter so we can now immediately obtain the scaling functions. Part of the finite reduced quark cross section can be obtained by applying (6.36) to (6.3). Our results fully agree with [46] in the unpolarized case. There is no LO contribution, and thus $\tilde{f}_{\gamma q}^{(0)} = 0$. Note that we have only calculated the contribution for the production of a heavy *anti*quark. But we can split up the squared matrix elements of photo- and hadroproduction in parts that are symmetric $|\tilde{M}|_S^2(p_2,p_1) = |\tilde{M}|_S^2(p_1,p_2)$ and antisymmetric $|\tilde{M}|_A^2(p_2,p_1) = -|\tilde{M}|_A^2(p_1,p_2)$ with respect to exchanging $p_1 \leftrightarrow p_2$, respectively. However, applying $p_1 \leftrightarrow p_2$ to the phase space integrations means that instead of the heavy quark p_1 one integrates out the heavy antiquark p_2 (plus a gluon k_3 in both cases in the $2 \to 3$ processes), i.e., the heavy quark is observed. So we can directly apply $p_1 \leftrightarrow p_2$ to the double differential partonic cross sections for heavy antiquark production to obtain those for heavy quark production

$$\begin{aligned}
\frac{d^2\sigma^{\overline{Q}}(t_1,u_1)}{dt_1du_1} &\sim \int d^np_1\left[|\tilde{M}|_S^2(p_1,p_2) + |\tilde{M}|_A^2(p_1,p_2)\right] \\
&\overset{p_1\leftrightarrow p_2}{=} \int d^np_2\left[|\tilde{M}|_S^2(p_2,p_1) + |\tilde{M}|_A^2(p_2,p_1)\right] \\
&= \int d^np_2\left[|\tilde{M}|_S^2(p_1,p_2) - |\tilde{M}|_A^2(p_1,p_2)\right] \sim \frac{d^2\sigma^Q(t_1^Q,u_1^Q)}{dt_1^Q du_1^Q} , \\
t_1^Q \equiv (k_1-p_1)^2 - m^2 &\qquad \text{and} \qquad u_1^Q \equiv (k_2-p_1)^2 - m^2 ,
\end{aligned} \tag{7.10}$$

i.e., the sign of the antisymmetric part changes. But one has to keep in mind that now t_1 and u_1 are taken with respect to the *observed* heavy quark p_1 instead of the heavy

[2] One has to keep in mind though, that in the quark-antiquark case we are absorbing β_0 terms in $\tilde{\tilde{f}}_{lm}^{(1)}$, which normally would be absent.

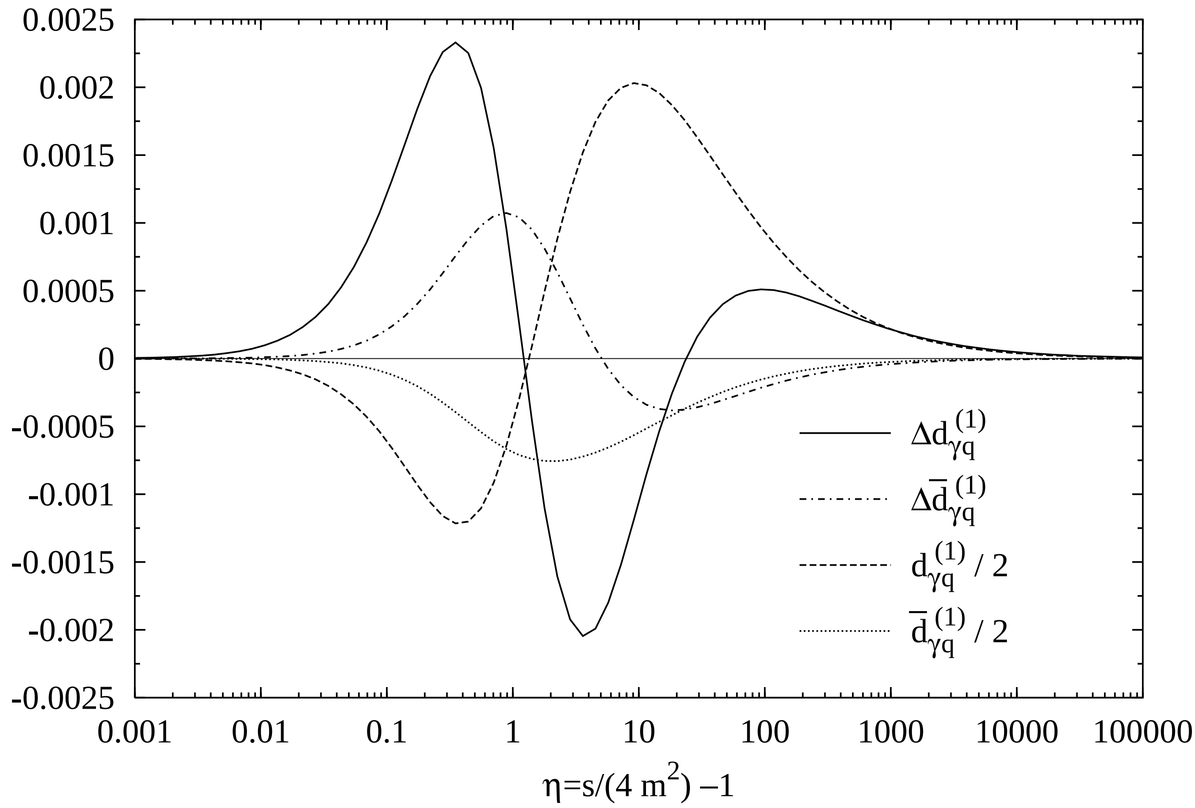

Figure 7.2: The NLO polarized and unpolarized "Compton" scaling functions $\tilde{d}_{\gamma q}^{(1)}$ and $\tilde{\bar{d}}_{\gamma q}^{(1)}$ in the $\overline{\mathrm{MS}}$ scheme as function of η as defined in (7.12). The unpolarized scaling functions have been divided by 2.

antiquark p_2, as it was in (5.12). This redefinition is always implied for quark production in the following, i.e., we will write t_1 and u_1 also there. For the $2 \to 2$ processes there is of course no difference between these definitions. In the case at hand, $\tilde{A}_1$ and $\tilde{A}_2$ in (6.3) stay unchanged for $p_1 \leftrightarrow p_2$, whereas $\tilde{A}_3$ changes sign. Thus if one wants to observe a heavy quark instead of a heavy antiquark, one can use $[e_Q^2 \tilde{A}_1 + e_q^2 \tilde{A}_2 - e_q e_Q \tilde{A}_3]$ in (6.2) with the same expressions for the $\tilde{A}_i$ [46].

In addition charge conjugation gives us even more information, since we have a light quark in the initial and final state

$$\frac{d^2\hat{\tilde{\sigma}}}{dt_1 du_1}\left(\gamma\bar{q} \to \overline{Q}\right) = \frac{d^2\hat{\tilde{\sigma}}}{dt_1 du_1}\left(\gamma q \to Q\right) \quad \text{and} \quad \frac{d^2\hat{\tilde{\sigma}}}{dt_1 du_1}\left(\gamma\bar{q} \to Q\right) = \frac{d^2\hat{\tilde{\sigma}}}{dt_1 du_1}\left(\gamma q \to \overline{Q}\right) \ . \tag{7.11}$$

Thus one can use the same $\tilde{A}_i$ for the contribution due to an incoming antiquark in (6.1) as well, taking into account a negative sign for $\tilde{A}_3$ again [46]. Note that the sign change of $\tilde{A}_3$ also implies that $\tilde{A}_3$ does *not* contribute to the *total* cross section (7.2), since the result cannot depend on whether the heavy quark or heavy antiquark is integrated first. This is also expected from Furry's theorem, which can be applied to the interference term if we integrate over the complete phase space. So there will be no scaling function $\sim e_q e_Q$ and the scaling function $\tilde{f}^{(1)}_{\gamma q}$ can be written as the sum of the "Bethe-Heitler" contribution $\tilde{c}^{(1)}_{\gamma q}$ and the "Compton" contribution $\tilde{d}^{(1)}_{\gamma q}$

$$\tilde{f}^{(1)}_{\gamma q}(\eta) = e_Q^2 \tilde{c}^{(1)}_{\gamma q}(\eta) + e_q^2 \tilde{d}^{(1)}_{\gamma q}(\eta) \;, \tag{7.12}$$

and similarly for the "bar" scaling function $\tilde{\bar{f}}^{(1)}_{\gamma q}$. There is no LO scaling function, of course. We plot $\tilde{c}_{\gamma q}$ in Fig. 7.1 and $\tilde{d}_{\gamma q}$ in Fig. 7.2. In both cases the solid line represents the NLO polarized, the dot-dashed line the NLO polarized "bar", the dashed line the NLO unpolarized and the dotted line the NLO unpolarized "bar" scaling function. The unpolarized scaling functions have been divided by a constant factor in order to fit into the same plot.

We see that the form of the unpolarized and corresponding polarized scaling functions differs quite strongly. What one cannot see in the plots, because the functions become small and because the unpolarized ones have been divided by a factor, is that for $\eta \to 0$ the scaling functions have the behavior $\Delta c^{(1)}_{\gamma q} \to c^{(1)}_{\gamma q}$, $\Delta d^{(1)}_{\gamma q} \to -d^{(1)}_{\gamma q}$, and similarly for the "bar" scaling functions. By inspecting

$$\hat{\sigma} = \frac{1}{2}\left[\hat{\sigma}(++) + \hat{\sigma}(+-)\right] \;, \qquad \Delta\hat{\sigma} = \frac{1}{2}\left[\hat{\sigma}(++) - \hat{\sigma}(+-)\right] \;, \tag{7.13}$$

we conclude that for $\eta \to 0$ in the "Bethe-Heitler" $\tilde{c}^{(1)}_{\gamma q}$ part of the partonic cross section $\hat{\sigma}(+-) \to 0$, whereas in that limit for the "Compton" $\tilde{d}^{(1)}_{\gamma q}$ part we find $\hat{\sigma}(++) \to 0$. Or more precisely - that one helicity combination goes faster to zero than the other. On the other hand for $\eta \to \infty$, we find $c^{(1)}_{\gamma q}$ becomes constant whereas $\Delta c^{(1)}_{\gamma q} \to 0$ and the same happens for the "bar" functions, implying $\hat{\sigma}(++) \to \hat{\sigma}(+-)$ for the "Bethe-Heitler" process. For the "Compton" process we find no obvious high energy limit of the partonic cross sections numerically. The observed plateau in the unpolarized $c^{(1)}_{\gamma q}$ is due to a flavor excitation process, in which a t-channel gluon is exchanged in the subprocess $Q^* q \to Qq$, and the virtual heavy quark is produced in $\gamma \to Q^* Q$ first, and similarly for the heavy virtual antiquark, compare Fig. 6.1 (a) and(b).

7.2 Photon-Gluon Scaling Functions

Next we turn to the NLO corrections to the PGF process (2.17)

$$\vec{\gamma}(k_1) + \vec{g}^{\,a}(k_2) \to Q_i(p_1) + \overline{Q}_j(p_2) \;, \tag{7.14}$$

where one-loop virtual and gluon bremsstrahlung contributions have to be taken into account. We start with the one-loop virtual corrections displayed in Fig. 7.3. They are calculated by the methods of Chap. 3. Remember that they have the same $2 \to 2$

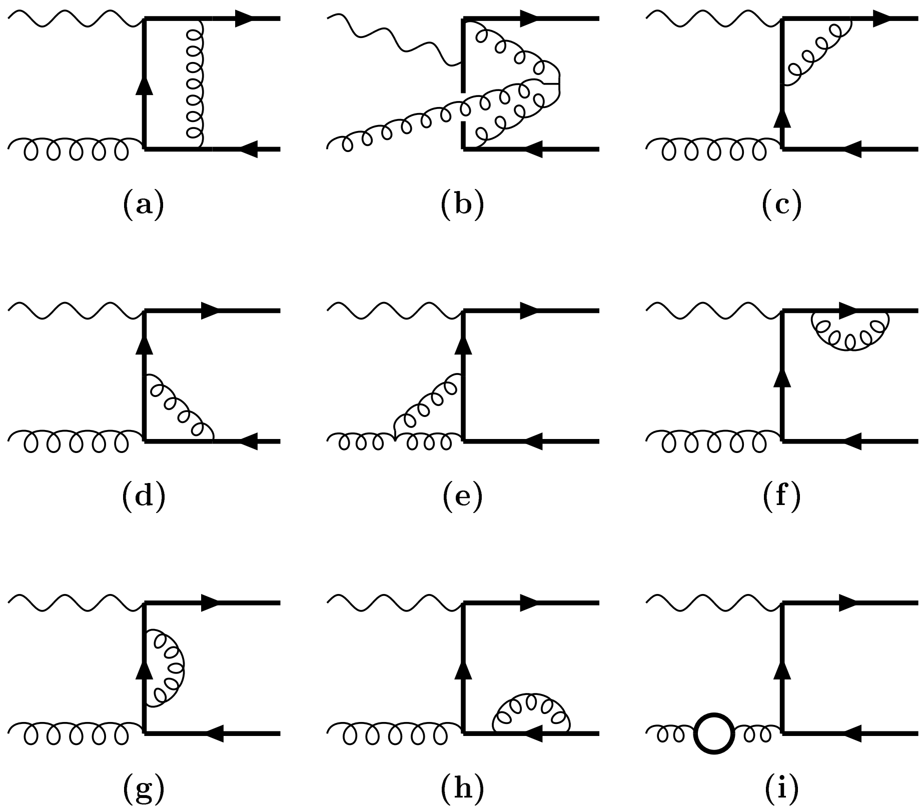

Figure 7.3: The NLO virtual corrections to $\vec{\gamma}\vec{g} \to Q\overline{Q}$. Reversing the heavy quark lines, except for the non-planar graph (b), yields the remaining graphs. Massless particle loops similar to graph (i) vanish, similarly to (3.3).

kinematics as the LO reaction (7.14) and thus can be calculated using (2.18) and (2.24). As mentioned, at $\mathcal{O}(\alpha\alpha_s^2)$ only the interference between the virtual V and Born B amplitudes of Fig. 7.3 and Fig. 2.2 contributes

$$|\tilde{M}|^2_{VB} = 2\mathrm{Re}\left(\widetilde{M_V M_B^*}\right) = E_\varepsilon^2 g^4 e^2 e_Q^2 \left[2C_F \tilde{V}_{\mathrm{QED}} + C_A \tilde{V}_{\mathrm{OK}}\right] \,, \tag{7.15}$$

where all quantities with a tilde denote as always, both the unpolarized and polarized expressions, e.g., $\tilde{V}_{\mathrm{QED}}$ denotes either V_{QED} or the spin-dependent ΔV_{QED}. The results have been sorted according to the color-factors $2C_F$ and C_A. We will not show the reduced virtual cross sections because of their length, but they can be reconstructed from the virtual plus soft cross sections discussed later. We note that $\tilde{V}_{\mathrm{QED}}$, which receives contributions only from the graphs (a), (c), (d) and (f)-(h) in Fig. 7.3, corresponds to the process where the gluon is replaced by a photon in the initial state, i.e., $\vec{\gamma}\vec{\gamma} \to Q\overline{Q}$. Complete NLO QCD $\mathcal{O}(\alpha^2\alpha_s)$ calculation of this process have been performed recently in [60] for both the unpolarized and polarized case. Our NLO results for the QED-part of $\vec{\gamma}\vec{g} \to Q\bar{Q}$ agree analytically with the ones presented in [60].

Each fermion propagator and each triple-gluon vertex in the loop introduces a loop momentum q^μ in the numerator. A glance at Fig. 7.3 then reveals that the maximal number of loop momenta we face in the numerator is one less than the number of propagators, except for graph (i). In particular, one has to deal with tensor four-point integrals of first (q^μ) to third ($q^\mu q^\nu q^\rho$) order and with tensor three- and two-point integrals of first (q^μ) and second ($q^\mu q^\nu$) order. We use our program, described in Chap. 3, to reduce these tensor integrals to a set of scalar ones by using an adapted Passarino-Veltman decomposition method [47]. This accounts properly for all possible n-dimensionally regulated divergencies in QCD. For graph (i) we need (3.51). In the results ultraviolet (UV), infrared (IR) and collinear/mass (M) singularities show up as $1/\varepsilon$ poles. In the non-abelian "OK"-part also double poles $1/\varepsilon^2$ occur when IR and M singularities coincide. The UV divergencies are removed by the renormalization procedure of Chap. 4. The IR and IR+M singularities cancel against the soft part of the gluon bremsstrahlung, which we will derive below. A left over M singularity cancels against the soft $\delta(1-x)$ part of $\tilde{P}_{gg}$, see (6.28), when we obtain the reduced bremsstrahlung cross section using (6.27) in the mass factorization procedure.

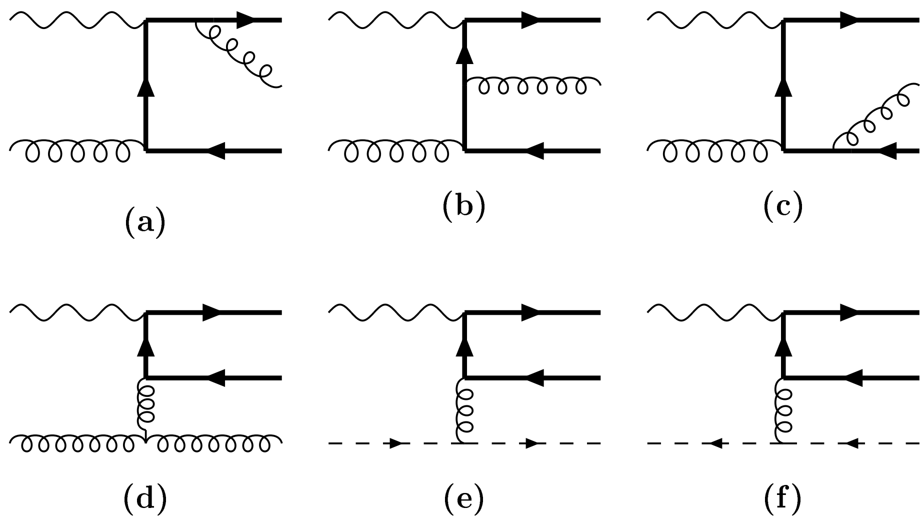

Figure 7.4: Feynman diagrams for the NLO gluon bremsstrahlung process $\vec{\gamma}\vec{g} \to Q\overline{Q}g$. Reversing the heavy quark lines yields the remaining graphs. In the unpolarized calculation the ghost contributions (e) and (f) have to be subtracted to cancel unphysical polarization contributions, see Fig. 2.1 and App. B.4.

In order to be able to present finite results, we will thus first calculate the corresponding real gluon emission reactions as well. The corresponding Feynman diagrams are shown in Fig. 7.4 and the momentum and color assignment is

$$\vec{\gamma}(k_1) + \vec{g}^{\,a}(k_2) \to Q_i(p_1) + \overline{Q}_j(p_2) + g^b(k_3)\ . \tag{7.16}$$

The techniques for handling these graphs, in particular our program for automatic partial fractioning of the angular integrals, have been explained in detail in Chap. 5. The squared matrix element, to be inserted in (5.19), can again be split into an abelian and a non-abelian part like (7.15)

$$|\tilde{M}_R|^2 = \widetilde{M_R M_R^*} = E_\varepsilon^2 g^4 e^2 e_Q^2 \left[2C_F \tilde{R}_{\mathrm{QED}} + C_A \tilde{R}_{\mathrm{OK}}\right] . \tag{7.17}$$

We use the phase space slicing of Sec. 5.4 to isolate the hard and soft parts. The collinear pole part of the hard photon-gluon cross section then becomes

$$\left(\frac{d^2\tilde{\sigma}^{(1)}_{\gamma g,\mathrm{OK}}}{dt_1 du_1}\right)^H = C_A F_\varepsilon G_\varepsilon^H E_\varepsilon^2 \alpha_s^2 \alpha e_Q^2 \frac{2}{\varepsilon} \tilde{H}^{\mathrm{pole}}_{\mathrm{OK}} + \mathcal{O}(1) , \tag{7.18}$$

$$H^{\mathrm{pole}}_{\mathrm{OK}} = -\frac{1}{u_1}\left[\frac{1}{1-x_2} + \frac{1}{x_2} - 2 - x_2(1-x_2)\right] \cdot \left\{\frac{x_2 t_1}{u_1} + \frac{u_1}{x_2 t_1} + \frac{4m^2(x_2 s)}{(x_2 t_1)u_1}\left[1 - \frac{m^2(x_2 s)}{(x_2 t_1)u_1}\right]\right\} , \tag{7.19}$$

$$\Delta H^{\mathrm{pole}}_{\mathrm{OK}} = -\frac{1}{u_1}\left(\frac{1}{1-x_2} - 2x_2 + 1\right)\left(\frac{x_2 t_1}{u_1} + \frac{u_1}{x_2 t_1}\right)\left[\frac{2m^2(x_2 s)}{(x_2 t_1)u_1} - 1\right] , \tag{7.20}$$

where only the non-abelian “OK” part is shown, because the hard abelian “QED” part is completely finite. G_ε^H is defined in (6.5) and x_2 in (6.4). As expected, we find the form necessary for the mass factorization in (6.27), see the hard $\Theta(1-x-\delta)$ part of (6.28). The finite contributions are too long to be presented here in an analytical form, but they can be found in our computer program, which is available upon request. Remember that one can extract the finite rest of the pole part in (7.18) after mass factorization, by applying (6.36). Our unpolarized results agree with those of [46].

We now turn to the soft gluon emission. According to the discussion in Sec. 5.4, we only need to isolate the $1/s_4^2$ poles of the squared matrix element by applying (5.23) and (5.24). In this way one can easily derive the soft limit of $\tilde{R}_{\mathrm{QED}}$ and $\tilde{R}_{\mathrm{OK}}$ in (7.17)

$$\tilde{S}_{\mathrm{QED}} = -\frac{2}{s_4^2}\left[m^2\left(1 + \frac{1}{\underline{s_3^2}}\right) + \frac{(2m^2-s)}{\underline{s_3}}\right]\tilde{B}_{\mathrm{QED}} , \tag{7.21}$$

$$\tilde{S}_{\mathrm{OK}} = \frac{2}{s_4^2}\left[\frac{1}{\underline{t'}}\left(\frac{t_1}{\underline{s_3}} + u_1\right) + \frac{(2m^2-s)}{\underline{s_3}}\right]\tilde{B}_{\mathrm{QED}} , \tag{7.22}$$

using the polarized and unpolarized ΔB_{QED} and B_{QED} given in (2.21), respectively. We agree again in the unpolarized case with [46]. The soft cross section is obtained from (7.21) and (7.22) with the $1/s_4^2 \to s_4^{-1+\varepsilon}$ replaced by $\delta(s_4)\Delta^\varepsilon/\varepsilon$ according to (5.65) and (5.66). Using this replacement and performing the angular integrations $d\Omega_\varepsilon$ the soft gluon cross section is then given by

$$\left(\frac{d^2\tilde{\sigma}^{(1)}_{\gamma g,\mathrm{QED}}}{dt_1 du_1}\right)^S = 2C_F F_\varepsilon G^S_\varepsilon E^2_\varepsilon \alpha_s^2 \alpha e_Q^2 \frac{\tilde{B}_{\mathrm{QED}}}{2}\left\{-\frac{2}{\varepsilon}+1+\frac{2m^2-s}{s\beta}\left[\ln\varkappa - S(\varkappa)\right]\right\}\delta(s_4)\ , \tag{7.23}$$

$$\left(\frac{d^2\tilde{\sigma}^{(1)}_{\gamma g,\mathrm{OK}}}{dt_1 du_1}\right)^S = C_A F_\varepsilon G^S_\varepsilon E^2_\varepsilon \alpha_s^2 \alpha e_Q^2 \frac{\tilde{B}_{\mathrm{QED}}}{2}\left[\frac{4}{\varepsilon^2}+\frac{2}{\varepsilon}\ln\frac{t_1}{u_1}+\ln\varkappa\ln\frac{u_1}{t_1}+\frac{1}{2}\ln^2\frac{u_1}{t_1}-\frac{1}{2}\ln^2\varkappa\right.$$
$$\left.+\mathrm{Li}_2\left(1-\frac{t_1}{\varkappa u_1}\right)-\mathrm{Li}_2\left(1-\frac{u_1}{\varkappa t_1}\right)+\frac{2m^2-s}{s\beta}S(\varkappa)\right]\delta(s_4)\ , \tag{7.24}$$

with $\tilde{B}_{\mathrm{QED}}$ defined in (2.21) and

$$S(\varkappa) \equiv -\frac{2}{\varepsilon}\ln\varkappa + \mathrm{Li}_2\left(\varkappa^2\right) - \ln^2\varkappa + 2\ln\varkappa\ln(1-\varkappa^2) - \zeta(2)\ , \tag{7.25}$$

$$G^S_\varepsilon \equiv 4(4\pi)^3 C_\varepsilon\left(1-\frac{3}{8}\zeta(2)\varepsilon^2\right)\left(\frac{\Delta}{m^2}\right)^\varepsilon \,\widehat{=}\, \frac{2(4\pi)^4 m^2\varepsilon}{s_4^2}G_\varepsilon\ , \tag{7.26}$$

where we have used $\varkappa \equiv (1-\beta)/(1+\beta)$, the dilogarithm function Li_2 as defined in App. B.2, and the Riemann zeta function $\zeta(2) = \pi^2/6$. Our unpolarized results for the soft bremsstrahlung cross section are again identical to those of [46]. In addition we have checked that the abelian "QED" part of the polarized (and unpolarized) total bremsstrahlung cross section is in complete analytical agreement with the NLO expressions for $\gamma\gamma \to Q\bar{Q}$ presented in [60].

To complete the calculation of the photon-gluon cross section, we now add the $\delta(1-x) \to \delta(s_4)$ mass factorization contribution from (6.27), see (6.29), to the renormalized virtual plus soft part $V+S$. We write the result in three parts using the usual abelian and non-abelian split and, in addition, separating off the part[3] proportional to β_0. The latter piece vanishes if one identifies the renormalization scale with the factorization scale, $\mu_r = \mu_f$, as is usually done, and corresponds to the α_s redefinition of (7.8):

$$\left(\frac{d^2\hat{\tilde{\sigma}}^{(1)}_{\gamma g}}{dt_1 du_1}\right)^{V+S} = \frac{\alpha_s^2\alpha e_Q^2}{s^2}\left[2C_F\left(\tilde{L}_{\mathrm{QED}}+\tilde{L}^\Delta_{\mathrm{QED}}\right)+C_A\left(\tilde{L}_{\mathrm{OK}}+\tilde{L}^\Delta_{\mathrm{OK}}\right)+\frac{\beta_0}{4}\tilde{L}_{\mathrm{RF}}\right]\delta(s_4)\ . \tag{7.27}$$

The $\tilde{L}^\Delta$ explicitly depend on the auxiliary cutoff Δ. The polarized ΔL are presented in App. C and the unpolarized L are in complete agreement with those obtainable from App. A of [46] and App. D of [44]. The treatment of the $\tilde{L}^\Delta$ terms has been discussed in Sec. 5.4. Both for numerical stability and in order to be able to present the $V+S$ and H

[3]The factor 1/2 compared with the expression in [35] is compensated by the squares in the logarithm of (C.11).

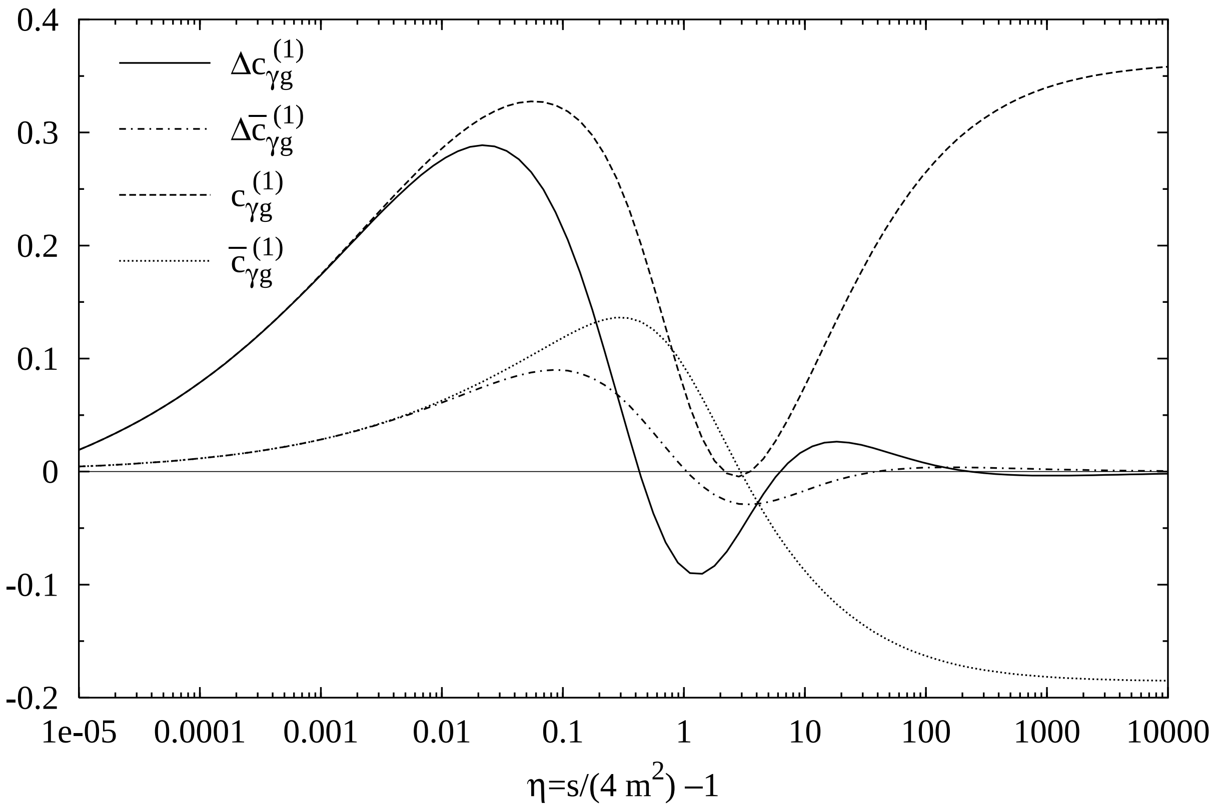

Figure 7.5: The NLO polarized and unpolarized scaling functions $\tilde{c}_{\gamma g}^{(1)}$ in the $\overline{\mathrm{MS}}$ scheme as function of η as defined in (7.28). The "bar" scaling functions $\tilde{\bar{c}}_{\gamma g}^{(1)}$ are also shown.

parts separately in the plots, we shift the $\ln^k \Delta/m^2$ terms with $k = 1, 2$ from the $V + S$ to the H part. So written symbolically, the meaning of soft and hard is "soft" $= S + V - \Delta$ and "hard" $= H + \Delta$, respectively. Note that again the presented results have been calculated for a detected heavy *anti*quark in the final state, because the heavy quark was integrated out in the calculations. Due to the $p_1 \leftrightarrow p_2$ symmetry of the matrix elements, the same double differential photon-gluon cross section can be used for a detected heavy quark as well [46]. Only then t_1 and u_1 are defined with respect to the observed heavy quark, see (7.10). On the other hand there is an *asymmetry* in the non-abelian part of the photon-gluon cross section with respect to $k_1 \leftrightarrow k_2$, since the outgoing gluon with momentum k_3 can only "couple" to the incoming gluon with momentum k_2, but not to the photon with momentum k_1. So the photon-gluon cross section is $t_1 \leftrightarrow u_1$ asymmetric.

The scaling functions for photon-gluon have the form

$$\tilde{f}_{\gamma q}(\eta) = e_Q^2 \tilde{c}_{\gamma q}(\eta) \; , \tag{7.28}$$

which is valid for LO, NLO and for the "bar" scaling functions $\tilde{\bar{c}}_{\gamma g}^{(1)}$ as well. In Fig. 7.5 we display the NLO scaling functions. Again the solid line represents the NLO polarized,

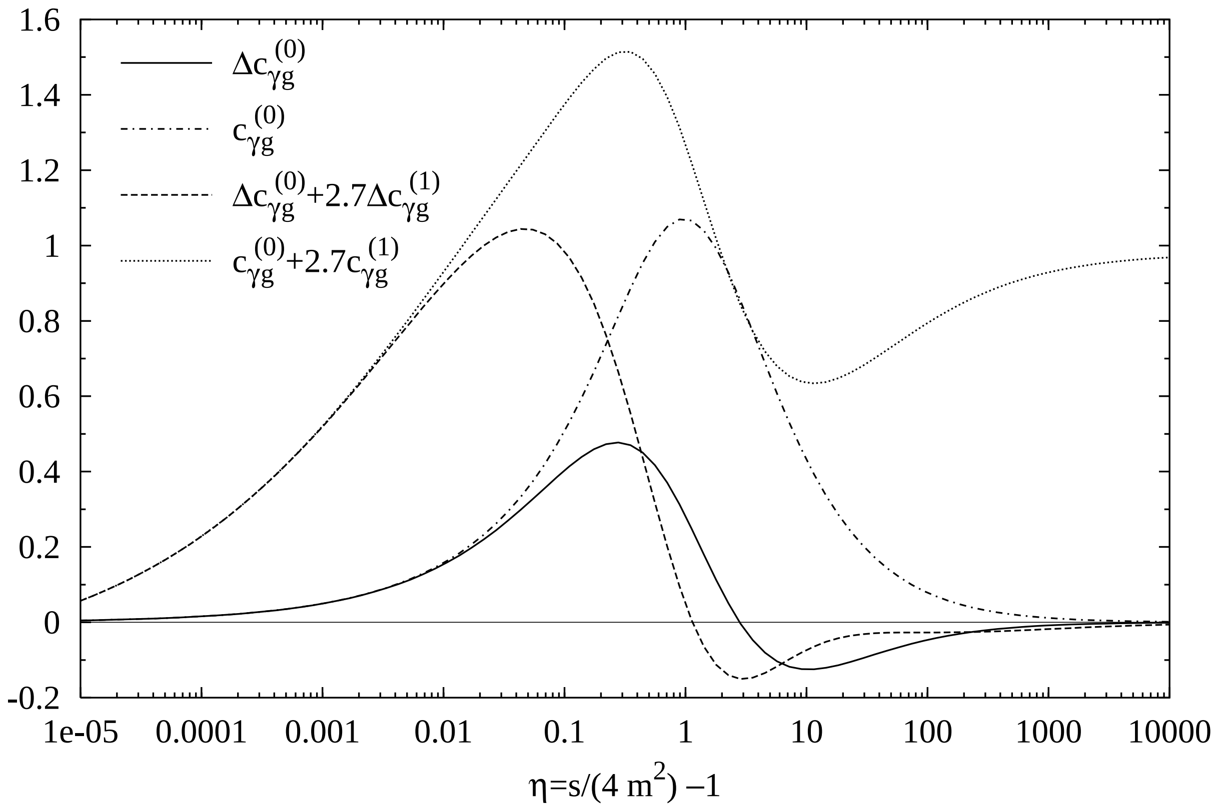

Figure 7.6: The LO polarized and unpolarized scaling functions $\tilde{c}_{\gamma g}^{(0)}$ in the $\overline{\mathsf{MS}}$ scheme as function of η as defined in (7.28). For comparison the effective NLO combinations $\tilde{c}_{\gamma g}^{(0)}+2.7\tilde{c}_{\gamma g}^{(1)}$ are also shown.

the dot-dashed line the NLO polarized "bar", the dashed line the NLO unpolarized and the dotted line the NLO unpolarized "bar" scaling function. In Fig. 7.6 we show the LO polarized (solid line) and unpolarized (dot-dashed line) scaling functions, as well as the combination $\tilde{c}_{\gamma q}^{(0)} + 2.7\tilde{c}_{\gamma q}^{(1)}$ in the polarized (dashed line) and unpolarized case (dotted line). The reason for showing this particular combination is that $4\pi\alpha_s(m_c^2) \simeq 2.7$ for charm production at COMPASS [31], where our photoproduction cross section will be mainly used. We see from (7.2), that in order to obtain an estimate of the size of the corrections LO $\tilde{f}_{lm}^{(0)}$ and NLO $\tilde{f}_{lm}^{(0)} + 4\pi\alpha_s\tilde{f}_{lm}^{(1)}$ should be compared with each other.

The form of the unpolarized and polarized scaling functions again differs quite strongly. This time we can see directly that the scaling functions have in LO and in NLO the behavior $\Delta c_{\gamma g} \to c_{\gamma g}$ for $\eta \to 0$, and similarly for the "bar" scaling functions. Thus we can conclude using (7.13), that as $\eta \to 0$ the PGF partonic cross section $\hat{\sigma}(+-) \to 0$. In LO this means that one helicity combination goes faster to zero than the other, but in NLO actually $\hat{\sigma}(++)$ becomes a non-zero constant in the $\eta \to 0$ limit. The reason for this is on one hand the graph Fig. 7.3 (a). Close to threshold the corresponding matrix

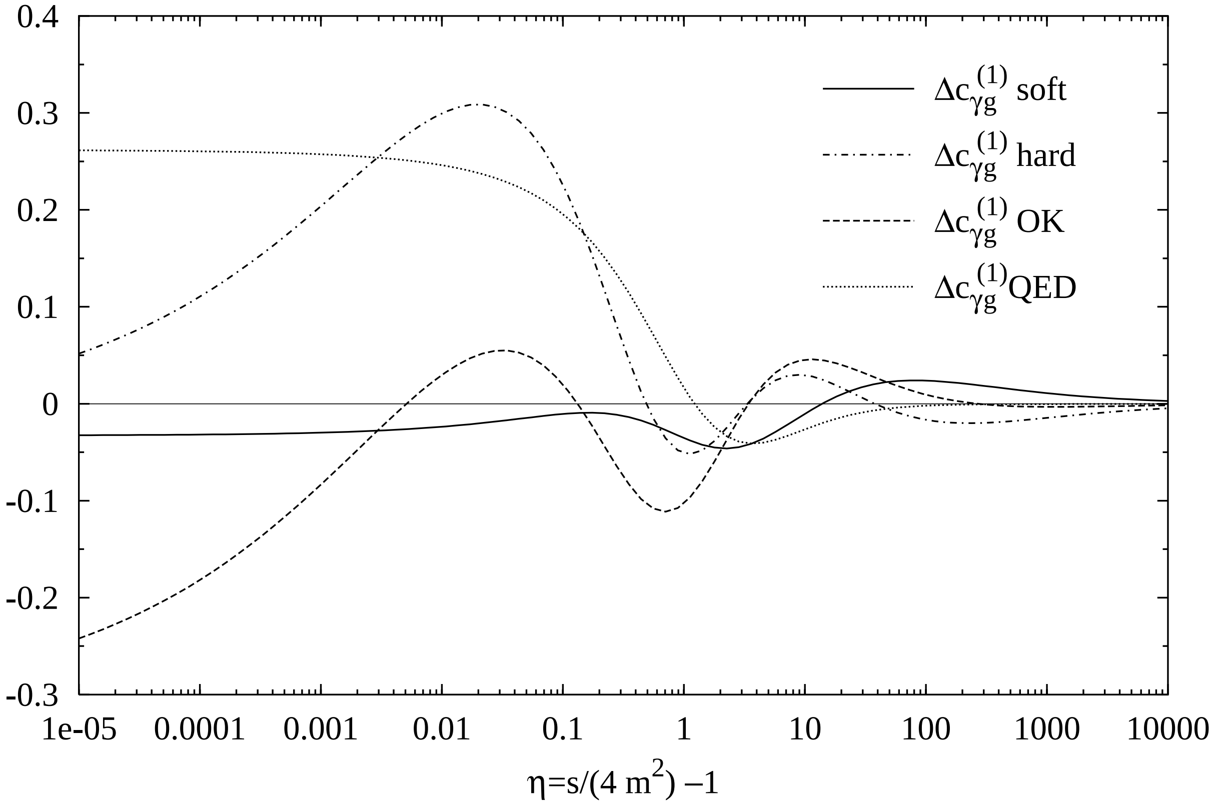

Figure 7.7: The soft ($V+S-\Delta$), hard ($H+\Delta$), non-abelian (OK), and abelian (QED) parts of the NLO polarized scaling function $\Delta c_{\gamma g}^{(1)}$ in the $\overline{\text{MS}}$ scheme as function of η. Soft+hard and OK+QED will both give $\Delta c_{\gamma g}^{(1)}$ of Fig. 7.5.

element diverges $\sim 1/\beta$, which corresponds to a Coulomb singularity for the heavy quark-antiquark pair produced in close proximity and almost at rest. This becomes suppressed by phase space integration $\sim \beta$, and one ends up with a non-zero *constant* at threshold. The LO matrix element does not diverge close to threshold since there is no interaction between the produced heavy quark and heavy antiquark, compare Fig. 2.2, and so due to the phase space the LO partonic cross section goes to zero. On the other hand soft gluon emission from the diagrams in Fig. 7.4 actually enhances the "hard" cross section at threshold, since we have shifted the $\ln^k(\Delta/m^2)$ terms. Looking for example at $\mathcal{A}_1$ in (5.68), we see that it does cancel a $1/s_4$ soft $s_4 \to 0$ divergence when added to the hard cross section. But it also introduces a finite term, which after integration[4] over s_4 results in a $\ln(s_4^{\max}/m^2)$. Since $s_4^{\max}/m^2 \sim \beta^2$ for small β, we get together with the phase space

[4] $s_4^{\max}(t_1, u_1)$ occurs for $t_1 u_1 = m^2 s$, so in practice we transform the $-u_1$ integration to an s_4 integration from Δ to $s_4^{\max}(t_1)$ in (7.2). Then the $\mathcal{A}_i$ depend on $s_4^{\max}(t_1) = s + t_1 + m^2 s/t_1$. If we do not transform, then $s_4^{\max} = s - 2\sqrt{m^2 s}$ with $t_1 = u_1 = \sqrt{m^2 s}$. We cannot go closer to threshold than $s_4^{\max} = \Delta$.

suppression a term $\sim \beta \ln \beta^2$. So these remaining logarithms give large contributions up to small values of β. We can clearly see in Fig. 7.7 both threshold effects: the "soft" part (solid line), containing the Coulomb singularity goes to a constant and the "hard" part (dot-dashed line) containing the remainders of soft gluon emission falls very slowly to zero. Also shown is the separation according to color-factors, the $2C_F$ "QED" part is displayed as a dashed line and the C_A "OK" part as a dotted line. We see that there are strong cancellations between these two close to threshold: $\Delta c^{(1)}_{\gamma g}(\eta = 0) = (2C_F - C_A)\pi/32$.

For $\eta \to \infty$, we find, like for $\tilde{c}^{(1)}_{\gamma q}$, that $c^{(1)}_{\gamma g}$ becomes constant, whereas $\Delta c^{(1)}_{\gamma q} \to 0$ and the same happens for the "bar" functions. So (7.13) implies $\hat{\sigma}(++) \to \hat{\sigma}(+-)$. The observed plateau in the unpolarized $c^{(1)}_{\gamma g}$ again comes from a flavor excitation process, this time a t-channel gluon is exchanged in the process $\overline{Q}^* g \to \overline{Q} g$, compare Fig. 7.4 (d), and similarly for the heavy virtual quark in the crossed graph. This appearance of *qualitatively* new diagrams for the first time in NLO suggests, that really only NLO can be considered to be the first relevant order for this process. The large difference between the "effective" NLO combination and the LO result in Fig. 7.6 is thus no surprise. It is reasonable to expect, that at NNLO we will not see similar drastic changes again, since corrections to the Coulomb singularity, to soft gluon emission and to flavor excitation will be suppressed by α_s and no qualitatively new diagrams appear in NNLO in comparison to NLO. To demonstrate clearly the NLO effects, we display in Fig. 7.8 ratios of the partonic cross sections. To avoid zeroes in the denominator at least in the gluon case, we will use $f_{lm}(++)$ and $f_{lm}(+-)$ instead of f_{lm} and Δf_{lm}. We show as solid $(++)$ and dot-dashed $(+-)$ lines the ratios of the "effective" NLO to the LO results, e.g., the solid line corresponds to $1 + 2.7c^{(1)}_{\gamma g}(++)/c^{(0)}_{\gamma g}(++)$. The dashed line represents the absolute value of $2.7[c^{(1)}_{\gamma q}(++) + 0.6d^{(1)}_{\gamma q}(++)]/[c^{(0)}_{\gamma g}(++) + 2.7c^{(1)}_{\gamma g}(++)]$ and the dotted line similarly for $(+-)$. These two lines are supposed to give a rough idea[5] of how large the light quark scaling functions are compared to the gluon ones. To explain the crosses with associated $x_{\min}$ values in the plot, note that when we calculate the hadronic photoproduction process by folding in the appropriate parton densities, we will use $s = xS$, where S is the hadronic center-of-mass energy[6]. Then

$$\eta = \frac{x}{x_{\min}} - 1\,, \qquad \text{with} \quad \frac{4m^2}{S} \equiv x_{\min} \le x \le 1 \tag{7.29}$$

We obviously have $\eta_{\max} = 1/x_{\min} - 1$. So the crosses show the maximally probed $\eta_{\max}$ for different $x_{\min}$. It is also indicated which η range the COMPASS experiment [31] will probe with charm photoproduction ($m \simeq 1.5$ GeV and $\sqrt{S} \simeq 10$ GeV for $E_\mu = 100$ GeV).

We see from Fig. 7.8, that the light quark scaling functions only contribute significantly at high energies. There they can reach up to 35% of the gluon scaling functions. The large η region is folded with the partons at large x, so the light quark contribution will get

[5] The factor 0.6 multiplying $d^{(1)}_{\gamma q}(++)$ is a simple minded average of $e_q^2/e_Q^2 = 1/4$ or $= 1$ for $e_Q = 2/3$.

[6] For photoproduction $f_\gamma^\gamma(x_1, \mu_f) = \delta(1 - x_1)$, so that in (6.21) only the $x = x_2$ integration remains, and from $k_1 = x_1 K_1 = K_1$ and $k_2 = x_2 K_2 = x K_2$ we find $s = x_1 x_2 S = xS$.

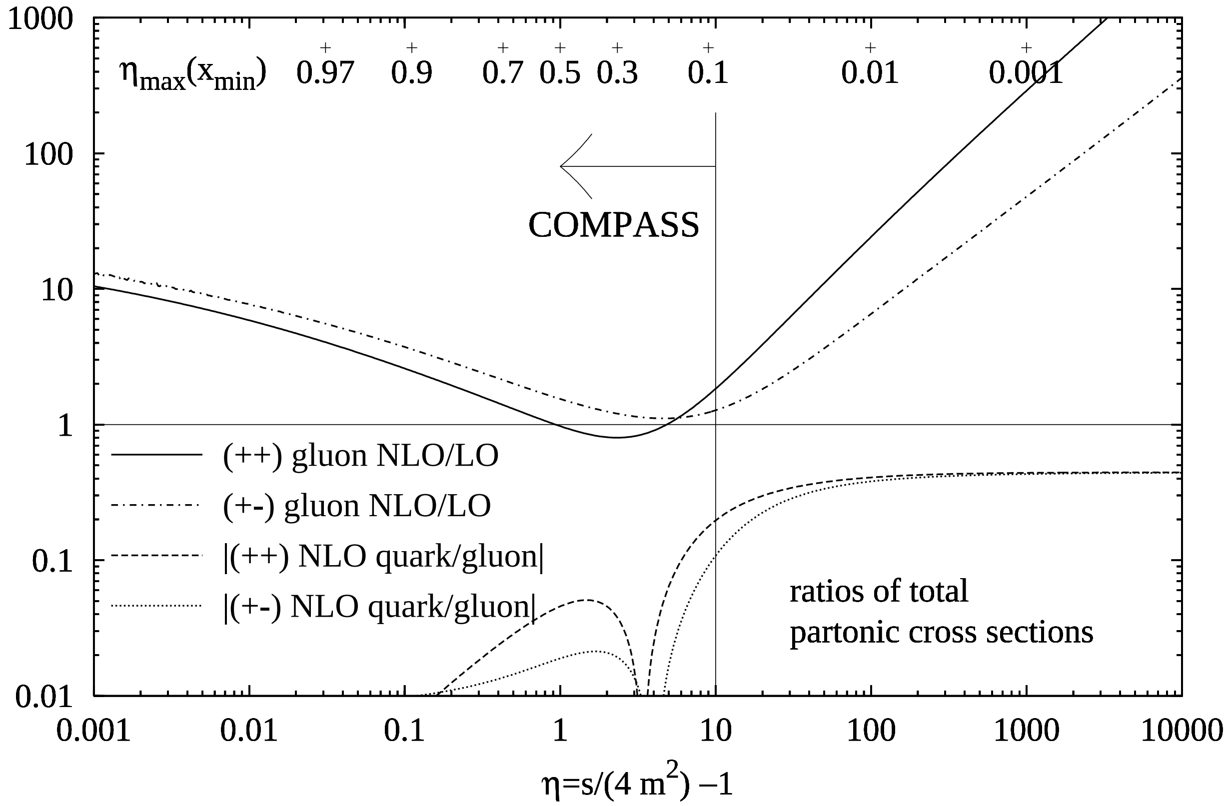

Figure 7.8: Ratios of NLO to LO gluon photoproduction scaling functions for the helicity combinations $(++)$ and $(+-)$. Also shown are the absolute values of the ratios of NLO quark to NLO gluon scaling functions. For details on the ratios, see the text. $\eta_{\mathsf{max}} = 1/x_{\mathsf{min}} - 1$ is displayed by crosses with corresponding x_{min} values. The η range that will be probed by COMPASS [31] is indicated by an arrow.

enhanced there relative to the gluon one. But for COMPASS energies, we do not expect much "contamination" from the quark sector, unless Δg is very small. We also see, that the high energy NLO enhancements from flavor excitation is irrelevant for COMPASS. We should not be worried by the massive growth of the NLO to LO ratio: LO goes to zero and NLO to a plateau, so obviously the ratio becomes infinite for $\eta \to \infty$. On the other hand COMPASS will see the threshold enhancement from the Compton singularity and from soft gluon bremsstrahlung, in particular since the gluon scaling functions at the smallest η will be folded with the gluons at the smallest x. However, for COMPASS "small" x are still rather large $x_{\min} \simeq 0.1$ and the factorization scale $\mu_f^2 \simeq m^2 \simeq 2.25$ GeV^2 is rather low, so the enhancement due to the rising gluon at small x will not be too strong. Furthermore both helicity combinations are enhanced, so we can expect less changes for the NLO asymmetry *ratios* of polarized to unpolarized results. For $\eta \to 0$ we indeed see from Fig. 7.6, that at least on the partonic level LO and NLO ratios both become one.

7.3 Gluon-(Anti)Quark and Quark-Antiquark Scaling Functions

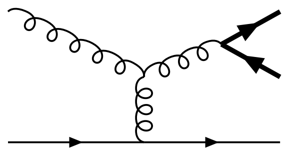

Figure 7.9: The only new Feynman diagram appearing in the $\vec{g}\vec{q} \to Q\overline{Q}q$ process. The others follow from Fig. 6.1 by replacing the photon by a gluon.

We now turn to the scaling functions for hadroproduction. Our first task will be to compute the scaling functions for the process

$$\vec{g}^{\,a}(k_1) + \vec{q}_j(k_2) \to Q_k(p_1) + \overline{Q}_l(p_2) + q_i(k_3) \; . \tag{7.30}$$

This is rather simple, since there is only *one* additional Feynman diagram. It is shown in Fig. 7.9. The other contributions come from the diagrams of Fig. 6.1 with the photon replaced by a gluon, which naturally leads to a more complicated color-structure. Furthermore, of course we have to compute the complete squared matrix element, which includes the interference between the "new" graph and the "old" graphs. We can split up the squared matrix element according to two color-factors:

$$|\tilde{M}_{gq}|^2 = \widetilde{M_{gq}M_{qg}^*} = E_\varepsilon g^6 \frac{1}{8N_C}\left[2C_F\tilde{J}_{\mathrm{QED}} + C_A\tilde{J}_{\mathrm{OK}}\right] \; . \tag{7.31}$$

By inspecting the color-factors of the amplitudes and comparing with (6.2), we can immediately conclude that

$$\tilde{J}_{\mathrm{QED}} = \tilde{A}_1 + \tilde{A}_2 + 2\tilde{A}_3 \; . \tag{7.32}$$

Thus we do not have to calculate the "QED" part! We can completely construct it from the already known $\tilde{A}_i$.

The pole structure of the "QED" cross section can be obtained from (6.3), and we set $e_q, e_Q \to 1$ and $e \to g$ and divide by $1/(2N_C)$ to get the factors right. Note that for the pole part we do not have to worry about the factor two in front of $\tilde{A}_3$, since it is finite and does not appear. Also, as has been mentioned below (7.11), $\tilde{A}_3$ does not contribute to the total cross section. So by defining two color-factor sorted scaling functions as

$$\tilde{f}^{(1)}_{gq}(\eta) = \tilde{f}^{(1)}_{gq,\mathrm{QED}}(\eta) + \tilde{f}^{(1)}_{gq,\mathrm{OK}}(\eta) \; , \tag{7.33}$$

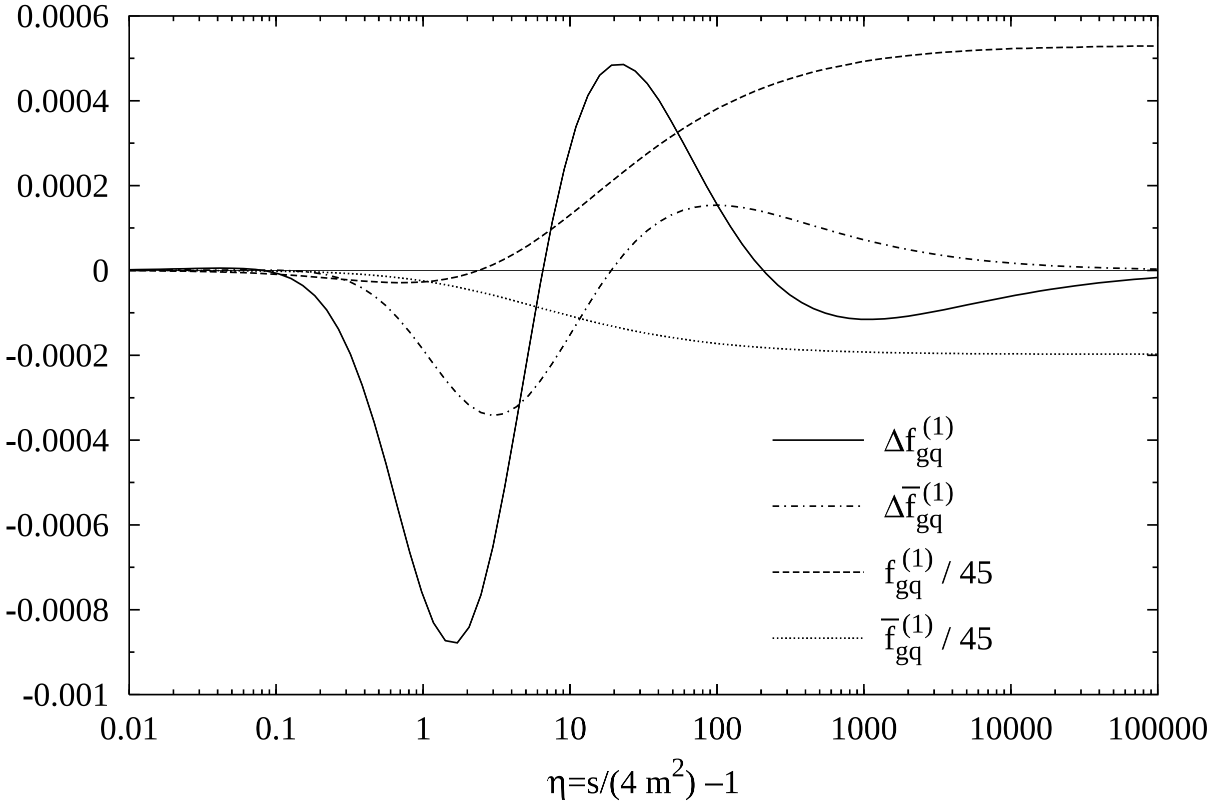

Figure 7.10: The NLO polarized and unpolarized scaling functions $\tilde{f}^{(1)}_{gq}$ and $\tilde{\bar{f}}^{(1)}_{gq}$ in the $\overline{\text{MS}}$ scheme as function of η. The unpolarized scaling functions have been divided by 45.

corresponding to the parts of the total partonic cross sections that follow from the $\tilde{J}_{\text{QED}}$ and $\tilde{J}_{\text{OK}}$ parts, respectively, we already know that

$$\tilde{f}^{(1)}_{gq,\text{QED}}(\eta) = \frac{1}{2N_C}\left[\tilde{c}^{(1)}_{\gamma q}(\eta) + \tilde{d}^{(1)}_{\gamma q}(\eta)\right] , \tag{7.34}$$

with $\tilde{c}^{(1)}_{\gamma q}$ and $\tilde{d}^{(1)}_{\gamma q}$ defined in (7.12). Once more we get the "usual" factor $1/(2N_C)$ for replacing a photon by a gluon. Analogous expressions to (7.33) and (7.34) are true for the "bar" scaling functions $\tilde{\bar{f}}^{(1)}_{gq}$.

So we only need to calculate the non-abelian part. Its pole part is given by

$$\frac{d^2\tilde{\sigma}^{(1)}_{gq,OK}}{dt_1du_1} = \frac{C_A}{8N_C}F_\varepsilon G^H_\varepsilon E_\varepsilon \alpha_s^3 \frac{2}{\varepsilon}\left(-\frac{2(x_2t_1)u_1}{(x_2s)^2}\right)\tilde{A}^{\text{pole}}_1 + \mathcal{O}(1) , \tag{7.35}$$

with $\tilde{A}^{\text{pole}}_1$ as in (6.3). G^H_ε is defined in (6.5) and x_2 in (6.4). Of course we see that we obtain exactly the necessary form for the mass factorization (6.31), if we compare the newly appearing factor with the C_A part of (2.27). Again we do not quote the rather lengthy finite parts of both the "QED" and "OK" corrections. Our unpolarized results are in complete agreement with those in [45].

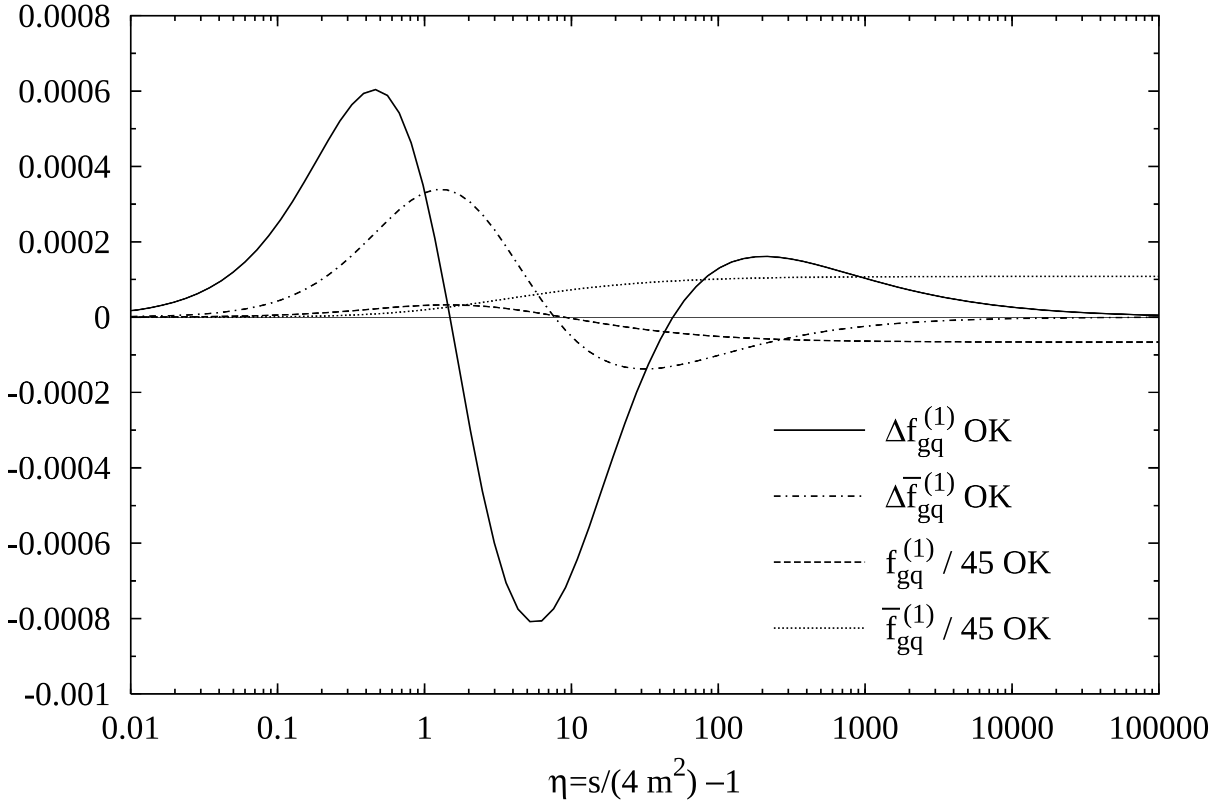

Figure 7.11: The non-abelian "OK" parts of Fig. 7.11 associated with the color-factor C_A. The abelian "QED" parts with color-factor $2C_F$ can be obtained from (7.34), and thus can be compared to Figs. 7.1 and 7.2.

In Fig. 7.10 we show the corresponding scaling functions, the solid line shows the polarized $\Delta f_{gq}^{(1)}$ and the dot-dashed line shows $\Delta \bar{f}_{gq}^{(1)}$ for the factorization logarithm. The dashed and dotted lines display the corresponding unpolarized scaling functions, scaled down by a factor 45 in order to fit in the same plot. We see again the behavior, that for $\eta \to \infty$ there is a plateau in the unpolarized part due to flavor excitation, whereas the polarized part goes to zero, so we have $\hat{\sigma}(++) \to \hat{\sigma}(+-)$ for this process. There is however no clean numerical limit for $\eta \to 0$, which is not surprising, since we have here basically a combination of $\tilde{c}_{gq}^{(1)}$ and $\tilde{d}_{gq}^{(1)}$, which have different behaviors in that limit. The rôle played by the additional $\tilde{f}_{gq,\mathrm{OK}}^{(1)}(\eta)$ and the corresponding "bar" functions is examined in Fig. 7.11. The lines show the corresponding non-abelian "OK" parts for the color-factor C_A of the scaling functions plotted in Fig. 7.10. The abelian "QED" part with $2C_F$ is not plotted, since it can be constructed from the $\tilde{c}_{gq}^{(1)}$ and $\tilde{d}_{gq}^{(1)}$, see (7.34). We find that the $\tilde{f}_{gq,\mathrm{OK}}^{(1)}(\eta)$ and also the "bar" counterparts share the properties of the $\tilde{c}_{gq}^{(1)}$ and their "bar" functions with respect to the η limits. This is no surprise, since its cross sections are related in form, see (7.35) and (6.3). We see that in the polarized case, the non-abelian parts in Fig. 7.11 are of similar size but quite different shapes compared to the totals in Fig. 7.10, which means that we have strong cancellations with the abelian parts. On the other hand in the unpolarized parts we observe similar shapes, but opposite signs. So there are similar cancellations. Finally we would like to mention, that we can obtain the reduced cross section for the production of a heavy quark instead of a heavy antiquark by switching $p_1 \leftrightarrow p_2$ with t_1 and u_1 defined with respect to the heavy quark. The behavior of the abelian "QED" part for $p_1 \leftrightarrow p_2$ is clear from the γq case, see (7.32) and the discussion following (7.10). The non-abelian "OK" contribution to heavy antiquark production can be similarly split into the sum of $p_1 \leftrightarrow p_2$ symmetric and antisymmetric parts. Then the heavy quark production contribution is obtained by simply subtracting instead of adding the antisymmetric part. Once more, charge conjugation

$$\frac{d^2\hat{\tilde{\sigma}}}{dt_1du_1}\left(g\overline{q} \to \overline{Q}\right) = \frac{d^2\hat{\tilde{\sigma}}}{dt_1du_1}\left(gq \to Q\right) \quad \text{and} \quad \frac{d^2\hat{\tilde{\sigma}}}{dt_1du_1}\left(g\overline{q} \to Q\right) = \frac{d^2\hat{\tilde{\sigma}}}{dt_1du_1}\left(gq \to \overline{Q}\right)\ , \tag{7.36}$$

allows us to directly derive the reduced cross section of an incoming light antiquark [43].

Now we turn to the NLO corrections to the process

$$\vec{q}_j(k_1) + \vec{\overline{q}}_i(k_2) \to Q_k(p_1) + \overline{Q}_l(p_2)\ . \tag{7.37}$$

The needed Feynman diagrams for the virtual corrections, which have the same external momentum and color assignment as the LO process (7.37) and are computed with the $2 \to 2$ phase space (2.24), are shown in Fig. 7.12. We can separate the squared matrix element of the interference of virtual with Born graphs according to the color factors

$$|\tilde{M}|^2_{VB} = 2\mathrm{Re}\left(\widetilde{M_V M_B^*}\right) = g^6\frac{C_F}{4N_C}\left[2C_F\tilde{N}_{\mathrm{QED}} + C_A\tilde{N}_{\mathrm{OK}} + \tilde{N}_{\mathrm{QL}}\right]\ , \tag{7.38}$$

where the only diagrams contributing to $\tilde{N}_{\mathrm{QL}}$ are the quark loops of Fig. 7.12 (g). The reduced partonic cross sections can be constructed for each color-part separately. The one following from the quark loop $\tilde{N}_{\mathrm{QL}}$ is finite after renormalization and yields

$$\left(\frac{d^2\hat{\tilde{\sigma}}^{(1)}_{q\bar{q},\mathrm{QL}}}{dt_1du_1}\right)^V = \frac{\alpha_s(\mu_r^2)}{3\pi}\left(-\frac{5(n_{lf}+1)}{3} - \frac{4m^2}{s} + n_{lf}\ln\frac{s}{\mu_r^2} - \frac{\beta(s+2m^2)}{s}\ln\varkappa\right)\frac{d^2\tilde{\sigma}_{q\bar{q},\mathrm{LO}}}{dt_1du_1}\ , \tag{7.39}$$

where the LO cross section can be read off (2.24) and (2.29) with $\varepsilon \to 0$. In the unpolarized case this is equivalent to Eqn. (2.15) in [45] upon taking the limit $m_L \to 0$, where m_L is the mass of the light quarks. We will not show the other reduced virtual cross sections because of their length, but they can be reconstructed from the virtual plus soft cross sections discussed later.

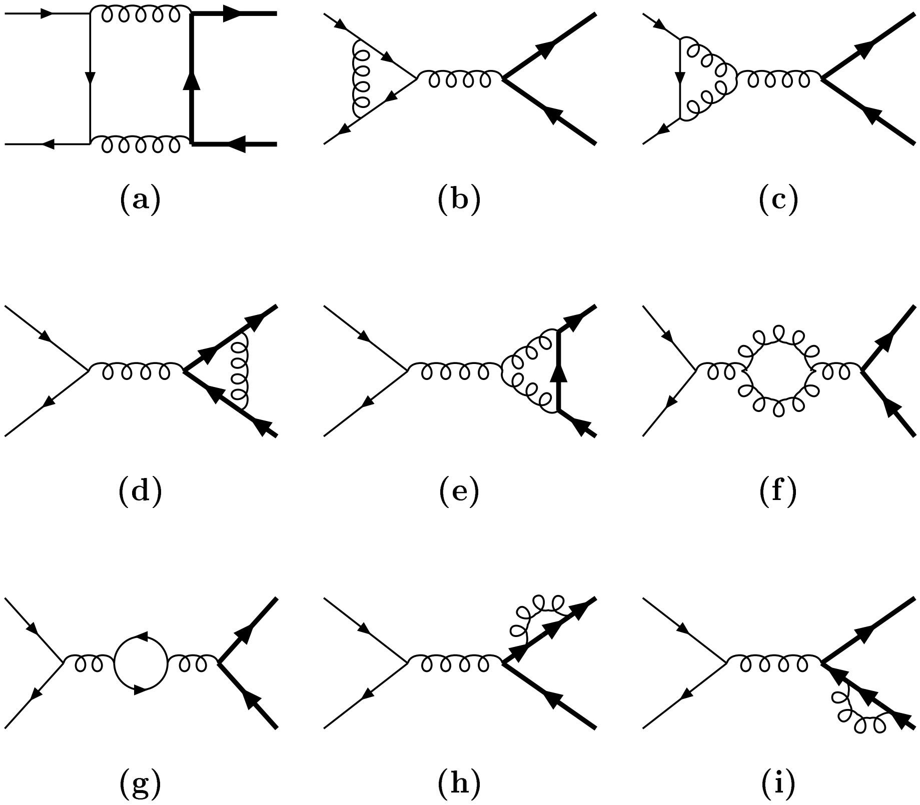

Figure 7.12: The NLO virtual corrections to $\vec{q}\,\vec{\bar{q}} \to Q\overline{Q}$. There are two additional diagrams, one is obtained from reversing the heavy quark lines of graph (a), the other from replacing the gluon loop of graph (f) by a ghost loop. The quark loop of graph (g) has to be computed for massless and massive quarks. Vanishing light quark self-energy loops on the incoming lines, see (3.3), are not shown.

Next we need to calculate the bremsstrahlung process

$$\vec{q}_j(k_1) + \vec{\bar{q}}_i(k_2) \to Q_k(p_1) + \overline{Q}_l(p_2) + g^a(k_3) \; . \tag{7.40}$$

The corresponding Feynman diagrams are shown in Fig. 7.13 and lead to a squared matrix element

$$|\tilde{M}_R|^2 = \widetilde{M_R M_R^*} = g^6 \frac{C_F}{4N_C} \left[2C_F \tilde{O}_{\text{QED}} + C_A \tilde{O}_{\text{OK}} \right] \; , \tag{7.41}$$

where we have again sorted according to the occurring color factors. We have calculated these graphs, but in the unpolarized case they can also be obtained from those for the $g\bar{q} \to Q\overline{Q}\bar{q}$ process, by crossing $k_3 \leftrightarrow -k_1$ and multiplying with (-1) for crossing a boson and fermion. By crossing and comparing graph by graph, we have a consistency check of our unpolarized results. The collinear pole part of the hard bremsstrahlung cross section

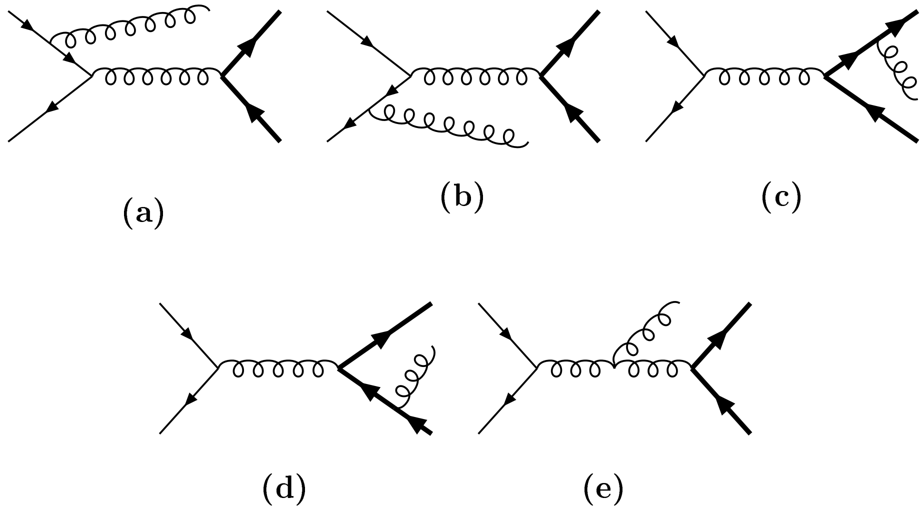

Figure 7.13: Feynman diagrams for the NLO gluon bremsstrahlung process $q\bar{q} \to Q\overline{Q}g$.

then becomes

$$\left(\frac{d^2\tilde{\sigma}^{(1)}_{q\bar{q},\mathrm{QED}}}{dt_1 du_1}\right)^H = \frac{C_F}{4N_C} 2C_F F_\varepsilon G^H_\varepsilon \alpha_s^3 \frac{2}{\varepsilon} \tilde{H}^{\mathrm{pole}}_{\mathrm{QED}} + \mathcal{O}(1) \,, \tag{7.42}$$

$$\begin{aligned} H^{\mathrm{pole}}_{\mathrm{QED}} &= -\frac{1}{t_1}\frac{1+x_1^2}{1-x_1}\left[\frac{t_1^2+(x_1u_1)^2}{(x_1 s)^2} + \frac{2m^2}{x_1 s}\right] \\ &\quad - \frac{1}{u_1}\frac{1+x_2^2}{1-x_2}\left[\frac{(x_2t_1)^2+u_1^2}{(x_2 s)^2} + \frac{2m^2}{x_2 s}\right] \,, \end{aligned} \tag{7.43}$$

$$\Delta H^{\mathrm{pole}}_{\mathrm{QED}} = -H^{\mathrm{pole}}_{\mathrm{QED}} \,. \tag{7.44}$$

where only the abelian "QED" part is shown, because the hard non-abelian "OK" part is completely finite. G^H_ε is defined in (6.5) and x_1, x_2 in (6.4). As expected, we find the form necessary for the mass factorization in (6.33), see the hard $\Theta(1-x-\delta)$ part of (6.34). The lengthy finite contributions can be found in our computer program, which is available upon request. Our unpolarized results agree with those of [45].

We can quickly derive the soft limits of the $\tilde{O}_{\mathrm{QED}}$ and $\tilde{O}_{\mathrm{OK}}$, as we did in the case of $\vec{\gamma}\vec{g}$ in (7.21) and (7.22)

$$\tilde{S}_{\mathrm{QED}} = \frac{8}{s_4^2}\left[\frac{s}{\underline{t'u'}} + \frac{2t_1}{\underline{s_3t'}} + \frac{2t_1}{\underline{u'}} - \frac{2u_1}{\underline{t'}} - \frac{2u_1}{\underline{s_3u'}} + \frac{s-2m^2}{\underline{s_3}} - \frac{m^2}{\underline{s_3}^2} - m^2\right]\tilde{A}_{\mathrm{QED}} \,, \tag{7.45}$$

$$\tilde{S}_{\mathrm{OK}} = \frac{8}{s_4^2}\left[-\frac{s}{\underline{t'u'}} - \frac{t_1}{\underline{s_3t'}} - \frac{t_1}{\underline{u'}} + \frac{2u_1}{\underline{t'}} + \frac{2u_1}{\underline{s_3u'}} - \frac{s-2m^2}{\underline{s_3}}\right]\tilde{A}_{\mathrm{QED}} \,, \tag{7.46}$$

in agreement with [45] in the unpolarized case. From them we derive the soft cross section, as for (7.23) and (7.24):

$$\left(\frac{d^2\tilde{\sigma}^{(1)}_{q\bar{q},\mathrm{QED}}}{dt_1du_1}\right)^S = \frac{C_F}{4N_C}2C_F F_\varepsilon G^S_\varepsilon \alpha_s^3 \tilde{A}_{\mathrm{QED}}\Bigg\{\frac{8}{\varepsilon^2}-\frac{4}{\varepsilon}+\frac{4}{\varepsilon}\ln\frac{sm^2}{t_1u_1}+\frac{16}{\varepsilon}\ln\frac{t_1}{u_1}+2 - 8\ln\varkappa\ln\frac{t_1}{u_1}+\ln^2\frac{sm^2}{t_1u_1}+2\,\mathrm{Li}_2\left(1-\frac{sm^2}{t_1u_1}\right)+8\,\mathrm{Li}_2\left(1-\frac{t_1}{\varkappa u_1}\right) - 8\,\mathrm{Li}_2\left(1-\frac{u_1}{\varkappa t_1}\right)+\frac{2(2m^2-s)}{s\beta}\left[\ln\varkappa - S(\varkappa)\right]\Bigg\}\delta(s_4)\,, \tag{7.47}$$

$$\left(\frac{d^2\tilde{\sigma}^{(1)}_{q\bar{q},\mathrm{OK}}}{dt_1du_1}\right)^S = \frac{C_F}{4N_C}C_A F_\varepsilon G^S_\varepsilon \alpha_s^3 \tilde{A}_{\mathrm{QED}}\Bigg\{-\frac{4}{\varepsilon}\ln\frac{sm^2}{t_1u_1}-\frac{12}{\varepsilon}\ln\frac{t_1}{u_1}-\ln^2\frac{sm^2}{t_1u_1}+6\ln\varkappa\ln\frac{t_1}{u_1} + \ln^2\frac{t_1}{u_1}-\ln^2\varkappa-2\,\mathrm{Li}_2\left(1-\frac{sm^2}{t_1u_1}\right)-6\,\mathrm{Li}_2\left(1-\frac{t_1}{\varkappa u_1}\right) + 6\,\mathrm{Li}_2\left(1-\frac{u_1}{\varkappa t_1}\right)+\frac{2(2m^2-s)}{s\beta}S(\varkappa)\Bigg\}\delta(s_4)\,, \tag{7.48}$$

where $S(\varkappa)$ and G^S_ε are defined in (7.25) and (7.26), respectively. $\tilde{A}_{\mathrm{QED}}$ is the LO expression of (2.30). Our unpolarized results for the soft bremsstrahlung cross section once more are identical to those of [45].

We now perform mass factorization for the hard H and the renormalized virtual plus soft $V+S$ part, keeping in mind to use (6.35) to guarantee helicity conservation. We can then split the $V+S$ part as

$$\left(\frac{d^2\hat{\tilde{\sigma}}^{(1)}_{q\bar{q}}}{dt_1du_1}\right)^{V+S} = \frac{\alpha_s^3}{s^2}\frac{C_F}{4N_C}\Big[2C_F\left(\tilde{K}_{\mathrm{QED}}+\tilde{K}^{\Delta}_{\mathrm{QED}}\right)+C_A\left(\tilde{K}_{\mathrm{OK}}+\tilde{K}^{\Delta}_{\mathrm{OK}}\right) + \tilde{K}_{\mathrm{QL}}+2\beta_0\tilde{K}_{\mathrm{RF}}\Big]\delta(s_4)\,, \tag{7.49}$$

where we have included the virtual quark loop contribution of (7.39) in the $\tilde{K}_{\mathrm{QL}}$ and explicitly separated out the part proportional to β_0, which corresponds to (7.8) and vanishes for $\mu_r=\mu_f$. The coefficients are given in App. C and are exactly equal in the unpolarized case to those found in App. A of [45]. Actually we show in App. C the *unpolarized* results, which then can be directly compared to the results of [45]. We find for our polarized results that as expected helicity conservation holds and thus the polarized coefficients are simply (-1) times the unpolarized ones[7]. We find that helicity conservation holds for the hard part as well after mass factorization. Thus our unpolarized *and* polarized H parts

[7]Helicity conservation requires for a quark-*anti*quark vertex that $|M|^2(++)=0$ and hence that $\overline{|M|}^2=-\Delta|M|^2$, see (2.10) and (2.11).

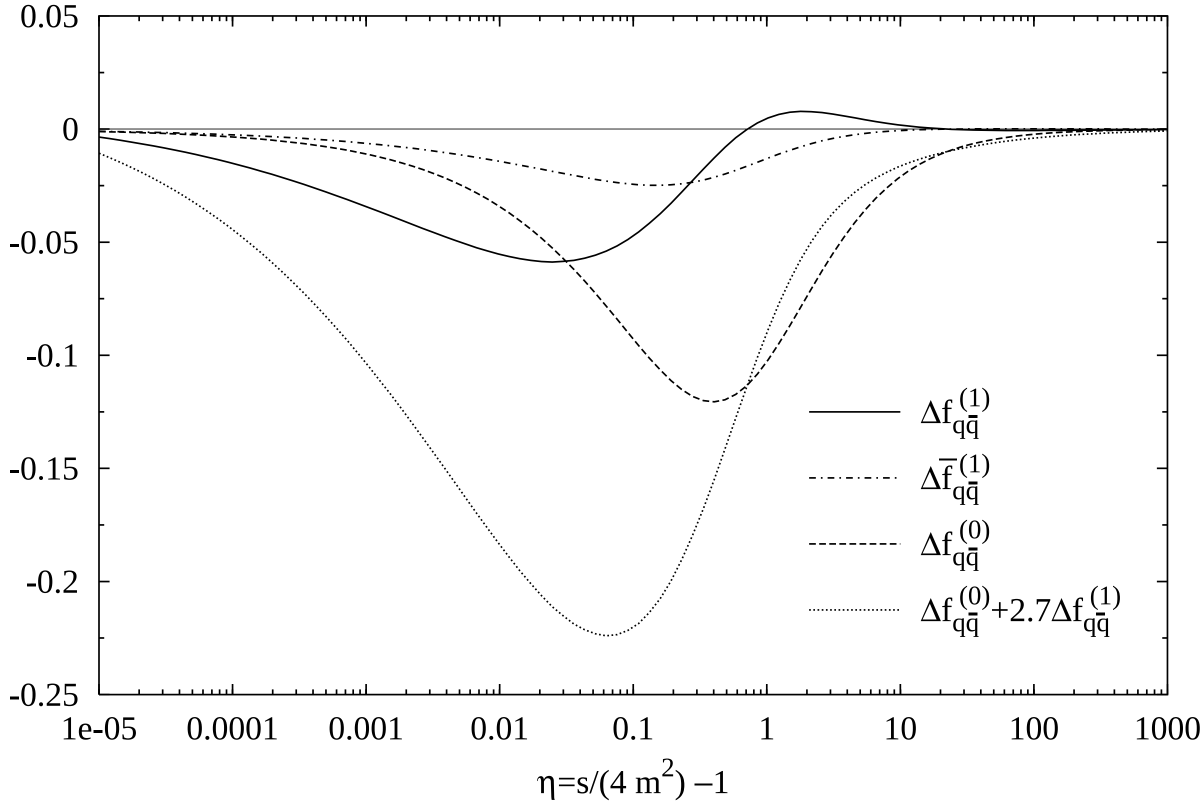

Figure 7.14: The polarized quark-antiquark scaling functions in LO $\Delta f^{(0)}_{q\bar{q}}$, and NLO $\Delta f^{(1)}_{q\bar{q}}$ and $\Delta \bar{f}^{(1)}_{q\bar{q}}$, in the $\overline{\mathrm{MS}}$ scheme as function of η. The quark loop contribution is included with the number of light flavors $n_{lf} = 3$. For comparison the effective NLO combination $\Delta f^{(0)}_{q\bar{q}} + 2.7\Delta f^{(1)}_{q\bar{q}}$ is also shown.

are equal to those of [45], with a sign for the polarized case. It is important to keep in mind though, that this would not have happened, if we had not corrected the helicity breaking of the HVBM γ_5 scheme [54] by using (6.35). Furthermore we would also not have obtained this result without calculating the hat momenta contributions, which happen to be equal to one half the HVBM corrections.

We can of course again extract scaling functions from our results according to (7.2). Note that we enforce (7.8), i.e., the only dependence on the renormalization scale apart from $\alpha_s(\mu_r^2)$ is due to a logarithm $\ln(\mu_r^2/\mu_f^2)$. So $\ln(\mu_r^2/m^2)$ terms from $\tilde{K}_{\mathrm{OK}}$ and $\tilde{K}_{\mathrm{QL}}$ are changed to $\ln(\mu_f^2/m^2)$ and the additional $\tilde{K}_{\mathrm{RF}}$ collects the $\ln(\mu_r^2/\mu_f^2)$ pieces to keep the sum unchanged. This means $\tilde{\bar{f}}^{(1)}_{q\bar{q}}$ multiplying $\ln(\mu_f^2/m^2)$ receives additional contributions when requiring (7.8). We plot the polarized scaling functions in Fig. 7.14. Apart from extending the η-range and having a sign due to helicity conservation, this plot does not exactly reproduce Fig. 5 of [45], though the differences, which occur in the medium η range, are small. The reason is that when one includes the quark loop contributions

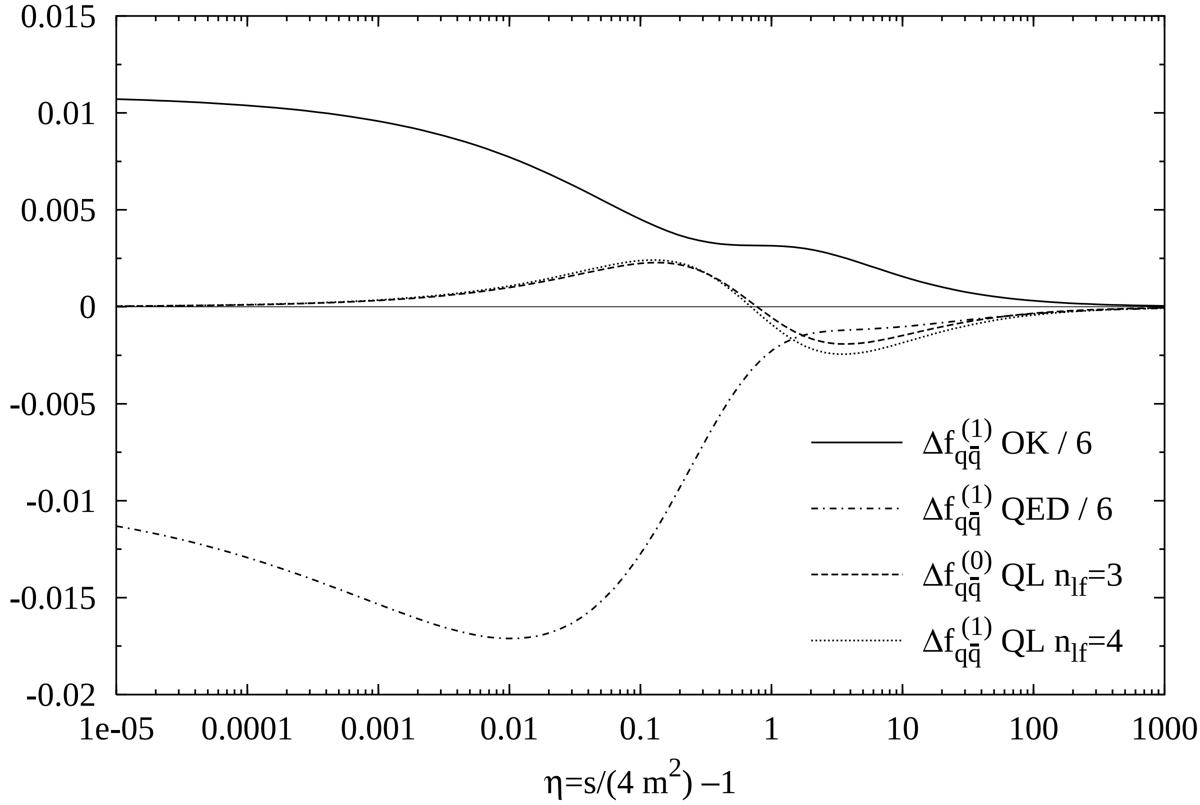

Figure 7.15: The non-abelian (OK), abelian (QED), and quark loop (QL) parts of the NLO polarized scaling function $\Delta f^{(1)}_{q\bar{q}}$ in the $\overline{\mathrm{MS}}$ scheme as function of η. The quark loop contribution is shown for three and four light flavors n_{lf}, and the OK and QED scaling functions have been divided by six. OK+QED+QL($n_{lf}=3$) will give the $\Delta f^{(1)}_{q\bar{q}}$ of Fig. 7.14.

$\tilde{K}_{\mathrm{QL}}$, one has to specify the number of light flavors n_{lf}. We have chosen $n_{lf}=3$ with charm production in mind, whereas the authors of [45] have chosen $n_{lf}=4$. Thus there are slight differences in the soft plus virtual parts, which disappear when we also set $n_{lf}=4$. We have again plotted the "effective" NLO combination for charm production $\Delta f^{(0)}_{q\bar{q}} + 2.7\Delta f^{(1)}_{q\bar{q}}$, which gives an estimate of the total scaling function at NLO with $4\pi\alpha_s(m_c^2) \simeq 2.7$. We see that the NLO contributions strongly dominate towards threshold $\eta \to 0$. Again this comes about on one hand because of a Coulomb singularity yielding a constant at threshold in the $S+V$ part, see Fig. 7.12 (d), and on the other hand because of soft gluon emission left-overs in the hard part, see Fig. 7.13. There are no flavor excitation graphs in this process, so we do not find an enhancement at $\eta \to \infty$. Note that the NLO part $\Delta f^{(1)}_{q\bar{q}}$ changes sign in the η range of approximately 0.7 to 20. Thus the effective NLO combination (dotted line) is above the LO result (dashed line) in that region. Concerning hadronic cross sections at RHIC [32] with $\sqrt{S}=200$ GeV and $m_c=1.5$ GeV, we find $x_{\min}=2.25\cdot 10^{-4}$. So using (7.29) we get for the product x_1x_2, which replaces the single x of photoproduction, $3.8 \cdot 10^{-4}$ to $4.5 \cdot 10^{-3}$ in this η range. Thus we can expect significant contributions from this region.

Finally, in Fig. 7.15 we show $\Delta f_{q\bar{q}}^{(1)}$ split according to its color-structure. The sum of the non-abelian, abelian and quark loop contributions gives back $\Delta f_{q\bar{q}}^{(1)}$, see (7.41) and (7.49). To make the small quark loop parts more visible, we have divided the other contributions by a factor six in the plot. We see once more the strong cancellations between the "OK" and "QED" parts. But even their sum dominates over the "QL" contribution for $\eta \lesssim 0.4$, there the ratio "QL/(OK+QED)" is below 10%. At threshold we find $\Delta f_{q\bar{q}}^{(1)} = -\frac{C_F}{4N_C}(2C_F - C_A)\frac{\pi}{16}$. The "QL" part is shown for three and four light flavors and we see that the changes introduced by adding one light flavor are small, and will mainly be felt in the medium η range. Finally we would like to mention that we can again obtain the results for the production of a heavy quark instead of a heavy antiquark by switching $p_1 \leftrightarrow p_2$. In this case it is however easier to use charge conjugation

$$\frac{d^2\hat{\tilde{\sigma}}}{dt_1 du_1}\left(q\bar{q} \to \overline{Q}\right) = \frac{d^2\hat{\tilde{\sigma}}}{dt_1 du_1}\left(\bar{q}q \to Q\right) \quad \text{and} \quad \frac{d^2\hat{\tilde{\sigma}}}{dt_1 du_1}\left(q\bar{q} \to Q\right) = \frac{d^2\hat{\tilde{\sigma}}}{dt_1 du_1}\left(\bar{q}q \to \overline{Q}\right)\ , \tag{7.50}$$

and additionally $k_1 \leftrightarrow k_2$ or equivalently $t_1 \leftrightarrow u_1$, which crosses the initial states $q\bar{q} \leftrightarrow \bar{q}q$. So in this case one obtains the corresponding heavy quark production expressions by interchanging $t_1 \leftrightarrow u_1$, with t_1 and u_1 now referring to the heavy quark [45]. Naturally we can also derive the results for a light antiquark instead of a light quark as parton for one hadron and vice versa for the other hadron by using $k_1 \leftrightarrow k_2$ ($t_1 \leftrightarrow u_1$) [45].

7.4 Gluon-Gluon Scaling Functions

The final subprocesses we have to calculate for hadroproduction are the NLO corrections to gluon-gluon fusion

$$\vec{g}^{\,a}(k_1) + \vec{g}^{\,b}(k_2) \to Q_i(p_1) + \overline{Q}_j(p_2)\ . \tag{7.51}$$

The virtual corrections, with the same external momentum and color assignment as in LO (7.51), are computed with the $2 \to 2$ phase space (2.24), and are displayed in Fig. 7.16. We can again split the squared matrix element according to color factors

$$|\tilde{M}|^2_{VB} = 2\mathrm{Re}\left(\widetilde{M_V M_B^*}\right) = E_\varepsilon^2\, g^6 \frac{1}{2(N_C^2-1)}\left[(2C_F)^2\tilde{U}_{\mathrm{QED}} + C_A^2\tilde{U}_{\mathrm{OQ}} + \tilde{U}_{KQ} + C_A\tilde{U}_{\mathrm{QL}}\right]\ , \tag{7.52}$$

where the "abelian" $\tilde{U}_{\mathrm{QED}}$ is connected to $\tilde{V}_{\mathrm{QED}}$ of (7.15) with the usual factor $1/(2N_C)$ for replacing a photon by a gluon. $\tilde{U}_{\mathrm{QL}}$ only receives contributions from the quark loops. The other two collect "non-abelian" contributions. Compared to Eq. (3.3) in [44], we have averaged over color and chosen a slightly different way of splitting the results according

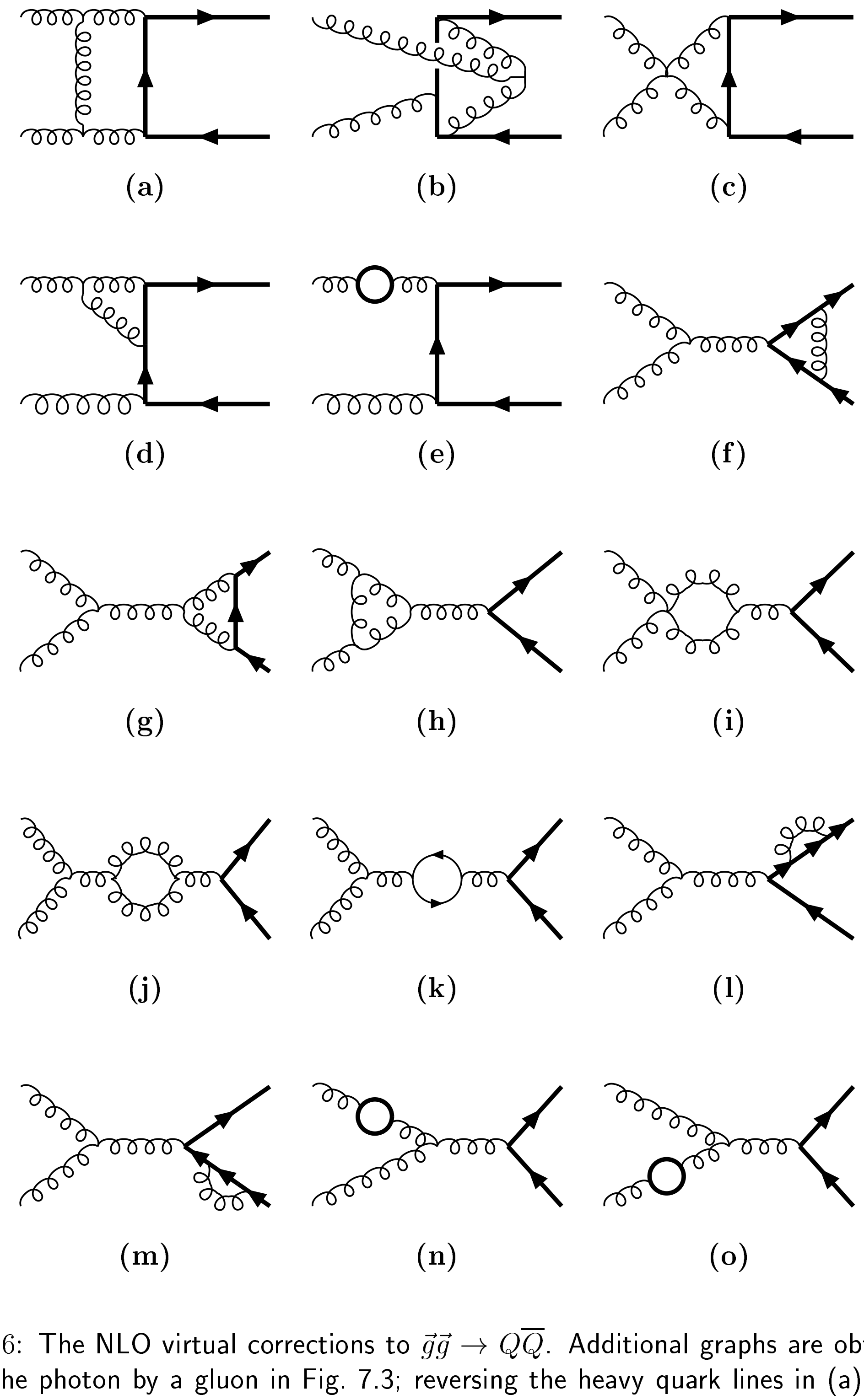

Figure 7.16: The NLO virtual corrections to $\vec{g}\vec{g} \to Q\overline{Q}$. Additional graphs are obtained by: replacing the photon by a gluon in Fig. 7.3; reversing the heavy quark lines in (a), (d), and (e); and setting the loop particle to a (heavy) quark and ghost in (h), a ghost in (j) and a heavy quark in (k). Massless particle loops similar to graph (e), (n) and (o) vanish, see (3.3).

to color. Also we already include a factor 1/4 for spin-averaging in the unpolarized and as a convention in the polarized case. Taking all this into account, for comparisons with [44] one should use

$$\begin{aligned} U_{\rm QED} &= \frac{1}{2} V_{\rm QED}^{\rm BKNS} \,, & U_{\rm OQ} &= \frac{1}{2} (V_{\rm O}^{\rm BKNS} - V_{\rm QED}^{\rm BKNS}) \,, \\ U_{\rm KQ} &= \frac{1}{2} (V_{\rm K}^{\rm BKNS} + 3 V_{\rm QED}^{\rm BKNS}) \,, & U_{\rm QL} &= \frac{1}{2} V_{\rm f}^{\rm BKNS} \,, \end{aligned} \tag{7.53}$$

where the coefficients marked "BKNS" are those of [44]. Note that due to our "ghost trick", see Fig. 2.1 and App. B.4, for the diagram structures (a), (f), (g), (h), (j), (l) and (m) in Fig. 7.16, there are also diagrams with incoming ghosts to be considered, which are not shown. We postpone further discussion of the virtual results, and examine first the bremsstrahlung reactions.

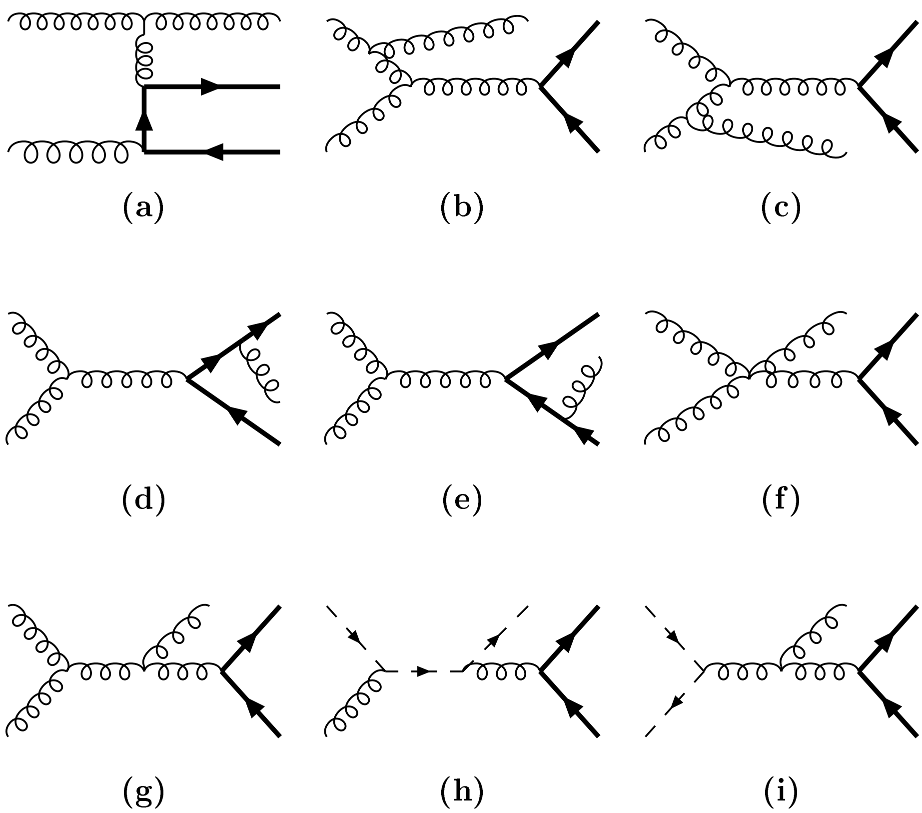

Figure 7.17: Feynman diagrams for the NLO gluon bremsstrahlung process $\vec{g}\vec{g} \to Q\overline{Q}g$. Replacing the photon by a gluon in Fig. 7.4 and reversing the heavy quark lines of (a) yields the remaining graphs. Many initial to final or initial to initial ghost contributions, for example (h) and (i), have to be subtracted in the unpolarized case to cancel unphysical polarization contributions, compare Fig. 2.1 and App. B.4.

The bremsstrahlung diagrams are presented in Fig. 7.17 and we assign color and momentum according to

$$\vec{g}^{\,a}(k_1) + \vec{g}^{\,b}(k_2) \to Q_i(p_1) + \overline{Q}_j(p_2) + g^c(k_3)\ . \tag{7.54}$$

Note that we have this time external ghost graphs both for replacing two initial gluons and for replacing one initial and one final state gluon. There is a similar color split for the squared matrix element

$$|\tilde{M}_R|^2 = \widetilde{M_R M_R^*} = E_\varepsilon^2\, g^6 \frac{1}{2(N_C^2-1)} \left[(2C_F)^2 \tilde{D}_{\rm QED} + C_A^2 \tilde{D}_{\rm OQ} + \tilde{D}_{KQ}\right]\ , \tag{7.55}$$

and compared to the R_i in Eq. (4.4) of [44] analogous relations as in (7.53) apply. The collinear pole part of the hard gluon-gluon cross section then becomes

$$\left(\frac{d^2\tilde{\sigma}^{(1)}_{gg,\rm OQ}}{dt_1 du_1}\right)^H = \frac{C_A^2}{2(N_C^2-1)} F_\varepsilon G_\varepsilon^H E_\varepsilon^2 \alpha_s^3 \frac{2}{\varepsilon}\left[(1-H_{\rm L1})\tilde{H}^{\rm pole}_{\rm OK1} + (1-H_{\rm L2})\tilde{H}^{\rm pole}_{\rm OK2}\right] + \mathcal{O}(1)\ , \tag{7.56}$$

$$\left(\frac{d^2\tilde{\sigma}^{(1)}_{gg,\rm KQ}}{dt_1 du_1}\right)^H = -\frac{1}{2(N_C^2-1)} F_\varepsilon G_\varepsilon^H E_\varepsilon^2 \alpha_s^3 \frac{2}{\varepsilon}\left[\tilde{H}^{\rm pole}_{\rm OK1} + \tilde{H}^{\rm pole}_{\rm OK2}\right] + \mathcal{O}(1)\ , \tag{7.57}$$

$$H_{\rm L1} = \frac{2t_1(x_1u_1)}{(x_1s)^2}\ , \qquad H_{\rm L2} = \frac{2(x_2t_1)u_1}{(x_2s)^2}\ , \tag{7.58}$$

$$\begin{aligned} H^{\rm pole}_{\rm OK1} &= -\frac{1}{t_1}\left[\frac{1}{1-x_1} + \frac{1}{x_1} - 2 - x_1(1-x_1)\right] \\ &\quad \cdot \left\{\frac{t_1}{x_1u_1} + \frac{x_1u_1}{t_1} + \frac{4m^2(x_1s)}{t_1(x_1u_1)}\left[1 - \frac{m^2(x_1s)}{t_1(x_1u_1)}\right]\right\}\ , \end{aligned} \tag{7.59}$$

$$\Delta H^{\rm pole}_{\rm OK1} = -\frac{1}{t_1}\left(\frac{1}{1-x_1} - 2x_1 + 1\right)\left(\frac{t_1}{x_1u_1} + \frac{x_1u_1}{t_1}\right)\left[\frac{2m^2(x_1s)}{t_1(x_1u_1)} - 1\right]\ ,$$

$$\begin{aligned} H^{\rm pole}_{\rm OK2} &= -\frac{1}{u_1}\left[\frac{1}{1-x_2} + \frac{1}{x_2} - 2 - x_2(1-x_2)\right] \\ &\quad \cdot \left\{\frac{x_2t_1}{u_1} + \frac{u_1}{x_2t_1} + \frac{4m^2(x_2s)}{(x_2t_1)u_1}\left[1 - \frac{m^2(x_2s)}{(x_2t_1)u_1}\right]\right\}\ , \end{aligned} \tag{7.60}$$

$$\Delta H^{\rm pole}_{\rm OK2} = -\frac{1}{u_1}\left(\frac{1}{1-x_2} - 2x_2 + 1\right)\left(\frac{x_2t_1}{u_1} + \frac{u_1}{x_2t_1}\right)\left[\frac{2m^2(x_2s)}{(x_2t_1)u_1} - 1\right]\ ,$$

and the "QED" part is completely finite. G_ε^H is defined in (6.5) and x_1, x_2 in (6.4). We have written the results in a form which is easily comparable with the mass factorization formula (6.30). To this end note that $2C_FC_A = C_A^2 - 1$. Our unpolarized results agree[8]

[8] The comparison is somewhat protracted, since they do not bring the result in a simple "factorization" form. Replacing $s + t_1 \to -u_1/x_2$ in their expressions helps to disentangle the terms.

with those of [44]. The finite results are too long to be quoted here, but can be found in our computer program.

We take the soft limit of the matrix elements in (7.55) and find

$$\tilde{S}_{\mathrm{QED}} = -\frac{2}{s_4^2}\left[m^2 + \frac{m^2}{\underline{s_3}^2} + \frac{2m^2-s}{\underline{s_3}}\right]\tilde{B}_{\mathrm{QED}}\ , \tag{7.61}$$

$$\tilde{S}_{\mathrm{OQ}} = \frac{2}{s_4^2}\Bigg[\frac{2m^2-s}{\underline{s_3}} + \frac{t_1^2+u_1^2}{s\underline{t'}\underline{u'}} + \frac{2m^2 t_1 u_1}{s^2}\left(1+\frac{1}{\underline{s_3}^2}\right) + \frac{t_1^2 u_1}{s^2}\left(\frac{1}{\underline{t'}} + \frac{1}{\underline{s_3}\underline{u'}}\right)$$
$$+ \frac{t_1 u_1^2}{s^2}\left(\frac{1}{\underline{u'}} + \frac{1}{\underline{s_3}\underline{t'}}\right)\Bigg]\tilde{B}_{\mathrm{QED}}\ , \tag{7.62}$$

$$\tilde{S}_{\mathrm{KQ}} = -\frac{2}{s_4^2}\Bigg[\frac{2(2m^2-s)}{\underline{s_3}}\left(1+\frac{t_1u_1}{s^2}\right) + \frac{2m^2 t_1 u_1}{s^2}\left(1+\frac{1}{\underline{s_3}^2}\right) + t_1\left(\frac{1}{\underline{u'}} + \frac{1}{\underline{s_3}\underline{t'}}\right)$$
$$+ u_1\left(\frac{1}{\underline{t'}} + \frac{1}{\underline{s_3}\underline{u'}}\right)\Bigg]\tilde{B}_{\mathrm{QED}}\ . \tag{7.63}$$

Using relations analogous to (7.53), we find that these limits are indeed equal to those found in [44] for the unpolarized case.

From these soft matrix elements we can directly derive the soft cross sections as before, and obtain

$$\left(\frac{d^2\tilde{\sigma}^{(1)}_{gg,\mathrm{QED}}}{dt_1du_1}\right)^S = \frac{(2C_F)^2}{2(N_C^2-1)}F_\varepsilon G_\varepsilon^S E_\varepsilon^2 \alpha_s^3 \frac{\tilde{B}_{\mathrm{QED}}}{2}\left\{-\frac{2}{\varepsilon} + 1 + \frac{2m^2-s}{s\beta}\left[\ln\varkappa - S(\varkappa)\right]\right\}\delta(s_4)\ , \tag{7.64}$$

$$\left(\frac{d^2\tilde{\sigma}^{(1)}_{gg,\mathrm{OQ}}}{dt_1du_1}\right)^S = \frac{C_A^2}{2(N_C^2-1)}F_\varepsilon G_\varepsilon^S E_\varepsilon^2 \alpha_s^3 \frac{\tilde{B}_{\mathrm{QED}}}{2}\Bigg\{\frac{2t_1u_1}{s^2}\left(\frac{2}{\varepsilon}-1\right) + \left(1-\frac{2t_1u_1}{s^2}\right)$$
$$\cdot\left[\frac{8}{\varepsilon^2} + \frac{2}{\varepsilon}\ln\frac{m^2 s}{t_1u_1} + \frac{1}{2}(\ln^2\frac{m^2s}{t_1u_1} + \ln^2\frac{t_1}{u_1} - \ln^2\varkappa) + \mathrm{Li}_2\left(1-\frac{m^2s}{t_1u_1}\right)\right]$$
$$+ \frac{t_1^2-u_1^2}{s^2}\left[\ln\frac{t_1}{u_1}\left(-\frac{2}{e} + \ln\varkappa\right) - \mathrm{Li}_2\left(1-\frac{t_1}{u_1\varkappa}\right) + \mathrm{Li}_2\left(1-\frac{u_1}{t_1\varkappa}\right)\right]$$
$$- \frac{2m^2-s}{s\beta}\left[\frac{2t_1u_1}{s^2}\ln\varkappa - S(\varkappa)\right]\Bigg\}\delta(s_4)\ , \tag{7.65}$$

$$\left(\frac{d^2\tilde{\sigma}^{(1)}_{gg,\mathrm{KQ}}}{dt_1du_1}\right)^S = \frac{C_A^2}{2(N_C^2-1)}F_\varepsilon G_\varepsilon^S E_\varepsilon^2 \alpha_s^3 \frac{\tilde{B}_{\mathrm{QED}}}{2}\Bigg\{-\frac{8}{\varepsilon^2} - \frac{2t_1u_1}{s^2}\left(\frac{2}{\varepsilon}-1\right) - \ln^2\frac{t_1}{u_1}$$
$$+ \ln^2\varkappa - \frac{2(2m^2-s)}{s\beta}\left[-\frac{t_1u_1}{s^2}\ln\varkappa + \left(1+\frac{t_1u_1}{s^2}\right)S(\varkappa)\right]\Bigg\}\delta(s_4)\ , \tag{7.66}$$

where $S(\varkappa)$ and G_ε^S are defined in (7.25) and(7.26), respectively. Our unpolarized results agree[9] with those of [44]. We see comparing (7.61) and (7.64) with (7.21) and (7.23), that the "QED" part of the gluon-gluon partonic cross section is indeed just $1/(2N_C)$ of the "QED" part of the photon-gluon one. So our choice is "natural" concerning the color-factor of the "QED" part, since we get the usual factor for replacing a photon by a gluon.

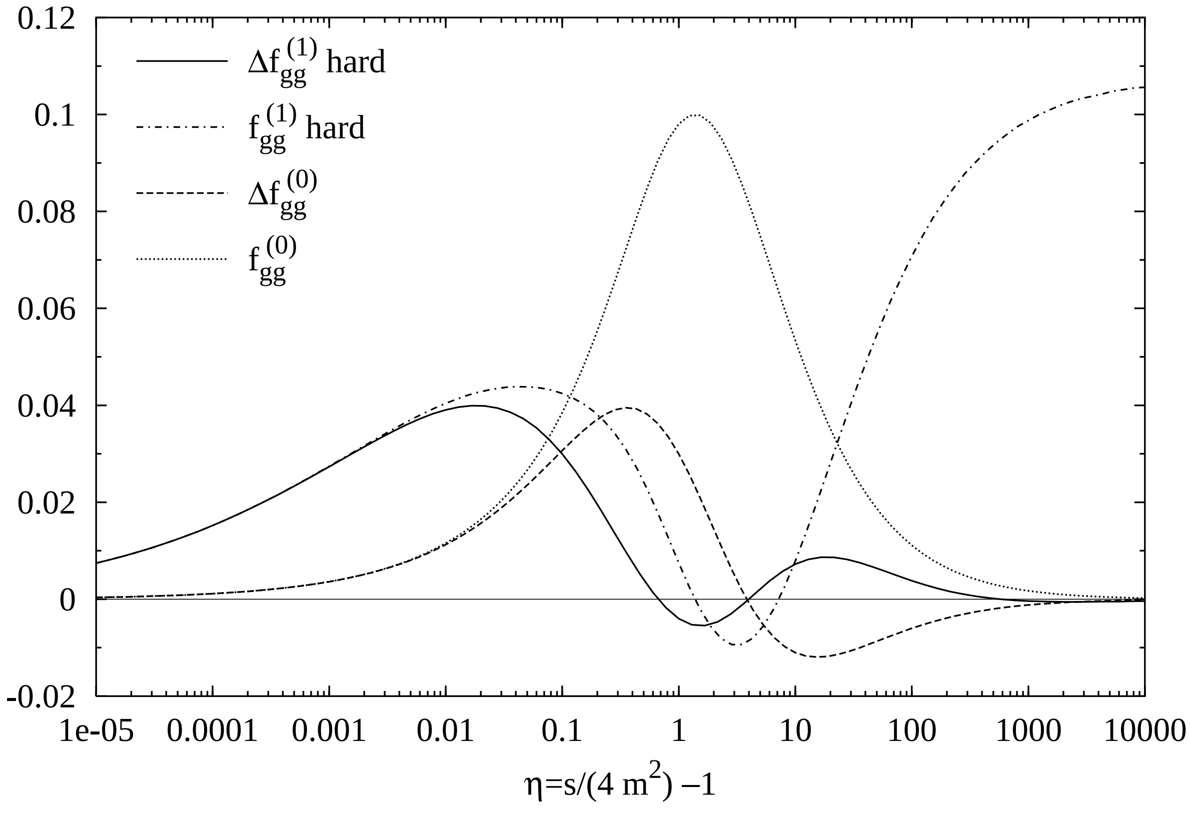

Figure 7.18: The hard $(H + \Delta)$ part of the NLO polarized and unpolarized scaling functions $\Delta f_{gg}^{(1)}$ and $f_{gg}^{(1)}$, respectively, in the $\overline{\mathrm{MS}}$ scheme as function of η. For comparison the LO polarized and unpolarized scaling functions $\Delta f_{gg}^{(0)}$ and $f_{gg}^{(0)}$, respectively, are also shown.

Now we should combine the virtual and soft cross sections. However, though the matrix elements and tensor integrals have been calculated, we have not yet combined the virtual results. This will be done in a later publication. For the time being we will just take the $\ln(\Delta/m^2)$ parts of the soft cross sections (7.64) to (7.66) and add them to the reduced hard parts after mass factorization. This way we can already present the "hard" part of the $\tilde{f}_{gg}^{(1)}$ coefficient functions in Fig. 7.18. There the solid line shows the "hard" part of the polarized scaling function $\Delta f_{gg}^{(1)}$, and the dot-dashed line displays

[9]It is useful to note that their color-factor $K\bar{C}_{\mathrm{QED}} = 2[(2C_F)^2 - C_A^2 + 3]/[2(N_C^2 - 1)]$.

the corresponding unpolarized scaling function $f_{gg}^{(1)}$. For comparison we also plot the dashed and dotted curves, displaying the polarized $\Delta f_{gg}^{(0)}$ and unpolarized $f_{gg}^{(0)}$ LO scaling functions, respectively. We see that the situation is very similar to the γg case concerning the threshold and high energy limits. But here the NLO corrections are even larger, in particular at high energies. The corresponding heavy quark production expressions have the same form, but with t_1 and u_1 referring to the heavy quark, since the squared matrix elements are $p_1 \leftrightarrow p_2$ symmetric [43]. We postpone further discussions of the gg scaling functions till the time when the virtual plus soft part and hence the complete result is available.

Chapter 8

Hadron Level Results

8.1 Hadronic Cross Sections

Let us first of all recall the relevant formulae for calculating differential single-inclusive heavy (anti)quark distributions. We denote the momenta in the heavy (anti)quark production cross section of a hadron of type a with a hadron of type b by

$$H^a(K_1) + H^b(K_2) \to \overline{Q}(p_2)\,[Q(p_1)] + X \;, \tag{8.1}$$

and use the following hadronic invariants for the observed heavy *anti*quark

$$\begin{aligned} S &\equiv (K_1 + K_2)^2 && \text{with} \quad s = (x_1 K_1 + x_2 K_2)^2 = x_1 x_2 S \;, \\ T_1 &\equiv (K_2 - p_2)^2 - m^2 && \text{with} \quad t_1 = (x_2 K_2 - p_2)^2 - m^2 = x_2 T_1 \;, \\ U_1 &\equiv (K_1 - p_1)^2 - m^2 && \text{with} \quad u_1 = (x_1 K_1 - p_1)^2 - m^2 = x_1 U_1 \;, \end{aligned} \tag{8.2}$$

where we have introduced the momentum fractions x_1 in $k_1 = x_1 K_1$ and x_2 in $k_2 = x_2 K_2$ to relate the hadronic to the partonic variables in (2.18), thus $K_1^2 = K_2^2 = 0$. For an observed heavy *quark* one would set $p_1 \to p_2$ in (8.2). Thus the hadronic and partonic Mandelstam variables are always defined with respect to the *observed* heavy (anti)quark. How one can obtain the reduced partonic cross sections for heavy quark instead of heavy antiquark production has been discussed for each subprocess individually in Chap. 7.

We have in the hadronic cross section formula (6.21) the conditions $0 \le x_1, x_2 \le 1$. But we know that

$$s_4 = s + t_1 + u_1 = x_1 x_2 S + x_1 T_1 + x_2 U_1 \overset{!}{\ge} \Delta \;, \tag{8.3}$$

where $\Delta > 0$ only for the "hard" parts and zero otherwise. Hence we can derive lower limits from the process kinematics

$$\frac{d\tilde{\sigma}^{ab}(K_1, K_2)}{dT_1 dU_1} = \sum_{l,m} \int_{x_1^{\min}}^1 dx_1 \int_{x_2^{\min}}^1 dx_2 \; x_1 \tilde{f}_l^a(x_1, \mu_f^2)\; x_2 \tilde{f}_m^b(x_2, \mu_f^2)\; \frac{d\hat{\tilde{\sigma}}_{lm}(x_1 K_1, x_2 K_2)}{dt_1 du_1} \;, \tag{8.4}$$

with

$$x_1^{\min} = -\frac{T_1}{S+U_1} \; , \qquad \text{and} \qquad x_2^{\min} = \frac{\Delta - x_1 U_1}{x_1 S + T_1} \; , \tag{8.5}$$

and $\Delta = 0$ in (8.5) except for the "hard" parts of the cross section[1]. Note that the extra factor $x_1 x_2$ on the r.h.s. in comparison to (6.21) comes from $dt_1 du_1 = x_1 x_2 dT_1 dU_1$. $2 \to 2$ partonic cross sections (Born, virtual and soft ones) have a factor $\delta(s + t_1 + u_1) = \delta(x_1 x_2 S + x_2 T_1 + x_1 U_1)$, so then (8.4) becomes

$$\frac{d\tilde{\sigma}^{ab}(K_1,K_2)}{dT_1 dU_1} = \sum_{l,m} \int_{x_1^{\min}}^1 \frac{dx_1}{x_1 S + T_1} x_1 \tilde{f}_l^a(x_1,\mu_f^2)\; x_2^{\min} \tilde{f}_m^b(x_2^{\min},\mu_f^2)\; \frac{d\hat{\tilde{\sigma}}_{lm}^{2\to 2}(x_1 K_1, x_2^{\min} K_2)}{dt_1 du_1} \; , \tag{8.6}$$

with $\Delta = 0$ in $x_2^{\min}$. For the hard $2 \to 3$ parts it is advantageous to change the inner integration variable $x_2 \to s_4$, then we have

$$\begin{aligned} \frac{d\tilde{\sigma}^{ab}(K_1,K_2)}{dT_1 dU_1} = \sum_{l,m} \int_{x_1^{\min}}^1 \frac{dx_1}{x_1 S + T_1} x_1 \tilde{f}_l^a(x_1,\mu_f^2) \\ \cdot \int_{\Delta}^{s_4^{\max}} ds_4 \; x_2' \tilde{f}_m^b(x_2',\mu_f^2)\; \frac{d\hat{\tilde{\sigma}}_{lm}^{2\to 3}(x_1 K_1, x_2' K_2)}{dt_1 du_1} \; , \end{aligned} \tag{8.7}$$

with

$$x_2' = \frac{s_4 - x_1 U_1}{x_1 S + T_1} \qquad \text{and} \qquad s_4^{\max} = x_1 S + T_1 + x_1 U_1 \; . \tag{8.8}$$

Note the common factor $1/(x_1 S + T_1)$ in (8.6) and (8.7). Written this way, it is obvious that (8.6) is the $s_4 \to 0$ limit of (8.7). Also we can easily see how $2 \to 2$ processes can be included in the $2 \to 3$ integration of (8.7) by using (5.67) for the partonic cross sections and $x_2' \to x_2^{\min}(\Delta = 0)$ in $x_2' \tilde{f}_m^b(x_2',\mu_f^2)$.

To obtain the integration limits for the total hadronic cross section, we can proceed like for the derivation of the limits for the partonic cross sections, see the discussion leading to (7.2). We just have to replace the s, t_1, u_1 by their hadronic counterparts S, T_1, U_1 and so the result is

$$\begin{aligned} \tilde{\sigma}^{ab}(S,m^2) &= \int_{\frac{S}{2}(1-\beta_S)}^{\frac{S}{2}(1+\beta_S)} d(-T_1) \int_{-\frac{m^2 S}{T_1}}^{S+T_1} d(-U_1)\; \frac{d^2\tilde{\sigma}^{ab}(S,T_1,U_1)}{dT_1 dU_1} \\ &= \sum_{l,m} \int_{x_{\min}}^1 dx_1 \int_{\frac{x_{\min}}{x_1}}^1 dx_2\; \tilde{f}_l^a(x_1,\mu_f^2)\; \tilde{f}_m^b(x_2,\mu_f^2)\; \hat{\tilde{\sigma}}_{lm}(x_1 x_2 S, m^2) \; , \end{aligned} \tag{8.9}$$

[1] The tilde notation refers here, as throughout the text, to both the polarized case, $\tilde{a} \to \Delta a$, and the unpolarized case, $\tilde{a} \to a$.

$$\beta_S = \sqrt{1 - \frac{4m^2}{S}} \ , \qquad x_{\min} = \frac{4m^2}{S} = 1 - \beta_S^2 \ , \tag{8.10}$$

where the $\hat{\hat{\sigma}}_{lm}$ are the total partonic cross section of (7.2). The second line of (8.9) follows from inserting (8.4) and reshuffling the integrations. In the case of "direct" photoproduction we can insert

$$f_\gamma^\gamma(x_1, \mu_f^2) = \delta(1 - x_1) \ , \tag{8.11}$$

in the formulae (8.4) to (8.9) we have just derived, see the discussion leading to (6.26), which immediately yields simpler formulae by collapsing the x_1-integration to $x_1 = 1$.

The differential heavy (anti)quark cross section (8.4) should be expressed in variables more suited for experimental measurements:

$$\begin{aligned} \text{transverse momentum/mass}: \quad & x_T \equiv \frac{p_T}{p_T^{\max}} \ , \qquad m_T^2 \equiv m^2 + p_T^2 \overset{\text{hCMS}}{=} \frac{T_1 U_1}{S} \ , \\ \text{rapidity}: \quad & y \equiv \operatorname{artanh} \frac{p_L}{E} \overset{\text{hCMS}}{=} \frac{1}{2} \ln \frac{U_1}{T_1} \ , \\ \text{Feynman} - x: \quad & x_F \equiv \frac{p_L}{p_L^{\max}} \overset{\text{hCMS}}{=} \frac{1}{\beta_S} \frac{T_1 - U_1}{S} \ , \end{aligned} \tag{8.12}$$

where the relations to invariant hadronic Mandelstam variables (8.2) are valid in the hadronic center of mass system (hCMS). The energy and the longitudinal momentum of the heavy antiquark are given by $E = m_T \cosh y$ and $p_L = m_T \sinh y$, respectively. $p_T = |\vec{p}_T|$ is the absolute size of the transverse momentum and

$$p_T^{\max} = p_L^{\max} = \frac{\sqrt{S}\beta_S}{2} \ . \tag{8.13}$$

y and x_F of the observed $\overline{Q}$ in (8.12) are defined in the hCMS with the forward direction $(y, x_F > 0)$ along the incoming particle with K_1 (the photon in photoproduction), i.e.,

$$\begin{aligned} T_1 &= -\sqrt{S} m_T e^{-y} = -\sqrt{S} p_L^{\max} (\chi - x_F) \ , \\ U_1 &= -\sqrt{S} m_T e^{y} = -\sqrt{S} p_L^{\max} (\chi + x_F) \ , \end{aligned} \tag{8.14}$$

where $\chi \equiv \sqrt{x_F^2 + (m_T/p_L^{\max})^2}$. Under a boost in the direction of the unit vector $\vec{e}_L$ with $p_L = \vec{p} \cdot \vec{e}_L$ to a frame K^* with velocity β^*, $p_T^* = p_T$ is of course invariant and $y^* = y - \operatorname{artanh} \beta^*$. Hence also the *shape* of a rapidity distribution $df(y^*)/dy^* = df(y)/dy$ remains *unchanged* by such a boost.

The Jacobians needed to express (8.4) in the variables (8.12) are

$$dT_1 dU_1 = S dm_T^2 dy = \frac{S}{\chi} dm_T^2 dx_F \ , \tag{8.15}$$

and $dm_T^2 = 2x_T(p_T^{\max})^2 dx_T$, etc. By integrating the variables in (8.12) over the appropriate limits

$$S \int_{m^2}^{S/4} dm_T^2 \int_{-\operatorname{arcosh}\frac{\sqrt{S}}{2m_T}}^{\operatorname{arcosh}\frac{\sqrt{S}}{2m_T}} dy = S \int_{-\frac{1}{2}\ln\frac{1+\beta_S}{1-\beta_S}}^{\frac{1}{2}\ln\frac{1+\beta_S}{1-\beta_S}} dy \int_{m^2}^{\frac{S}{4\cosh^2 y}} dm_T^2 \;, \tag{8.16}$$

$$S \int_{m^2}^{S/4} dm_T^2 \int_{-\frac{1}{\beta_S}\sqrt{1-\frac{4m_T^2}{S}}}^{\frac{1}{\beta_S}\sqrt{1-\frac{4m_T^2}{S}}} \frac{dx_F}{\chi} = S \int_{-1}^{1} dx_F \int_{m^2}^{\frac{S}{4}(1-\beta_S^2 x_F^2)} \frac{dm_T^2}{\chi} \tag{8.17}$$

the total cross section (8.9) is of course recovered.

Finally it should be noted that experiments do not determine the (differential) longitudinally polarized cross section $(d)\Delta\sigma$ itself, but rather the corresponding spin asymmetry

$$A^{ab} = \frac{(d)\Delta\sigma^{ab}}{(d)\sigma^{ab}} \;. \tag{8.18}$$

In (8.18), which is nothing but the counting rate asymmetry for the two possible helicity alignments of the incoming hadrons (2.2), the experimental normalization uncertainty and some systematical errors conveniently drop out. However, in the following we will concentrate on the polarized cross section itself as well, since we are interested in the influence of the spin-dependent NLO corrections. The calculation of the spin asymmetry (8.18) introduces additional theoretical uncertainties associated with the *unpolarized* (differential) cross section.

8.2 Numerical Studies for Photoproduction

Equipped with the necessary technical framework, we now turn to some numerical applications. Unless otherwise stated we use here the GRV'94 [62] and GRSV standard [15] set of unpolarized and longitudinally polarized parton distributions, respectively. However, it should be mentioned that the detailed choices with respect to the running of α_s and the evolution of the parton distributions used in the $\overline{\text{MS}}$ parton density fits are usually not exactly the same as in our $\overline{\text{MS}}_m$ scheme. Generally n_f instead of n_{lf} is used in $\beta_{0,1}$, i.e., the produced heavy quark flavor is not explicitly decoupled at low energies. Furthermore, bottom production in the $\overline{\text{MS}}_m$ scheme requires *four* light flavors, i.e., charm is treated as "massless" and should enter the calculation with its own evolving probability distribution. But for example in the case of GRV/GRSV [62, 15], flavor thresholds are only introduced in the running of α_s, i.e., there is no charm distribution. On the other hand, the effect of setting $n_{lf} \to n_f$ on the running of α_s is negligible. Also the quark contribution is small compared to the gluon one, as we will see, but particularly so for "heavy" (massless) quarks, which are introduced only at high scales and are always suppressed due to the longer evolution length of the light partons. Hence we will simply use n_f instead of n_{lf} in $\beta_{0,1}$ for the running of α_s and use only three light flavors even when calculating bottom production. So our conventions for calculating hadronic cross sections match those of the GRV/GRSV parton densities [62, 15], but we nevertheless use our $\overline{\mathrm{MS}}_m$ results for the reduced partonic cross sections. The errors introduced by this slight inconsistency are completely swamped by the scale variation uncertainties we will discuss next and hence are of no practical relevance. Since only the photoproduction result is complete in NLO, we can only examine this reaction[2]. Unfortunately we have no data so far, but in the near future COMPASS [31] is going to measure the total (anti)charm spin asymmetry $A^{c\bar{c}}_{\gamma p}$ with sufficient accuracy. Therefore we mainly focus on the kinematical range accessible by COMPASS in our analysis below, i.e., $\sqrt{S} = \sqrt{S_{\gamma p}} = 10$ GeV. It is currently under scrutiny whether it is physically feasible and sensible to run HERA in a polarized collider mode in the future [28], and therefore we either show or comment on the corresponding results at HERA collider energies as well. At HERA a sizable portion of the *ep* c.m. energy 300 GeV can be transferred to the *photon*-proton system. We use $\sqrt{S_{\gamma p}} \simeq 200$ GeV in the following as typical[3] HERA photoproduction energy.

In order to investigate the theoretical uncertainty of predictions for the total polarized cross section induced by the dependence on μ_r, μ_f and m_c, we define

$$R(r,f,c) = \frac{\Delta\sigma^c_{\gamma p}(r,f,c) - \Delta\sigma^c_{\gamma p}(r=f=2.5, c=1.5)}{\Delta\sigma^c_{\gamma p}(r=f=2.5, c=1.5)} \qquad (8.19)$$
$$\mu_r^2 = r m_c^2\ , \quad \mu_f^2 = f m_c^2\ , \quad m_c = c \text{ GeV}\ ,$$

which uses the prediction for one particular choice of scales $\Delta\sigma^c_{\gamma p}(\mu_r^2 = \mu_f^2 = 2.5 m_c^2, m_c = 1.5\text{ GeV})$ as basic value for computing relative deviations. In the plots of R the LO and NLO GRSV standard parton densities [15] have been used. We start by keeping $m_c = 1.5$ GeV fixed and varying only μ_r and μ_f. Thus we plot $R(r,f,1.5)$ in Fig. 8.1 for two center of mass energies $\sqrt{S} = 10$ and 200 GeV. R is shown in percent and contour lines in steps of 5% are drawn on the surface of the plot and as projection on the base. A small circle marks $R(r = 2.5, f = 2.5, c = 1.5) \equiv 0$, so the contour of zero R runs through this circle. At the base we also draw a line for the usual choice $\mu_r = \mu_f$ to guide the eye. Note that in plot (d) we have multiplied R with (-1) to to achieve a nice presentation in the same form, i.e., the change in the low r and high f region is *opposite* to the one for the LO plot (c). As can be inferred from comparing the LO and NLO results at both center of mass energies in Fig. 8.1 (a) vs. (b) and (c) vs. (d), respectively, the scale dependence has been drastically reduced in NLO over the entire range of μ_f and μ_r, which underlines the importance of the NLO results. Moreover, in NLO the choice $\mu_f = \mu_r$ is approximately on the contour for $R = 0$, and R is flattest for large μ_f and μ_r. This motivates the choice of scales, $\mu_f = \mu_r$, which we will use henceforth. For reasonable changes of μ_f and μ_r in Fig. 8.1, the polarized total charm production cross section (8.9) varies by about 15% at $\sqrt{S} = 10$ GeV and 25% at $\sqrt{S} = 200$ GeV in NLO as compared

[2] Also we are forced to ignore the resolved contributions. However, they are not expected to introduce major changes to the results presented here, see the discussion above (6.27).

[3] For example the "ETAG33" sample of [22] has $\langle \sqrt{S_{\gamma p}} \rangle = 194$ GeV.

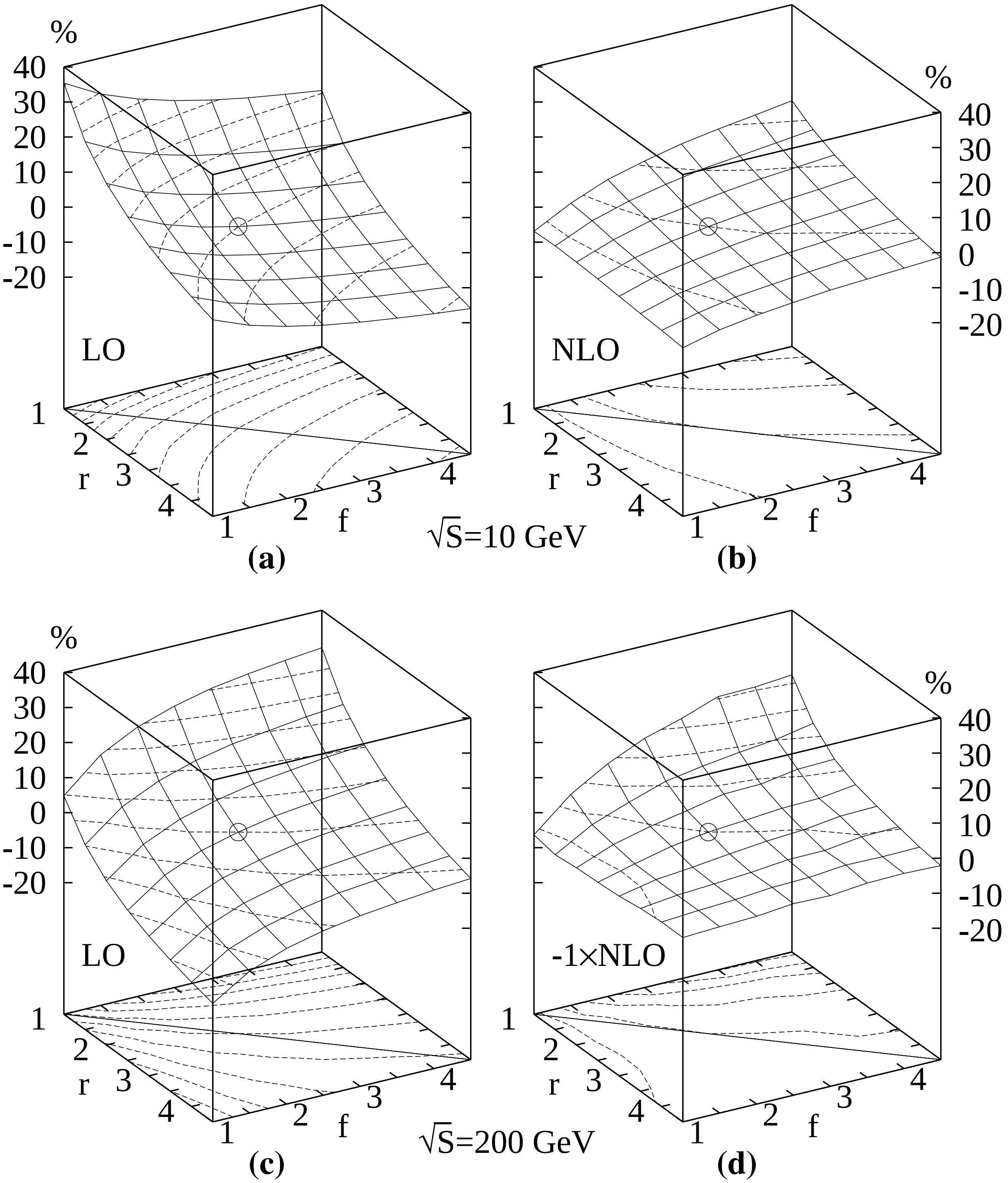

Figure 8.1: $R(r, f, 1.5)$ in percent, see (8.19), for renormalization $\mu_r^2 = rm_c^2$ and factorization $\mu_f^2 = fm_c^2$ scale variations with $\sqrt{S} = 10$ GeV: LO (a) and NLO (b), and $\sqrt{S} = 200$ GeV: LO (c) and NLO, times (-1), (d). The charm mass $m_c = c$ GeV is set to $c = 1.5$. Also shown are a $\bigcirc$ symbol at $R(2.5, 2.5, 1.5) \equiv 0$, contour steps of 5% and a $r = f$ line at the base.

to about 45% at $\sqrt{S} = 10$ GeV and 50% at $\sqrt{S} = 200$ GeV in LO. Contrary to the naïve expectation, the scale dependence becomes slightly stronger for higher energies. But this effect mainly comes from the corner of low r and high f. For larger r, the dependence on f is reduced at higher energies in NLO. Note also that at $\sqrt{S} = 200$ GeV, the LO $R = 0$ contour has moved closer to the $\mu_r = \mu_f$ line. This is in contrast to $\sqrt{S} = 10$ GeV, where this line is basically the direction of strongest change. We have not studied whether this trend persists at even higher energies, since the numerical integrations become very time consuming and since LO is expected to be inadequate at high energies due to the lack of flavor excitation subprocesses.

Next we wish to examine the dependence on m_c. Fig. 8.2 shows $R(r,r,c)$, i.e., we now keep $\mu_r = \mu_f = \mu$ all the time, but still vary μ to see whether the m_c dependence of the total polarized cross section is influenced. Again contours show steps in percent, but now they mean differences of 15% each! So we can immediately conclude that the dependence on the charm mass is much stronger than the one on the factorization and renormalization scales, in particular at lower energies. Again a small circle marks $R(r = 2.5, f = 2.5, c = 1.5) \equiv 0$ and we show a line for $r = f = 2.25$ at the base of the plots. We see that at low energies NLO is much more stable than LO, we get about 135% variation in LO compared to about 45% in NLO in Fig. 8.2 (a) and (b), respectively. However, at large energies LO and NLO both vary by about 45%. So in NLO the dependence on m_c stays roughly constant, whereas it strongly increases in LO at lower energies. It is surprising that NLO improves the stability of the predictions against variations of m_c. But we have set $\mu_f^2 = \mu_r^2 = r m_c^2$, so we indirectly probe the stability along the $\mu_r = \mu_f$ line! Obviously then the differences between LO and NLO are largely due to their behavior for $\mu_r = \mu_f$ discussed above. Note that at $\sqrt{S} = 10$ GeV the dependence on m_c is least in NLO for small $r = f$ values, in particular there is little variation for low values of m_c. But concerning the dependence on r and f separately in Fig. 8.1 we would favor larger values to stay in the "flattest" region. We will use a compromise value of $\mu_r = \mu_f = 1.5\ m_c$, which means $r = f = 2.25$, as standard value in the following. This choice is shown by the line included at the base of the plot in Fig. 8.2. It is lower than the choice $\mu_r = \mu_f = 2m_c$ used in [34, 35], which optimized the dependence on μ_r and μ_f. Here we will basically only vary m_c, since comparing Fig. 8.2 and Fig. 8.1 makes obvious that this will give the major part of the theoretical uncertainties. Note in particular that the changes induced by varying m_c are more or less independent of the variation of $r = f$, i.e., the contours are close to being parallel to the $r = f$ axis. Finally it is perhaps more natural to use a standard value for $\mu_{r,f}$, which is not at the high edge but rather in the middle of the usual variation range $m_c \leq \mu_{r,f} \leq 2m_c$. We will in the rest of the paper vary m_c in the range from 1.4 to 1.6 GeV, instead of the larger range 1.35 to 1.7 GeV in the $R(r,r,c)$ plot, to give a rough estimate of the theoretical uncertainty. This basically amounts to taking the results for the charm mass collected in[4] [1] at face value instead of using the conservative range also quoted there.

[4]Note that their table shows all results converted to the running mass of the $\overline{\text{MS}}$ scheme. The pole mass we need here is approximately 20% larger.

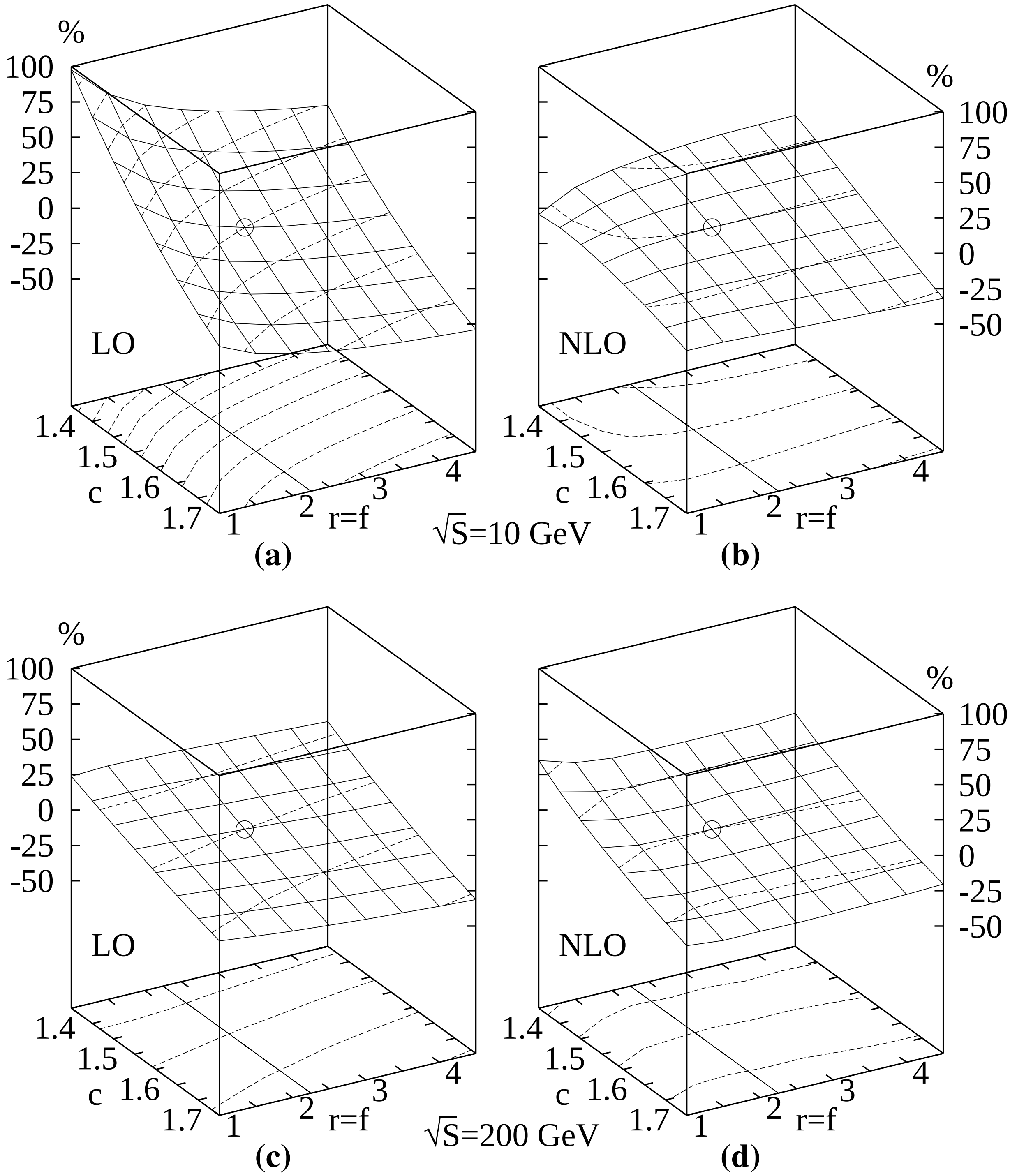

Figure 8.2: $R(r, r, c)$ in percent, see (8.19), for charm mass $m_c = c$ GeV and renormalization scale $\mu_r^2 = r m_c^2$ variations with $\sqrt{S} = 10$ GeV: LO (a), NLO (b) and $\sqrt{S} = 200$ GeV: LO (c), NLO (d). The factorization scale $\mu_f^2 = f m_c^2$ is set to $f = r$. Also shown are a $\bigcirc$ symbol at $R(2.5, 2.5, 1.5) \equiv 0$, contour steps of 15% and a $r = f = 2.25$ line at the base.

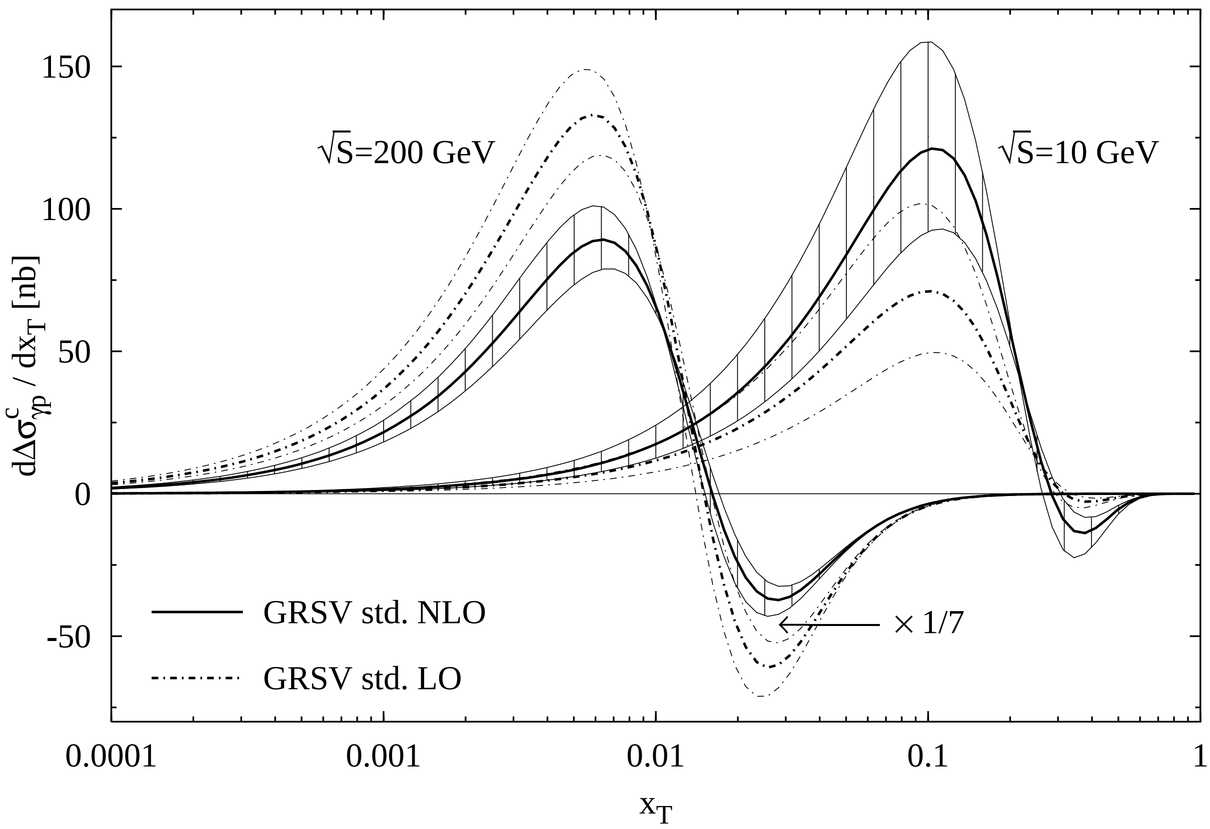

Figure 8.3: x_T-differential polarized anticharm photoproduction cross section $d\Delta\sigma^{\bar{c}}_{\gamma p}/dx_T$ in LO and NLO at $\sqrt{S} = 10,\ 200$ GeV with the GRSV standard polarized parton densities [15]. Thick lines have $m_c = 1.5$ GeV, thin lines with largest positive peak have $m_c = 1.4$ GeV, and the other thin lines have $m_c = 1.6$ GeV. In NLO the thin lines are connected to form a band. We have set $\mu_r^2 = \mu_f^2 = 2.25(m_c^2 + p_T^2)$. The curves for $\sqrt{S} = 200$ GeV are multiplied by $1/7$.

We will now take a look at p_T, or equivalently x_T, see (8.12), differential results. The reason is that we wish to derive a good value for an acceptance cut on p_T in order to enhance the asymmetry. We expect that the COMPASS experiment [31] will not be able to accurately measure differential distributions. But they are still useful as a guide for possible cuts. Fig. 8.3 shows[5] $d\Delta\sigma^{\bar{c}}_{\gamma p}/dx_T$ for $\sqrt{S} = 10$ GeV and 200 GeV. We use $\mu_r^2 = \mu_f^2 = 2.25(m_c^2 + p_T^2)$ here, since it can be expected that p_T^2 becomes a relevant scale when it is not integrated out. This choice reduces to the standard choice for the total cross section $\mu_r = \mu_f = 1.5m_c$ in the limit of small p_T. Here and in the following we always plot as thick line the result for $m_c = 1.5$ GeV and for the thin lines we vary the

[5]There are changes in the ballpark of 10% in the following *differential* curves as compared to [35] due to the scheme inconsistency corrected in [37]. For the total polarized cross section the changes are smaller.

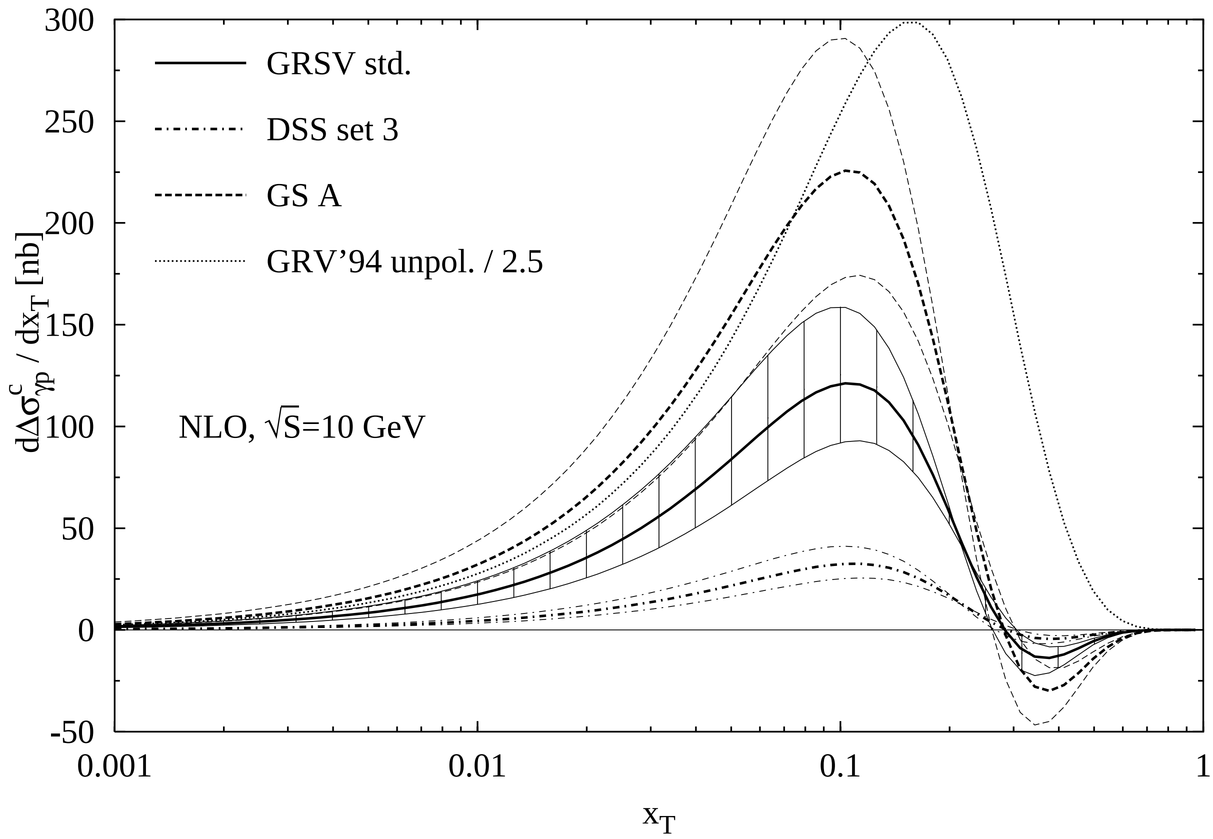

Figure 8.4: x_T-differential polarized anticharm photoproduction cross section $d\Delta\sigma^{\bar{c}}_{\gamma p}/dx_T$ in NLO at $\sqrt{S} = 10$ GeV with the GRSV standard, DSS set 3, and GS A polarized parton densities [15, 17, 18]. Thick lines have $m_c = 1.5$ GeV, thin lines with largest positive peak have $m_c = 1.4$ GeV, and the other thin lines have $m_c = 1.6$ GeV. The GRSV standard curves are connected to form a band. We have set $\mu_r^2 = \mu_f^2 = 2.25(m_c^2 + p_T^2)$. An analogous unpolarized curve (NLO GRV'94 parton densities [62], $m_c = 1.5$ GeV) is shown divided by 2.5.

charm mass from $m_c = 1.4$ GeV to $m_c = 1.6$ GeV. By adding p_T^2 in our scale definition we shift towards larger μ_r and μ_f, where the dependence on independent μ_r and μ_f variations becomes less and the dependence on m_c slightly larger for the total polarized cross section. Thus varying m_c still is a reasonable estimate for the theoretical uncertainty, at least for the lower energy $\sqrt{S} = 10$ GeV, and with an integrated cross section in mind. The independent variation of μ_r^2 and μ_f^2 as $a(p_t^2 + m_c^2)$ with $a = 1/4, \ldots, 4$ has already been shown in Fig. 10 of [35]. Note that the range of a chosen there is rather conservative and yields large uncertainties. The lower and upper limits in this case come from one scale set to $a = 1/4$ and the other set to $a = 4$. Since $(m_c^2 + p_T^2)/4 < m_c^2$ for $x_T \lesssim 0.54$ at $\sqrt{S} = 10$ GeV (for $x_T \lesssim 2.6 \cdot 10^{-2}$ at $\sqrt{S} = 200$ GeV), the large uncertainties of the differential distribution shown in Fig. 10 of [35] are mainly due to a scale choice *lower* than the lowest one $\mu_{r,f} = m_c$ used for the total cross sections. For $\sqrt{S} = 200$ GeV varying

m_c will underestimate the theoretical uncertainty, as p_t can become quite large and then dominates the sum $m_c^2 + p_T^2$. We nevertheless show the m_c variation in order to compare with $\sqrt{S} = 10$ GeV and because the *total* polarized cross section uncertainty is dominated by it, as we just showed. In Fig. 8.3 the NLO curves are connected to form bands and we have multiplied the curves for $\sqrt{S} = 200$ GeV by 1/7 in order to fit them into the same plot. We see that in NLO the variation with m_c is slightly reduced in comparison to LO. On the other hand going to higher energies suppresses the variations more strongly than for the total polarized cross section. The reason is that the amplitude of the oscillating x_T-differential polarized cross section is both larger positive and larger negative for lower m_c, so that in the integration part of the larger relative variations cancel.

The oscillating behavior in x_T is explored further in Fig. 8.4 for $\sqrt{S} = 10$ GeV only. We show the result for three different sets of polarized parton densities, GRSV standard (solid line), DSS set 3 (dot-dashed line), and GS A (dashed line) [15, 17, 18]. The prediction for the polarized cross section turns negative at approximately the same x_T, no matter which parton distribution is chosen. Also the variation of m_c does not strongly change the position of the zero. We see that by taking a cut $x_T \lesssim 0.25$ or equivalently $p_T \lesssim 1.2$ GeV, the negative contributions are cut off and hence the total polarized cross section is *enhanced*. On the other hand the unpolarized cross section, which is shown multiplied with a factor 1/2.5 by the dotted line, does of course not oscillate. Thus the cut takes out a significant part of the unpolarized cross section. Hence we expect that the asymmetry $A = \Delta\sigma/\sigma$ should be strongly enhanced by this cut, since the numerator grows and at the same time the denominator is diminished. This should take place for all the polarized parton densities and m_c values we are exploring.

We see exactly the expected features in Fig. 8.5, which shows the total NLO anticharm photoproduction spin asymmetry $A_{\gamma p}^{\bar{c}}$ with a cut $p_T \leq 1.2$ GeV. Comparing the bands for the GRSV standard parton density prediction with cut (solid lines) and without cut (dotted lines) at NLO, we see that the asymmetry is strongly enhanced, by about 60% at $\sqrt{S} = 10$ GeV! Examining the effect of introducing different parton densities, we see that there are strong differences in the predicted asymmetry. Certainly these differences are larger than the theoretical uncertainties of our calculation, estimated here again by varying m_c. Also compared to the expected statistical error for the COMPASS experiment [31] the situation looks favorable. We use an expected asymmetry error 20% larger than the estimate $\delta A_{\gamma p}^{c\bar{c}} = 0.051$ of [31]. This corresponds to the loss of statistics due to the cut, i.e., for the unpolarized cross section $\sqrt{\sigma_{\text{no cut}}/\sigma_{\text{cut}}} \simeq 1.2$. The appropriately larger error is shown by the point with error bar placed on the GRSV standard curve. It should be possible to distinguish the different parton densities, even when the theoretical uncertainties are taken into account.

However, for a small gluon density like in the DSS set 3 fit, an improved experimental measurement is required in order to unambiguously measure the asymmetry. Smaller $\sqrt{S}$ lead to a larger spread of the predictions, but COMPASS will not be able to measure at lower $\sqrt{S}$. Higher energies are obviously not preferred for this measurement. There is a simple reason why we show no LO predictions. For these values of $\sqrt{S}$ only large $x \gtrsim 0.1$

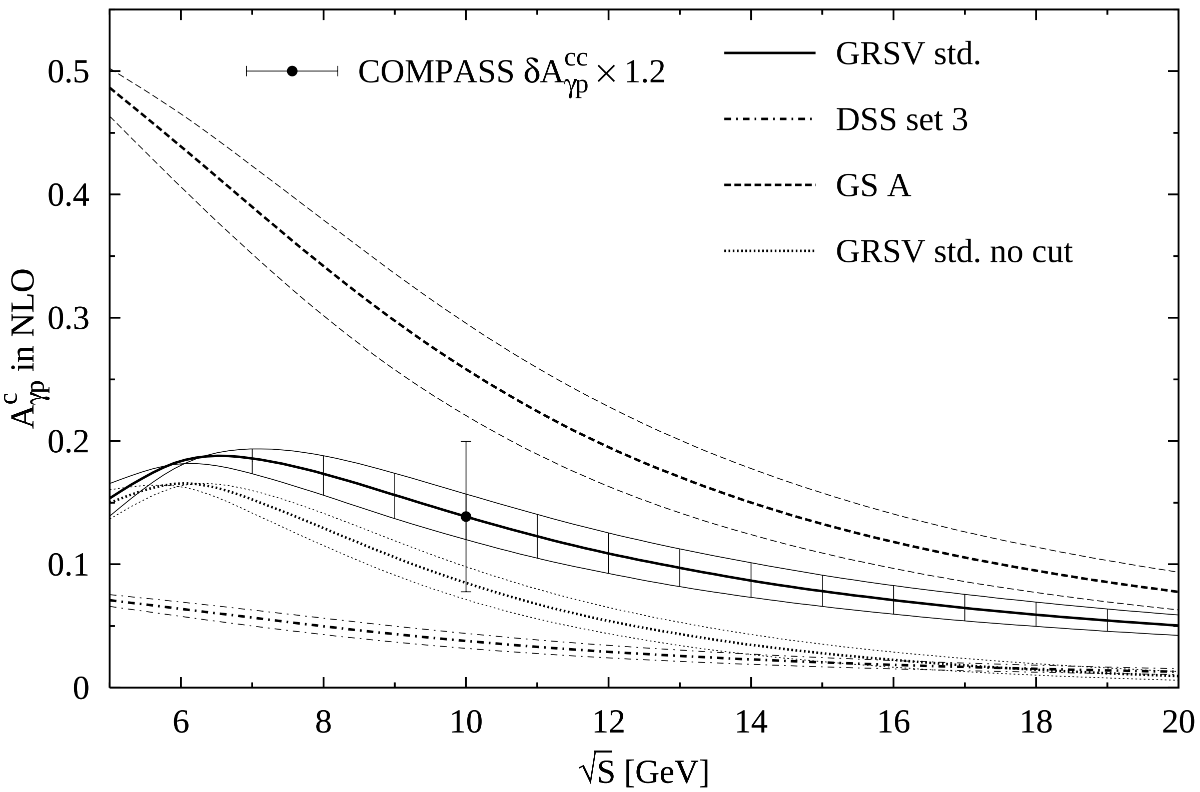

Figure 8.5: NLO anticharm photoproduction spin asymmetry $A^{\bar{c}}_{\gamma p}$ with a cut $p_T \leq 1.2$ GeV using the GRSV standard, DSS set 3, and GS A polarized parton densities [15, 17, 18]. For the unpolarized cross section GRV'94 parton densities [62] were used. The thick lines have $m_c = 1.5$ GeV, the upper thin lines have $m_c = 1.4$ GeV, and the lower ones have $m_c = 1.6$ GeV (order reverses at $\sqrt{S} \lesssim 6$ GeV for GRSV standard). The GRSV standard curves are connected to form a band. We have set $\mu_r^2 = \mu_f^2 = 2.25(m_c^2 + p_T^2)$. GRSV standard curves without p_T-cut and the expected error at COMPASS [31], see text, are also shown.

are probed. In Fig. 8.6 we plot the ratio of the NLO to the LO gluon for several different polarized gluon densities in this large x region. We see that for GRSV standard and DSS set 3 [15, 17], the NLO gluon can be up to a factor two larger than the LO gluon. For GS A [18] the situation is even worse, here the NLO gluon is up to 15 times larger than the LO gluon. This massive enhancement is completely accidental in the parton density fits, since the polarized gluon is currently not constrained at these values of x. In comparison the NLO to LO ratio for the unpolarized GRV'94 [62] gluon stays fairly flat and close to unity up to very large x. Due to the artificially enhanced gluonic contribution we would obtain large differences between LO and NLO predictions, see [34]. One could for example use the NLO parton densities also for the LO curves to avoid this [34, 96]. But as we have argued in Chap. 7, NLO is here the first order in which all important classes of graphs are included. So we refrain from showing LO curves, they can be found in [34].

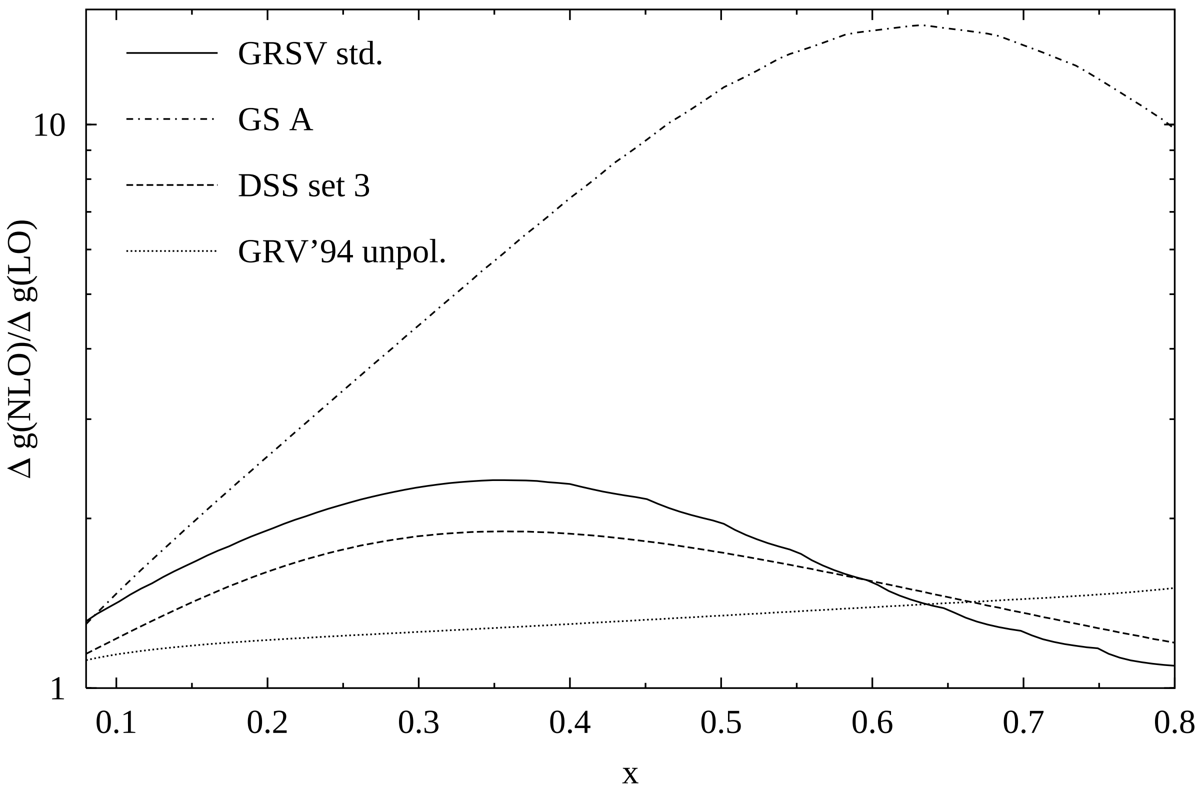

Figure 8.6: Ratios of NLO to LO polarized gluon distributions in the large x region. Shown is $\Delta g(NLO)/\Delta g(LO)$ for the GRSV standard [15], DSS set 3 [17], and GS A [18] polarized parton densities. For comparison the ratio NLO to LO for the unpolarized GRV'94 [62] parton densities is also shown.

Unfortunately, a measurement of $A_{\gamma p}^{\bar{c}}$ at collider energies, where one could access smaller x, appears to be not feasible, since $A_{\gamma p}^{\bar{c}}$ is at best of the same size as the expected statistical error for such a measurement [33]. This also does not improve for p_T or y differential charm distributions. Since $A_{\gamma p}^{\bar{c}}$ already appears to be unmeasurable at HERA, the prospects for a meaningful measurement of $A_{\gamma p}^{\bar{b}}$ seem to be not very promising at first, since bottom cross sections are smaller due to the larger b quark mass and the smaller heavy quark charge $(e_b/e_c)^2 = 1/4$. However, b quarks are experimentally much easier to detect, e.g., through their longer lifetime (secondary vertex tag), which might compensate these shortcomings. By looking at the curves for $\sqrt{S} = 200$ GeV in Fig. 8.3, which is for anticharm but qualitatively shows what is to be expected for antibottom as well, we can guess that introducing a cut in p_T will also help here. However, experimentally it will not be possible to measure very small p_T at HERA, so we use a cut $p_T \geq 1.5$ GeV instead, i.e., now we are cutting off the *positive* part of the polarized cross section. Thus in Fig. 8.7 we turn to the longitudinal spin asymmetry $A_{\gamma p}^{\bar{b}}$ of polarized antibottom photoproduction in NLO at the polarized HERA option [28] for three different sets of polarized parton

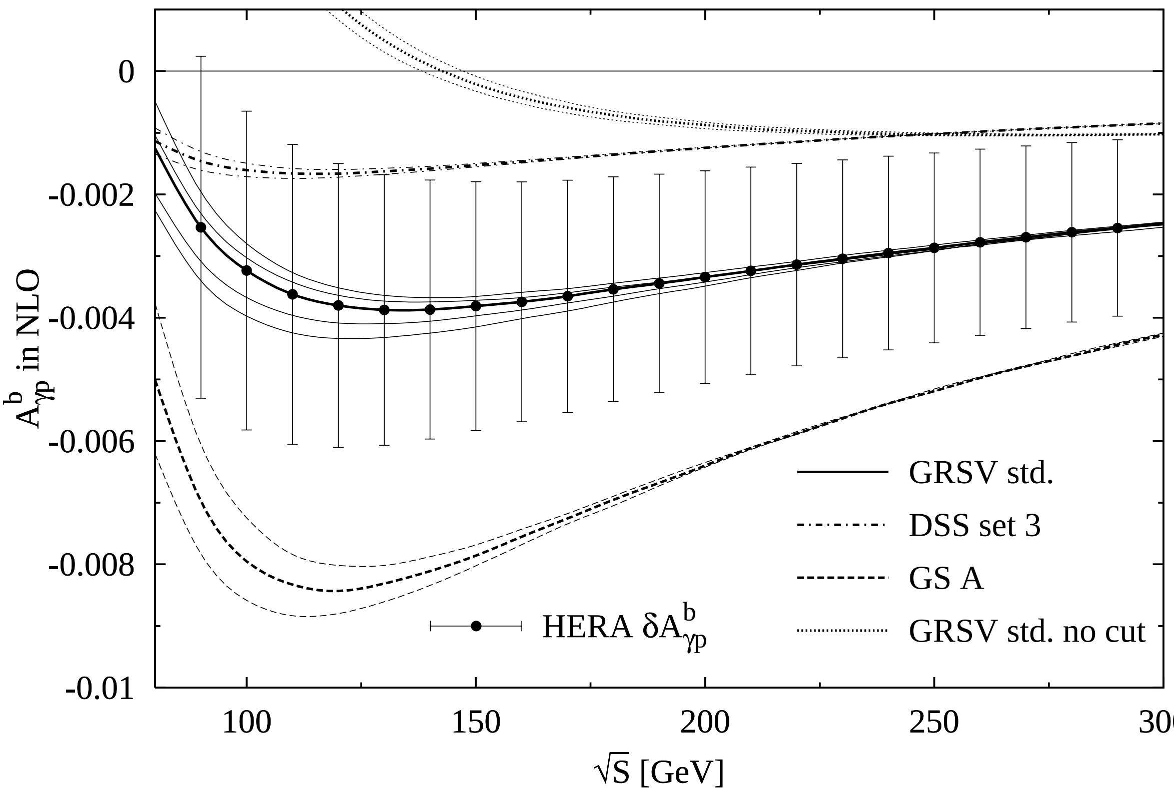

Figure 8.7: NLO antibottom photoproduction spin asymmetry $A^{\bar{b}}_{\gamma p}$ with a cut $p_T \geq 1.5$ GeV using the GRSV standard, DSS set 3, and GS A polarized parton densities [15, 17, 18]. For the unpolarized cross section GRV'94 parton densities [62] were used. The thick lines have $m_b = 4.5$ GeV, the lower thin lines have $m_b = 4.4$ GeV, and the upper ones have $m_b = 4.6$ GeV. We have set $\mu_r^2 = \mu_f^2 = 2.25(m_b^2 + p_T^2)$. For GRSV standard varying μ_r^2 and μ_f^2 independently with $a(m_b^2 + p_T^2)$, $m_b = 4.5$ GeV, and $a = 1, \ldots, 3.5$ yields the outer thin lines. GRSV standard curves without p_T-cut and points with the expected statistical error according to (8.20) are also shown.

distributions [15, 17, 18]. Again thin lines show the variation with the heavy quark mass, here from $m_b = 4.4$ GeV to $m_b = 4.6$ GeV, and the thick line is for the central value $m_b = 4.5$ GeV. Choosing a more conservative range hardly matters at the higher $\sqrt{S_{\gamma p}}$ mainly probed by experiment. The results obtained for the different sets of parton densities are well separated and sensitive to the different Δg, but $A^{\bar{b}}_{\gamma p}$ is extremely small. The points with error bars in Fig. 8.7 illustrate the expected statistical accuracy for such a measurement at HERA estimated via

$$\delta A^{\bar{b}}_{\gamma p} \simeq \frac{1}{P_e P_p} \frac{1}{\sqrt{\varepsilon_b \mathcal{L} \sigma^{\bar{b}}_{\gamma p}}} \tag{8.20}$$

assuming a polarization $P_e P_p \simeq 0.5$ of the electron and proton beams, an (optimistic) integrated luminosity of $\mathcal{L} = 500\,\mathrm{pb}^{-1}$ [28], and an optimal detection efficiency of $\varepsilon_b = 0.05$ [97]. Note that we do not bin in $\sqrt{S_{\gamma p}}$ here, i.e., the errors are estimated at the point where they are drawn. Since HERA is an ep, not γp, collider, the center of mass energy of the γp system varies and usually one averages over a large $\sqrt{S_{\gamma p}}$ bin.

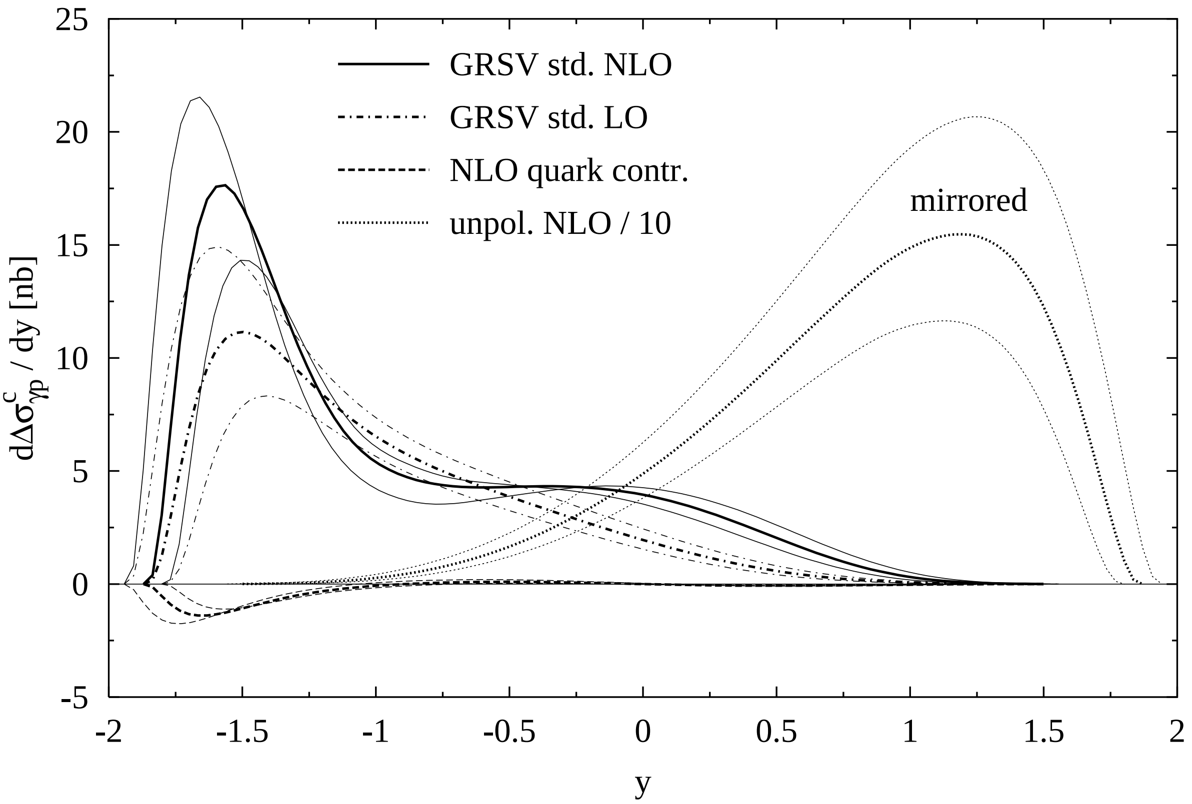

Figure 8.8: y-differential polarized anticharm photoproduction cross section $d\Delta\sigma^{\bar{c}}_{\gamma p}/dy$ in LO and NLO at $\sqrt{S} = 10$ GeV with the GRSV standard densities [15] as measured in the hCMS. The thick lines have $m_c = 1.5$ GeV, the thin lines with largest positive peak have $m_c = 1.4$ GeV, and the ones with smallest positive peak have $m_c = 1.6$ GeV. We have set $\mu_r = \mu_f = 1.5 m_c$. The initial light quark contributions to the NLO curves are shown separately, for them the $m_c = 1.4$ GeV curve has the largest negative peak and so on. For comparison analogous unpolarized curves with NLO GRV'94 densities [62] are shown divided by 10. They are also mirrored, i.e., we plot $d\sigma(-y)$.

For comparison we also display the GRSV standard curves without p_T-cut as dotted lines. They show that we succeeded in cutting off the positive part of the polarized cross section, which otherwise cancels the negative part, i.e., the total asymmetry without p_T-cut is close to zero for these energies. Instead we now see a decent separation of the predictions for different parton densities, which yield asymmetries distinguishable from

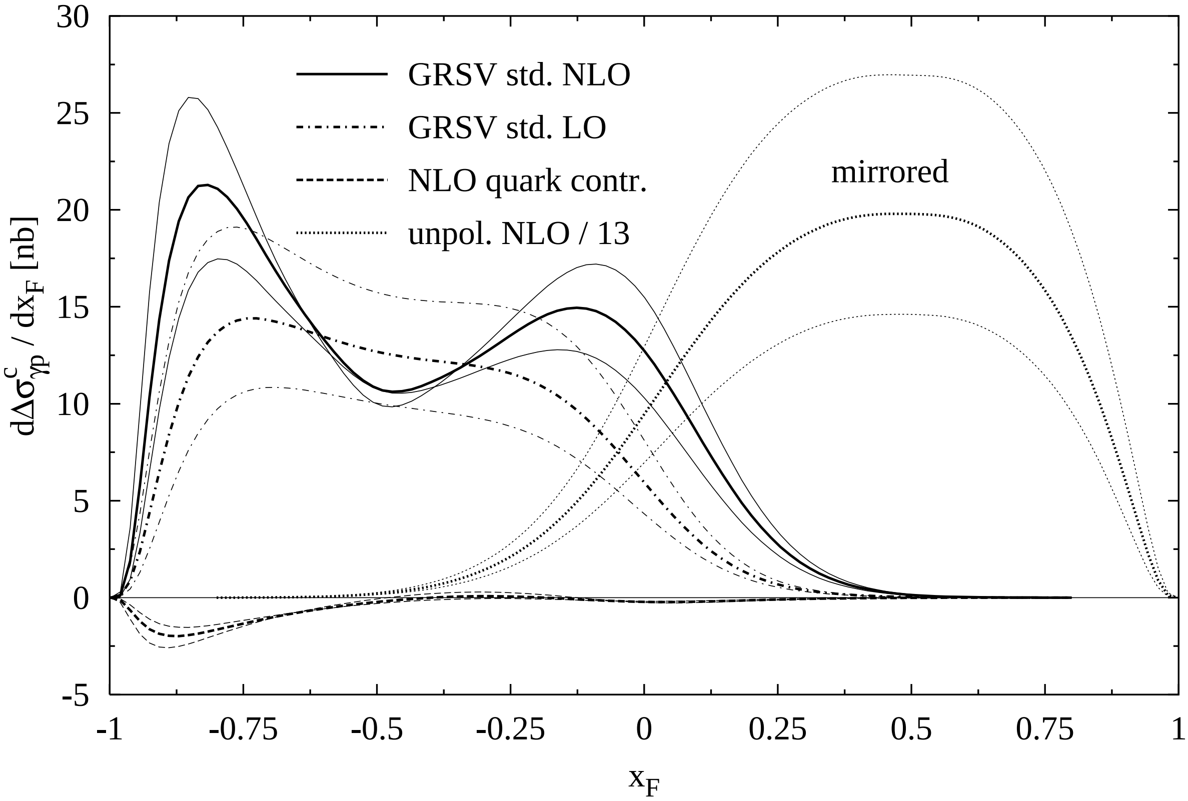

Figure 8.9: x_F-differential polarized anticharm photoproduction cross section $d\Delta\sigma^{\bar{c}}_{\gamma p}/dx_F$ in LO and NLO at $\sqrt{S} = 10$ GeV with the GRSV standard densities [15] as measured in the hCMS. The thick lines have $m_c = 1.5$ GeV, the thin lines with largest positive peak have $m_c = 1.4$ GeV, and the ones with smallest positive peak have $m_c = 1.6$ GeV. We have set $\mu_r = \mu_f = 1.5 m_c$. The initial light quark contributions to the NLO curves are shown separately, for them the $m_c = 1.4$ GeV curve has the largest negative peak and so on. For comparison analogous unpolarized curves with NLO GRV'94 densities [62] are shown divided by 13. They are also mirrored, i.e., we plot $d\sigma(-x_F)$.

zero except perhaps for the small DSS set 3 gluon. We see that the dependence on the bottom mass is quite small, in particular at larger energies. Since we know that we underestimate the theoretical uncertainty by only varying the bottom mass, we also vary μ_r^2 and μ_f^2 independently according to $a(m_b^2 + p_T^2)$, where $m_b = 4.5$ GeV and[6] $a = 1, \ldots, 3.5$. This gives the outer thin lines for the GRSV standard densities. We see that this is not a much larger uncertainty than for the m_b variation. The uncertainty also basically vanishes for larger energies, so we see that from a theoretical point of view (anti)bottom photoproduction allows very precise predictions. One has to keep in mind

[6]This is a less conservative choice than the usual $a = 1/4, \ldots, 4$. We limit the lowest possible scale to $\mu_{r,f} = m_b$ and vary a by ± 1.25 around the standard value $a = 2.25$.

though that we have calculated here only the direct (point-like photon) part of the cross section as a first approximation, see the discussion above (6.27). Thus the uncertainties due to the resolved contributions have not been taken into account. Also we will discuss in the next section that in the unpolarized case theoretical predictions describe bottom data less well than charm data. This is unexpected, since the larger bottom mass should provide a better scale for perturbation theory. Without solving this issue the usefulness of future polarized bottom data will be limited, at least for the extraction of the polarized gluon density Δg.

Finally, let us turn to further results for differential distributions. Although their experimental relevance seems to be remote, apart from y and x_F acceptance cuts, a comparison of the LO and NLO distributions is of theoretical interest to understand in which kinematical regions the corrections are most relevant. In Fig. 8.8 and Fig. 8.9 we show the polarized rapidity y- and x_F-differential anticharm photoproduction cross sections as measured in the hadronic center of mass system (hCMS). We here revert to $\sqrt{S} = 10$ GeV and since p_T is integrated over the entire kinematical range, we again choose $\mu_f = \mu_r = 1.5m_c$. The distributions are asymmetric in y and x_F and the heavy quark is dominantly produced "backward" with respect to the incoming photon, i.e., in the direction of the proton. The NLO results are always larger than the LO ones and deviate in shape, having a larger backward peak. In both figures the unpolarized distributions, scaled down to approximately the size of the polarized one, are shown for comparison. Note that we have mirrored the unpolarized distributions in order to disentangle the lines. This means, we have plotted the unpolarized distributions as a function of $-y$ and $-x_F$, respectively. We see that the more complicated shape only emerges in the polarized case in NLO. The additional contribution with light quarks in the initial state at NLO is included and also shown separately. It appears to be basically negligible in the entire y and x_F range at this energy. We have also again varied the charm mass, but this does not change the general appearance of the distributions. However, the induced variations are quite large and for the NLO polarized case lead to a more pronounced peak structure for lower charm masses. We see however that the structures we observe in these cases do not immediately suggest simple cuts in order to enhance the asymmetry, as had been the case for p_T.

8.3 Current State of Experiment vs. Theory

To make a fair assessment of the *practical* usefulness of our results, we now examine how well heavy quark production theory and experimental data have matched in the past. Our conclusion that heavy quark reactions are useful for the determination of the polarized gluon density Δg is based on the *theoretical* predictions of the last section, but the experience in the unpolarized case raises some serious caveats. However, we will find that we are in a "win-win" situation, provided the future experiments also measure the corresponding *unpolarized* reactions and possibly obtain independent information about Δg. Then we will either improve our knowledge about Δg or obtain valuable information for the solution of the "heavy quark enigma" discussed below. The scope of this section is limited. First, we will focus exclusively on the (QCD) production of *open* charm and bottom. In particular we will not discuss heavy quarkonium production, like the production of the charmonium bound state J/ψ. Concerning heavy quarkonia, we just remark that the sophisticated nonrelativistic QCD (NRQCD) calculations seems to be in serious trouble due to preliminary experimental data on the transverse polarization of charmonium states at high p_T [98]. It remains to be seen whether this can be cured. Perhaps other approaches like the color evaporation model (CEM), which has been revived recently [99] but was proposed over twenty years ago, see for example [61], now become more attractive. However, at least there *are* alternatives to the color-singlet model (CSM) available, which do not utterly fail to describe the direct production cross section of J/ψ and ψ', as the CSM does [100].

Second, we can of course only comment on comparisons of *unpolarized* theoretical calculations and data, as we are still waiting for the first polarized experimental results. Third, we are relying here mainly on the work of other authors. In principle we could of course use our unpolarized results and compare them to part of the existing data. However, we have not yet completed the NLO hadroproduction calculation, so thus far we have concentrated on deriving the missing reduced *partonic* cross sections. The hadron level results shown in the last section are thus first rough predictions. For in-depth phenomenological studies of photoproduction at lepton-nucleon colliders, we should include the convolution of the photoproduction cross section with the photon distribution in the electron according to the Weizsäcker-Williams approximation (WWA) [101, 102, 103]. Then we could compare directly to lepton-nucleon data without depending on any approximate "WWA flux factor" treatment. Also the "resolved" photoproduction processes should be taken into account. Finally, experiments do not really detect heavy quarks, but rather (the decay products of) hadrons. Thus we should include fragmentation functions like the one suggested by Peterson *et al.* [104] to model hadronization. These improvements will be implemented in future versions of our program[7]. Note that we can expect the numerical evaluation to become much slower then, since more convolutions are needed. So for the time being we will turn to the comparisons available in the literature.

We begin by examining fixed-target production of open charm, using the results of [106]. A convenient compilation of experimental results with references is provided there, so we refer the reader to [106] concerning the experiments mentioned in the following. The total cross sections both for hadroproduction (experimental collaborations for charm in pion-nucleon – E653, E769, NA27, NA32, E769; charm in proton-nucleon – E653, E769, E743, NA27, NA32; bottom in pion-nucleon – E653, E672, E706, NA10, WA78, WA92; bottom in proton-nucleon – E605, E771) and photoproduction (experimental collaborations for charm in photon-nucleon – E687, E691, NA14/2) are well described by the NLO unpolarized calculations *within* the conservatively estimated theoretical uncertainty. The covered center of mass energies are about 20 to 40 GeV in hadroproduction and 10 to 20 GeV in photoproduction. The major theoretical uncertainty is due to the variation

[7] A version including the WWA exists, but has not been thoroughly tested yet.

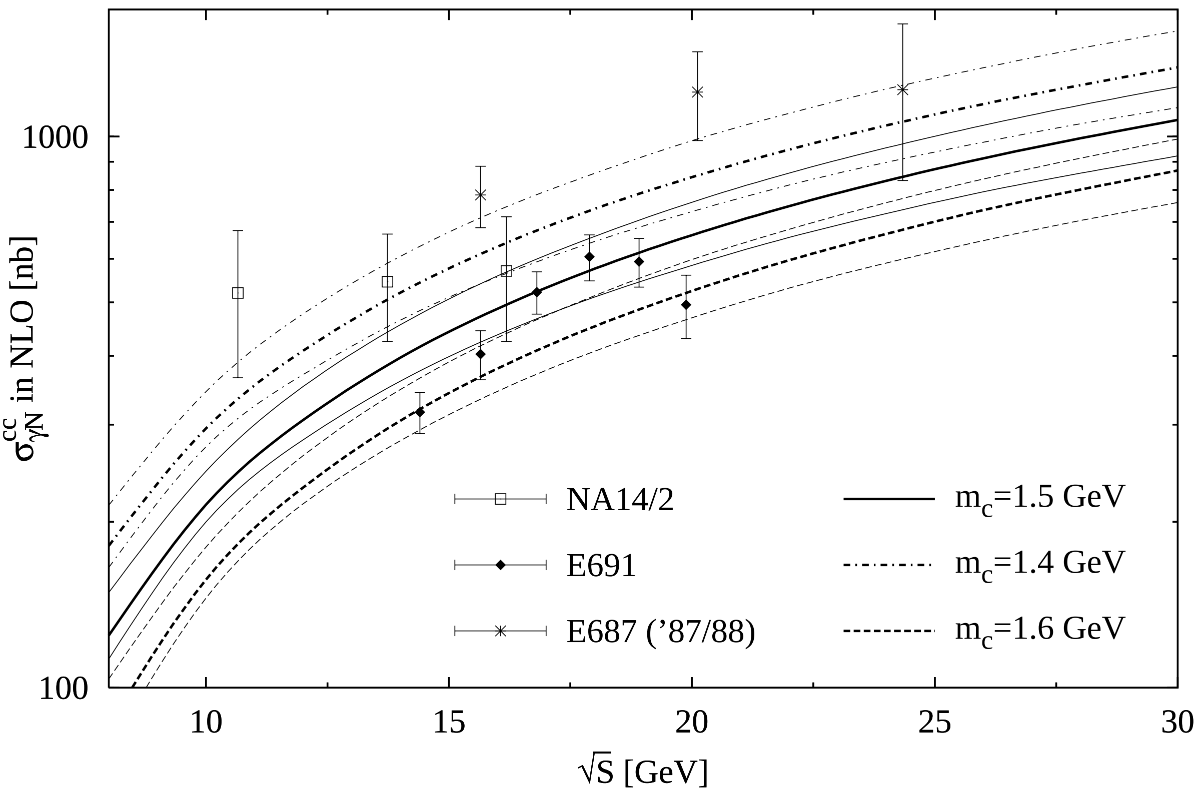

Figure 8.10: Unpolarized total charm-pair photoproduction cross section $\sigma_{\gamma N}^{c\bar{c}} \simeq \sigma_{\gamma p}^{\bar{c}}$ compared with experimental data [105]. Predictions for the charm masses 1.4 GeV (dot-dashed lines), 1.5 GeV (solid lines), and 1.6 GeV (dashed lines) are shown, where the thick lines have $\mu_r^2 = \mu_f^2 = 2.25 m_c^2$ and the thin lines are obtained by independent variations of $\mu_{r,f}^2$ by $\pm 1.25 m_c^2$. The GRV'94 unpolarized parton densities [62] were used.

of the heavy quark mass in the case of charm, as expected from our results of the last section. In the case of bottom this uncertainty is also sizable[8], but variations of $\mu_{r,f}$ still dominate the uncertainty there. Compared to the predictions of [106], the data for the hadroproduction of charm prefer the value $m_c = 1.5$ GeV we have been using, but values down to $m_c = 1.2$ GeV are possible. High values like $m_c = 1.8$ GeV are disfavored. In photoproduction $m_c = 1.5$ GeV again gives the best description. Here both high and low values of m_c give worse agreement. However, this always just means that the overall agreement with the broad band of theoretical uncertainties obtained for the conservative range $m_c/2 \leq \mu_r \leq 2m_c$ with $\mu_f = 2m_c$ is better in one case than the other. Experimental data tend to scatter within the uncertainty band and sometimes are inconsistent, e.g., E687 vs. E691 in photoproduction. The variations tried in [106] for the bottom mass from 4.5 to 5 GeV all are in accord with the data in the same sense. Here both scales

[8]Note that the uncertainty due to m_b variations increases for lower c.m. energies in Fig. 8.7.

have been varied in the conservative range $m_b/2 \le \mu_{r,f} \le 2m_b$. Furthermore, the authors of [106] have also varied $\Lambda_{\rm NLO}$. Apart from correlations with the parton densities, this is equivalent to an even larger range of μ_r being probed, up to the point where in the case of charm the variations "induce values of $\alpha_s(m_c)$ too large to be used in a perturbative expansion" [106].

Since we can calculate the direct part of the total photoproduction cross section with our results and have assumed that the resolved contribution is small at these energies, we can check their conclusions for this case. We will adopt here the opposite approach to [106]: since they have already explored the possible theoretical uncertainty up to the inapplicability of perturbation theory itself, we wish to see if "optimistic" scale variations are still compatible with data. So in Fig. 8.10 we present curves for[9] $\sigma^{c\bar{c}}_{\gamma N}$ with three choices for the charm mass $m_c = 1.4,\ 1.5$, and 1.6 GeV as dot-dashed, solid, and dashed lines, respectively. The thick lines are obtained for our standard choice $\mu_r^2 = \mu_f^2 = 2.25 m_c^2$, whereas the thin lines are obtained for independent variations of μ_r^2 and μ_f^2 by $\pm 1.25 m_c^2$. We use the GRV'94 parton densities [62] and keep $\Lambda_{\rm NLO} = 200$ MeV fixed. Thus our Fig. 8.10 corresponds to Fig. 3 in [106]. We see that even with our "optimistic" choices, the overall theoretical uncertainty forms a band broad enough to still "agree" with the available data [105]. Note that the dependence on the mass scales is *worse* in the unpolarized case than in the polarized case. It is also evident that the experiments do not match well with each other in the region where they overlap and also there seem to be differences in the energy dependence. With our "optimistic" scale variations one cannot say that one choice of m_c fits best, rather one could claim that $m_c = 1.5$ GeV is a compromise value which fits all three experiments to some extent. We draw the conclusion for the future COMPASS [31] measurement that in order to be able to extract Δg from the total charm spin asymmetry one should measure the unpolarized total cross section as well. Though a rough agreement with the NLO QCD prediction is found, the "optimistic" theoretical uncertainty we have explored here, which were basically also used for the predictions of the last section, is the *minimum* required to "fit" current unpolarized experiments, mainly because the experiments disagree with each other. An unpolarized COMPASS measurement could be very helpful in that respect.

As a final point concerning the unpolarized fixed target experiments we note that in the *differential* distributions usually the introduction of intrinsic transverse momentum of the partons (a k_T "kick") is required to match the theoretical description with the data. Strangely enough the NLO QCD predictions for pure heavy quarks, i.e., without hadronization, fit the hadroproduction data of the WA92 and E769 experiments on p_T- and x_F-distributions well. However, the introduction of fragmentation functions [104] softens the p_T-distribution and then a rather large k_T-kick $\langle k_T^2 \rangle = 1 - 2$ GeV^2 is needed to agree with that data. The x_F-distributions of most other hadroproduction experiments are harder than the predictions for pure heavy quarks, in particular in the case of "leading particles", see [106] for details. Here the introduction of other non-perturbative

[9] We use the approximation $\sigma^{c\bar{c}}_{\gamma N} = (\sigma^{c}_{\gamma N} + \sigma^{\bar{c}}_{\gamma N})/2 \simeq \sigma^{\bar{c}}_{\gamma p}$, which is valid since charge asymmetry and quark contributions are small. The data have been read off the plots in [105].

QCD phenomena like beam-drag effects [107] may be necessary, we will briefly comment on this below. However, we are mainly interested in the p_T-distributions here, since we want to introduce p_T-cuts. In Fig. 8.11 we show Fig. 6 of [106], which compares the NLO QCD prediction for the unpolarized p_T^2 distribution with data from the E687 and E691 collaborations. We see that the introduction of fragmentation functions (they used the form of [104] with the parameter $\epsilon_c = 0.06$) is required to describe the data. But the good news is that the k_T kick does not significantly change the prediction for variations $\langle k_T^2 \rangle = 0.5 - 2$ GeV^2 and a fair description of the data is achieved. Thus we should be able to estimate the non-perturbative effects with good accuracy when using a p_T-cut to enlarge the asymmetry in the polarized measurement. However, it would be preferable if the COMPASS collaboration [31] would scan over different p_T-cut values and publish the corresponding integrated unpolarized cross sections. That would allow us to test our understanding of this issue. All in all we think that the prospects for a meaningful measurement of the polarized gluon density Δg at COMPASS are still good after these considerations, provided the unpolarized cross section can be determined. Also one can check this determination of Δg against an independent measurement of the gluon polarization at COMPASS, which uses correlated high p_T hadron pairs [108].

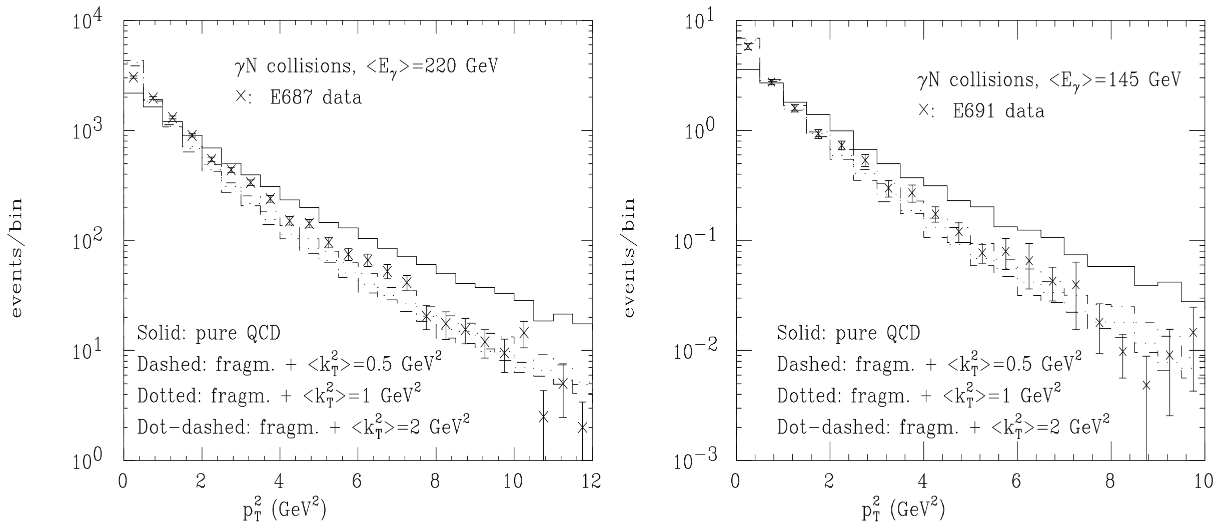

Figure 8.11: p_T^2-differential distribution for unpolarized charm production in γN collisions vs. experimental data. The solid line shows the "pure" NLO QCD prediction for $m_c = 1.5$ GeV, the other lines include fragmentation (according to [104] with $\epsilon_c = 0.06$) and different amounts of intrinsic k_T assumed for the incoming partons. See [106] for details, this is their Fig. 6.

Next we turn briefly to the HERA *ep collider*. First we remark that the description of charm production in deep inelastic scattering (DIS) has been very successful so far. The data for the charm tagged content of the inclusive proton structure function F_2, called F_2^c, are well described by theoretical predictions, see for example [24]. Data on differential distributions are also in accordance with theory as is conveniently summarized in [109].

However, for the distributions depending on the longitudinal momentum, like x_F, one has to include non-perturbative effects like beam-drag to obtain satisfactory agreement. The idea is basically that the produced charm quark is usually color-connected to the beam remnant of the incoming particle [107, 110]. Thus it can be “dragged” along in the direction of the outgoing remnant and gain energy and momentum. The net effect is that more than expected charmed hadrons are produced “forward” (in the direction of the remnant), and less are produced “backward”. This mechanism was first proposed for the fixed target data, but also works well here. It is encouraging that charm production in DIS is described so well by NLO QCD calculations. But of course the large virtuality of the photon in DIS may very well be responsible for that success. So we will now turn to photoproduction. Photons of (almost) zero virtuality, where the electron is scattered by a small angle, are dominant in the heavy flavor production at HERA. In particular comparisons with (preliminary) ZEUS results from the large statistics sample collected in the 1996 and 1997 runs with an integrated luminosity of 37 pb^{-1} are interesting. For charm production once more increased forward production is observed. For the data taken with photon-gluon c.m. energies between 130 and 280 GeV [111], beam-drag effects once more may cure the observed discrepancies for differential distributions between theory and data [112]. But this seems to work less well for events in the low photon-gluon c.m. energy range between 80 and 120 GeV [113]. We note that the successful gluon extraction from photoproduction [22] is based on two older data sets from 1994-96, with an integrated luminosity of $(10.7 + 10.2)$ pb^{-1}. The results of this analysis were already shown in the right half of Fig. 1.2. Here the problems in the differential distributions with forward production seem to be less severe and occur only at high p_T. Furthermore, the *total* $c\bar{c}$ pair photoproduction cross section is compatible with theory within errors [106]. Thus it is in line with the fixed target measurements, in spite of being measured at energies one order of magnitude larger. We find that at the higher energy of HERA the picture of charm production has become less clear. However, we still conclude that charm production at HERA is or will be describable with currently available theoretical methods, if non-perturbative effects like beam-drag are taken into account for the differential distributions. But we have already mentioned in Chap. 6 that charm spin asymmetries at HERA will probably be unmeasurable anyway [33].

So we will now turn to bottom production. A general statement can be made about bottom production at colliders, both for photo- (electro-) and hadroproduction: the theoretical predictions are about a factor *two* (or more) off! H1 measures a visible cross section $\sigma(ep \to b\bar{b}X \to \mu X')$ of about 176 pb, compared to a NLO QCD prediction of 104 pb [116]. Their estimate of the experimental error towards smaller values is about 23 pb (statistical and systematical error added in quadrature), whereas they estimate the theoretical uncertainty to be 17 pb. However, it would be interesting to examine the rôle of the `AROMA` Monte Carlo event generator [117] used in the extraction of their data more closely, since after all the prediction of the same `AROMA` program for the visible cross section is[10] 38 nb. A second method of measuring the production of $b\bar{b}$ pairs at

[10]The LO QCD prediction is 69 nb, so the `AROMA` prediction is even lower than LO.

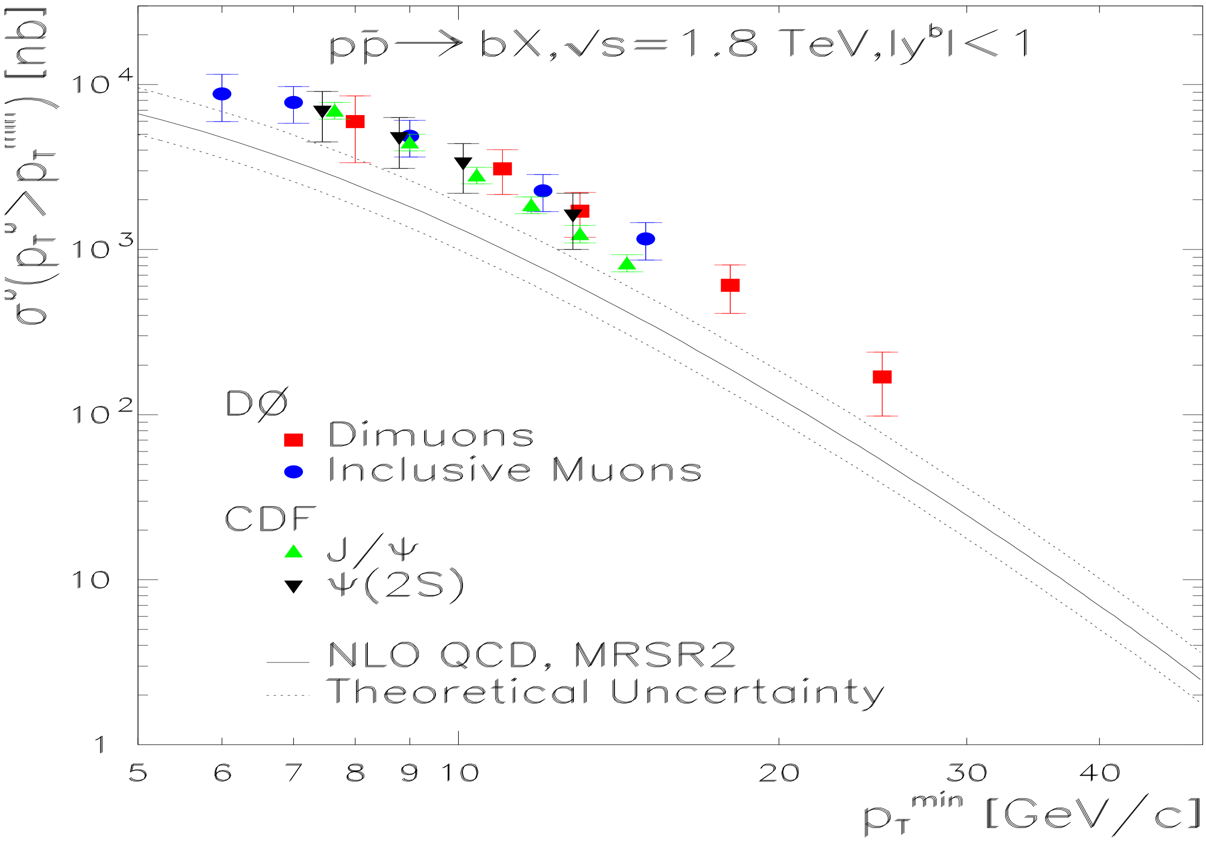

Figure 8.12: Bottom quark production data from CDF and DØ compared with the NLO QCD prediction. The theoretical uncertainty displayed by the band is associated with μ_r, μ_f, and m_b variations. The dependence of the integrated cross section on a cut $p_T > p_T^{\rm min}$ is shown. This is Fig. 11 of [114].

H1 gives similar large discrepancies between the experimental measurement and the LO `AROMA` prediction [118]. Finally preliminary experimental results from ZEUS on $b\bar{b}$ production also show a factor 4 disagreement of data with the predictions from a different LO Monte Carlo [119, 112]. Even if the evidence from HERA is not as clear yet as one may wish, the results for hadroproduction, mainly from the TEVATRON at FERMILAB, have stood the test of time. Two recent articles [114, 120] conveniently summarize the complex situation for bottom hadroproduction, details and references can be found therein. Fig. 8.12, which is Fig. 11 of [114], shows what is typically found at the TEVATRON by the CDF and DØ collaborations: While the shape of the NLO QCD prediction is fine, the normalization is wrong. Displayed in Fig. 8.12 is the integrated p_T-distribution for bottom quark production depending on a p_T-cut, i.e., a similar plot as our Fig. 2.5 but with *bottom*, at a c.m. energy of 1.8 TeV and compared to NLO QCD calculations. We find a ratio "data/theory$\simeq$ 2.5" in this plot. The data displayed there have been taken in the central rapidity region, for forward production the shape still agrees, but then

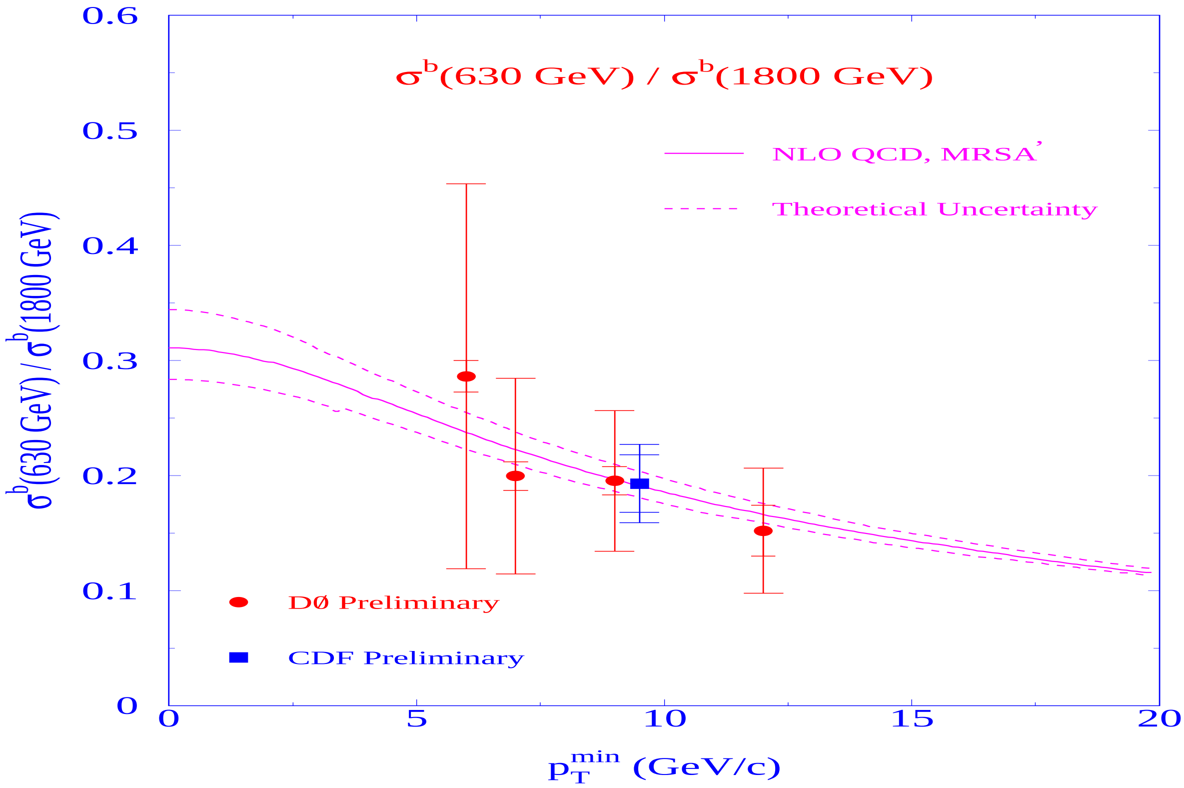

Figure 8.13: Ratio of bottom quark production data taken by CDF and DØ at $\sqrt{S} = 630$ GeV and 1.8 TeV compared with the NLO QCD prediction. The theoretical uncertainty displayed by the band is associated with μ_r, μ_f and m_b variations. The dependence of the ratio of the integrated cross section on a cut $p_T > p_T^{\rm min}$ is shown. The figure is taken from [115].

"data/theory$\simeq$ 4" [120]. A considerable amount of effort has been spent on improving the theoretical description of these data, which have been consolidated over the years, basically without avail[11]! This is very puzzling, since we can describe charm production to a considerable extent, as we have just seen. Thus we are in the strange situation that NLO QCD seems to be working better at the "dangerously low" scale $m_c^2 \simeq 2.25$ GeV^2, whereas it fails drastically at the "safe" scale $m_b^2 \simeq 20.25$ GeV^2. This deserves to be called the "heavy quark enigma". But the fact that NLO QCD at least describes the *shape* of the data offers some hope. Furthermore, Fig. 8.13, taken from [115], shows that NLO QCD also has the right energy dependence! In this plot the *ratio* of the p_T-integrated bottom production cross section measured at two *different* energies 630 GeV and 1.8 TeV is displayed and obviously within the rather large experimental errors the NLO QCD prediction fits perfectly. The DØ errors are expected to become smaller after correlations have been taken into account. Only CDF and DØ data have been used in order to reduce common systematic errors, but older UA1 data at $\sqrt{S} = 630$ GeV are compatible [106].

[11] If α_s is *maximized* by an extreme choice of scales, then theory can fit the data [106].

What does all this mean for our plan of extracting the polarized gluon distribution Δg from bottom production? Obviously it is seriously compromised, since we cannot be sure that our theoretical treatment is correct. But it looks as if a common trend of all bottom measurements in photoproduction (electroproduction) and in hadroproduction is that basically only the normalization is off by a factor. Let us assume that a polarized collider is able to measure the unpolarized cross section separately and can perform at least one independent measurement of Δg using a different process. In this case we should be in a "win-win" situation: *Either* the normalization of the polarized measurement is wrong by the *same* factor we have determined in the unpolarized case, i.e., the effect is not spin-dependent. In this case of course the spin asymmetry $d\Delta\sigma/d\sigma$ is not affected and we would find it to be compatible with a prediction that also fits the independent Δg determination. So then we can go ahead and measure Δg by determining the asymmetry, in spite of the fact that $d\Delta\sigma$ is off. *Or* the normalization of the polarized measurement is not the same, i.e., a Δg that fits the independent polarized measurement does not yield the experimental bottom spin asymmetry, when the theoretical prediction is multiplied with the factor determined by unpolarized bottom production. The information that a spin-dependence is observed could then possibly provide a tool for solving the "heavy quark enigma"! In practice of course the question will be, whether the experimental accuracy is good enough to distinguish the two cases. But here the rather large normalization factors involved may be of advantage.

Polarized HERA and RHIC fulfill the conditions mentioned above, the corresponding unpolarized measurement has or will be done and several independent measurements of Δg are planned [28, 32]. Furthermore we note that RHIC will perform a first measurement of hadroproduction of *open* charm at collider energies, in addition to open bottom production. Thus they will be able to compare with open charm production at fixed target experiments and at HERA, with bottom production at HERA and at FERMILAB, and internally the results for both flavors. Their planned c.m. energies of 200 and 500 GeV are perfect for bridging the energy gap between HERA and FERMILAB. We conclude that in spite of the "heavy quark enigma", measurements of polarized bottom production still make sense. Polarized hadroproduction of charm at RHIC is still expected to be a good candidate for measuring Δg, if we can assume that the situation will not be worse than what has been found at HERA for photoproduction of charm. However, the HERA results suggest, that we may have to consider non-perturbative effects like intrinsic k_T to achieve consistency with *differential* charm data. It may be possible to test some of these non-perturbative model assumptions using other observables, for example azimuth correlations of the bottom pair were measured at the TEVATRON and disfavor large intrinsic k_T in their bottom production reactions [114]. To sum up, we conclude for all the mentioned experiments that polarized heavy quark production can be used to determine Δg, but that the corresponding unpolarized measurement is *required* in order to check the validity of the theoretical methods. Furthermore, independent measurements of Δg using other processes at the same experiment should be used as a cross check.

Chapter 9

Summary

In this thesis we have presented the first complete NLO QCD calculation of the spin-dependent production of heavy quarks in collisions of (point-like) photons and hadrons. Furthermore, we have included our work on the spin-dependent hadroproduction of heavy quarks. In order to obtain the full NLO QCD corrections for the latter reaction, we still have to sum and simplify the already calculated gluon-gluon virtual loop contributions. All other partonic cross sections of these two processes have been completed and are documented here. We have tried to provide a sort of mini-review of the methods applied in our calculation: On one hand, we explain how they are derived from the basic framework of (perturbative) QCD. On the other hand, we demonstrate how they are used efficiently in practice. To the best of our knowledge, some of the techniques have not been explained before either in detail, like the automatic partial fractioning of angular variables, or at all, like the systematic expansion of hypergeometric functions. We hope that it will prove advantageous for future perturbative QCD calculations that all the needed methods now have been collected in one reference.

Our main goal has been to provide the theoretical basis for an experimental determination of the polarized gluon distribution Δg in open heavy quark production. For this reason we have presented predictions for spin asymmetries at experiments that will either take data soon (COMPASS [31] and RHIC [32]) or have a chance to be realized in the near future (polarized HERA [28]). We have improved our previous hadron level predictions [34, 35] by investigating the theoretical uncertainties due to the not precisely known heavy quark (pole) mass and by using cuts on the transverse momentum to enhance the spin asymmetries. One should keep in mind that our NLO calculations are indispensable for a meaningful interpretation of future experimental data: First, our NLO predictions are much more stable against variations of the renormalization and factorization scales than the LO ones. Second, in the reactions considered here several Feynman graph topologies occur for the first time in NLO, which yield large contributions both close to the production threshold and at high energies. Thus LO calculations may be misleading and should ultimately be replaced by NLO ones. Finally, we have discussed in this paper the current state of comparisons between theory and experimental data in the analogous unpolarized case. From this discussion we conclude that a measurement of only the *ratio* of polarized and unpolarized cross sections will not be sufficient. The unpolarized cross section itself has to be measured, if our goal to determine Δg is to remain realistic.

After this general overview, we now give a brief description of the salient features of our work chapter by chapter. In the introduction we have emphasized that the full QCD improved parton model is required to describe experimental data on the spin of the nucleon and that the polarized gluon distribution Δg represents the major remaining uncertainty of this model. Polarized exclusive reactions can be used to determine Δg better and open heavy quark production is our suggestion. Chap. 2 shows how one can obtain polarized and unpolarized cross sections simultaneously by projecting onto helicities, which makes checks against previous unpolarized calculations possible. Also the LO cross sections and the $2 \to 2$ phase space have been derived there in $n = 4 + \varepsilon$ dimensions for later use with the dimensionally regulated NLO pieces.

The treatment of the virtual loops occurring in NLO has been elucidated in the next chapter. The Passarino-Veltman decomposition [47] of the occurring tensor integrals has been derived there. This decomposition is simple in principle, but the results are very lengthy. Take for illustration a 4PF tensor integral of third rank, it has thirteen different Lorentz covariant structures, so one has to calculate thirteen parts for just one matrix element. Each of these parts is multiplied by a scalar coefficient, which is in general a complicated function of basic scalar integrals, invariants, and in particular also of the heavy quark mass. We have constructed a program that computes these coefficients, have checked the lengthy general expressions, and have simplified them for each specific case. Second, the re-calculation of all the needed basic scalar integrals [44], which we have included here, was non-trivial in the case of vertex and box integrals. The main problems are the calculation in non-integer $4 + \varepsilon$ dimensions, the branch cuts of the occurring functions, and the increased complexity of the integral kernels due to the non-vanishing heavy quark mass.

In Chap. 4 we have spent some time on the renormalization procedure, since the $\overline{\mathrm{MS}}_m$ scheme we employ is widely used, but not well documented in the literature. We have demonstrated how subtracting the heavy quark loop part of the gluon self-energy changes the running of the strong coupling constant α_s, so that only light flavors contribute. Furthermore, we have explicitly shown how the commonly used effective renormalization formula for the coupling constant sums up all the counterterms, except for the one connected to mass renormalization. So mass renormalization has to be performed separately. Our treatment of the real contributions has been expounded in the next chapter. Since we have used the HVBM scheme [54] for extending γ_5 and $\epsilon_{\mu\nu\rho\sigma}$ to n-dimensions, we first had to generalize the n-dimensional $2 \to 3$ phase space integration by deriving an integral operator for the ensuing ε-dimensional "hat-space" terms.

In addition, we have created a program which *automatically* rewrites the phase space integration over the six different angular Mandelstam variables as a sum of basic angular integrals. Extensive partial fractioning is needed for this and we have explained the procedure in detail. We have also recalculated the needed basic angular integrals [44] here, explaining how "tricks" can be used to reduce their number considerably. Most of the integrals have been extended to $\mathcal{O}(\varepsilon)$, which may prove useful for future calculations. Finally, we have demonstrated in this chapter how phase space slicing isolates the soft real singularities, so that they can be canceled analytically against the infrared virtual ones.

Mass factorization is another topic which is seldomly explored in detail. So in Chap. 6 we have bridged the gap between the general formulae and the practical prescriptions by exhibiting the factorization of collinear singularities for one of our subprocesses. This also enables us to derive the LO renormalization group equations. Naturally we have compiled the other needed factorization formulae as well. In the next chapter we have calculated the other subprocesses. In each case we have shown the needed set of Feynman diagrams and the final parton level results. In order to facilitate comparisons with our calculation, we have displayed the total partonic cross sections for each of the subprocesses. Furthermore we have analyzed the properties of these partonic cross sections, in particular their spin dependence and size at threshold and at high energies.

We have checked our unpolarized results either analytically (for the virtual plus "soft" real part) or numerically (for the "hard" real part) against previous unpolarized calculations [44, 45, 46]. Also the "abelian" parts of $\vec{g}\vec{\gamma} \to \overline{Q}$ have been compared with the polarized and unpolarized NLO results for $\vec{\gamma}\vec{\gamma} \to \overline{Q}$ [60]. Finally, we have checked each subprocess separately against the almost completely independent calculation of Dr. M. Stratmann: First, the matrix elements have been compared analytically. Second, the agreement after integration (loop and phase space, respectively), has been tested. Third, the programs for the partonic cross sections (and later for the hadron level predictions) give the same results. The `Fortran` source code of our photoproduction program, which includes a simple script based user interface for future use by other people, is about 100 KByte long. Considerable time has been spent on testing the program, for example by re-inserting all the programmed `Fortran` partonic cross sections into `Mathematica` and comparing them with the original results[1].

The final chapter then considers the hadron level and the main points already have been discussed above. In the appendices we have collected some technical material. In particular App. B contains additional topics of general interest, for example the automatic calculation of color factors. To sum up, we have presented NLO QCD calculations that will be used to interpret experimental results very soon. It is probable that our knowledge about the polarized gluon distribution Δg, and thus of the spin of the nucleon, will be improved considerably by the experimental measurements and their theoretical analysis in NLO QCD.

[1]Very recently a second calculation of the complete NLO QCD corrections to polarized photoproduction has been finished [121]. Their virtual, soft, and collinear contributions are in full agreement [121]. However, in *numerical* comparisons at the *hadron* level differences of a few percent are seen [121]. In order to pin down the origin of these minor discrepancies, we hope that the authors of [121] will publish details about their *parton* level results and about comparisons of their unpolarized results to previous unpolarized calculations.

Appendix A

Additional Material Concerning Virtual Corrections

A.1 General Formula for Virtual Integrals

The integrals of the type (3.4) can be brought into the form

$$\mu^{4-n} \int \frac{d^n q}{(2\pi)^n} \frac{1}{(q^2 - K)^j} \ , \tag{A.1}$$

by introducing Feynman parameter integrals (3.7), i.e., (A.1) would have to be integrated with $\mathcal{J}_j$. For example in the case of D_0 in the denominator one obtains with three Feynman parameters $x,\ y,\ z$ running from 0 to 1

$$a(q^2 - m_1^2 + i\epsilon) + b\left[(q+q_1)^2 - m_2^2 + i\epsilon\right] + c\left[(q+q_1+q_2)^2 - m_3^2 + i\epsilon\right] \\ + d\left[(q+q_1+q_2+q_3)^2 - m_4^2 + i\epsilon\right] \ , \tag{A.2}$$

where the parameters $\{a, b, c, d\}$ are arbitrarily assigned to functions of the Feynman parameters: $\{1-x, x(1-y), xy(1-z), xyz\}$. Substituting

$$q \to q + bq_1 + c(q_1+q_2) + d(q_1+q_2+q_3) \ , \tag{A.3}$$

will bring (A.2) in the form $q^2 - K$ with K as given in Tab. 3.1. Next we perform a Wick rotation on (A.1), rotating the energy component

$$q_0 \to ix_1 \ , \quad q_{1,2,\dots,n-1} \to x_{2,3,\dots,n} \ , \tag{A.4}$$

to get an Euclidean integration. So the integral kernel is now $(-1)^j/(r^2+K)^j$ with

$$r^2 \equiv x_1^2 + x_2^2 + \ldots + x_n^2 \ , \tag{A.5}$$

and the integral measure is $id^n x$. Then we switch to n-dimensional spherical coordinates, by setting

$$\begin{aligned} x_k &= r \prod_{i=k}^{n-1} \sin\theta_i \cos\theta_{k-1} \ , \\ x_1 &= r \prod_{i=1}^{n-1} \sin\theta_i \ , \quad x_n = r\cos\theta_{n-1} \ , \end{aligned} \tag{A.6}$$

with $k = 1, \dots, n$. The integration ranges are

$$0 \leq r \leq \infty, \quad 0 \leq \theta_1 \leq 2\pi \quad \text{and} \quad 0 \leq \theta_{k>1} \leq \pi \ . \tag{A.7}$$

From the Jacobian we then get the integration measure $r^{n-1} dr d\Omega_{n-1}$, with

$$d\Omega_{n-1} \equiv \prod_{i=1}^{n-1} \sin^{i-1}\theta_i d\theta_i \ . \tag{A.8}$$

So finally we have for (A.1)

$$\mu^{4-n} i(-1)^j \int dr \frac{r^{n-1}}{(r^2+K)^j} \int \frac{d\Omega_{n-1}}{(2\pi)^n}. \tag{A.9}$$

Using

$$\int_0^\pi d\theta \sin^m\theta = \frac{\sqrt{\pi}\,\Gamma\left(\frac{m+1}{2}\right)}{\Gamma\left(\frac{m+2}{2}\right)} \ , \tag{A.10}$$

we obtain for the angular integration $2(16\pi^2)^{-n/4}/\Gamma\left(\frac{n}{2}\right)$ and the first integration corresponds to a beta function giving $K^{n/2-j} B\left(j - \frac{n}{2}, \frac{n}{2}\right)/2$. So the grand total is

$$\frac{i\mu^{-\varepsilon}}{(16\pi^2)^{1+\varepsilon/4}} (-1)^j K^{-j+2+\varepsilon/2} \frac{\Gamma\left(j-2-\frac{\varepsilon}{2}\right)}{\Gamma(j)} \ , \tag{A.11}$$

where $n = 4 + \varepsilon$ has been put in. Now we note that

$$\begin{aligned} \frac{\Gamma\left(1-\frac{\varepsilon}{2}\right)}{(4\pi)^2} \left(\frac{4\pi\mu^2}{m^2}\right)^{-\varepsilon/2} &= C_\varepsilon \left(1 + \frac{\varepsilon^2}{8}\zeta(2)\right) + \mathcal{O}(\varepsilon^3) \ , \\ \frac{\Gamma\left(j-2-\frac{\varepsilon}{2}\right)}{\Gamma(j)\Gamma\left(1-\frac{\varepsilon}{2}\right)} &= \frac{1}{\left(j-2-\frac{\varepsilon}{2}\right)\left(j-1-\frac{\varepsilon}{2}\right)} \frac{\Gamma\left(j-\frac{\varepsilon}{2}\right)}{\Gamma(j)\Gamma\left(1-\frac{\varepsilon}{2}\right)} \\ &= \frac{1 - \frac{\varepsilon}{2}\sum\limits_{k=1}^{j-1}\frac{1}{k} + \frac{\varepsilon^2}{8}\left[\left(\sum\limits_{k=1}^{j-1}\frac{1}{k}\right)^2 + \sum\limits_{k=1}^{j-1}\frac{1}{k^2}\right] + \mathcal{O}(\varepsilon^3)}{\left(j-2-\frac{\varepsilon}{2}\right)\left(j-1-\frac{\varepsilon}{2}\right)} \ , \end{aligned} \tag{A.12}$$

which directly leads to (3.5).

A.2 Calculation of Basic Scalar Integrals

In the following we will always use the formulae (3.5) to (3.7) and Tab. 3.1. The end results will be given up to $\mathcal{O}(1)$ and imaginary parts from the Feynman parameter integrals will be dropped, as explained in Sec. 3.2. The integrations are, if not mention otherwise, straightforward using standard integration tables like [82, 122] or programs like `Mathematica` [57]. The results are often only obtained after a fair amount of simplification using relations of higher transcendental functions, tabulated for example in [66, 122, 123]. Starting with the 1PF, we have $j = 1$, which directly gives the result

$$A_0(m) = iC_\varepsilon m^2 \left(-\frac{2}{\varepsilon} + 1\right) , \tag{A.13}$$

with $A_0(0) = 0$ in accordance with (3.3).

For the 2PF, with $j = 2$, we notice that the Feynman parameter integration itself cannot result in a pole. Thus we can use a series expansion in ε there, when this simplifies the integration. However, due to the pole of $P_\varepsilon(2)$, we need to expand up to $\mathcal{O}(\varepsilon)$:

$$B_0(k_1, 0, 0) = iC_\varepsilon \left(-\frac{2}{\varepsilon}\right) \int_0^1 dx\, 0^{\frac{\varepsilon}{2}} = 0 , \tag{A.14}$$

$$B_0(k_1, m, m) = iC_\varepsilon \left(-\frac{2}{\varepsilon}\right) \int_0^1 dx\, 1^{\frac{\varepsilon}{2}} = iC_\varepsilon \left(-\frac{2}{\varepsilon}\right) , \tag{A.15}$$

$$\begin{aligned} B_0(p_1, 0, 0) &= iC_\varepsilon \left(-\frac{2}{\varepsilon}\right) \int_0^1 dx\, \left[-x(1-x)\right]^{\frac{\varepsilon}{2}} = iC_\varepsilon \left(-\frac{2}{\varepsilon}\right) (-1)^{\frac{\varepsilon}{2}} \\ &\cdot \left\{1 + \frac{\varepsilon}{2} \int_0^1 dx [\ln x + \ln(1-x)]\right\} = iC_\varepsilon \left(-\frac{2}{\varepsilon} + 2\right) , \end{aligned} \tag{A.16}$$

$$B_0(p_1, 0, m) = iC_\varepsilon \left(-\frac{2}{\varepsilon}\right) \int_0^1 dx\, x^\varepsilon = iC_\varepsilon \left(-\frac{2}{\varepsilon} + 2\right) , \tag{A.17}$$

$$B_0(p_1 + p_2, 0, 0) = \left(\frac{s}{m^2}\right)^{\frac{\varepsilon}{2}} B_0(p_1, 0, 0) = iC_\varepsilon \left(-\frac{2}{\varepsilon} + 2 - \ln \frac{s}{m^2}\right) , \tag{A.18}$$

$$\begin{aligned} B_0(p_1 + p_2, m, m) &= iC_\varepsilon \left(-\frac{2}{\varepsilon}\right) \int_0^1 dx\, \left[1 - x(1-x)\frac{s}{m^2}\right]^{\frac{\varepsilon}{2}} = iC_\varepsilon \left(-\frac{2}{\varepsilon}\right) \\ &\cdot \left\{1 + \frac{\varepsilon}{2} \int_0^1 dx\, \left[\ln(1 - (1+\varkappa)x) + \ln\left(1 - \frac{1+\varkappa}{\varkappa}x\right)\right]\right\} \\ &= iC_\varepsilon \left(-\frac{2}{\varepsilon} + 2 + \beta \ln \varkappa\right) , \end{aligned} \tag{A.19}$$

$$\begin{aligned} B_0(p_1 - k_1, 0, m) &= iC_\varepsilon \left(-\frac{2}{\varepsilon}\right) \int_0^1 dx\, \left[-\frac{t_1}{m^2} x (1 - \frac{t}{t_1} x)\right]^{\frac{\varepsilon}{2}} = iC_\varepsilon \left(-\frac{2}{\varepsilon}\right) \\ &\cdot \left(-\frac{t_1}{m^2}\right)^{\frac{\varepsilon}{2}} \left\{1 + \frac{\varepsilon}{2} \int_0^1 dx\, \left[\ln x + \ln\left(1 - \frac{t}{t_1} x\right)\right]\right\} \end{aligned}$$

$$= iC_\varepsilon \left[-\frac{2}{\varepsilon} + 2 - \frac{t_1}{t} \ln \left(-\frac{t_1}{m^2} \right) \right] , \tag{A.20}$$

where $\beta \equiv \sqrt{1 - 4m^2/s}$ and $\varkappa \equiv (1-\beta)/(1+\beta)$.

For $j = 3$, we begin with three finite 3PF integrals. The $C_0(p_1, -k_1, 0, m, m)$ kernel can be written as $K = x\left[x - (1-x)y\frac{t_1}{m^2}\right]$, which is raised to the power $-1 + \varepsilon/2$. With the additional x in the numerator from (3.7), we get a finite integral, which is evaluated easily upon setting $\varepsilon \to 0$:

$$C_0(p_1, -k_1, 0, m, m) = iC_\varepsilon \frac{1}{t_1} \left[\zeta(2) - \mathrm{Li}_2 \left(\frac{t}{m^2} \right) \right] . \tag{A.21}$$

Turning to $C_0(-k_1, -k_2, m, m, m)$, the integral is obviously finite. With $\varepsilon \to 0$ and the parameters set so that $K = \frac{1-\beta^2-4(1-x)xy}{1-\beta^2}$, the integral over y is simple and leads to an integration over $\frac{\ln[((1-2x)^2-\beta^2)/(1-\beta^2)]}{1-x}$. Substituting $z = 1 - 2x$ and integrating over z gives

$$C_0(-k_1, -k_2, m, m, m) = iC_\varepsilon \frac{1}{s} \left[\frac{1}{2} \ln^2 \varkappa - 3\zeta(2) \right] . \tag{A.22}$$

Next $C_0(p_1, p_2, 0, m, 0)$ is also obviously finite and after setting $\varepsilon \to 0$ most easily calculated by taking $K = -x(1-x)(1-y)(1+\varkappa)^2/\varkappa + x^2 y$, which after integrating x leads to a term $\frac{\ln[-(1+\varkappa)^2(1-y)/(\varkappa y^2)]}{(1+\varkappa-\varkappa y)(1+\varkappa-y)}$, and the final result is

$$C_0(p_1, p_2, 0, m, 0) = iC_\varepsilon \frac{1}{s\beta} \left[2\,\mathrm{Li}_2(-\varkappa) + \frac{1}{2} \ln^2 \varkappa + \zeta(2) \right] . \tag{A.23}$$

The integral $C_0(p_2, p_1, m, 0, m)$ leads to $K = -x^2 y(1-y)\frac{s}{m^2} + x^2$. We thus get separate integrations for x and y, with the x integration simply giving a pole $1/\varepsilon$. The left over y integration is finite and so we can expand up to $\mathcal{O}(1)$, getting a remaining integration over $(\frac{2}{\varepsilon} + \ln r)/r$ with $r \equiv (1 - (1+\varkappa)y)\left(1 - \frac{1+\varkappa}{\varkappa} y\right)$. So in the end

$$C_0(p_2, p_1, m, 0, m) = \frac{iC_\varepsilon}{s\beta} \left[-\frac{2}{\varepsilon} \ln \varkappa - 2 \ln \varkappa \ln(1-\varkappa) - 2\,\mathrm{Li}_2(\varkappa) + \frac{1}{2} \ln^2 \varkappa - 4\zeta(2) \right] . \tag{A.24}$$

$C(-k_1, -k_2, 0, 0, 0)$ is a very simple integral, since with $K = -xy(1-x)\frac{s}{m^2}$ one finds again two separate integrations. The one over y directly gives $2/\varepsilon$ and the one over x corresponds to a beta function $B(1 + \frac{\varepsilon}{2}, \frac{\varepsilon}{2})$, so that the series expansion in ε is

$$C_0(-k_1, -k_2, 0, 0, 0) = iC_\varepsilon \frac{1}{s} \left[\frac{4}{\varepsilon^2} + \frac{2}{\varepsilon} \ln \frac{s}{m^2} + \frac{1}{2} \ln^2 \frac{s}{m^2} - \frac{7}{2}\zeta(2) \right] . \tag{A.25}$$

Finally $C_0(-k_1, p_1, 0, 0, m)$ can be directly integrated to a double pole and a hypergeometric function using $K = (1-x)\left[xy\left(-\frac{t_1}{m^2}\right) + 1 - x\right]$ and with the appropriate expansion for the hypergeometric function (B.6) the result

$$C_0(-k_1,p_1,0,0,m) = \frac{iC_\varepsilon}{t_1}\left[\frac{2}{\varepsilon^2}+\frac{2}{\varepsilon}\ln\left(-\frac{t_1}{m^2}\right)+\ln^2\left(-\frac{t_1}{m^2}\right)+\mathrm{Li}_2\left(\frac{t}{m^2}\right)+\frac{\zeta(2)}{4}\right], \tag{A.26}$$

is obtained. This completes the set of needed 3PFs.

Turning to the box integrals, the calculation of

$$D_0(-k_1,p_1,p_2,0,0,m,0) = \frac{iC_\varepsilon}{st_1}\left[\frac{8}{\varepsilon^2}+\frac{2}{\varepsilon}\left(2\ln\tilde{t}+\ln\tilde{s}\right)+2\ln\tilde{s}\ln\tilde{t}-4\zeta(2)\right], \tag{A.27}$$

is shown in Sec. 3.2. The second 4PF needed is $D_0(-k_1,p_1,-k_2,0,0,m,m)$. The kernel can be chosen as $K = xy\{x[\tilde{t}-(\tilde{t}-1)y]+[\tilde{u}(1-x)-\tilde{t}x(1-y)]z\}$, with $\tilde{t}\equiv -t_1/m^2$ and $\tilde{u}\equiv -u_1/m^2$. We can integrate over $x^2yK^{-2+\varepsilon/2}$ with respect to z to get the result $I_{xy}+II_{xy}$ with

$$\underbrace{-\frac{2x^{-1+\varepsilon}y^{-1+\frac{\varepsilon}{2}}[\tilde{t}-(\tilde{t}-1)y]^{-1+\frac{\varepsilon}{2}}}{(-2+\varepsilon)[\tilde{u}(1-x)-\tilde{t}x(1-y)]}}_{I_{xy}}+\underbrace{\frac{2x^{\frac{\varepsilon}{2}}y^{-1+\frac{\varepsilon}{2}}[\tilde{u}(1-x)+xy]^{-1+\frac{\varepsilon}{2}}}{(-2+\varepsilon)[\tilde{u}(1-x)-\tilde{t}x(1-y)]}}_{II_{xy}}. \tag{A.28}$$

The integration of I_{xy} over x is straightforward:

$$I_y = -\frac{2y^{-1+\frac{\varepsilon}{2}}[\tilde{t}-(\tilde{t}-1)y]^{-1+\frac{\varepsilon}{2}}}{(-2+\varepsilon)\varepsilon\tilde{u}}\,{}_2\mathrm{F}_1\left(1,\varepsilon,1+\varepsilon;\frac{\tilde{u}+\tilde{t}(1-y)}{\tilde{u}}\right). \tag{A.29}$$

The hypergeometric function can be expanded, see (B.5), and we define an appropriate counterterm for the diverging $y\to 0$ limit

$$I_y^c = -\frac{2y^{-1+\frac{\varepsilon}{2}}\tilde{t}^{-1+\frac{\varepsilon}{2}}}{(-2+\varepsilon)\varepsilon\tilde{u}}\left[1-\varepsilon\ln\left(-\frac{\tilde{t}}{\tilde{u}}\right)-\varepsilon^2\,\mathrm{Li}_2\left(1+\frac{\tilde{t}}{\tilde{u}}\right)\right]. \tag{A.30}$$

Integration of the counterterm and adding the integration of the expansion of $I_y - I_y^c$ leads to

$$I = \frac{1}{\tilde{t}\tilde{u}}\left[\frac{2}{\varepsilon^2}+\frac{1+2\ln\tilde{u}}{\varepsilon}+\frac{1}{2}+\frac{\pi^2}{6}-\ln^2\tilde{t}+\ln\tilde{u}+2\ln\tilde{t}\ln\tilde{u}-2\,\mathrm{Li}_2\left(1+\frac{\tilde{t}}{\tilde{u}}\right)\right]. \tag{A.31}$$

Turning to II_{xy} we can expand $x^{e/2}$ because the integral over x does not diverge for $x\to 0$. Starting with order one, $x^{e/2}\to 1$, we get

$$II_y^{\mathcal{O}(1)} = -\frac{4\tilde{u}^{-1+\frac{\varepsilon}{2}}y^{-1+\frac{\varepsilon}{2}}[\tilde{t}-(\tilde{t}-1)y]^{-1+\frac{\varepsilon}{2}}(\tilde{u}-y)^{-\frac{\varepsilon}{2}}}{(-2+\varepsilon)\varepsilon}\left\{-i\varepsilon\pi\eta^{-\frac{\varepsilon}{2}}+\left[(-1)^{\frac{\varepsilon}{2}}\right.\right.$$

$$\left.\left.\cdot\,{}_2\mathrm{F}_1\left(\frac{\varepsilon}{2},\frac{\varepsilon}{2},1+\frac{\varepsilon}{2};\eta\right)-\tilde{t}^{-\frac{\varepsilon}{2}}(1-y)^{-\frac{\varepsilon}{2}}y^{\frac{\varepsilon}{2}}\,{}_2\mathrm{F}_1\left(\frac{\varepsilon}{2},\frac{\varepsilon}{2},1+\frac{\varepsilon}{2};-\frac{y\eta}{\tilde{t}(1-y)}\right)\right]\right\}, \tag{A.32}$$

with $\eta \equiv \frac{\tilde{t}+\tilde{u}-\tilde{t}y}{\tilde{u}-y}$. We use again (B.6) and the $y \to 0$ counterterm is

$$II_y^{\mathcal{O}(1)c} = -\frac{4\tilde{u}^{-1+\frac{\varepsilon}{2}} y^{-1+\frac{\varepsilon}{2}} \tilde{t}^{-1+\frac{\varepsilon}{2}}}{(-2+\varepsilon)\varepsilon} \Bigg\{ - i\varepsilon\pi(\tilde{t}+\tilde{u})^{-\frac{\varepsilon}{2}} + \tilde{u}^{-\frac{\varepsilon}{2}} \cdot \left[(-1)^{\frac{\varepsilon}{2}} \left(1 + \frac{\varepsilon^2}{4} \operatorname{Li}_2\left(1+\frac{\tilde{t}}{\tilde{u}}\right)\right) - \tilde{t}^{-\frac{\varepsilon}{2}} y^{\frac{\varepsilon}{2}} \right] \Bigg\} . \quad (A.33)$$

This again enables us to calculate $II^{\mathcal{O}(1)}$. But there is also the next order of $x^{\varepsilon/2}$ to consider, with $x^{e/2} \to \frac{\varepsilon}{2} \ln x$ in II_{xy}. Since for $y \to 0$ there is no divergence for $x \to 1$ because of the $\ln x$, and since the y-integration can only deliver a $1/\varepsilon$-pole, this is also the last order we have to consider. Furthermore we can set $\varepsilon \to 0$ in $[\tilde{u}(1-x)+xy]^{-1+\varepsilon/2}$ for the same reason and the only term that contributes after partial fractioning is

$$I_{xy}^{\mathcal{O}(\varepsilon)} = \frac{\varepsilon y^{-1+\frac{\varepsilon}{2}} \ln x}{(-2+\varepsilon)(\tilde{u}(1-x)-\tilde{t}x)(1-x)\tilde{u}} , \quad (A.34)$$

which can be easily integrated. So the sum becomes

$$II = \frac{1}{\tilde{t}\tilde{u}} \left[\frac{2}{\varepsilon^2} + \frac{1+2\ln\tilde{t}}{\varepsilon} + \frac{1}{2} - \frac{5\pi^2}{6} + \ln\tilde{t} + \ln^2\tilde{t} + 2\operatorname{Li}_2\left(1+\frac{\tilde{t}}{\tilde{u}}\right) \right] , \quad (A.35)$$

and we obtain the final result

$$D_0(-k_1,p_1,-k_2,0,0,m,m) = \frac{iC_\varepsilon}{t_1 u_1} \left\{ \frac{4}{\varepsilon^2} + \frac{2}{\varepsilon}\left[\ln\tilde{t} + \ln\tilde{u}\right] + 2\ln\tilde{t}\ln\tilde{u} - \frac{7\zeta(2)}{2} \right\} . \quad (A.36)$$

The last box integral needed is $D_0(p_1,-k_1,-k_2,0,m,m,m)$. We can write the kernel as $K = \frac{x}{\varkappa}\left\{x\left[\varkappa-(1+\varkappa)^2(1-y)y\right] + \left[\varkappa\tilde{t}(1-x)+(1+\varkappa)^2 x(1-y)\right] yz\right\}$, so we get for the z-integration $I_{xy} + II_{xy}$, with

$$\begin{aligned} I_{xy} &= \frac{2\varkappa x^{\frac{\varepsilon}{2}}\left(x+\tilde{t}(1-x)y\right)^{-1+\frac{\varepsilon}{2}}}{(-2+\varepsilon)\left[x+\varkappa\left(\tilde{t}+(2+\varkappa-\tilde{t})x\right)-(1+\varkappa)^2 xy\right]} , \\ II_{xy} &= -\frac{2\varkappa^{2-\frac{\varepsilon}{2}} x^{-1+\varepsilon}\left[x-(1+\varkappa)^2(1-y)y\right]^{-1+\frac{\varepsilon}{2}}}{(-2+\varepsilon)\left[x+\varkappa\left(\tilde{t}+(2+\varkappa-\tilde{t})x\right)-(1+\varkappa)^2 xy\right]} . \end{aligned} \quad (A.37)$$

The integration of I_{xy} does not diverge and one easily gets upon setting $\varepsilon \to 0$

$$I = \frac{m^4}{\beta s t_1}\left[\ln^2\varkappa + 4\operatorname{Li}_2(-\varkappa) + \frac{\pi^2}{3}\right] . \quad (A.38)$$

Integrating II_{xy} over x gives

$$II_y = -\frac{2\varkappa^{1-\frac{\varepsilon}{2}}\left[\varkappa-(1+\varkappa)^2(1-y)y\right]^{-1+\frac{\varepsilon}{2}} {}_2\mathrm{F}_1\left(1,\varepsilon,1+\varepsilon,1-\frac{(1+\varkappa)^2(1-y)}{\varkappa\tilde{t}}\right)}{(-2+\varepsilon)\varepsilon\tilde{t}} . \quad (A.39)$$

The integration over y does not give an additional pole, so we can expand to $\mathcal{O}(1)$ using (B.5) and then integrate to obtain

$$II = -\frac{m^4}{\beta s t_1}\left\{\frac{2\ln\varkappa}{\varepsilon} + \ln\varkappa\left[1 + 2\ln\beta + \ln\varkappa + 2\ln\tilde{t}\right] + \mathrm{Li}_2\left(\varkappa^2\right) + \frac{5\pi^2}{6}\right\} . \quad \text{(A.40)}$$

The final result is then

$$\begin{aligned} D_0(p_1, -k_1, -k_2, 0, m, m, m) \\ = -\frac{iC_\varepsilon}{\beta s t_1}\left\{\frac{2}{\varepsilon}\ln\varkappa + 2\left[\ln\varkappa\ln(\beta\tilde{t}) - \mathrm{Li}_2(-\varkappa) + \mathrm{Li}_2(\varkappa)\right] + 3\zeta(2)\right\} . \quad \text{(A.41)}\end{aligned}$$

This recalculation of the needed basic scalar integrals is in complete agreement with the results presented in [44].

A.3 Passarino-Veltman Decomposition

In Sec. 3.3 the necessary projection mechanisms for the decomposition of the tensor integrals was constructed. Here we list the obtained formulae. Auxiliary coefficients are named like in [67], to facilitate comparisons. Two additional relations as compared to [67] will be derived to complete the consistency checks, i.e., for every coefficient that can be obtained in more than one way at least two equations are given. Of course, all consistency checks were successful. The notation for scalar integrals used here follows the conventions employed in Sec. 3.3: Any non-standard product of propagators in integrals of the form (3.4) is indicated by listing the numbers i of the propagator functions L_i in brackets. From (3.4) we have as standard 2PF and 3PF $B_0 = B_0(1,2)$ and $C_0 = C_0(1,2,3)$, respectively. Naturally there is only one 1PF $A_0 = A_0(1) = A_0(2) = A_0(3) = A_0(4)$, since we can always redefine the loop momentum. Furthermore, there are only four external particles in our (virtual) subprocesses, so the standard $D_0 = D_0(1,2,3,4)$ is the *only* 4PF that occurs here. There is one non-standard 2PF: $B_0(2,3)$, see (3.27), and there are three non-standard 3PFs: $C_0(1,2,4)$, $C_0(1,3,4)$ and $C_0(2,3,4)$. The first two can be found in the example given in (3.19) and $C_0(2,3,4)$ then corresponds to

$$\begin{aligned} C_0(2,3,4) &= \mu^{-\varepsilon}\int\frac{d^nq}{(2\pi)^n}\frac{1}{\left[(q+q_1)^2 - m_2^2\right]\left[(q+q_1+q_2)^2 - m_3^2\right]\left[(q+q_1+q_2+q_3)^2 - m_4^2\right]} \\ &= \mu^{-\varepsilon}\int\frac{d^nq}{(2\pi)^n}\frac{1}{(q^2 - m_2^2)\left[(q+q_2)^2 - m_3^2\right]\left[(q+q_2+q_3)^2 - m_4^2\right]} . \end{aligned} \quad \text{(A.42)}$$

The tensor 2PF coefficients are

$$B_1 = \frac{1}{2q_1^2}[f_1 B_0 + A_0(m_1) - A_0(m_2)] , \quad \text{(A.43)}$$

$$B_{21} = \frac{1}{q_1^2}\left\{\frac{1}{2}[f_1 B_1 + A_0(m_2)] - B_{22}\right\} , \quad \text{(A.44)}$$

C_a	C_b	M_a	M_b
C_{11}	C_{12}	R_1	R_2
C_{21}	C_{23}	$R_3 - C_{24}$	R_4
C_{23}	C_{22}	R_5	$R_6 - C_{24}$
C_{35}	C_{36}	R_{10}	R_{11}
C_{31}	C_{33}	$R_{12} - 2C_{35}$	R_{13}
C_{34}	C_{32}	R_{14}	$R_{15} - 2C_{36}$
C_{33}	C_{34}	$R_{16} - C_{36}$	$R_{17} - C_{35}$

Table A.1: The Passarino-Veltman matrix coefficients of the 3PFs, to be inserted in (A.47). The R_i are shown in (A.48).

$$B_{22} = \frac{1}{n-1}\left\{m_1^2 B_0 - \frac{1}{2}[f_1 B_1 - A_0(m_2)]\right\} \ . \tag{A.45}$$

For the 3PFs we have one scalar equation

$$C_{24} = \frac{1}{n-2}[B_0(2,3) + m_1^2 C_0 - R_3 - R_6] \ , \tag{A.46}$$

and the R_i are given in (A.48) below. The rest is in matrix form

$$\begin{pmatrix} C_a \\ C_b \end{pmatrix} = X_C^{-1} \begin{pmatrix} M_a \\ M_b \end{pmatrix} \ , \tag{A.47}$$

and the combinations are presented in Tab. A.1.

The R-coefficients of the 3PFs are

$$\begin{aligned}
R_1 &= \frac{1}{2}[f_1 C_0 + B_0(1,3) - B_0(2,3)] \ , & R_2 &= \frac{1}{2}[f_2 C_0 + B_0(1,2) - B_0(1,3)] \ , \\
R_3 &= \frac{1}{2}[f_1 C_{11} + B_1(1,3) + B_0(2,3)] \ , & R_4 &= \frac{1}{2}[f_2 C_{11} + B_1(1,2) - B_1(1,3)] \ , \\
R_5 &= \frac{1}{2}[f_1 C_{12} + B_1(1,3) - B_1(2,3)] \ , & R_6 &= \frac{1}{2}[f_2 C_{12} - B_1(1,3)] \ , \\
R_{10} &= \frac{1}{2}[f_1 C_{24} + B_{22}(1,3) - B_{22}(2,3)] \ , & R_{11} &= \frac{1}{2}[f_2 C_{24} + B_{22}(1,2) - B_{22}(1,3)] \ , \\
R_{12} &= \frac{1}{2}[f_1 C_{21} + B_{21}(1,3) - B_0(2,3)] \ , & R_{13} &= \frac{1}{2}[f_2 C_{21} + B_{21}(1,2) - B_{21}(1,3)] \ , \\
R_{14} &= \frac{1}{2}[f_1 C_{22} + B_{21}(1,3) - B_{21}(2,3)] \ , & R_{15} &= \frac{1}{2}[f_2 C_{22} - B_{21}(1,3)] \ ,
\end{aligned}$$

D_a	D_b	D_c	M_a	M_b	M_c
D_{11}	D_{12}	D_{13}	R_{20}	R_{21}	R_{22}
D_{21}	D_{24}	D_{25}	$R_{30} - D_{27}$	R_{31}	R_{32}
D_{24}	D_{22}	D_{26}	R_{33}	$R_{34} - D_{27}$	R_{35}
D_{25}	D_{26}	D_{23}	R_{36}	R_{37}	$R_{38} - D_{27}$
D_{311}	D_{312}	D_{313}	R_{40}	R_{41}	R_{42}
D_{31}	D_{34}	D_{35}	$R_{43} - 2D_{311}$	R_{44}	R_{45}
D_{36}	D_{32}	D_{38}	R_{46}	$R_{47} - 2D_{312}$	R_{48}
D_{37}	D_{39}	D_{33}	R_{49}	R_{50}	$R_{51} - 2D_{313}$
D_{34}	D_{36}	D_{310}	$R_{52} - D_{312}$	$R_{53} - D_{311}$	R_{54}
D_{35}	D_{310}	D_{37}	$R_{55} - D_{313}$	R_{56}	$R_{57} - D_{311}$
D_{310}	D_{38}	D_{39}	R_{58}	$R_{59} - D_{313}$	$R_{60} - D_{312}$

Table A.2: The Passarino-Veltman matrix coefficients of the 4PFs, to be inserted in (A.50). The R_i are shown in (A.51). The last two rows show results that complete the set of consistency checks.

$$R_{16} = \frac{1}{2}[f_1 C_{23} + B_{21}(1,3) + B_1(2,3)] \,, \qquad R_{17} = \frac{1}{2}[f_2 C_{23} - B_{21}(1,3)] \,. \tag{A.48}$$

In the 4PFs we also have only one scalar equation

$$D_{27} = \frac{1}{n-3}[C_0(2,3,4) + m_1^2 D_0 - R_{30} - R_{34} - R_{38}] \,, \tag{A.49}$$

and the R_i can be found in (A.51) below. The rest is again in matrix form

$$\begin{pmatrix} D_a \\ D_b \\ D_c \end{pmatrix} = X_D^{-1} \begin{pmatrix} M_a \\ M_b \\ M_c \end{pmatrix} \,, \tag{A.50}$$

and the combinations are presented in Tab. A.2. The R-coefficients of the 4PFs are

$$R_{20} = \frac{1}{2}[f_1 D_0 + C_0(1,3,4) - C_0(2,3,4)] \,, \qquad R_{21} = \frac{1}{2}[f_2 D_0 + C_0(1,2,4) - C_0(1,3,4)] \,,$$
$$R_{22} = \frac{1}{2}[f_3 D_0 + C_0(1,2,3) - C_0(1,2,4)] \,, \qquad R_{30} = \frac{1}{2}[f_1 D_{11} + C_{11}(1,3,4) + C_0(2,3,4)] \,,$$

$$
\begin{aligned}
R_{31} &= \frac{1}{2}[f_2 D_{11} + C_{11}(1,2,4) - C_{11}(1,3,4)]\,, \quad R_{32} = \frac{1}{2}[f_3 D_{11} + C_{11}(1,2,3) - C_{11}(1,2,4)]\,,\\
R_{33} &= \frac{1}{2}[f_1 D_{12} + C_{11}(1,3,4) - C_{11}(2,3,4)]\,, \quad R_{34} = \frac{1}{2}[f_2 D_{12} + C_{12}(1,2,4) - C_{11}(1,3,4)]\,,\\
R_{35} &= \frac{1}{2}[f_3 D_{12} + C_{12}(1,2,3) - C_{12}(1,2,4)]\,, \quad R_{36} = \frac{1}{2}[f_1 D_{13} + C_{12}(1,3,4) - C_{12}(2,3,4)]\,,\\
R_{37} &= \frac{1}{2}[f_2 D_{13} + C_{12}(1,2,4) - C_{12}(1,3,4)]\,, \quad R_{38} = \frac{1}{2}[f_3 D_{13} - C_{12}(1,2,4)]\,,\\
R_{40} &= \frac{1}{2}[f_1 D_{27} + C_{24}(1,3,4) - C_{24}(2,3,4)]\,, \quad R_{41} = \frac{1}{2}[f_2 D_{27} + C_{24}(1,2,4) - C_{24}(1,3,4)]\,,\\
R_{42} &= \frac{1}{2}[f_3 D_{27} + C_{24}(1,2,3) - C_{24}(1,2,4)]\,, \quad R_{43} = \frac{1}{2}[f_1 D_{21} + C_{21}(1,3,4) - C_{0}(2,3,4)]\,,\\
R_{44} &= \frac{1}{2}[f_2 D_{21} + C_{21}(1,2,4) - C_{21}(1,3,4)]\,, \quad R_{45} = \frac{1}{2}[f_3 D_{21} + C_{21}(1,2,3) - C_{21}(1,2,4)]\,,\\
R_{46} &= \frac{1}{2}[f_1 D_{22} + C_{21}(1,3,4) - C_{21}(2,3,4)]\,, \quad R_{47} = \frac{1}{2}[f_2 D_{22} + C_{22}(1,2,4) - C_{21}(1,3,4)]\,,\\
R_{48} &= \frac{1}{2}[f_3 D_{22} + C_{22}(1,2,3) - C_{22}(1,2,4)]\,, \quad R_{49} = \frac{1}{2}[f_1 D_{23} + C_{22}(1,3,4) - C_{22}(2,3,4)]\,,\\
R_{50} &= \frac{1}{2}[f_2 D_{23} + C_{22}(1,2,4) - C_{22}(1,3,4)]\,, \quad R_{51} = \frac{1}{2}[f_3 D_{23} - C_{22}(1,2,4)]\,,\\
R_{52} &= \frac{1}{2}[f_1 D_{24} + C_{21}(1,3,4) + C_{11}(2,3,4)]\,, \quad R_{53} = \frac{1}{2}[f_2 D_{24} + C_{23}(1,2,4) - C_{21}(1,3,4)]\,,\\
R_{54} &= \frac{1}{2}[f_3 D_{24} + C_{23}(1,2,3) - C_{23}(1,2,4)]\,, \quad R_{55} = \frac{1}{2}[f_1 D_{25} + C_{23}(1,3,4) + C_{12}(2,3,4)]\,,\\
R_{56} &= \frac{1}{2}[f_2 D_{25} + C_{23}(1,2,4) - C_{23}(1,3,4)]\,, \quad R_{57} = \frac{1}{2}[f_3 D_{25} - C_{23}(1,2,4)]\,,\\
R_{49} &= \frac{1}{2}[f_1 D_{26} + C_{23}(1,3,4) - C_{23}(2,3,4)]\,, \quad R_{50} = \frac{1}{2}[f_2 D_{26} + C_{22}(1,2,4) - C_{23}(1,3,4)]\,,\\
R_{51} &= \frac{1}{2}[f_3 D_{26} - C_{22}(1,2,4)]\,. \qquad \text{(A.51)}
\end{aligned}
$$

Appendix B

Some Technical Issues

B.1 Series Expansion of Hypergeometric Functions

In the calculation of integrals in dimensional regularization one often obtains hypergeometric functions ${}_2\mathrm{F}_1(a, b, c; z)$, in which the parameters a, b and c depend on the "hat space" dimension parameter ε. This is due to integrals having forms similar to

$$ {}_2\mathrm{F}_1(a, b, c; z) = \frac{\Gamma(c)}{\Gamma(b)\Gamma(c-b)} \int_0^1 dt\, \frac{t^{b-1}(1-t)^{c-b-1}}{(1-tz)^a} \quad \text{for } Re(c) > Re(b) > 0\,. \qquad \text{(B.1)} $$

A straightforward evaluation or even worse further integration of the hypergeometric function for non-integer values of a, b, c is usually not feasible. On the other hand a series expansion in ε of these functions is sufficient, if we can obtain the appropriate order. In our calculations the strongest poles are $\mathcal{O}(1/\varepsilon^2)$, so that at most a series expansion to $\mathcal{O}(\varepsilon^2)$ is necessary. There are a few expansions collected in the literature, for example in [65], but we have found no comment on how they were obtained. The following efficient method may have been too simple to be mentioned explicitly.

The hypergeometric functions are solutions of the following differential equation and boundary condition:

$$ z(1-z)w''(z) + [c - (a+b+1)z]w'(z) - abw(z) = 0 \quad \text{with} \quad w(0) = 1\,, \qquad \text{(B.2)} $$

in which the derivative is with respect to z. Now we simply set for finite[1] ${}_2\mathrm{F}_1$

$$ w(z) = r(z) + \varepsilon s(z) + \varepsilon^2 t(z) + \ldots \qquad \text{(B.3)} $$

In our case the first three terms are sufficient. By inserting (B.3) and the ε-dependent values of a, b and c in (B.2) and expanding the differential equation in ε, we obtain a system of simpler differential equations, since each coefficient of the powers of ε has to be

[1]One can always use linear transformations of ${}_2\mathrm{F}_1$ to move a $\varepsilon \to 0$ divergence in a, b, c out of the hypergeometric function.

zero. These equations are coupled, but since the parameters a, b and c have no poles in ε, we can proceed step by step: first at $\mathcal{O}(1)$ we can obtain $r(z)$, which is then inserted in the $\mathcal{O}(\varepsilon)$ differential equation to get $s(z)$ and so on. Furthermore (B.2) means that we get the boundary conditions $r(0) = 1$ and $s(z) = t(z) = \ldots = 0$.

An example should make this clear, ${}_2\mathrm{F}_1(1, \varepsilon, 1+\varepsilon; z)$ leads to the following set of differential equations:

$$\left.\begin{matrix} \mathcal{O}(1) \\ \mathcal{O}(\varepsilon) \\ \mathcal{O}(\varepsilon^2) \end{matrix}\right\} \Rightarrow \begin{cases} (1-2z)r' + (1-z)zr'' = 0 \\ -r + (1-z)r' + (1-2z)s' + (1-z)zs'' = 0 \\ -s + (1-z)s' + (1-2z)t' + (1-z)zt'' = 0 \, . \end{cases} \tag{B.4}$$

Solving the $\mathcal{O}(1)$ part with $r(0) = 1$ yields $r(z) = 1$. This we can put in the $\mathcal{O}(\varepsilon)$ part and using $s(z) = 0$ we have $s(z) = -\ln(1-z)$. Finally inserting $r(z)$ and $s(z)$ into the $\mathcal{O}(\varepsilon^2)$ equation with $t(0) = 0$ leads to $t(z) = -\operatorname{Li}_2(z)$. Putting all together we have

$${}_2\mathrm{F}_1(1, \varepsilon, 1+\varepsilon; z) = 1 - \varepsilon \ln(1-z) - \varepsilon^2 \operatorname{Li}_2(z) + \mathcal{O}(\varepsilon^3) \, . \tag{B.5}$$

Other needed hypergeometric functions, which can be easily obtained using this method, are

$$\begin{aligned} {}_2\mathrm{F}_1(1, -\varepsilon, 1+\varepsilon; z) &= 1 + \varepsilon \ln(1-z) + \varepsilon^2 \left[\ln^2(1-z) + \operatorname{Li}_2(z)\right] + \mathcal{O}(\varepsilon^3) \, , \\ {}_2\mathrm{F}_1(\varepsilon, 1+\varepsilon, 2+\varepsilon; z) &= 1 - \varepsilon \left[1 + \frac{1-z}{z} \ln(1-z)\right] + \mathcal{O}(\varepsilon^2) \, , \\ {}_2\mathrm{F}_1(\varepsilon, \pm\varepsilon, 1+\varepsilon; z) &= 1 \pm \varepsilon^2 \operatorname{Li}_2(z) + \mathcal{O}(\varepsilon^3) \, , \\ {}_2\mathrm{F}_1(1, 1+\varepsilon, 2+\varepsilon; z) &= -\frac{\ln(1-z)}{z} - \varepsilon \frac{1}{z} \left[\ln(1-z) + \operatorname{Li}_2(z)\right] + \mathcal{O}(\varepsilon^2) \, . \end{aligned} \tag{B.6}$$

Sometimes it is simpler to use the differentiation properties of the hypergeometric function directly. For example using the above method it is straightforward to obtain

$${}_2\mathrm{F}_1\left(1, 1+\frac{\varepsilon}{2}, 2+\varepsilon; z\right) = -\frac{\ln(1-z)}{z} - \frac{\varepsilon}{z}\left[\ln(1-z) + \frac{1}{4}\ln^2(1-z) + \operatorname{Li}_2(z)\right] + \mathcal{O}(\varepsilon^2) \, . \tag{B.7}$$

But it becomes increasingly difficult to solve ${}_2\mathrm{F}_1\left(1, 1+\frac{\varepsilon}{2}, 2+\varepsilon+k; z\right)$ for growing k. Instead one can employ the formula

$$\frac{\partial^k}{\partial z^k}\left[(1-z)^{a+b-c}\, {}_2\mathrm{F}_1(a, b, c; z)\right] = \frac{(c-a)_k (c-b)_k}{(c)_k} (1-z)^{a+b-c-k}\, {}_2\mathrm{F}_1(a, b, c+k; z) \, , \tag{B.8}$$

where $(x)_k \equiv \Gamma(x+k)/\Gamma(x)$ is the Pochhammer symbol. Since the differentiation with respect to z of (B.7) is simple, we can quickly obtain the needed results. There are several differentiation formulae to be found in the literature, see for example [66].

B.2 Dilogarithmic and Logarithmic Branch Cuts

The dilogarithm Li_2 is defined by

$$\mathrm{Li}_2(x) \equiv -\int_0^1 dy \frac{\ln(1-yx)}{y} = -\int_0^x dy \frac{\ln(1-y)}{y} \ . \tag{B.9}$$

We use the common prescription for the branch cut of the complex logarithm, i.e., we place it along the negative real axis from 0 to $-\infty$. That means for real x

$$\begin{aligned} \ln(x \pm i\epsilon) &= \ln|x| \pm i\pi\Theta(-x) \ , \\ \lim_{\epsilon\to 0+}[\ln(x+i\epsilon) - \ln(x-i\epsilon)] &\overset{x\leq 0}{=} 2i\pi \ . \end{aligned} \tag{B.10}$$

So by using (B.9) we find for the discontinuity of the dilogarithm

$$\lim_{\epsilon\to 0+}[\mathrm{Li}_2(x+i\epsilon) - \mathrm{Li}_2(x-i\epsilon)] \overset{x\geq 1}{=} 2i\pi \ln x \ , \tag{B.11}$$

at the branch cut extending from 1 to ∞ on the real axis.

One often uses relations like the following [122] for the transformation of the dilogarithms:

$$\begin{aligned} \mathrm{Li}_2(y) + \mathrm{Li}_2(1-y) &= -\ln(y)\ln(1-y) + \zeta(2) \ , \\ \mathrm{Li}_2(y) + \mathrm{Li}_2\left(\frac{1}{y}\right) &= -\frac{1}{2}\ln^2(-y) - \zeta(2) \ , \\ \mathrm{Li}_2(y) - \mathrm{Li}_2\left(\frac{y-1}{y}\right) &= -\ln(y)\ln(1-y) + \frac{1}{2}\ln^2(y) + \zeta(2) \ , \\ \mathrm{Li}_2(y) + \mathrm{Li}_2\left(\frac{y}{y-1}\right) &= -\frac{1}{2}\ln^2(1-y) \ , \\ \mathrm{Li}_2(y) + \mathrm{Li}_2(-y) &= \frac{1}{2}\mathrm{Li}_2(y^2) \ . \end{aligned} \tag{B.12}$$

So if we have arguments which are slightly shifted to the imaginary, in order to stay away from the (di)logarithmic branch cuts, in principle we would have to carefully consider to which side we have shifted, see (B.11). But as explained in Sec. 3.2, we can drop all purely imaginary parts anyway. Since the dilogarithms only occur linearly with real coefficients, we can actually ignore the problems completely for the dilogarithms and just compute their *real* parts.

On the other hand logarithms do occur squared or with partly imaginary coefficients, so we have to use (B.10), or we will not be able to correctly calculate the π^2-terms of the integrals. An efficient way of proceeding is to simply calculate with the kernels K of Tab. 3.1 as if the causal $i\epsilon$ was not there. Then in the end logarithms occur which have arguments *on* the branch cut. We can now treat the original kinematic invariants occurring in the logarithms as if they had small positive imaginary parts. For example, we find in the kernel the term $\ldots - ac(q_1+q_2)^2/m^2 + \ldots - i\epsilon$. Say $q_1 = k_1$ and $q_2 = k_2$, then $(q_1+q_2)^2 = s$. Now a, c, m are positive and we can consider s to have a small positive imaginary part in order to preserve the correct shift away from the branch cut, e.g.,

$$\ln\left(-\frac{s}{m^2}\right) \to \ln\left(-\frac{s+i\epsilon m^2}{m^2}\right) = \ln\left(\frac{s}{m^2}\right) - i\pi \; . \tag{B.13}$$

In cases where the argument of the logarithm is a complicated function of the original variable, we can perform a series expansion of it in ϵ, e.g.,

$$\ln\left(-\frac{\varkappa}{1-\varkappa}\right) \to \ln\left(-\frac{\varkappa}{1-\varkappa} + i\epsilon\frac{m^4}{s^2\beta^3}\right) = \ln(\varkappa) - \ln(1-\varkappa) + i\pi \; , \tag{B.14}$$

where $\varkappa = (1-\beta)/(1+\beta)$ and $\beta = \sqrt{1-4m^2/s}$. Using these methods one arrives at the correct *real* parts of the integrals, which are needed exclusively here.

B.3 Calculation of $SU(N)$ Color-Factors

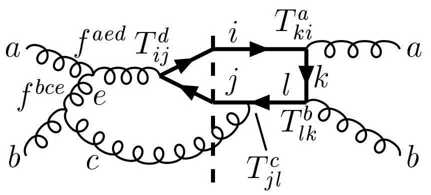

(a) $f^{aed}f^{bce}\mathrm{Tr}\left\langle T^aT^dT^cT^b\right\rangle$

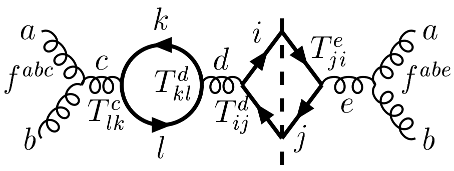

(b) $f^{abc}f^{abe}\mathrm{Tr}\left\langle T^cT^d\right\rangle \mathrm{Tr}\left\langle T^dT^e\right\rangle$

Figure B.1: Contributions to the real (a) and the virtual (b) NLO squared matrix element occurring in hadroproduction are used to illustrate the pairing of all occurring color indices.

In calculating a cross section, one obviously has to sum over all the color degrees of freedom of the internally exchanged particles. But since observable hadrons are "white", i.e., carry no color, there is no information at all on the color of their (unobserved) partons. These partons enter as external particles in the partonic subprocess, so one also has to sum over all their colors. Thus *all* color indices are summed over in the partonic subprocess[2]. Furthermore as Fig. B.1 indicates, the Feynman rules will always result in *paired* color indices for the squared matrix elements. The external particles have to match in colors to be coherently added and the internal particles couple at two points. We will see below, that then for every squared QCD matrix element one finds that the color structure of the particles is reduced to a *number* which multiplies a colorless squared matrix element similar to what one gets in a QED calculation. These numbers are called color-factors and

[2]To obtain a proper normalization one should *average* over the incoming color states, i.e., divide the sum over color indices of incoming partons by their total number of colors.

we can calculate them independently of the remaining colorless squared matrix elements. Though the calculation is rather simple in principle, it quickly becomes tedious for the multiple color exchanges in higher orders. In the following an algorithm for calculating $SU(N)$ color factors is described which was inspired by the general ideas of [124].

First let us specify the notation for the N^2-1 independent $N \times N$-matrix generators, which yield the lowest-dimensional representation of the Lie algebra of $SU(N)$:

$$T^a_{ij} = \frac{1}{2}\lambda^a_{ij}\ , \quad \mathrm{Tr}\left\langle T^a\right\rangle = 0\ , \quad \mathrm{Tr}\left\langle T^a T^b\right\rangle = \frac{1}{2}\delta^{ab}\ , \tag{B.15}$$

$$[T^a, T^b] = if^{abc}T^c\ , \quad \{T^a, T^b\} = \frac{1}{N}\delta^{ab}\mathbb{1}_N + d^{abc}T^c\ . \tag{B.16}$$

Here and below the fundamental ("quark") indices range over $i, j, \ldots = 1, 2, \ldots, N$ and are written as subscripts. In QCD, the quarks are in the fundamental representation of $SU(3)_{\text{color}}$. The fundamental representation has the dimension N, i.e., in QCD the quarks have $N = N_C = 3$ color states. The adjoint ("gluon") indices range over $a, b, \ldots = 1, 2, \ldots, N^2-1$ and are written as superscripts. The gluons of QCD are in the adjoint representation of $SU(3)_{\text{color}}$. The adjoint representation has the dimension N^2-1, since a special unitary group has N^2-1 generators. Thus in QCD there are $N_C^2-1 = 8$ gluon color states. The structure constants f^{abc} and d^{abc} are totally antisymmetric and symmetric, respectively, under the interchange of any two indices. The λ^a matrices correspond to those introduced by Gell-Mann [125] in the case of $SU(3)$. The notation is valid for $SU(N)$, but commonly used only for $SU(3)$. For $SU(2)$ the conventional notation is recovered by setting $(\lambda^a, f^{abc}, d^{abc}) \to (\sigma^a, \epsilon^{abc}, 0)$ with the Pauli matrices σ^a and the Levi-Civita tensor ϵ^{abc}.

The central relations employed in the automatic evaluation of color-factors are

$$T^a_{ij}T^a_{kl} = \frac{1}{2}\left[\delta_{il}\delta_{jk} - \frac{1}{N}\delta_{ij}\delta_{kl}\right]\ , \tag{B.17}$$

$$f^{abc} = -2i\mathrm{Tr}\left\langle T^a[T^b, T^c]\right\rangle\ , \quad d^{abc} = 2\mathrm{Tr}\left\langle T^a\{T^b, T^c\}\right\rangle\ . \tag{B.18}$$

Any structure constants appearing[3] can be turned into strings of generators using the trace relations with the (anti)commutator of generators in (B.18). Since all "gluon" color indices come in pairs, relation (B.17) is sufficient to reduce the corresponding collection of generators into δ-functions of "quark" indices. Thus repeated application of this relation results in a color sum over δ-functions, which yields the wanted color-factor.

In order to speed up the process it is also helpful to use (B.16) to reduce terms like like $f^{abc}T^a$ to terms with two generators directly, instead of having four generators in an intermediate step upon rewriting f^{abc} with the help of (B.18). Also

$$T^a_{ij}T^b_{ji} = \mathrm{Tr}\left\langle T^a T^b\right\rangle = \frac{1}{2}\delta^{ab} \tag{B.19}$$

[3] In QCD only f^{abc} will enter due to the gluon self-coupling.

can be used to quickly reduce some color structures. In QCD they will occur for (potentially cut) "bubbles" of quarks, see graph (b) of Fig. B.1. Of course then some trivial relations like $\delta^{ab}T^b = T^a$ have to be built into the program as well. A nice feature of this automatic procedure is that it does not rely on "advanced" color relations like $\mathrm{Tr}\left\langle T^aT^bT^aT^c\right\rangle = -\delta^{bc}/(4N)$. Thus one does not have to worry about building up traces and applying rules in the correct order. In particular it is enough to write down the color structure of the occurring *amplitudes*. Say M_i has a color structure c_i, then to obtain the color-factor of the squared matrix element $M_iM_j^*$ one can simply use $c_ic_j^T$, with the transpose of c_j generated automatically, without first analyzing which traces may be formed. So obtaining the color factors with the program basically proceeds as fast as one can define the c_i and enter the needed combinations into the program.

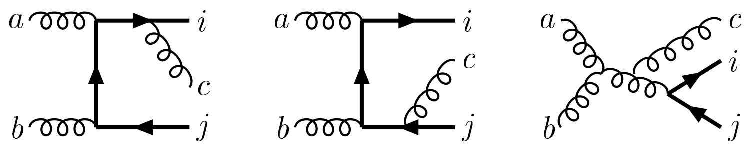

$M_I,\ c_I$ $M_{II},\ c_{II}$ $M_{III},\ c_{III}$

Figure B.2: Three real NLO amplitudes occurring in hadroproduction serve as examples for the calculation of color-factors. The naming of matrix elements M_i and color-structures c_i is indicated. Note that in the `Mathematica` [57] syntax $c_I \curvearrowright$ `cI` etc.

For example, the color definitions entered in the `Mathematica` [57] program for the three sample graphs in Fig. B.2 would be simply `cI=L[c,a,b,i,j]`, `cII=L[a,b,c,i,j]` and `cIII=T[d,i,j] f[a,b,e] f[e,d,c]`. Here `T[d,i,j]` $\curvearrowright T^d_{ij}$, `f[a,b,e]` $\curvearrowright f^{abe}$ and the `L[a,b, ... ,i,j]` function automatically constructs a string of generators by inserting auxiliary "quark" indices, e.g., `L[c,a,b,i,j]` $\to$ `T[c,i,k] T[a,k,l] T[b,l,j]`. The color-factor of $M_IM_{II}^*$ is then obtained by typing `su[cI t[cII]]/(N^2-1)^2`, where the function `t[c]` generates c^T, the function `su[c]` calculates the color factor according to the method described above and we have divided by $(N^2-1)^2$ to average over the two incoming gluon color indices. The result is $\frac{1}{8N^2(N^2-1)}$. Furthermore `su[cI t[cIII]]/(N^2-1)^2` gives $-\frac{N^2}{8(N^2-1)}$ and `su[cII t[cIII]]/(N^2-1)^2` yields $\frac{N^2}{8(N^2-1)}$.

It is often advantageous to decompose the color factors into different parts in order to collect the matrix elements. We have chosen to rewrite them in terms of the Casimir operator color factors $C_F \equiv \frac{N^2-1}{2N}$ and $C_A \equiv N$. In the real gluon-gluon matrix elements, of which Fig. B.2 shows three examples, all color factors have a common factor $\frac{1}{8(N^2-1)}$ and the rest can be decomposed into linear combinations of $(2C_F)^2$, C_A^2 and 1. So the total result can be organized into three different color parts. On one hand this allows cancellations between different squared matrix elements to take place and on the other hand we can directly obtain results which have similar colorless amplitudes. For example the corresponding real photon-photon matrix element result can be read off as the $(2C_F)^2$

coefficient. But one has to keep in mind that this decomposition is not unique, but rather a tool for efficiently organizing the results.

B.4 Two Useful Slavnov-Taylor Identities

Instead of employing the most general Slavnov-Taylor identity in its functional form to derive our special result, we use the fact that the Green's functions themselves are directly invariant under Becchi-Rouet-Stora (BRS) transformations [75], see for example [126, 50]. The BRS transformations are given by

$$\begin{aligned} \delta_{\mathrm{BRS}} A^a_\mu &= \delta\omega D^{ab}_\mu \xi^b \ , \\ \delta_{\mathrm{BRS}} \xi^a &= -\frac{1}{2} g_r f^{abc} \xi^b \xi^c \delta\omega \ , \\ \delta_{\mathrm{BRS}} \xi^{a*} &= -\frac{1}{\alpha} \delta\omega \partial^\mu A^a_\mu \ , \\ \delta_{\mathrm{BRS}} \Psi &= i g_r T^a \delta\omega \xi^a \Psi \ , \\ \delta_{\mathrm{BRS}} \overline{\Psi} &= i g_r \overline{\Psi} T^a \delta\omega \xi^a \ , \end{aligned} \tag{B.20}$$

where $\delta\omega$ is an infinitesimal Grassmann variable $\delta\omega^2 = 0$, which anticommutes with the (Grassmann) ghost fields. The other notations for the fields and covariant derivatives correspond to those used in (4.2) to (4.5). We will for simplicity use the unrenormalized Lagrangian, but exactly the same derivations can be made for the renormalized Lagrangian, using the corresponding *renormalized* BRS transformations, see for example [64].

We consider the time-ordered four-point function $\langle 0|\mathrm{T}(\overline{\Psi}(x_4)\Psi(x_3)\xi^{a*}(x_1)A^b_\nu(x_2)|0\rangle$, where the fields are considered to be external and are to be used in the S-matrix. Its invariance under BRS transformations means

$$\begin{aligned} 0 &\overset{!}{=} \delta_{\mathrm{BRS}} \langle 0|\mathrm{T}(\overline{\Psi}\Psi\xi^{a*}A^b_\nu)|0\rangle \\ &= \langle 0|\mathrm{T}[(\delta_{\mathrm{BRS}}\overline{\Psi})\Psi\xi^{a*}A^b_\nu]|0\rangle + \langle 0|\mathrm{T}[\overline{\Psi}(\delta_{\mathrm{BRS}}\Psi)\xi^{a*}A^b_\nu]|0\rangle \\ &\quad + \langle 0|\mathrm{T}[\overline{\Psi}\Psi(\delta_{\mathrm{BRS}}\xi^{a*})A^b_\nu]|0\rangle + \langle 0|\mathrm{T}[\overline{\Psi}\Psi\xi^{a*}(\delta_{\mathrm{BRS}}A^b_\nu)]|0\rangle \ . \end{aligned} \tag{B.21}$$

Let us examine the first term in more detail, it yields with (B.20)

$$\begin{aligned} &\langle 0|\mathrm{T}[(\delta_{\mathrm{BRS}}\overline{\Psi}(x_4))\Psi(x_3)\xi^{a*}(x_1)A^b_\nu(x_2)]|0\rangle \\ &\qquad = i g_r \delta\omega \langle 0|\mathrm{T}[\overline{\Psi}(x_4)T^c\xi^c(x_4)\Psi(x_3)\xi^{a*}(x_1)A^b_\nu(x_2)]|0\rangle \ , \end{aligned} \tag{B.22}$$

Now we wish to know if this can contribute to the S-matrix. In the LSZ reduction formalism, $\langle 0|\mathrm{T}(\overline{\Psi}\Psi\xi^{a*}A^b_\nu)|0\rangle$ will be multiplied by the inverse propagators of the external fields, which for $\overline{\Psi}$ gives $\not{k}_4 - m$, i.e., the external legs are "amputated". Here we have considered the transformation to (external) momentum space with $x_{1,2,3,4} \to k_{1,2,3,4}$. But from the $\overline{\Psi}$ in the two particle state of (B.22), there will be no corresponding one particle propagator $\sim 1/(\not{k}_4 - m)$, since only the sum of the momenta of the two particles gives k_4. A momentum space representation of (B.22) is shown for illustration in Fig. B.3. Then taking the *on-shell* limit $\not{k}_4 \to m$ will give *zero* for the S-matrix contribution of (B.22), since there is no cancellation $(\not{k}_4 - m)/(\not{k}_4 - m) = 1$. The second term in (B.21) suffers the same fate when we put Ψ *on-shell*, and in the last term the covariant derivative reduces to a partial derivative if we set A^b_ν *on-shell*, since again the contribution due to two fields at one point vanishes with respect to the S-matrix. So we can, keeping the use with the S-matrix in mind, write (B.21) as

$$-\frac{1}{\alpha}\delta\omega\langle 0|\mathrm{T}[\overline{\Psi}\Psi(\partial^\mu A^a_\mu)A^b_\nu]|0\rangle + \delta\omega\langle 0|\mathrm{T}[\overline{\Psi}\Psi\xi^{a*}(\partial_\nu\xi^b)]|0\rangle = 0 \; . \tag{B.23}$$

Note that in the first term we now have two gluons, in the second a ghost and an antighost and that the only particle we did not have to set on-shell to proceed in our derivation was the original ghost field ξ^{a*}.

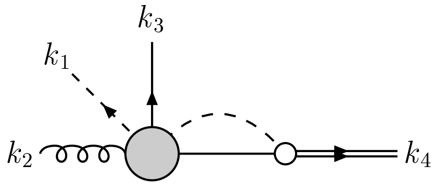

Figure B.3: The momentum space representation of (B.22) as it would appear in the S-matrix. This contribution vanishes due to the absence of a one-particle pole in k_4.

In Feynman gauge $\alpha = 1$ this will correspond to the condition on the amplitudes[4]

$$k_1^\mu M^{ab}_{\mu\nu} = -k_{2\nu} M^{ab}_{\mathrm{gh}} \; , \tag{B.24}$$

where on the l.h.s. we have a sum of all relevant amplitudes for two external gluons multiplied with k_1^μ, instead of a polarization vector $\varepsilon^\mu(k_1, \lambda_1)$. On the right hand side we have a corresponding sum of amplitudes, where instead of the gluons a ghost can "run through", i.e., since only connected diagrams contribute and one couples always a ghost-gluon-antighost, the external ghost and antighost are connected. Note that we can add an arbitrary number of external *on-shell* fermions without changing the derivation of (B.24). Also if the unreplaced gluon on the left hand side is *transverse*, then as we multiply by $\varepsilon_2^\nu = \varepsilon^\nu(k_2, \lambda_2)$ in the S-matrix and $\varepsilon_2 \cdot k_2 = 0$, the contribution vanishes. Hence we could also add an arbitrary number of external *transverse* on-shell gluons to the initial vacuum expectation value and still obtain (B.24). Obviously by exchanging positions and labels we can also derive

$$k_2^\nu M^{ab}_{\mu\nu} = -k_{1\mu} M^{ab}_{\mathrm{gh}} \; , \tag{B.25}$$

[4]Both sides will also be multiplied by the polarization tensor ε_2^ν of the gluon in the original vacuum expectation value to obtain the S-matrix.

and all considerations given above apply to the other leg, respectively. If we replace both polarization tensors with the momenta and set $k_1^2 = k_2^2 = 0$, then obviously

$$k_1^\mu k_2^\nu M_{\mu\nu}^{ab} = 0 \; . \tag{B.26}$$

The results (B.24) to (B.26) are the generalization in QCD of the well known result, that in QED due to gauge invariance we get zero when replacing a polarization vector by the corresponding momentum. We can now use (B.24) to (B.26) to easily calculate

$$P^{\mu\alpha}(k_1)P^{\nu\beta}(k_2)M_{\mu\nu}^{ab}M_{\alpha\beta}^{ab*} = (-g^{\mu\alpha})(-g^{\nu\beta})M_{\mu\nu}^{ab}M_{\alpha\beta}^{ab*} - M_{\mathrm{gh}\downarrow}^{ab}M_{\mathrm{gh}\uparrow}^{ab*} - M_{\mathrm{gh}\uparrow}^{ab}M_{\mathrm{gh}\downarrow}^{ab*} \; , \tag{B.27}$$

where $P^{\mu\alpha}(k_1)$ and $P^{\nu\beta}(k_2)$ are physical polarization tensors as defined by summing over λ_1 and λ_2, respectively, in (2.14). The arrows at the ghost amplitudes indicate the direction of the ghost line, from k_1 to k_2 or vice versa. The dependence on the arbitrary light-like η drops out completely and we have thus proven the "external ghost trick". The identity Fig. B.4 was derived first in [52] and later shown to survive the renormalization process in [53].

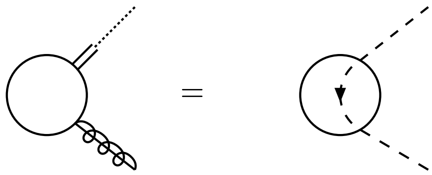

Figure B.4: Pictorial representation of the Slavnov-Taylor identity (B.24). The dotted line with a double line end represent the replacement of a polarization vector $\varepsilon_1^\mu \to k_1^\mu$ with possibly $k_1^2 \neq 0$, the spiral with line represents an on-shell gluon $k_2^2 = 0$ which is *not* transverse $\varepsilon_2 \cdot k_2 \neq 0$. The circle represents the set of all relevant Feynman graphs, and there can be other external lines which have to be on-shell (and for gluons transverse).

A second useful Slavnov-Taylor identity is obtained from $\langle 0|\mathrm{T}[(\partial^\mu A_\mu^a(x))\xi^{b*}(y)]|0\rangle$, where this time we put no conditions on the fields. Setting its BRS transformation to zero yields

$$\frac{1}{\alpha}\langle 0|\mathrm{T}[(\partial^\mu A_\mu^a(x))(\partial^\nu A_\nu^b(y))]|0\rangle \stackrel{!}{=} \langle 0|\mathrm{T}[(\partial^\mu D_\mu^{ab}\xi^b(x))\xi^{b*}(y)]|0\rangle = 0 \; , \tag{B.28}$$

where we have used the equation of motion for ξ^b from

$$\partial^\mu \frac{\partial \mathscr{L}}{\partial(\partial^\mu \xi^{a*})} - \frac{\partial \mathscr{L}}{\partial \xi^{a*}} = \partial^\mu D_\mu^{ab}\xi^b = 0 \; . \tag{B.29}$$

The choice for gauge fixing (4.3) leads to the following regularization prescription for equal times

$$\langle 0|\mathrm{T}[(\partial^\mu A_\mu^a(x))(\partial^\nu A_\nu^b(y))]|0\rangle = \partial_x^\mu \partial_y^\nu \langle 0|\mathrm{T}[A_\mu^a(x)A_\nu^b(y)]|0\rangle + i\delta_{ab}\delta^{(4)}(x-y) \; , \tag{B.30}$$

see [64]. Taking the Fourier transform $x - y \to k$ of $\langle 0|\mathrm{T}[A^a_\mu(x)A^b_\nu(y)]|0\rangle$ gives the full gluon propagator $\tilde{D}^{ab}_{\mu\nu}$ in momentum space, and we derive

$$\frac{i}{\alpha}k^\mu k^\nu \tilde{D}^{ab}_{\mu\nu} = \delta_{ab} \; . \tag{B.31}$$

Appendix C

Virtual Plus Soft Coefficients

First we list the polarized coefficients for the virtual plus soft ($V+S$) photon-gluon reduced partonic cross section as defined by (7.27), i.e., sorted according to their color-factors. Furthermore, the $\ln(\Delta/m^2)$ terms are collected in separate coefficients and all the logarithms depending on the renormalization scale μ_r have been rewritten, so that the only dependence now resides in the $\ln(\mu_r^2/\mu_f^2)$ of (C.5). Note that in [35] this coefficient was written with $\ln(\mu_r/\mu_f)$. ΔB_{QED} is given by (2.21), $\beta \equiv \sqrt{1-4m^2/s}$, $\varkappa \equiv (1-\beta)/(1+\beta)$, and t and u are defined in (2.18).

$$
\begin{aligned}
\Delta L_{\mathrm{QED}} = {} & \left[-t_1(2t_1+u_1)/(tu_1) - u_1(t_1+2u_1)/(t_1u)\right]/4 + \left[-4m^2s(2t_1^2 - t_1u_1 + 2u_1^2)\right. \\
& \left. + t_1u_1(5t_1^2 + 2t_1u_1 + 5u_1^2)\right]/(4t_1^2u_1^2) + \left\{\beta(2m^2s + t_1^2 + 4t_1u_1 + u_1^2)/(4t_1u_1)\right. \\
& \left. + \left[t_1^2u_1^2(3t_1^2 + 4t_1u_1 + 3u_1^2) + 4m^4(t_1^4 + 2t_1^3u_1 - 8t_1^2u_1^2 + 2t_1u_1^3 + u_1^4)\right]/(4t_1^3u_1^3)\right\}\zeta(2) \\
& - \left\{\beta(2m^2s + t_1^2 + 4t_1u_1 + u_1^2)/8 + (-24m^4 + 3t_1^2 + 4t_1u_1 + 3u_1^2)/8\right\}/(t_1u_1)\ln^2\varkappa \\
& + \Bigg\{ - \left[2m^2t_1^2(6m^4 + 9m^2t_1 + 4t_1^2) + t_1(2m^2 + t_1)(8m^4 + 9m^2t_1 + 2t_1^2)u_1\right. \\
& \left. + 3t(2m^2 + t_1)^2u_1^2\right]/(4t^2t_1^2u_1) - \left[st_1^2u_1(t_1 + 2u_1) + 4m^4(t_1^3 + 3t_1^2u_1 - t_1u_1^2 - u_1^3)\right. \\
& \left. + 2m^2(t_1^4 + t_1^3u_1 - 3t_1^2u_1^2 - 2t_1u_1^3 - u_1^4)\right]/(2\beta st_1^2u_1^2)\ln\varkappa\Bigg\}\ln\left(-\frac{t_1}{m^2}\right) \\
& + \Bigg\{ - \left[t_1u_1^3(3t_1 + 2u_1) + 4m^6(3t_1^2 + 4t_1u_1 + 3u_1^2) + m^2u_1^2(15t_1^2 + 13t_1u_1 + 8u_1^2)\right. \\
& \left. + 2m^4u_1(12t_1^2 + 13t_1u_1 + 9u_1^2)\right]/(4t_1u^2u_1^2) - \left[st_1u_1^2(2t_1 + u_1) - 4m^4(t_1^3 + t_1^2u_1\right. \\
& \left. - 3t_1u_1^2 - u_1^3) - 2m^2(t_1^4 + 2t_1^3u_1 + 3t_1^2u_1^2 - t_1u_1^3 - u_1^4)\right]/(2\beta st_1^2u_1^2)\ln\varkappa\Bigg\}\ln\left(-\frac{u_1}{m^2}\right) \\
& + \left\{(m^2s - t_1u_1)/(\beta t_1u_1) + \beta(2m^2s + t_1^2 + 4t_1u_1 + u_1^2)/(2t_1u_1)\ln(1+\varkappa)\right\}\ln\varkappa \\
& + \left\{2m^2t_1^2(u_1 - t_1) + t_1^2(2t_1^2 + 2t_1u_1 + u_1^2) - 2m^4(5t_1^2 + 2t_1u_1 + u_1^2)\right\}/(2t_1^3u_1) \\
& \cdot \mathrm{Li}_2\left(\frac{t}{m^2}\right) + \left\{2m^2(t_1 - u_1)u_1^2 + u_1^2(t_1^2 + 2t_1u_1 + 2u_1^2) - 2m^4(t_1^2 + 2t_1u_1 + 5u_1^2)\right\}
\end{aligned}
$$

$$
\begin{aligned}
&/(2t_1u_1^3)\,\mathrm{Li}_2\left(\frac{u}{m^2}\right)+\beta(2m^2s+t_1^2+4t_1u_1+u_1^2)/(2t_1u_1)\,\mathrm{Li}_2(-\varkappa)+\Delta B_{\mathrm{QED}}\\
&\cdot\left\{1+\frac{s-2m^2}{\beta s}\left(2\zeta(2)+\left[-1+\ln\left(\frac{-t_1}{m^2}\right)+\ln\left(-\frac{u_1}{m^2}\right)+4\ln(1-\varkappa)\right.\right.\right.\\
&\left.\left.\left.-\ln\varkappa\right]\ln\varkappa+4\,\mathrm{Li}_2(\varkappa)\right)\right\}/2\ ,
\end{aligned}
\tag{C.1}
$$

$$
\Delta L_{\mathrm{QED}}^{\Delta}=-\Delta B_{\mathrm{QED}}\left\{1+\frac{s-2m^2}{\beta s}\ln\varkappa\right\}\ln\frac{\Delta}{m^2}\ ,
\tag{C.2}
$$

$$
\begin{aligned}
\Delta L_{\mathrm{OK}}=&\ m^2s(t_1^2+u_1^2)/(2t_1^2u_1^2)+\Big\{-\beta(2m^2s+s^2+2t_1u_1)/(4t_1u_1)+\Big[-2t_1^2u_1^2(2t_1^2\\
&+t_1u_1+2u_1^2)+m^2st_1u_1(7t_1^2-8t_1u_1+7u_1^2)-m^4(t_1^4+2t_1^3u_1-26t_1^2u_1^2+2t_1u_1^3\\
&+u_1^4)\Big]/(2t_1^3u_1^3)\Big\}\zeta(2)+(-2m^2s+t_1^2+u_1^2)/(4t_1u_1)\left[\ln^2\left(-\frac{t_1}{m^2}\right)+\ln^2\left(-\frac{u_1}{m^2}\right)\right]\\
&-\left\{24m^4-3s^2+2t_1u_1-\beta(2m^2s+s^2+2t_1u_1)\right\}/(8t_1u_1)\ln^2\varkappa\\
&+\Big\{(m^2s+t_1^2)(-m^2s+t_1u_1)/(2tt_1^2u_1)+\left[t_1u_1(t_1^2+u_1^2)-2m^2s(2t_1^2-t_1u_1+2u_1^2)\right]\\
&/(2t_1^2u_1^2)\ln\left(-\frac{u_1}{m^2}\right)-\left\{st_1^2(s-u_1)u_1+2m^2\left[st_1^3+(s^2+2t_1^2)u_1^2\right]-4m^4\left[s^3+2t_1(s^2\right.\right.\\
&\left.\left.+\ t_1u_1)\right]\right\}/(2\beta st_1^2u_1^2)\ln\varkappa\Big\}\ln\left(-\frac{t_1}{m^2}\right)+\Big\{(-m^2s+t_1u_1)(m^2s+u_1^2)/(2t_1uu_1^2)\\
&-\left\{s(s-t_1)t_1u_1^2-4m^4\left[s^3+2u_1(s^2+t_1u_1)\right]+2m^2\left[su_1^3+t_1^2(s^2+2u_1^2)\right]\right\}/(2\beta st_1^2u_1^2)\\
&\cdot\ln\varkappa\Big\}\ln\left(-\frac{u_1}{m^2}\right)+\left\{-(m^2s-t_1u_1)/(\beta t_1u_1)-\beta(2m^2s+s^2+2t_1u_1)/(2t_1u_1)\right.\\
&\left.\cdot\ln(1+\varkappa)\right\}\ln\varkappa+\left\{m^2t_1^2(t_1-3u_1)-t_1^3(t_1+2u_1)+m^4(5t_1^2+2t_1u_1+u_1^2)\right\}/(2t_1^3u_1)\\
&\cdot\mathrm{Li}_2\left(\frac{t}{m^2}\right)+\left\{m^2u_1^2(-3t_1+u_1)-u_1^3(2t_1+u_1)+m^4(t_1^2+2t_1u_1+5u_1^2)\right\}/(2t_1u_1^3)\\
&\cdot\mathrm{Li}_2\left(\frac{u}{m^2}\right)-\beta(2m^2s+s^2+2t_1u_1)/(2t_1u_1)\,\mathrm{Li}_2(-\varkappa)+\Delta B_{\mathrm{QED}}\Big\{\Big[-3\zeta(2)\\
&+4\ln\frac{\mu_f^2}{m^2}\ln\left(-\frac{u_1}{m^2}\right)+\ln^2\frac{t_1}{u_1}-2\ln\frac{t_1}{u_1}\ln\varkappa-\ln^2\varkappa+2\,\mathrm{Li}_2\left(1-\frac{t_1}{u_1\varkappa}\right)\\
&-2\,\mathrm{Li}_2\left(1-\frac{u_1}{t_1\varkappa}\right)\Big]/4-\frac{s-2m^2}{\beta s}\Big[2\zeta(2)+\Big\{\ln\left(-\frac{t_1}{m^2}\right)+\ln\left(-\frac{u_1}{m^2}\right)\\
&+4\ln(1-\varkappa)-\ln\varkappa\Big\}\ln\varkappa+4\,\mathrm{Li}_2(\varkappa)\Big]/2\Big\}\ ,
\end{aligned}
\tag{C.3}
$$

$$
\Delta L_{\mathrm{OK}}^{\Delta}=\Delta B_{\mathrm{QED}}\left\{\ln\frac{\Delta}{m^2}-\ln\frac{\mu_f^2}{m^2}+\ln\frac{t_1}{u_1}+\frac{s-2m^2}{\beta s}\ln\varkappa\right\}\ln\frac{\Delta}{m^2}\ ,
\tag{C.4}
$$

$$\Delta L_{\mathrm{RF}} = \Delta B_{\mathrm{QED}} \ln \frac{\mu_r^2}{\mu_f^2} \,. \tag{C.5}$$

Next we list the coefficients of the *unpolarized* reduced $V+S$ partonic cross section for the quark-antiquark subprocess of hadroproduction, according to (7.49). The polarized parts follow *exactly* from $\Delta K_i = -K_i$ in each case, i.e., helicity is conserved. Again the coefficients are sorted according to their color-factors, the $\ln \Delta/m^2$ terms are collected separately, and the logarithms depending on the renormalization scale have been brought into the form $\ln \mu_r^2/\mu_f^2$ and are collected in (C.11). A_{QED} is given in (2.30).

$$\begin{aligned}
K_{\mathrm{QED}} = & -\frac{4(t_1-u_1)}{s\beta^2}\ln\frac{s}{m^2} - \frac{2(t_1-u_1)}{s}\left[2\zeta(2)+\ln^2\frac{s}{m^2}\right] - \frac{4(t_1u_1-2m^2s)}{st}\ln\left(-\frac{t_1}{m^2}\right) \\
& + \frac{4(t_1u_1-2m^2s)}{su}\ln\left(-\frac{u_1}{m^2}\right) + \frac{4m^2}{s\beta}\ln\varkappa + \frac{4(2m^2+t_1-u_1)}{s} \\
& \cdot\left[\ln\left(-\frac{s}{t_1}\right)\ln\left(-\frac{t_1}{m^2}\right) - \mathrm{Li}_2\left(\frac{t}{m^2}\right)\right] - \frac{4(2m^2-t_1+u_1)}{s} \\
& \cdot\left[\ln\left(-\frac{s}{u_1}\right)\ln\left(-\frac{u_1}{m^2}\right) - \mathrm{Li}_2\left(\frac{u}{m^2}\right)\right] - \frac{2(8m^4-8m^2s+s^2)(t_1-u_1)}{s^3\beta^3} \\
& \cdot\left[2\zeta(2)+\ln^2\varkappa+4\,\mathrm{Li}_2(-\varkappa)\right] + A_{\mathrm{QED}}\Bigg\{-10+4\zeta(2)+3\ln\frac{s}{m^2}-2\ln\frac{s}{m^2}\ln\frac{t_1u_1}{m^4} \\
& + \ln^2\frac{t_1u_1}{m^4} + \ln\frac{\mu_f^2}{m^2}\left[-3+2\ln\frac{t_1u_1}{m^4}\right] + \frac{1}{\beta}\ln\varkappa + 2\,\mathrm{Li}_2\left(1-\frac{m^2s}{t_1u_1}\right) - 8\Bigg[\ln\frac{t_1}{u_1} \\
& \cdot\left(\ln\frac{s}{m^2}+\ln\varkappa\right) - \mathrm{Li}_2\left(1-\frac{t_1}{\varkappa u_1}\right) + \mathrm{Li}_2\left(1-\frac{u_1}{\varkappa t_1}\right)\Bigg] - \frac{2m^2-s}{s\beta}\Big[6\zeta(2)+\ln\varkappa \\
& \cdot\left(-6+8\ln(1-\varkappa)-3\ln\varkappa+4\ln(1+\varkappa)\right)+4\,\mathrm{Li}_2(\varkappa)+2\,\mathrm{Li}_2(\varkappa^2)\Big]\Bigg\}\,,
\end{aligned} \tag{C.6}$$

$$K^{\Delta}_{\mathrm{QED}} = -4A_{\mathrm{QED}}\ln\frac{\Delta}{m^2}\left[1-\ln\frac{\Delta}{m^2}+\ln\frac{\mu_f^2}{m^2}-4\ln\frac{t_1}{u_1}+\ln\frac{t_1u_1}{m^2s}-\frac{2m^2-s}{s\beta}\ln\varkappa\right]\,, \tag{C.7}$$

$$\begin{aligned}
K_{\mathrm{OK}} = & -\frac{8m^2}{s\beta^2} + \frac{16m^4+12m^2s-s[s+3\beta^2(u_1-t_1)]}{s^2\beta^4}\ln\frac{s}{m^2} - \frac{2m^2-3t_1+3u_1}{2s} \\
& \cdot\left[2\zeta(2)+\ln^2\frac{s}{m^2}\right] + \frac{2(t_1u_1-2m^2s)}{st}\ln\left(-\frac{t_1}{m^2}\right) - \frac{4(t_1u_1-2m^2s)}{su}\ln\left(-\frac{u_1}{m^2}\right) \\
& - \frac{4m^2}{s\beta}\ln\varkappa - \frac{2(2m^2+t_1-u_1)}{s}\left[\ln\left(-\frac{s}{t_1}\right)\ln\left(-\frac{t_1}{m^2}\right)-\mathrm{Li}_2\left(\frac{t}{m^2}\right)\right] \\
& + \frac{4(2m^2-t_1+u_1)}{s}\left[\ln\left(-\frac{s}{u_1}\right)\ln\left(-\frac{u_1}{m^2}\right)-\mathrm{Li}_2\left(\frac{u}{m^2}\right)\right] \\
& - \frac{4m^2(16m^4-2m^2s+s^2)-3\beta^2(8m^4-8m^2s+s^2)(t_1-u_1)}{2s^3\beta^5}
\end{aligned}$$

$$\cdot\left[2\zeta(2)+\ln^2\varkappa+4\,\mathrm{Li}_2(-\varkappa)\right]+A_{\mathrm{QED}}\Bigg\{\frac{170}{9}+\frac{8m^2}{s\beta^2}-6\zeta(2)+\frac{22}{3}\ln\frac{\mu_f^2}{m^2}$$
$$+\left(-\frac{16}{3}+\frac{s-16m^2}{s\beta^4}\right)\ln\frac{s}{m^2}+\ln^2\frac{s}{m^2}-4\ln\left(-\frac{t_1}{m^2}\right)\ln\left(-\frac{u_1}{m^2}\right)-\frac{1}{\beta}\ln\varkappa$$
$$-\ln^2\varkappa-2\,\mathrm{Li}_2\left(1-\frac{m^2s}{t_1u_1}\right)+6\Bigg[\ln\frac{t_1}{u_1}\left(\ln\frac{s}{m^2}+\ln\varkappa\right)-\mathrm{Li}_2\left(1-\frac{t_1}{\varkappa u_1}\right)$$
$$+\mathrm{Li}_2\left(1-\frac{u_1}{\varkappa t_1}\right)\Bigg]+\frac{24m^4-7m^2s+s^2}{s^2\beta^5}\left[2\zeta(2)+\ln^2\varkappa+4\,\mathrm{Li}_2(-\varkappa)\right]$$
$$+\frac{2m^2-s}{s\beta}\Big[6\zeta(2)+\ln\varkappa\left(-4+8\ln(1-\varkappa)-3\ln\varkappa+4\ln(1+\varkappa)\right)+4\,\mathrm{Li}_2(\varkappa)$$
$$+2\,\mathrm{Li}_2(\varkappa^2)\Big]\Bigg\}\,, \tag{C.8}$$

$$K_{\mathrm{OK}}^{\Delta}=4A_{\mathrm{QED}}\ln\frac{\Delta}{m^2}\left[-3\ln\frac{t_1}{u_1}+\ln\frac{t_1u_1}{m^2s}-\frac{2m^2-s}{s\beta}\ln\varkappa\right]\,, \tag{C.9}$$

$$K_{\mathrm{QL}}=\frac{4}{3}A_{\mathrm{QED}}\left[-\frac{5(n_{lf}+1)}{3}-\frac{4m^2}{s}+n_{lf}\left(\ln\frac{s}{m^2}-\ln\frac{\mu_f^2}{m^2}\right)-\frac{\beta(s+2m^2)}{s}\ln\varkappa\right]\,, \tag{C.10}$$

$$K_{\mathrm{RF}}=A_{\mathrm{QED}}\ln\frac{\mu_r^2}{\mu_f^2}\,. \tag{C.11}$$

Bibliography

[1] C. Caso et al., Particle Data Group, Eur. Phys. J. **C3** (1998) 1.

[2] V. S. Shirley, C. M. Baglin, S. Y. F. Chu and J. Zipkin, eds., *Table of Isotopes, 8th Ed.*, John Wiley & Sons, 1996.

[3] M. Anselmino, A. Efremov and E. Leader, Phys. Rep. **261** (1995) 1. Erratum: **281** (1997) 399.

H.-Y. Cheng, Int. J. Mod. Phys. **A11** (1996) 5109.

M. C. Vetterli, in *Quantum Chromodynamics*, edited by A. Astbury, B. A. Campbell, F. C. Khanna, J. L. Pinfold and M. Vetterli, p. 49, Proceedings of the *Lake Louise Winter Institute*, Lake Louise, Canada, World Scientific, 1998.

[4] B. Lampe and E. Reya, *Spin Physics and Polarized Structure Functions*, Report DO-TH 98/02 and MPI-PhT/98-23, Universität Dortmund and Max-Planck-Institut für Physik, 1998. `hep-ph/9810270`.

[5] F. E. Close, *An Introduction to Quarks and Partons*, Academic Press, 1979.

[6] F. E. Close and R. G. Roberts, Phys. Lett. **B316** (1993) 165.

[7] L. M. Sehgal, Phys. Rev. **D10** (1974) 1663. Erratum: **D11** (1975) 2016.

[8] R. L. Jaffe and A. Manohar, Nucl. Phys. **B337** (1990) 509.

[9] M. Gourdin, Nucl. Phys. **B38** (1972) 418.

J. Ellis and R. L. Jaffe, Phys. Rev. **D9** (1974) 1444. Erratum: **D10** (1974) 1669.

[10] J. D. Bjørken, Phys. Rev. **148** (1966) 1467.

J. D. Bjørken, Phys. Rev. **D1** (1970) 1376.

[11] J. Ashman et al., EM Collab., Phys. Lett. **B206** (1988) 364.

J. Ashman et al., EM Collab., Nucl. Phys. **B328** (1989) 1.

[12] K. Abe et al., E143 Collab., Phys. Rev. Lett. **74** (1995) 346.

K. Abe et al., E143 Collab., Phys. Rev. Lett. **75** (1995) 25.

[13] B. Adeva et al., SM Collab., Phys. Lett. **B412** (1997) 414.

[14] J. Kodaira, S. Matsuda, K. Sasaki and T. Uematsu, Nucl. Phys. **B159** (1979) 99.

J. Kodaira, S. Matsuda, M. Muta, K. Sasaki and T. Uematsu, Phys. Rev. **D20** (1979) 627.

S. A. Larin and J. A. M. Vermaseren, Phys. Lett. **B259** (1991) 345.

[15] M. Glück, E. Reya, M. Stratmann and W. Vogelsang, Phys. Rev. **D53** (1996) 4775.

[16] E. Leader, A. V. Sidorov and D. B. Stamenov, Phys. Lett. **B462** (1999) 189.

Y. Goto et al., AA Collab., *Polarized Parton Distribution Functions from the A_1 Asymmetry Data*, Report RIKEN-AF-NP-324, SAGA-HE-143-99, KOBE-FHD-99-03 and FUT-99-02, The Institute of Physical and Chemical Research (RIKEN) and other institutions, 1999. `hep-ph/0001046`.

[17] D. de Florian, O. A. Sampayo and R. Sassot, Phys. Rev. **D57** (1998) 5803.

[18] T. Gehrmann and W. J. Stirling, Phys. Rev. **D53** (1996) 6100.

[19] B. Adeva et al., SM Collab., Phys. Rev. **D58** (1998) 112002.

[20] R. D. Ball, S. Forte and G. Ridolfi, Phys. Lett. **B378** (1996) 255.

[21] M. Klein, *Structure Functions in Deep Inelastic Lepton-Nucleon Scattering*, Talk given at the *"19th International Symposium on Lepton and Photon Interactions at High-Energies, LP 99"*, Stanford, USA, 9-14 Aug 1999. `hep-ex/0001059`.

[22] C. Adloff et al., H1 Collab., Nucl. Phys. **B545** (1999) 21.

[23] W. Vogelsang and A. Vogt, Nucl. Phys. **B453** (1995) 334.

J. Huston et al., Phys. Rev. **D58** (1998) 114034.

H. L. Lai et al., CTEQ Collab., Eur. Phys. J. **C12** (2000) 375.

[24] A. D. Martin, R. G. Roberts, W. J. Stirling and R. S. Thorne, Eur. Phys. J. **C4** (1998) 463.

M. Glück, E. Reya and A. Vogt, Eur. Phys. J. **C5** (1998) 461.

A. D. Martin, R. G. Roberts, W. J. Stirling and R. S. Thorne, *Parton Distributions and the LHC: W and Z Production*, Report DTP-99-64, Durham University, 1999.

[25] J. Blümlein, A. De Roeck, T. Gehrmann and W.-D. Nowak, eds., Proceedings of the Workshop *"Deep Inelastic Scattering off Polarized Targets"*, Zeuthen, Germany, DESY, 1997. Report DESY 97-200.

E. W. Hughes and R. Voss, Annu. Rev. Nucl. Part. Sci. **49** (1999) 303.

[26] R. Mertig and W. L. van Neerven, Z. Phys. **C70** (1996) 637.

[27] W. Vogelsang, Phys. Rev. **D54** (1996) 2023.

W. Vogelsang, Nucl. Phys. **B475** (1996) 47.

[28] A. De Roeck and T. Gehrmann, eds., Proceedings of the Workshop *"Physics with Polarized Protons at HERA"*, Hamburg and Zeuthen, Germany, DESY, 1997. Report DESY 97-233.

[29] A. Airapetian et al., HERMES Collab., *Measurement of the Spin Asymmetry in the Photoproduction of Pairs of High-p_T Hadrons at HERMES*, Report DESY-99-071, DESY, 1999. To appear in Phys. Rev. Lett.

[30] D. de Florian, M. Stratmann and W. Vogelsang, *private communication.*

[31] G. Baum et al., COMPASS Collab., *Common Muon and Proton Apparatus for Structure and Spectroscopy*, Report CERN/SPSLC 96-14, CERN, 1996.

G. Baum et al., COMPASS Collab., *Common Muon and Proton Apparatus for Structure and Spectroscopy – Addendum 1*, Report CERN/SPSLC 96-30, CERN, 1996.

[32] D. Hill et al., RHIC Spin Collab., *Letter of Intent*, Report RHIC-SPIN-LOI-1991, updated 1993, RIKEN BNL Research Center, 1991.

G. Bunce et al., RHIC Spin Collab., Particle World **3** (1992) 1.

Proceedings of the *RSC Annual Meeting,* Marseille, France, Centre de Physique Théorique, 1996. CPT-96/P.3400.

Proceedings of the 1998/2000 Workshops *"RHIC Spin Physics" / "Predictions and Uncertainties for RHIC Spin Physics",* RIKEN BNL Research Center, New York, USA, Brookhaven National Laboratory, to appear.

[33] M. Stratmann and W. Vogelsang, in *Future Physics at HERA*, edited by G. Ingelman, A. De Roeck and R. Klanner, p. 815, Proceedings of the 1995/96 Workshop *"Future Physics at HERA"*, Hamburg, Germany, DESY, 1996.

M. Stratmann and W. Vogelsang, Z. Phys. **C74** (1997) 641.

[34] I. Bojak and M. Stratmann, Phys. Lett. **B433** (1998) 411.

[35] I. Bojak and M. Stratmann, Nucl. Phys. **B540** (1999) 345.

[36] L. E. Gordon and W. Vogelsang, Phys. Rev. **D48** (1993) 3136.

[37] I. Bojak and M. Stratmann, Erratum for Nucl. Phys. **B540** (1999) 345: **B569** (2000) 694 and Erratum for Phys. Lett. **B433** (1998) 411: to be published.

[38] I. Bojak, in *DIS '99*, edited by J. Blümlein and T. Riemann, p. 599, Proceedings of the *"7th International Workshop on Deep Inelastic Scattering and QCD, DIS '99"*, Zeuthen, Germany, 1999,. Nucl. Phys. **B** (Proc. Suppl.) **79** (1999) October 1999.

[39] M. Glück and E. Reya, Z. Phys. **C39** (1988) 569.

[40] G. Altarelli and W. J. Stirling, Particle World **1** (1989) 40.

M. Glück, E. Reya, and W. Vogelsang, Nucl. Phys. **B351** (1991) 579.

S. I. Alekhin, V. I. Borodulin and S. F. Sultanov, Int. J. Mod. Phys. **A8** (1993) 1603.

S. Keller and J. F. Owens, Phys. Rev. **D49** (1994) 1199.

S. Frixione and G. Ridolfi, Phys. Lett. **B383** (1996) 227.

[41] A. P. Contogouris, S. Papadopoulos and B. Kamal, Phys. Lett. **B246** (1990) 523.

M. Karliner and R. W. Robinett, Phys. Lett. **B324** (1994) 209.

[42] R. K. Ellis and P. Nason, Nucl. Phys. **B312** (1988) 551.

[43] S. Dawson, R. K. Ellis and P. Nason, Nucl. Phys. **B303** (1988) 607.

[44] W. J. P. Beenakker, H. Kuijf, W. L. van Neerven and J. Smith, Phys. Rev. **D40** (1989) 54.

[45] W. J. P. Beenakker, W. L. van Neerven, R. Meng, G. A. Schuler and J. Smith, Nucl. Phys. **B351** (1991) 507.

[46] J. Smith and W. L. van Neerven, Nucl. Phys. **B374** (1992) 36.

[47] G. Passarino and W. Veltman, Nucl. Phys. **B160** (1979) 151.

[48] N. S. Craigie, K. Hidaka, M. Jacob and F. M. Renard, Phys. Rep. **99**, Nos. 2 & 3 (1983) 69.

[49] J. Babcock, D. Sivers and S. Wolfram, Phys. Rev. **D18** (1978) 162.

[50] T.-P. Cheng and L.-F. Li, *Gauge Theory of Elementary Particle Physics*, Clarendon Press, 1984.

[51] G. Sterman, *An Introduction to Quantum Field Theory*, Cambridge University Press, 1993.

[52] G. 't Hooft, Nucl. Phys. **B33** (1971) 173.

[53] J. C. Taylor, Nucl. Phys. **B33** (1971) 436.

[54] G. 't Hooft and M. Veltman, Nucl. Phys. **B44** (1972) 189.
P. Breitenlohner and D. Maison, Comm. Math. Phys. **52** (1977) 11.

[55] K. Gottfried and J. D. Jackson, Nuovo Cim. **34** (1964) 735.

[56] R. K. Ellis, M. A. Furman, H. E. Haber and I. Hinchliffe, Nucl. Phys. **B173** (1980) 397.

[57] S. Wolfram, `Mathematica` – *Ver. 3 or higher*, Wolfram Research, 1997.

[58] M. Jamin and M. E. Lautenbacher, Comp. Phys. Comm. **74** (1993) 265.

[59] L. M. Jones and H. W. Wyld, Phys. Rev. **D17** (1978) 759.

[60] B. Kamal, Z. Merebashvili and A. P. Contogouris, Phys. Rev. **D51** (1995) 4808.
G. Jikia and A. Tkabladze, Phys. Rev. **D54** (1996) 2030.

[61] M. Glück, J. F. Owens and E. Reya, Phys. Rev. **D17** (1978) 2324.
B. L. Combridge, Nucl. Phys. **B151** (1979) 429.

[62] M. Glück, E. Reya and A. Vogt, Z. Phys. **C67** (1995) 433.

[63] G. K. Mallot, *Accessing the Gluon Polarisation in Deep Inelastic Muon Scattering*, `http://www.compass.cern.ch/compass/sp/ps/erice_95.ps.gz`. Talk given at the Conference *"Quarks in Hadrons and Nuclei"*, Erice, Italy, 19-27 Sept. 1995.

[64] T. Muta, *Foundations of Quantum Chromodynamics*, World Scientific, 1987.

[65] M. A. Nowak, M. Praszalowicz and W. Slomiński, Ann. Phys. (NY) **166** (1986) 443.

[66] M. Abramowitz and I. A. Stegun, eds., *Handbook of Mathematical Functions*, National Bureau of Standards, 1964.

[67] W. J. P. Beenakker, *Electroweak Corrections: Techniques and Applications*, Ph.D. thesis, University of Leiden, 1989.

[68] S. Pokorski, *Gauge Field Theories*, Cambridge University Press, 1987.

[69] P. Pascual and R. Tarrach, *QCD: Renormalization for the Practitioner*, Springer, 1984.

[70] F. Bloch and A. Nordsieck, Phys. Rev. **52** (1937) 54.
A. Nordsieck, Phys. Rev. **52** (1937) 59.
T. Kinoshita, J. Math. Phys. **3** (1962) 650.
T. D. Lee and M. Nauenberg, Phys. Rev. **133** (1964) B1549.

[71] S. Qian, *A New Renormalization Prescription (CWZ Subtraction Scheme) for QCD and its Application to DIS*, Report ANL-HEP-PR-84-72, Argonne National Laboratory, 1984.

[72] A. A. Slavnov, Teor. Mat. Fiz. **10** (1972) 153. [Theor. Math. Phys. **10** (1973) 99].

[73] J. C. Ward, Phys. Rev. **78** (1950) 182.

Y. Takahashi, Nuovo Cim. **6** (1957) 371.

[74] J. C. Collins, *Renormalization*, Cambridge University Press, 1984.

[75] C. Becchi, A. Rouet and R. Stora, Ann. Phys. (NY) **98** (1976) 287.

[76] J. C. Collins, F. Wilczek and A. Zee, Phys. Rev. **D18** (1978) 242.

[77] J. C. Collins, Phys. Rev. **D58** (1998) 094002.

[78] D. Coleman and D. Gross, Phys. Rev. Lett. **31** (1973) 851.

[79] D. R. T. Jones, Nucl. Phys. **B75** (1974) 531.

W. E. Caswell, Phys. Rev. Lett. **33** (1974) 244.

É. Sh. Egoryan and O. V. Tarasov, Teor. Mat. Fiz. **41** (1979) 26. [Theor. Math. Phys. **41** (1979) 863].

[80] R. Tarrach, Nucl. Phys. **B183** (1981) 384.

[81] W. J. P. Beenakker, *private communication.*

[82] I. S. Gradshteyn and I. M. Ryzhik, *Table of Integrals, Series, and Products — Corrected and Enlarged Edition*, Academic Press, 1980.

[83] W. L. van Neerven, Nucl. Phys. **B268** (1986) 453.

[84] R. K. Ellis, H. Georgi, M. Machacek, H. D. Politzer and G. G. Ross, Nucl. Phys. **B152** (1979) 285.

[85] G. Altarelli and G. Parisi, Nucl. Phys. **B126** (1977) 298.

M. A. Ahmed and G. G. Ross, Nucl. Phys. **B111** (1976) 441.

V. N. Gribov and L. N. Lipatov, Yad. Fiz. **15** (1972) 781 and 1218. [Sov. J. Nucl. Phys. **15** (1972) 438 and 675].

Yu. L. Dokshitzer, Zh. Eksp. Teor. Fiz **73** (1977) 1216. [Sov. Phys. JETP **46** (1977) 641].

[86] F. Halzen and A. D. Martin, *Quarks and Leptons*, John Wiley & Sons, 1984.

[87] F. E. Paige, *QCD and Event Simulation*, Report BNL-43525, Brookhaven National Laboratory, Lectures given at the *Theoretical Advanced Summer Institute*, Boulder, USA, 1989.

[88] I. Bojak, *Gluonen und Strukturfunktionen bei kleinen Bjørken x*. Diploma Thesis, Universität Dortmund, Germany, 1995 (unpublished).

[89] E. G. Floratos, D. A. Ross and C. T. Sachrajda, Nucl. Phys. **B129** (1977) 66. Erratum: **B139** (1978) 545.

E. G. Floratos, D. A. Ross and C. T. Sachrajda, Nucl. Phys. **B152** (1979) 493.

A. González-Arroyo, C. López and F. J. Ynduráin, Nucl. Phys. **B153** (1979) 161.

A. González-Arroyo and C. López, Nucl. Phys. **B166** (1980) 429.

G. Curci, W. Furmanski and R. Petronzio, Nucl. Phys. **B175** (1980) 27.

W. Furmanski and R. Petronzio, Phys. Lett. **B97** (1980) 437.

E. G. Floratos, C. Kounnas and R. Lacaze, Nucl. Phys. **B192** (1981) 417.

W. Furmanski and R. Petronzio, Z. Phys. **C11** (1982) 293.

R. Hamberg and W. L. van Neerven, Nucl. Phys. **B379** (1992) 143.

[90] F. Oberhettinger, *Tables of Mellin Transforms*, Springer, 1974.

[91] M. Glück and W. Vogelsang, Z. Phys. **C55** (1992) 353.

M. Glück and W. Vogelsang, Z. Phys. **C57** (1993) 309.

M. Glück, M. Stratmann and W. Vogelsang, Phys. Lett. **B337** (1994) 373.

[92] M. Glück, E. Reya and A. Vogt, Phys. Rev. **D46** (1992) 1973.

M. Glück, E. Reya and I. Schienbein, Phys. Rev. **D60** (1999) 054019.

[93] M. Stratmann and W. Vogelsang, Phys. Lett. **B386** (1996) 370.

[94] M. Glück, E. Reya and A. Vogt, Phys. Rev. **D45** (1992) 3986.

[95] J. Kubar-André and F. E. Paige, Phys. Rev. **D19** (1979) 221.

B. Humpert and W. L. van Neerven, Nucl. Phys. **B184** (1981) 225.

[96] D. de Florian, S. Frixione, A. Signer and W. Vogelsang, Nucl. Phys. **B539** (1999) 455.

[97] G. Tsipolitis, *private communication.*

[98] E. Braaten, B. A. Kniehl and J. Lee, *Polarization of prompt J/ψ at the Tevatron*, Report DESY-99-175, DESY, 1999. `hep-ph/9911436`.

G. T. Bodwin, E. Braaten and G. P. Lepage, Phys. Rev. **D51** (1995) 1125.

[99] J. F. Amundson, O. J. P. Éboli, E. M. Gregores and F. Halzen, Phys. Lett. **B372** (1996) 127.

J. F. Amundson, O. J. P. Éboli, E. M. Gregores and F. Halzen, Phys. Lett. **B390** (1997) 323.

[100] A. Sansoni et al., CDF Collab., Nuovo Cim. **109A** (1996) 827.

[101] C. F. von Weizsäcker, Z. Phys. **88** (1934) 612.

E. J. Williams, Phys. Rev. **45** (1934) 729.

[102] S. Frixione, M. L. Mangano, P. Nason and G. Ridolfi, Phys. Lett. **B319** (1993) 339.

[103] D. de Florian and S. Frixione, Phys. Lett. **B457** (1999) 236.

[104] C. Peterson, D. Schlatter, I. Schmitt and P. M. Zerwas, Phys. Rev. **D27** (1983) 105.

[105] J. C. Anjos et al., E691 Collab., Phys. Rev. Lett. **62** (1989) 513.

M. P. Alvarez et al., NA14/2 Collab., Z. Phys. **C60** (1993) 53.

G. Bellini, in *Results and Perspective in Particle Physics*, edited by M. Greco, p. 435, Proceedings of *"Les Rencontres de Physique de la Vallé d'Aoste"*, La Thuille, France, Editions Frontières, 1994.

[106] S. Frixione, M. L. Mangano, P. Nason and G. Ridolfi, in *Heavy Flavours II*, edited by A. J. Buras and M. Lindner, Advanced Series on Directions in High Energy Physics – Vol. 15, p. 609, World Scientific, 1998.

[107] E. Norrbin and T. Sjöstrand, Phys. Lett. **B442** (1998) 407.

[108] A. Bravar, D. von Harrach and A. Kotzinian, Phys. Lett. **B421** (1998) 349.

[109] B. W. Harris, *Open Charm Production in Deep Inelastic Scattering at Next-to-Leading Order at HERA*, Report ANL-HEP-CP-99-69, Argonne National Laboratory, 1999. To appear in the Proceedings of the Ringberg Workshop *"New Results from HERA"*, Schloß Ringberg, Germany, 1999. `hep-ph/9909310`.

[110] E. Norrbin and T. Sjöstrand, in *Monte Carlo Generators for HERA physics*, edited by T. A. Doyle, G. Grindhammer, G. Ingelman and H. Jung, p. 506, Proceedings of the 1998 Workshop *"Monte Carlo Generators for HERA Physics"*, Hamburg, Germany, DESY, 1999.

[111] J. Breitweg et al., ZEUS Collab., Eur. Phys. J. **C6** (1999) 67.

[112] M. E. Hayes and M. Kramer, J. Phys. **G25** (1999) 1477.

[113] Y. Eisenberg, ZEUS Coll., in *DIS '99*, edited by J. Blümlein and T. Riemann, p. 406, Proceedings of the *"7th International Workshop on Deep Inelastic Scattering and QCD, DIS '99"*, Zeuthen, Germany, 1999,. Nucl. Phys. **B** (Proc. Suppl.) **79** (1999) October 1999.

[114] P. Nason et al., LHC Bottom Production Working Group, *Bottom Production*, Report `hep-ph/0003142`, CERN, 2000. To appear in the Proceedings of the *"1999 CERN Workshop on Standard Model Physics (and more) at the LHC (First Plenary Meeting)"*.

[115] M. M. Baarmand, *b-Quark Production at Tevatron*, Talk given at the *"1999 CERN Workshop on Standard Model Physics (and more) at the LHC (First Plenary Meeting) – LHC Bottom Production Working Group"*.

[116] C. Adloff et al., H1 Collab., Phys. Lett. **B467** (1999) 156.

[117] G. Ingelman, J. Rathsman and G. A. Schuler, Comp. Phys. Comm. **101** (1997) 135.

[118] P. Newman, H1 Coll., in *DIS '99*, edited by J. Blümlein and T. Riemann, p. 413, Proceedings of the *"7th International Workshop on Deep Inelastic Scattering and QCD, DIS '99"*, Zeuthen, Germany, 1999,. Nucl. Phys. **B** (Proc. Suppl.) **79** (1999) October 1999.

[119] M. Wing, ZEUS Coll., in *DIS '99*, edited by J. Blümlein and T. Riemann, p. 416, Proceedings of the *"7th International Workshop on Deep Inelastic Scattering and QCD, DIS '99"*, Zeuthen, Germany, 1999,. Nucl. Phys. **B** (Proc. Suppl.) **79** (1999) October 1999.

[120] M. M. Baarmand, *Recent Tevatron Results on b Quark Production*, Report FERMILAB-Conf-99/145-E, Fermi National Accelerator Laboratory, 1999. To appear in the Proceedings of the *"XXXIVth Rencontres de Moriond, QCD and High Energy Hadronic Interactions"*, Les Arcs, France, 1999.

[121] A. P. Contogouris, Z. Merebashvili and G. Grispos, *Polarized Photoproduction of Heavy Quarks in Next-to-Leading Order*, Report MCGILL-00-02 and UA/NPPS-01-00, McGill University and University of Athens, 2000. `hep-ph/0003204`.

[122] A. Devoto and D. W. Duke, Riv. Nuovo Cim. **7** (1984) 1.

[123] A. Erdélyi, W. Magnus, F. Oberhettinger and F. G. Tricomi, *Higher Transcendental Functions*, McGraw-Hill, 1953.

[124] J. Vermaseren, in *Perturbative and Nonperturbative Aspects of Quantum Field Theory*, edited by H. Latal and W. Schweiger, p. 255, Proceedings of the *"35. Internationale Universitätswochen für Kern- und Teilchenphysik"*, Schladming, Austria, Springer, 1997.

[125] M. Gell-Mann, Phys. Rev. **125** (1962) 1067.

[126] C. H. Llewellyn Smith, in *Quantum Flavordynamics, Quantum Chromodynamics, and Unified Theories*, edited by K. T. Mahanthappa and J. Randa, p. 59, Proceedings of the *1979 Nato Advanced Study Institute at the University of Colorado*, Boulder, USA, Plenum Press, 1979.

Acknowledgements

It is a pleasure to thank Prof. Dr. E. Reya for suggesting this very interesting research topic to me. His generous support and his helpful advice have kept me on track through the years. I have benefitted continuously from his ability to spot what is important.

I am also particularly grateful to Dr. M. Stratmann for the fruitful collaboration on this project. He has generously shared his insight with me and his knowledge has guided this investigation. It is amazing how well we have worked together, in spite of communicating only by email most of the time.

My colleagues next door, Dr. S. Kretzer and I. Schienbein, have sacrificed many hours of their valuable time for physics discussions with me. The free exchange of ideas with them has been very helpful and I enjoyed it immensely. I would also like to thank the last three persons for critically reading parts of the manuscript and J. Noritzsch for some LaTeX magic that improved its looks.

Finally, I would like express my gratitude to Prof. Dr. M. Glück and all the other members of TIV for creating such an inspiring work environment. The sheer number of talented, successful and open (former) TIV members I have met speaks for itself.